Characterisation of Macromolecules Using Electrospray Ionization and Fourier Transform Ion Cyclotron Resonance Mass Spectrometry

by

Liam Andrew McDonnell, MCHEM

A thesis submitted for the degree of

Doctor of Philosophy

Department of Chemistry

University of Warwick

September 2001

Contents

List of Figures

was dependent on m/z only whereas the kinetic energy was directly proportional to the ion's charge state. The simulations were run using a 10 mm mean free path and 3.54×10^{-13} C of space charge.

acetic acid was added, was used to spray the synthesised dye.

to ionise AX*.

spectrum.

List of tables

ethylene glycol unit peak.

List of reaction schemes

Acknowledgments

I would like to thank the following people for their help and advice, without which this thesis would not have been possible.

- My current supervisor Professor Peter J Derrick for allowing me to continue my PhD, and above all else his patience, help and advice.

- My initial supervisor Professor Albert J. R. Heck for giving me the opportunity to undertake this project, as well as his friendship, training and advice.

- Prof. David Parker and Dr Bernard Bakker who helped me obtain and understand the ion imaging results; Dr Anastassios Giannakopulos for his help and advice with the hexapole simulations; Dr Philip Double who helped me carryout the synthesis of poly – AQ – poly described here-in; Dr Roland Jertz and Dr Göhkan Baykut for their insight; and finally Brian Powell for his continual encouragment.

- Past and present colleagues Dr Daniel Lafitte, Dr Tessa Hill, Dr Helen Cooper, Dr Xidong Feng, Dr James Wallace, Dr Antuan Hoxha, Dr Mark Barrow, Marjaana Nousiainen, Philip Green, Jennifer Mitchell, Sajid Bashir and Alex Colburn and for their friendship and advice.

- Friends Laney, Wayne, Dunc, Nick, Danny, Pete, and Jim.

- EPSRC and Avecia for their financial support.

- Last but by no means least thanks to family for your love, support and continual encouragement.

Declaration

I hereby declare that this thesis is my own work and that, to the best of my knowledge and belief, it contains no material previously published or written by another person, nor material which has been accepted for the award of any other degree or diploma of a University or Institute of Higher Education, except where due acknowledgement is made in the text.

Liam Andrew McDonnell MCHEM

Abstract

Multipole storage-assisted dissociation (MSAD), in which ions are stored for extended periods of time in a multipole ion-trap, represents one of the most recent and simplest methods by which structurally informative fragments can be obtained. A potential array investigation of MSAD is reported. It was found that the average kinetic energy of the ion was similar to the energy of a single IR photon and the average kinetic energy of an ion during sustained off-resonance irradiation collision-induced dissociation (SORI-CID), thus explaining the similar fragments that have been obtained using these techniques.

The ion's average kinetic energy and its collision frequency was investigated as a function of the ion's charge, mass and mean free path, the space charge present in the hexapole ion trap and the applied radio frequency (RF) potential. All but one of the dependencies, namely the RF potential dependence, were in agreement with experimental results. The disagreement between the experimental results and the simulation results was due to the rate of charge accumulation depending on the applied RF potential.

Without prior isolation, MSAD is limited in that it does not permit the isolation of a parent ion and the detection of all fragment ions. Collision-induced dissociation (CID) inside a Fourier transform ion cyclotron resonance (FTICR) cell permits the isolation, fragmentation and detection of all daughter ions. Furthermore the inherent advantages of FTICR mass spectrometry, higher resolution and mass accuracy, are also afforded to the fragment ions as well as the initial parent ions. Using this technique, all of the components of a commercially available polymeric dye were assigned and the more intense components structurally characterised. This structural characterization highlighted new information regarding the low-energy multiple collision CID of substituted polyesters. Included in these findings was the charge-induced nature of the 1,4-H rearrangement, the participation of amino groups in the fragmentation mechanisms the collisional ring opening of a cyclic polymer.

The two previous techniques involve collisions with neutral atoms to increase the internal energy (vibrational) of the ion to obtain the structurally informative fragments. In a similar manner, the fragments obtained after electronic excitation provide a powerful tool with which the electronic structure of molecules can be studied. An ion imaging study of HCl (2+1) resonance-enhanced multiphoton ionisation (REMPI) revealed new predissociation channels, an electronic-vibrational-rotational state dependence of the angular distribution of the fragments and vibrational state dependent HCl^+ photodissociation. The additional predissociation channels continued the pseudo-Rydberg continuum of the superexcited states responsible for the previously detected predissociation channels. The complicated angular distribution behavior of the fragments is thought to reflect the diabatic state character of the resonant state, which then determines which superexcited states are accessible.

Abbreviations

2D	Two-dimensional
3D	Three-dimensional
a.i.	Arbitrary intensity
AQ	diaminoanthraquinone
BBO	β-Bariumborate
BDE	Bond dissociation energy (D_0)
BIRD	Blackbody infrared dissociation
CE	Capillary electrophoresis
CAD	Collision-activated dissociation
CCD	Charge coupled device
CID	Collision-induced dissociation
CIEF	Capillary iso-electric focusing
COSE	Correlated sweep excitation
CT	Connecticut
DBE	Double bond equivalence
DMAP	4-Dimethylammoniumpyridine
DMSO	Dimethylsulfoxide
DNA	DeoxyriboNucleic Acid
ECD	Electron capture dissociation
EO/PO	Ethyleneoxide / propylene oxide copolymer
ESI	Electrospray ionization
eV	Electron volts
FT	Fourier transform
FFT	Fast Fourier transform
FID	Free-induction decay

FRAGMENT	Focused radiation for gaseous multiphoton energy transfer
FTICR	Fourier transform ion cyclotron resonance
FWHM	Full width half maximum
GPC	Gel permeation chromatography
HP	Hewlett Packard
HPLC	High performance liquid chromatography
ICR	Ion cyclotron resonance
IE	Ionization energy
IRMPD	Infrared multiphoton dissociation
KE	Kinetic energy
KER	Kinetic energy release
LC	Liquid chromatography
LIF	Laser-induced fluorescence
MALDI	Matrix-assisted laser desorption/ionisation
MCP	Microchannel plate
MS	Mass spectrometry
MSAD	Multipole storage assisted dissociation
mpeg	methoxypolyethyleneglycol
NMR	Nuclear magnetic resonance
Pdi	Polydispersity index
peg	polyethyleneglycol
PES	Photoelectron spectroscopy
ppm	Parts per million
QEA	Quadrupolar excitation axialization
REMPI	Resonance-enhanced multiphoton dissociation
r.i.	Relative intensity

RF	Radio frequency
SFF	Space-fixed frame
SID	Surface-induced dissociation
SIDT	Single ion in droplet theory
SORI	Sustained off-resonance irradiation
SWIFT	Stored waveform inverse Fourier transform
S/N	Signal to noise ratio
THF	Tetrahydrofuran
TLC	Thin-liquid chromatography
TOF	Time-of-flight
UK	United Kingdom
USA	United States of America
UV	Ultraviolet
UVPD	Ultraviolet photodissociation
VADS	Velocity aligned Doppler spectroscopy
VUV	Vacuum ultraviolet
w/w	weight / weight
ZDV	Zero dead-volume
ZEKE	Zero-kinetic energy

Symbols

a	$\sin^2$ apodization parameter – introduction
	cross-sectional area of an analyte – chapter 5
A	Attenuation
$A(v)$	Absorption spectrum
B	Magnetic field strength (T)
C_x	Concentration of x ([x] also used)
d	distance (between electrodes)
$D(v)$	Dispersion spectrum
Di	i^{th} Delay
E_0	Electric field strength
E	Electrolyte
ε	Absorption coefficient – chapter 4
	Electric vector of electromagnetic radiation – chapter 6
ε_0	Permittivity of free space (8.854×10^{-12} J^{-1} C^2 m^{-1})
e	electron charge (1.6×10^{-19} C)
f	fraction of charge converted to gas phase ions
f_a	activity coefficient of a
F	Faraday constant (9.65×10^4 C mol^{-1})
γ	Charge per unit length
G_I	Ion cloud geometry factor
G_T	Ion trap geometry factor
I	Current
$I(v)$	Imaginary part of the complex Fourier transformation
J	Angular momentum quantum number
k	Rate constant

K	Equilibrium constant
λ	Mean free path
m	Mass
n, m, p, q	Numbers of repeat units – chapters 4 & 5
n	Number of photons absorbed – chapter 6
M	Angular momentum quantum number
$M(v)$	Magnitude mode FTICR spectrum
MLi	ith calibration constant
Mn	Number average molecular weight
Mw	Weight average molecular weight
μ	Ionic mobility – chapter 5
	Transition dipole moment – chapter 6.
N	Number of scans
N_I	Number of atoms i
m/z	mass (Da) / charge (e)
Ω	Angular momentum quantum number
p	sampling efficiency of mass spectrometer
Pi	ith pulse
p_i	Relative intensity of I
q	Charge
Q	Surface charge
R	Instrument response factor – chapters 1 & 5
	Internuclear distance – chapter 6
$R(v)$	Real part of the complex Fourier transformation
ρ	Ion density
r	Radial position

Γ	Flow rate
t, T	Time
τ	Damping constant
v	Velocity – chapter 3
v	Vibrational quantum number – chapter 6
ν	frequency
$V_{p\text{-}p}$	Peak to peak voltage
V_i	i^{th} voltage
ω	Angular frequency
ω_+	Cyclotron frequency – including static electric field shift XBB
	Frequency sweep step-size
#	Number

Units

M, k, m, μ n and p, correspond to 10^6, 10^3, 10^{-3}, 10^{-6} 10^{-9} and 10^{-12} respectively.

Publications & Oral Presentations

May 2001, Inaugural Avecia Case Symposium, Grasmere, the Lake District, UK – Characterization of a complex polymeric mixture using Fourier transform ion cyclotron resonance mass spectrometry

June 2000, 3rd Year PhD seminar, University of Warwick - Characterization of polymers by FTICR – MS

September 1999, 5th European Fourier Transform Mass Spectrometry work shop – Characterization of polymeric dyes by FTICR-MS

"5-methylthiopentose in lipoarabinomannan." A Truemann, X. Feng, L McDonnell, PJ Derrick, AE Ashcroft, D Chatterjee, SW Homans. *in press, J. Mol. Biol.*

"Theoretical investigation of the kinetic energy of ions contained in a radio-frequency hexapole ion trap." LA McDonnell, AE Giannakopulos, Y Tysbin, P Häkansson, PJ Derrick. *Submitted to Eur. J. Mass Spectrom.*

AFM Kilbinger, HJ Cooper, LA McDonnell, WJ Feast, PJ Derrick, APHJ Schenning, and EW Meijer, *Chem. Comm.*, 383-384 (2000), "Mass spectrometric evidence for aggregation of a substituted sexithiophene."

L McDonnell and AJR Heck, *J. Mass Spectrom.*, **33**, 415 (1998), "Gas-phase reaction dynamics studied by ion imaging."

In preparation

"HCl (2+1) REMPI: an ion imaging study." LA McDonnell, DH Parker, B Bakker, AJR Heck

"Sustained off-resonance irradiation collision-induced dissociation of linear polyesters, substituted polyesters and cyclic polyesters" LA McDonnell, P Double, B Powell, PJ Derrick

1 Introduction

1.1. General introduction

The experiment in the late 19th century by Sir Joseph John Thomson that proved the existence and measured the *m/z* ratio of the electron can be deemed the first mass spectrometry experiment. Since this inception, mass spectrometry has developed into a very large multidisciplinary field. The technique is widely used in the biological, chemical and physical sciences, and many different ion sources, analyzers and detectors have been developed.[1] The 200th volume of the International Journal of Mass Spectrometry (Elsevier, Amsterdam, 2000) is a collection of reviews and personal reflections on the different aspects and applications of modern mass spectrometry. Over the past decade mass spectrometry has received much new and renewed interest. The chief cause of this attention was the advent of the ionization techniques electrospray ionization (ESI)[2, 3] and matrix-assisted laser desorption / ionization (MALDI)[4], which permit the mass spectrometric analysis of biological molecules and polymers. Using these techniques, fragile and involatile macromolecules can be ionized and transferred to the gas-phase without significant fragmentation. As a result their molecular masses can be measured accurately. Under carefully controlled conditions, ESI can preserve the non-covalent interactions that are of such biochemical importance[5]. One of the driving forces for the renewed interest is the potential to use ESI to investigate biological systems. Applications already bearing fruit include protein-ligand binding studies, specifically protein-protein (peptide)[5], protein-DNA[6], protein-ion[7], and protein conformation studies[8]. Understandably polymer chemists have exploited these techniques to characterize their synthetic macromolecules[9-30].

If a mass measurement is sufficiently accurate, the respective numbers of each amino acid residue in a peptide can be determined, however this is insufficient to truly

define a biomolecule. Owing to the large number of ways the constituent residues can be arranged in a protein, even absolute mass accuracy (zero mass error) is insufficient. Furthermore, as the mass accuracy decreases the number of possible combinations of amino acids increases rapidly. A similar problem exists with copolymers; a random and a block copolymer that contain the same number of each repeat unit have exactly the same chemical composition, as a result they are completely indistinguishable using single stage mass spectrometry. However, as the schematic below demonstrates their fragments will have different masses (provided the repeat units have different masses). Tandem mass spectrometry, in which a single oligomer of the copolymer is isolated and fragmented, can in principle be used to obtain information about the polymer's primary structure[21].
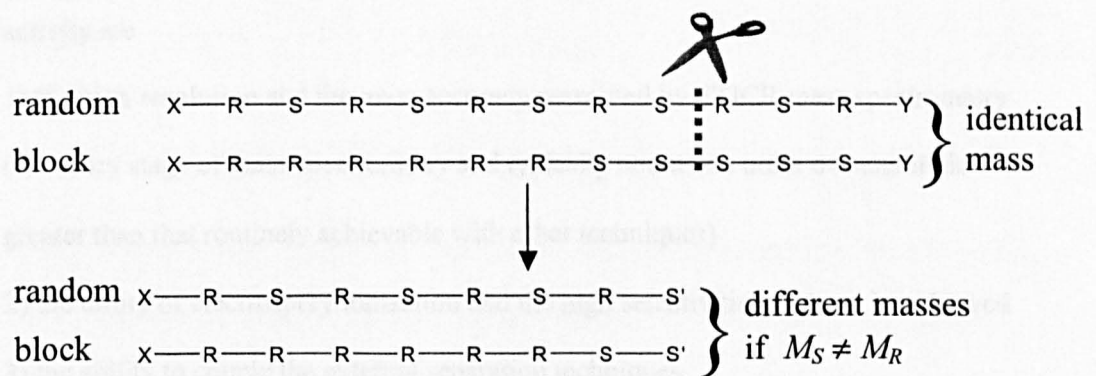
Figure 1.1.1. Schematic of a random and block copolymer and how fragmentation can separate their contributions.

In a similar manner a much more definitive and perhaps experimentally simpler method for protein / peptide identification is fragmentation. As the masses of a protein's/peptide's fragments are intrinsically related to its primary structure, a combination of parent and fragment ions are much more able to define a protein absolutely[31]. Furthermore, fragmentation can be used to localize protein modifications[32, 33] and determine regions possessing different secondary structure[34].

It is this ability to characterize / identify proteins that has given mass spectrometry its significant role in the rapidly growing proteomics industry.

There are numerous methods by which these fragments can be obtained, the identities fragments obtained being highly dependent on the technique employed[35]. These vary from the universal external methods, performing the fragmentation prior to sample injection / preparation, to a panoply of instrument dependent techniques that differ greatly in their methodology.[4, 27, 36-49]

One of the most active areas of mass spectrometry concerns Fourier transform ion cyclotron resonance (FTICR) mass spectrometry using an electrospray ionization (ESI) ion source[50]. As will be detailed in the following sections the principal reasons for this activity are

1) the high resolution and the mass accuracy permitted by FTICR mass spectrometry (for every stage of mass spectrometry and typically about one order of magnitude greater than that routinely achievable with other techniques)

2) the utility of electrospray ionization and the high sensitivities that can be achieved

3) the ability to couple the external separation techniques

4) the large number of fragmentation techniques available, and

5) the ability to investigate ion-molecule chemistry.

Although most analytical applications of ESI-FTICR mass spectrometry have concerned proteins / peptides, polymer chemists have also employed the technique for their own purposes[9, 12, 13, 15, 17-21, 23, 26].

1.2. Polymer characterization

It was pointed out that tandem mass spectrometry can provide information regarding the primary structure of copolymers[21]. The other information of interest concerns the

3

identities of the end groups and the molecular weight distribution of the polymer[17-19, 21, 26, 27]. As high mass accuracies are expected with FTICR mass spectrometry[51-53], the correct assignment should have a small mass error associated with it. In this manner, accurate-mass mass spectrometry can be used as a confidence gauge for characterizing previously unknown samples, see figure 1.2.1. Using a high-field magnet, e.g. 9.4 T, if an experiment is performed carefully FTICR mass spectrometry can deliver relative mass errors under one part per million (ppm) for ions of $m/z < 1000$ [51, 52].

$$\text{relative mass error (ppm)} = \frac{(\text{experimental mass - theoretical mass})}{\text{theoretical mass}} \times 10^6$$

| < 1 ppm | Confidence gauge | > 10 ppm |
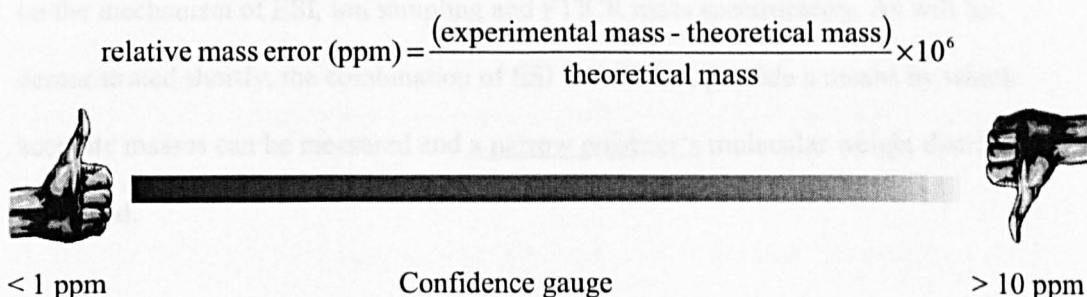
Figure 1.2.1. Schematic of the confidence gauge that accurate-mass mass spectrometry can provide.

Unless there is a good experimental reason for the result (see section 1.5) for an ion of $m/z < 1000$ a mass error of 10 ppm or more is indicative of an incorrect assignment. Furthermore, the high mass accuracy allows the mass analysis of relatively large ions, in which all combinations of user defined isotopes that satisfy user defined limits are calculated. Only with accurate mass measurements can such an analysis yield usable results for relatively large ions.

The molecular weight distribution of the polymer is more problematic. The straightforward approach, namely record the relative intensity, p_i, and mass of each ion and then calculate the number and weight average molecular weights, M_n and M_w respectively, using the equations

$$M_n = \frac{\sum_i m_i p_i}{\sum_i p_i} \qquad\qquad M_w = \frac{\sum_i m_i^2 p_i}{\sum_i m_i p_i} \qquad (1.2.i)$$

is permitted only if an oligomer's relative ion signal is equal to its relative concentration. For this to be true, ion generation, ion transport and ion detection must be uniform across the mass range of interest. The following sections give a brief overview on the mechanism of ESI, ion sampling and FTICR mass spectrometry. As will be demonstrated shortly, the combination of ESI and FTICR provide a means by which accurate masses can be measured and a narrow polymer's molecular weight distribution estimated.

1.3 Electrospray ionization.

Electrospray ionisation is one of the most widely used interfaces for the introduction of nonvolatile samples into the mass spectrometer. Many excellent reviews have been written on the electrospray process[3, 54-58], and the topic continues to receive much experimental attention[22, 59-69]. The first reports of the creation of gas phase ions at atmospheric pressure using an electrostatic sprayer, i.e. electrospray, were made by Malcolm Dole in the late 1960s and early 1970s.[70, 71] These first experiments concerned the production of polystyrene macroions that were separated by the use of a retarding potential and detected with a Faraday cage. In the 1980s, several research groups[2, 72-74] used mass spectrometry for the detection of the gas phase-ions generated from charged droplets at atmospheric pressure. In 1988, Fenn and workers demonstrated that multiply charged ions could be generated by electrospray ionization.[29]. This multiple charging along with the finding that large nonvolatile

species could be transferred into the gas phase without significant fragmentation permitted much larger molecules to be analysed with existing mass spectrometers and are the principal reasons behind the rapid growth of electrospray ionisation mass spectrometry.

The most common implementation of the electrospray process is shown in figure 1.3.1. A metallic capillary, through which a solution containing the analyte flows, is connected to a high-voltage power supply. The experimental set-up shown is that for positive ion generation (negative ions are obtained by reversing the polarity of the applied potentials). The needle capillary is connected to the positive terminal and the negative terminal is connected to a metal plate located a few millimetres downstream of the needle tip (from here on the sample capillary will be referred to as the needle to avoid confusion with the mass spectrometer's sampling capillary).
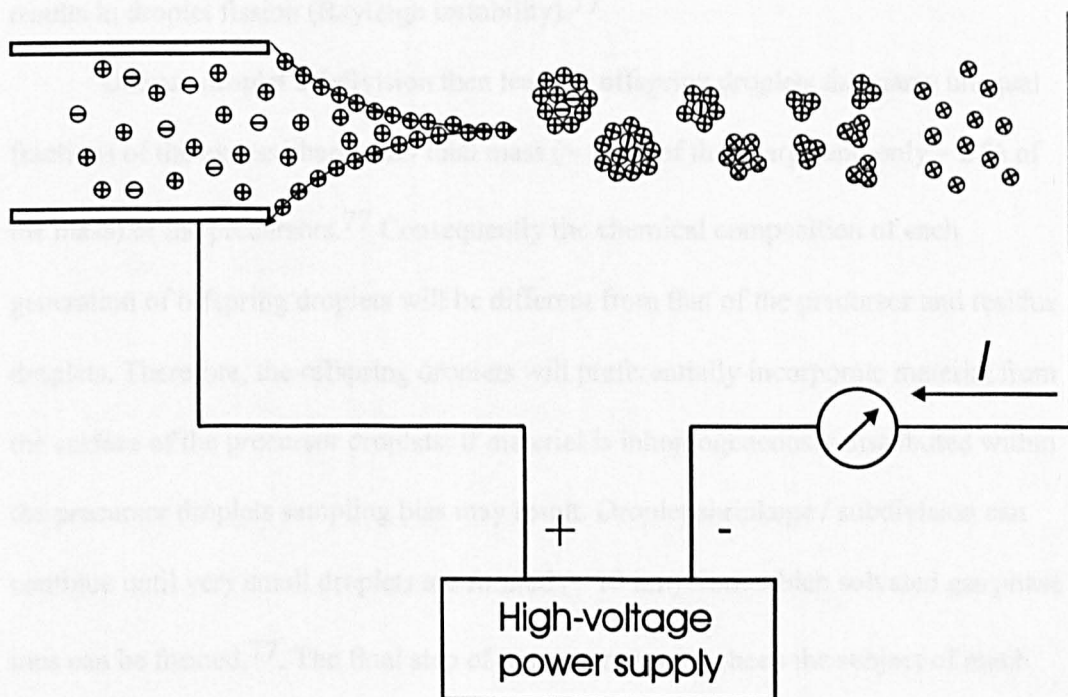
Figure 1.3.1. Schematic indicating several aspects of electrospray ionisation.

The electric field between the needle and the metal plate (a sampling capillary in a mass spectrometer) cause the positive ions present in the solution to migrate toward the liquid surface. The anions that formerly neutralised the charge are driven back toward the tip of the capillary. The resulting charge distribution (charge separation) counteracts the applied field. The electrohydrodynamics of the charged liquid surface cause it to take the shape of a cone (the Taylor cone) from which a thin filament of solution extends until it breaks into droplets.[75-78]

As a result of the field-induced charge separation that occurs at the Taylor cone, the droplets have a surface composition enriched in ions. These charge droplets drift under the influence of the field toward the counter electrode whilst simultaneously spreading out through coulombic repulsion. The droplets reduce in size as the solvent evaporates. Droplet shrinkage leads to high surface charge density, and at a given droplet radius, electrostatic charge repulsion overcomes the surface tension which results in droplet fission (Rayleigh instability).[77]

Uneven droplet subdivision then leads to offspring droplets that carry unequal fractions of the excess charge and total mass (~ 15 % of the charge and only ~ 2 % of the mass) of the precursors.[77] Consequently the chemical composition of each generation of offspring droplets will be different from that of the precursor and residue droplets. Therefore, the offspring droplets will preferentially incorporate material from the surface of the precursor droplets; if material is inhomogeneously distributed within the precursor droplets sampling bias may result. Droplet shrinkage / subdivision can continue until very small droplets are formed (~ 10 nm) from which solvated gas phase ions can be formed.[77]. The final step of ion generation has been the subject of much debate and will be discussed shortly. Nevertheless, it is this surface activity that led to the surface / interior equilibrium model of Enke[63]. Additionally, the effects of the

7

applied field on the surface concentration in the final droplets (electrophoretic migration effects) was recently correctly predicted.[67]

When the vapour-phase ions and the remaining charged droplets hit the counter electrode they are neutralised. The net motion of ions from the capillary tip to the metal plate constitutes part of an electrical circuit. The circuit is completed by electrochemical reactions that occur at the electrode / liquid surface interface. For positive ion electrospray ionisation, oxidation of the solvent and / or the electrode itself has been shown to complete the circuit[75]. Under typical ESI conditions the current is ~ 10^{-7} A. It should be noted that in a mass spectrometer the fraction of the ions and charged droplets that are sampled can not contribute to the detected current, see figure below.
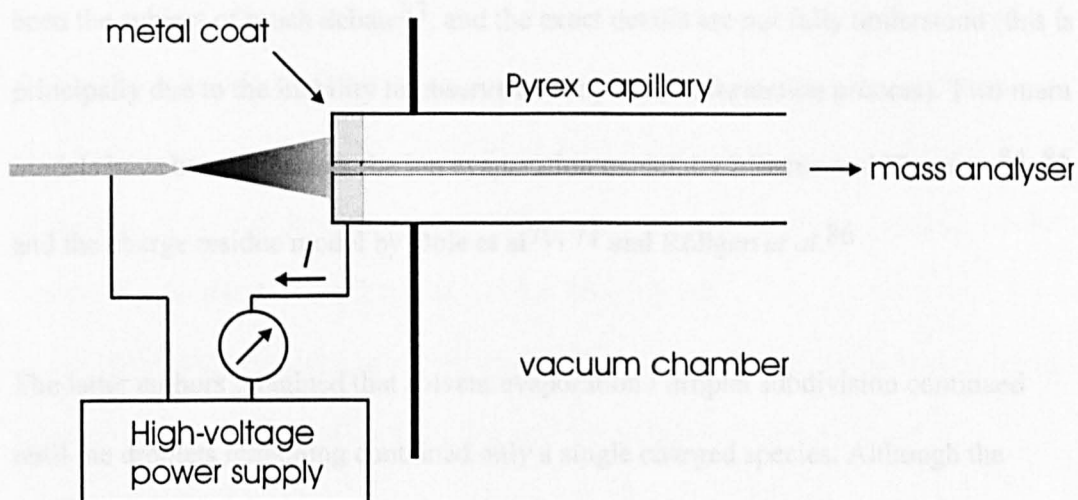
Figure 1.3.2. Schematic of the electric circuit of electrospray ionisation. The ions detected in the mass spectrometer do not contribute to that recorded by the ammeter.

In nanoflow electrospray (commonly called nanospray) ionisation[79, 80], which is similar to electrospray ionisation except that much smaller flow rates are used, much smaller droplets are formed. As a result, the time required for the generation of the offspring droplets from which the solvated ions are generated is much less and the needle is normally placed much closer to the sampling orifice. Consequently, the coulombic expansion of the droplet / ion mixture is less extensive for nanospray than for

8

regular electrospray and more ions are sampled by the mass spectrometer. It is for these reasons that the lower flow rate electrospray variations nanospray and microspray have been found to be more sensitive than electrospray[81].

1.3a Ion generation.

The general mechanism for electrospray ionisation detailed above, solvent evaporation and droplet subdivision, was greatly supported by a recent experiment in which a singly charged droplet was generated and held whilst it desolvated.[82] On average 40 ions were counted per single isolated droplet.

The actual mechanism by which gas phase ions are generated from the final droplets has been the subject of much debate[83], and the exact details are not fully understood (this is principally due to the inability to observe directly the ion formation process). Two main models have been proposed, the ion evaporation model, by Iribarne and Thomson[84, 85] and the charge residue model by Dole et al[70, 71] and Röllgen et al.[86]

The latter authors imagined that solvent evaporation / droplet subdivision continued until the droplets remaining contained only a single charged species. Although the absence of salt clusters (at high salt concentrations) was interpreted as evidence against the single ion in droplet theory (SIDT), these arguments assumed even fission. As first demonstrated by Kebarle and Tang[77] uneven fission can dramatically increase the ratio of ions to paired ions in the droplets. As a result the absence of salt clusters in the mass spectra obtained by ESI is still consistent with the SIDT model.

The other mechanism, ion evaporation, proposed that the increase in surface charge density, as a result of solvent evaporation / droplet subdivision, produces a Coulombic repulsion that exceeds the species' adhesion to the droplet surface[84, 85]. Consequently,

some ions are expelled from the surface. In particular, it predicted the dependence of the rates of ion production on the chemical properties of the ions. Observed differences in the gas-phase ion intensities of two ions present at equal concentrations were compared with predictions of the theory by Iribarne and Thomson[85] and by other workers.[87, 88] In general, qualitative agreement was obtained. Kebarle and Tang then extended this approach further and proposed a model based on the hypothesis that the ion evaporation rate from the droplets is proportional to the ion concentration in the droplet.[77] The fraction of the ion current due to the analyte species is represented as its fraction of the total ion formation rate, I. The resulting equation is

$$I(A^+) = fp \frac{k_A C_A}{k_E C_E + k_A C_A} \bullet I \tag{1.3a.i}$$

f is the fraction of droplet charge that is successfully converted into gas phase ions, p is the sampling efficiency of the mass spectrometer, k_A and k_E are the rate constants for the production of the analyte, A, and the electrolyte, E, respectively, and C_A and C_E are their analytical concentration (bulk solution in the final droplets).

Reflecting the fact that in both the SIDT and the ion evaporation models the ion is freed from the surface of the final droplet Enke developed a theory based on equilibria between the droplet surface and the droplet interior.[63] Those ions that prefer to be situated near the surface will be preferentially generated. When the assumption that the fraction of total analyte or electrolyte concentration on the surface is very small is valid an equation of similar form to that of Kebarle and Tang was obtained.

$$R_A = pf \frac{K_A C_A}{K_E C_E + K_A C_A} [Q] \tag{1.3a.ii}$$

where $[Q]$ is the concentration of excess charge produced by ESI and is given by the current, I, divided by the flow rate, Γ, and the Faraday constant, F, ($[Q] = I / F\Gamma$) and R_A is the instrumental response of the analyte.

When the assumption that the proportion of ions on the surface is very small is not valid and a mass balance equation is used instead, a quadratic equation is obtained for the surface concentration of the analyte, $[A^+]_s$.

$$[A^+]_s^2 \left(\frac{K_A}{K_E} - 1 \right) - [A^+]_s \left([Q] \left(\frac{K_A}{K_E} - 1 \right) + C_A \frac{K_A}{K_E} + C_E \right) + C_A [Q] \frac{K_A}{K_E} = 0$$

(1.3a.iii)

Similarly, for a system containing two analytes and an electrolyte a cubic expression was obtained that was shown to be able to describe the data of Kebarle and Tang more satisfactorily than their approach (which resembled the simplified model).[63, 77].
Recently Sjöberg *et al.* introduced a method based on Enke's approach for the determination of ion distribution within electrospray droplets.[89]
Zhou and Cook then extended this equilibrium approach by incorporating the effects of electrophoretic mobility on the surface concentrations of the analyte ions.[67] Although this work was based on the simplified models of Enke qualitative agreement was obtained. The dependence of the charge state of the ions on the magnitude of the external field had been previously interpreted by Fenn as indicating that ion generation could proceed from larger droplets in the presence of a stronger field.[62] Although the ion densities were smaller on the surface of these larger droplets the stronger fields could extract the ions (in a lower charge state) from the droplets.

In both models solution chemistry plays an important role. However predictions have proven difficult owing to the numerous processes that occur during the spray. The electrospray solution has been shown to change during the electrospray process owing to solvent fractionation[68], electrochemical redox reactions[69, 75] and charge enrichment[90]. Nevertheless, as will be shown in chapter five and demonstrated by the previous publications, owing to the similarity of the chemical composition of the

11

oligomers of a polymer the ion distributions obtained with ESI can display the expected intensity profile.

1.4 Ion sampling / ion transport

The ions that are ultimately detected by the mass spectrometer reflect the ions that are produced by the electrospray plume <u>and</u> are successfully transferred to the detector. Significant bias effects can occur in almost all stages of mass sampling and transport.

Recently Smith and workers demonstrated that surface active species are concentrated on the outer periphery of the electrospray plume and that this could effect the ions detected with a mass spectrometer.[65] As a result of a non-uniform distribution the ions successfully sampled will depend on the position of the electrospray needle, see figure 1.4.1.

Figure 1.4.1. Droplet plumes formed by ESI and nanospray. The ions sampled by ESI can depend on the position of the needle
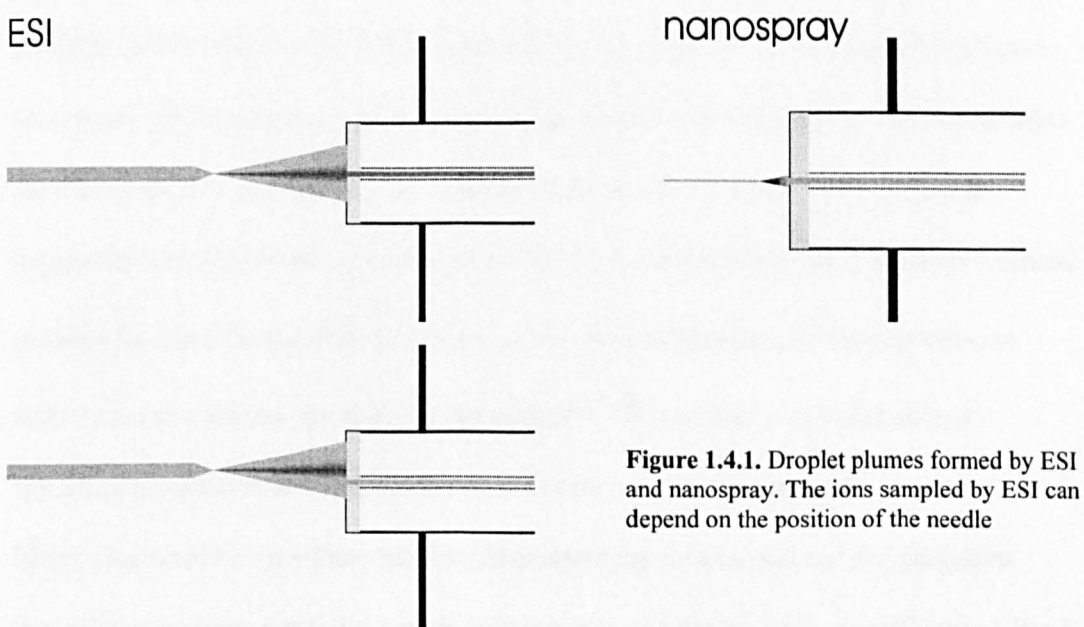
For nanospray, as the needle is much closer to the sampling orifice a significantly larger proportion of the ion plume is sampled. For this reason any sampling bias is expected to be much smaller for nanospray and microspray. The fact that the needle is closer to the

sampling orifice is one of the reasons that nanospray (and microspray) has proved to be more sensitive than electrospray[81].
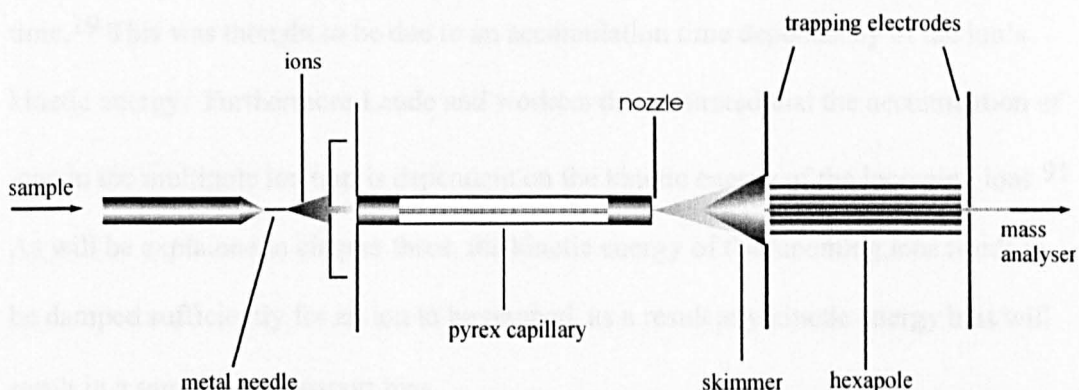
Figure 1.4.2. Schematic of an electrospray ion source.

A schematic of the ion source is shown above. Derrick and workers have shown that the supersonic expansion that occurs in the high pressure region of the electrospray ion source, namely the region between the nozzle and the skimmer, can cause an ion bias effect.[22] In their study it was found that the average molecular mass of a polymer was found to be dependent on the potential applied to these electrodes. The explanation for this result was as follows. The average position of an ion after the supersonic expansion was dependent upon the mass of the ion, consequently the potentials required to focus the ions through the skimmer was also mass dependent.[22] Furthermore, so called nozzle-skimmer reactions in this region[47, 48] can lead to ion bias effects, specifically, preferential fragmentation will skew any results obtained.

Many electrospray ionisation mass spectrometers use an external ion accumulation device to store ions, normally a multipole ion trap, see figure 1.4.2. Specifically, pulsed techniques such as time-of-flight, ion traps and FTICR use the external 'ion bottle' to convert the inherently continuous ESI source into a more amenable pulsed source (some of the contents of the trap can be pulsed into the analyser). However, a multipole ion

13

trap can introduce several potential bias effects. Wood and workers noticed that the average molecular mass of polyethyleneglycol varied with the hexapole accumulation time.[19] This was thought to be due to an accumulation time dependency of the ion's kinetic energy. Furthermore Laude and workers demonstrated that the accumulation of ions in the multipole ion trap is dependent on the kinetic energy of the incoming ions.[91] As will be explained in chapter three, the kinetic energy of the incoming ions needs to be damped sufficiently for an ion to be trapped, as a result any kinetic energy bias will result in a sampling / transport bias.

Another potential source of ion bias in the multipole ion trap of many ESI mass spectrometers concerns the recently reported radial stratification phenomena.[92] It was postulated that the average radial position of ions is dependent on the mass / charge ratio of the ion, with heavier ions on average being situated at larger radii. As a result those heavier ions whose average radial position is greater than the radius of the extracting electrode orifice will not be transferred to the analyser, see figure 1.4.3.
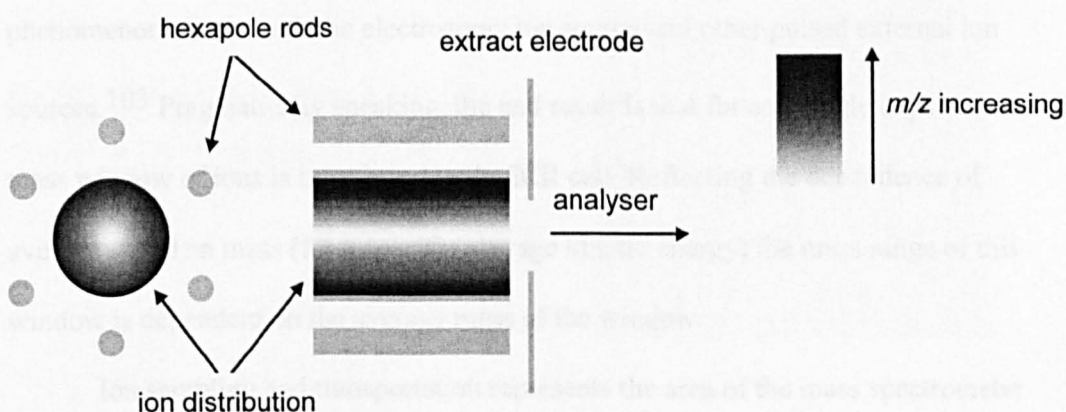
Figure 1.4.3. Schematic of how radial stratification could effect the ions transferred to the mass analyser

Fragmentation can also be affected inside the multipole ion trap. Multipole storage assisted dissociation[49, 93, 94] (MSAD), through preferential fragmentation, could lead to an ion transport bias, as the more fragile ions / adducts (non-covalent

especially) will be fragmented inside the multipole ion-bottle. One of the pertinent results reported here is that radial stratification combined with MSAD can lead to the preferential fragmentation of ions of larger m/z.[95]

Of course an ion will be contained in the multipole ion trap only if its trajectory is stable[96-99]. Although the mass filter mode is a widely used mode of operation for quadrupoles,[100] as a result of less well defined stability boundaries the hexapole and octopole (the most commonly used multipole ion traps in ESI sources) are less well suited to act as a mass filter.[97] Nevertheless, Marshall and workers demonstrated mass selective accumulation and fragmentation inside an octopole ion trap.[101]

The ions are then transferred from the ion-bottle to the mass analyser. For the case of a Fourier transform ion cyclotron resonance mass spectrometer this is commonly achieved with either a set of multipole ion guides[102] or an array of electrostatic lenses and deflection electrodes. Two papers have demonstrated time-of-flight effects for externally produced ions generated with a MALDI ion source.[13, 28] A similar phenomenon occurs with the electrospray ion source and other pulsed external ion sources.[103] Pragmatically speaking, the end result is that for any single experiment a mass window of ions is transferred to the ICR cell. Reflecting the dependence of average speed on mass (for a specific average kinetic energy) the mass range of this window is dependent on the average mass of the window.

Ion sampling and transportation represents the area of the mass spectrometer where most ions are lost. As a result it also represents the area that has received the most attention with regard to improving the sensitivity of the instrument. Using several recent developments Belov *et al.* recently demonstrated low zeptomole (10^{-21}) sensitivity.[104]

1.5 Ion detection

The detection system employed in these studies was Fourier transform ion cyclotron resonance mass spectrometry, like ESI excellent reviews have been written[39, 50, 105, 106].

The basic ion cyclotron phenomenon is taught during A-level (or equivalent) physics classes.[107] A charged particle moving with a velocity v in a magnetic field B experiences a force perpendicular to its direction of motion and perpendicular to the direction of the magnetic field. More accurately, the force is determined by the cross product of the ion's velocity and the magnetic field multiplied by the charge of the particle ($F_B = q\, v \times B$). Therefore the presence of velocity component perpendicular to the magnetic field will cause a force to be exerted on the ion, which continually deflects the ion and causes the ion to follow a circular path, see figure 1.5.1.

Figure 1.5.1. Electrons circulating in a chamber containing gas at a low pressure. The direction of the force can be determined using the right-hand rule.
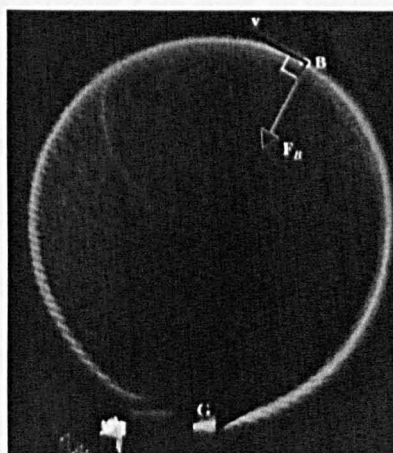
Equating the centripetal acceleration and the force experienced by the ion provides an expression for the angular frequency of the cyclotron motion. For an ion moving perpendicular to the magnetic field

$$qvB = m\frac{v^2}{r} \Rightarrow \omega = \frac{qB}{m} \qquad (1.5.i)$$

Consequently, if the strength of the magnetic field is known, through measuring the cyclotron frequency of an ion its mass over charge ratio (m/q) can be obtained. The method by which the cyclotron frequencies (and hence the m/q ratios) is obtained can be seen in figure 1.5.2.

When an external oscillating electric field is applied at the same frequency as the cyclotron frequency of the ion its cyclotron orbit is increased.[39, 106] For an ion initially at rest (for all but the smallest ions in a weak magnetic field the thermal cyclotron radius is small[39]) subjected to resonant excitation of field strength E_0 for a period of T_{excite}, the post excitation radius is given by

$$r = \frac{E_0 T_{excite}}{2B_0}$$

(1.5.ii)

For example, through the application of a constant RF resonating voltage of $\pm$ 1 V (2 V_{p-p}) applied to infinitely-extended parallel flat electrodes 2 cm apart, an ion in a 9.4 T magnetic field can be excited to a cyclotron radius of 0.53 cm. Thus, ions can be excited to detectably useful radii through the application of a relatively small RF voltage. It is important to note that the *post-excitation ion cyclotron orbital radius* is independent of m/z. Thus all ions of a given m/z range can be excited to the same ICR orbital radius by the application of a radio frequency (ICR frequencies lie in KHz – MHz range) electric field whose magnitude is constant with frequency.

The coherent ICR motion resulting from irradiation is then used for detection. As the ion packet sweeps past a detector plate, provided the cyclotron radius is sufficient, an image charge is induced in the plate. The difference, ΔQ, in image charge on two opposed infinitely-extended parallel flat conductive plates, induced by an ion of charge, q, between the plates is given by[39]

$$\Delta Q = -\frac{2\,qr}{d} \qquad\qquad (1.5.\text{iii})$$

The time-derivative of this charge provides the ion cyclotron current signal.[108] The ICR signal is independent of magnetic field strength and increases linearly with ion cyclotron post-excitation radius. Linearity is important for two reasons. Firstly, as the ICR signal varies linearly with the post-excitation radius (which in turn depends on the excitation) the <u>ICR frequency response at any frequency is proportional to the excitation magnitude (at that frequency)</u>. And secondly, a Fourier transform of the time-domain ICR response gives the same spectrum that would have been obtained by measuring power absorption while sweeping slowly across the m/z range. The whole process of excitation, detection and transformation is shown schematically in figure 1.5.2. for a single packet in a cylindrical ICR cell.

As can be seen below, through measuring the cyclotron resonance of an ion its m/q ratio can be measured. Furthermore, the "superposition" principle dictates that the signals from any number of ions of arbitrary m/z values simply add at the detector: thus, ions of a wide m/z range can be detected simultaneously. This statement is only true provided the data set is sufficiently large for beating effects to be small.[23] Nevertheless, simultaneous detection of all ionic species (multichannel) followed by Fourier transformation can yield a spectrum of N data points in $1/N$ of the time it would take to scan the spectrum one channel at a time.[106]

excite ~

intensity / a.i.

time / a.u.

FT

$\omega = qB/m$

Amplitude / a.i.

Frequency / a.i.
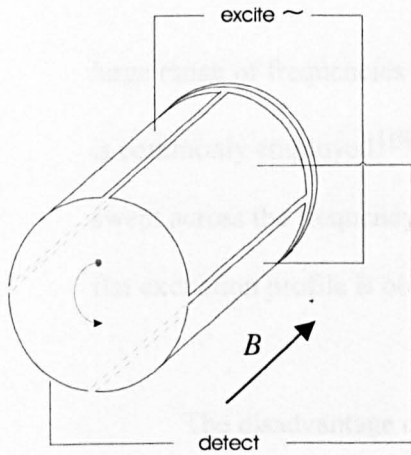
Figure 1.5.2. Schematic of the FTICR data acquisition system.
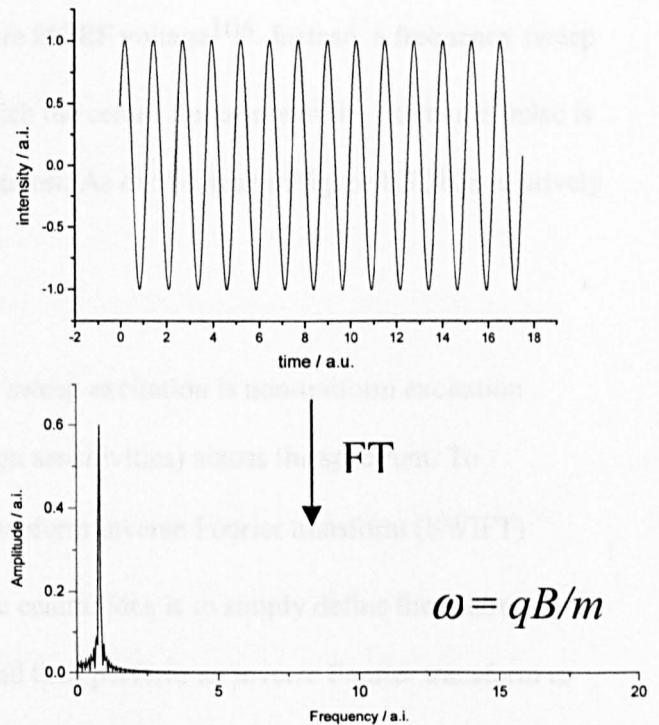
For simultaneous detection of all of the ions in a specific *m/z* range, all ions present in that mass window firstly need to be excited to detectable radii. Additionally, for the ion signals to reflect their abundance the excitation profile must be as uniform as possible. This is most commonly achieved using either a frequency sweep or a stored waveform inverse Fourier transform (SWIFT) waveform.[106] Marshall and workers have shown that the frequency-domain spectrum, $E(v)$, of single-frequency excitation at frequency ω_c, applied steadily for T_{excite} seconds is given by[106]

$$M(v) = E_0 \frac{\sin(2\pi v_c T_{excite})}{2\pi v_c} \qquad (1.5.iv)$$

The finite duration of the applied RF field broadens the spectral range of the excitation to a bandwidth of ~ $1/T_{excite}$ Hz (the range is centred at ω_c). Consequently, ions of cyclotron frequency, v_i, sufficiently close to ω_c (when $1/T_{excite} \geq |v_i - v_c|$) can also be excited. However, to apply such a single pulse approach is only permissible for narrow mass ranges (as performed in heterodyne mode, see later). For broadband detection the

19

large range of frequencies would require kV RF voltage[106]. Instead, a frequency sweep is commonly employed[109, 110] in which the centre frequency of the excitation pulse is swept across the frequency range of interest. As can be seen in figure 1.5.3b. a relatively flat excitation profile is obtained.

The disadvantage of frequency sweep excitation is non-uniform excitation amplitude (translating to variation in ion sensitivities) across the spectrum. To circumvent these difficulties stored waveform inverse Fourier transform (SWIFT) excitation was developed[111, 112]. The central idea is to simply define the desired frequency-domain excitation profile and then perform an inverse Fourier transform to obtain the required time-domain waveform, see figure 1.5.3c.
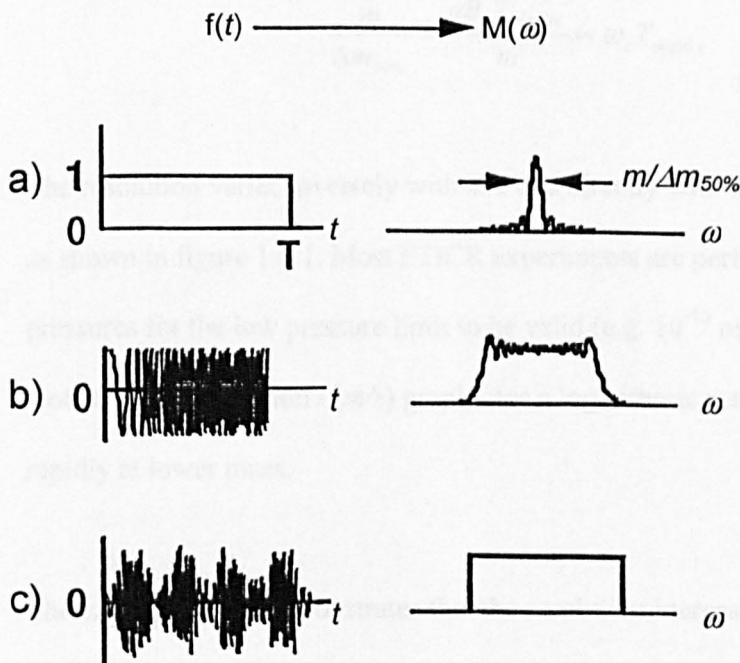
Figure 1.5.3. Time-domain and frequency domain excitation profiles. a) Rectangular pulse, b) frequency-sweep, and c) SWIFT

1.6. Advantages of FTICR mass spectrometry

The above section has demonstrated the basics of FTICR mass spectrometry and how it can permit all of the ionic species within a specified mass range to be detected simultaneously with uniform (or near uniform) sensitivity. However the principal advantages of FTICR mass spectrometry are high resolution and high mass accuracy, both of which can be utilised for tandem mass spectrometry.

The resolution of the peak is determined by the length of the transient, the cyclotron frequency of the ion and the collisional damping constant, τ, (collisions in the cell limit the duration of the coherent ion motion responsible for the ICR signal). In the low pressure limit ($T_{acquire} \ll \tau$) the resolution is given by[39]

$$\frac{m}{\Delta m_{50\%}} \propto \frac{qB_0 T_{acquire}}{m} \propto \omega_c T_{acquire} \qquad (1.6.i)$$

The resolution varies inversely with m/z and directly with the transient duration, $T_{acquire}$, as shown in figure 1.6.1. Most FTICR experiments are performed at low enough pressures for the low pressure limit to be valid (e.g. 10^{-10} mbar).

Note that the resolution / (m/z) graph uses a logarithmic scale, the resolution increases rapidly at lower mass.

The lower diagram demonstrates that the resolution increases with transient duration ($T_{acquire}$) and magnetic field strength. Although the resolution decreases with m/z the lower diagram clearly shows that high resolutions can be obtained at $m/z \approx 1000$, especially with a high field magnet.

21

Resolution dependence on magnetic
field strength and *m/z* ($T_{acquire}$ = 0.5 s)

1.0 T
3 T
4.7 T
7.0 T
9.4 T

Resolution dependence on $T_{acquire}$ and
magnetic field strength (*m/z* = 1000)

1 T
3 T
4.7 T
7.0 T
9.4 T

$m/\Delta m_{50\%}$
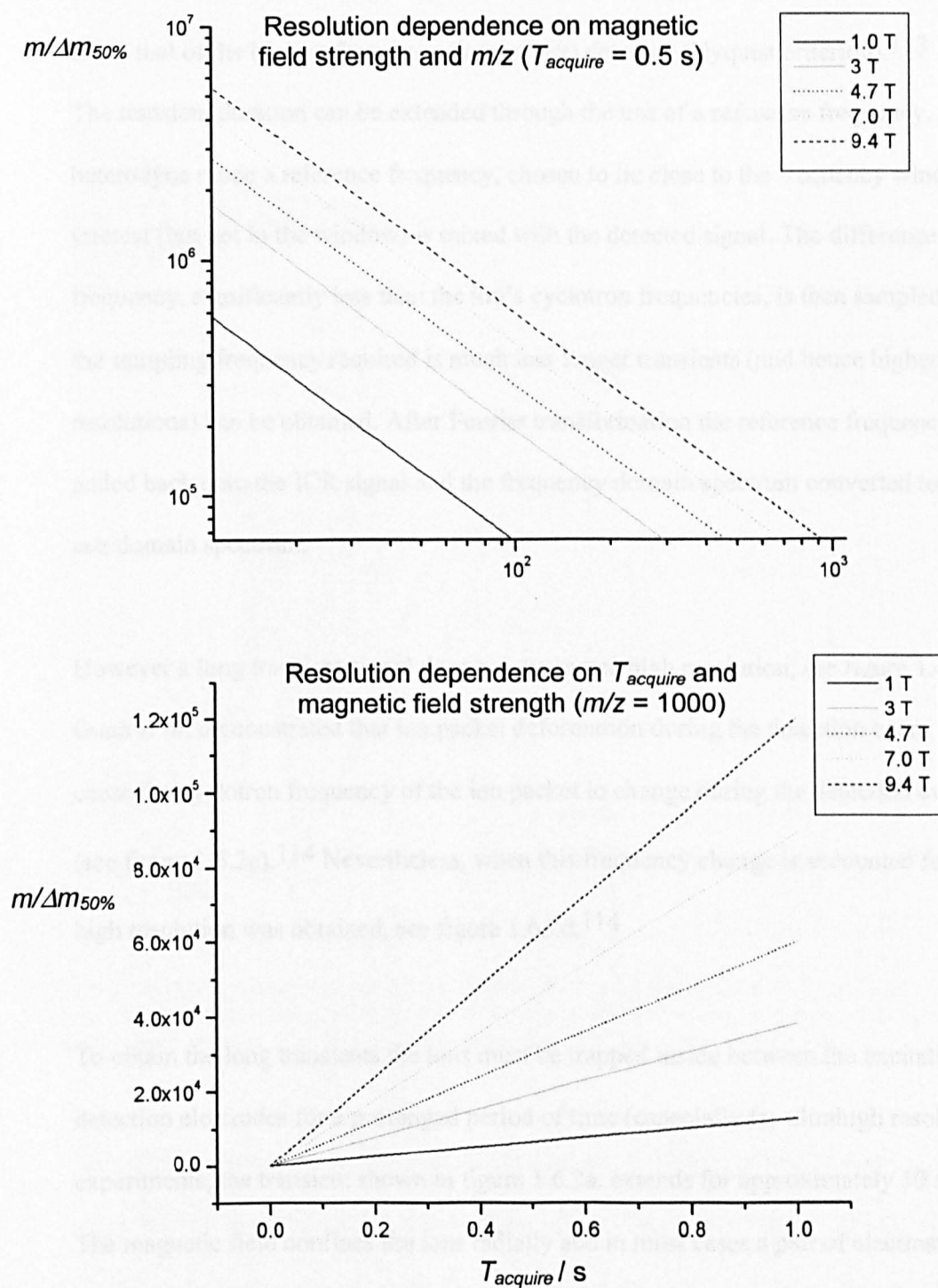
$T_{acquire}$ / s

Figure 1.6.1. Resolution dependence on *m/z*, magnetic field strength and transient duration ($T_{acquire}$).

The lower diagram also clearly demonstrates the pivotal role of transient duration on the resolution obtained. The transient duration is determined by the data file size (user

defined) and the sampling rate, which is in turn defined by the lower limit of the mass range detected. To reliably describe a peak, the sampling frequency must be at least twice that of the highest frequency (lowest m/z) detected (Nyquist criterion).[113] The transient duration can be extended through the use of a reference frequency. In heterodyne mode a reference frequency, chosen to lie close to the frequency window of interest (but not in the window) is mixed with the detected signal. The difference frequency, significantly less than the ion's cyclotron frequencies, is then sampled. As the sampling frequency required is much less longer transients (and hence higher resolutions) can be obtained. After Fourier transformation the reference frequency is added back onto the ICR signal and the frequency domain spectrum converted to the m/z domain spectrum.

However a long transient signal does not guarantee high resolution, see figure 1.6.2a&b. Guan *et al*. demonstrated that ion packet deformation during the detection event can cause the cyclotron frequency of the ion packet to change during the detection event. (see figure 1.6.2c).[114] Nevertheless, when this frequency change is accounted for ultra-high resolution was obtained, see figure 1.6.2d.[114]

To obtain the long transients the ions must be trapped inside between the excitation / detection electrodes for a prolonged period of time (especially for ultrahigh resolution experiments, the transient shown in figure 1.6.2a. extends for approximately 50 s). The magnetic field confines the ions radially and in most cases a pair of electrostatic electrodes are used to confine the ions axially, thus allowing prolonged transients to be obtained.[39] As will be shown shortly, the axial trapping field affects the cyclotron frequencies of the ions present in the cell.
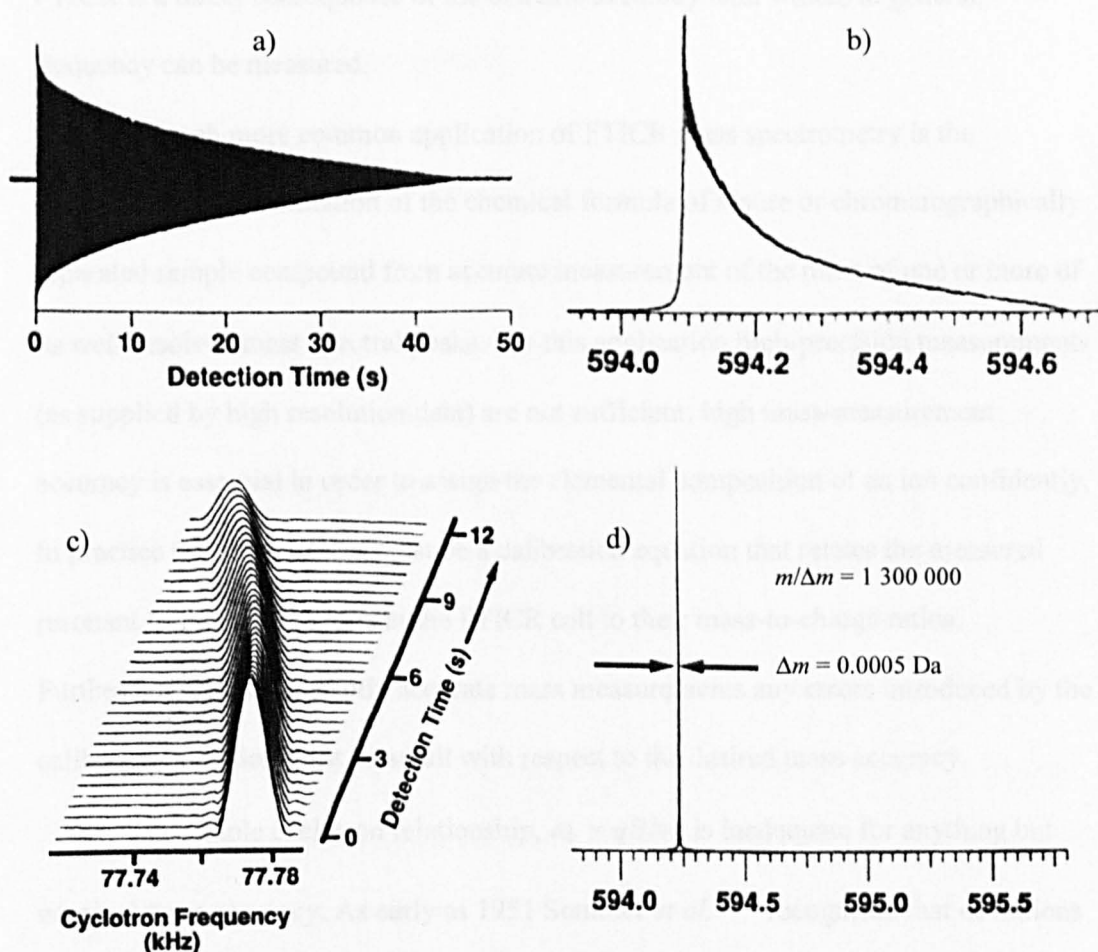
Figure 1.6.2. a) Free-induction decay (FID) of ICR signal of leucine enkephalin and b) the FT of the FID. c) Fourier transformation of segments of the FID shows a frequency drift during the data acquisition. d) Ultrahigh resolution mass spectrum after deconvolution. All diagrams obtained from reference 114.

Ultrahigh resolution is arguably the single feature that Fourier transform ion cyclotron resonance mass spectrometry is famous for. For example, as early as 1993 Gorshkov *et al.*[115] published results in which the methylene cation was detected with a resolution ($m/\Delta m$) of 20 000 000, which corresponds to a peak width (full-width half-maximum) of 0.0000007 Da. Although processes such as peak coalescence[116] make resolving isobaric peaks (ions of same nominal mass but different chemical formulae) more

24

difficult, recent achievements have included the resolution of isobaric peaks that differed by less than the mass of a single electron[117]. The ultrahigh mass resolution of FTICR is a direct consequence of the extreme accuracy with which, in general, frequency can be measured.

A much more common application of FTICR mass spectrometry is the determination / confirmation of the chemical formula of a pure or chromatographically separated sample compound from accurate measurement of the mass of one or more of its well-resolved mass spectral peaks. For this application high-precision measurements (as supplied by high resolution data) are not sufficient; high mass-measurement accuracy is essential in order to assign the elemental composition of an ion confidently. In practice this means there must be a calibration equation that relates the measured resonant frequencies of ions in the FTICR cell to their mass-to-charge ratios. Furthermore, for consistently accurate mass measurements any errors introduced by the calibration equation must be small with respect to the desired mass accuracy.

The simple cyclotron relationship, $\omega_c = qB/m$, is inadequate for anything but nominal mass accuracy. As early as 1951 Sommer *et al.*[118] recognised that deviations from the simple cyclotron relationship are produced by electric fields and these "originate from at least two sources not altogether independent – from the applied trapping voltage and from any space charge...". Owing to the contribution of the trapping field, the absolute sizes of these shifts are instrument (more precisely, cell) dependent. The numerous cells reviewed by Guan and Marshall include efforts to minimise the influence of the trapping field through intelligent cell design.[119] For example, the trapping field of the elongated cell[120] does not penetrate very far into the centre of the cell, and as a result the frequency shifts caused by the trapping field are smaller.

The radial component of the static trapping and space-charge static electric fields acts against the Lorentz force due to the ion's motion inside the homogeneous magnetic field. The result is an effective cyclotron frequency that is slightly smaller than that predicted by the cyclotron relationship.

The first paper to describe quantitatively the effects of space charge as well as that of the trapping field on the observed ICR frequency was that of Jeffries et $al.$[121] Through modelling the trapped ions as an ellipsoid, an expression was obtained for the effective cyclotron frequency as a function of the unperturbed cyclotron frequency, ω_c, trapping voltage, V_T, ion density, ρ, and two geometry factors, G_i and G_T.

$$\omega_{\pm} = \frac{\omega_c}{2}\left\{1 \pm \left[1 - \frac{4K'}{\omega_c^2}\right]^{\frac{1}{2}}\right\}$$

(1.6.ii)

where $K' = 2qV_TG_T/m + \rho q^2 G_i/\varepsilon_0 m$. The two geometry factors, G_T and G_i, were used to account for different cell designs and the shape of the ion cloud (which is influenced by the cell geometry), respectively.

Francl et $al.$[122] used the approximation that when the ion space charge and trapping voltage shifts are small compared with the cyclotron frequency, the square root term can be expanded in a Taylor series to give

$$\omega_+ = \omega_c - \frac{K'}{\omega_c} - \frac{(K')^2}{\omega_c^3}\cdots$$

(1.6.iii)

from which, by taking just the first two terms and substituting the expression for K' and ω_c gives the simple relationship

$$\omega_+ = \omega_c - \frac{2V_TG_T}{B} - \frac{q\rho G_i}{\varepsilon_0 B}$$

(1.6.iv)

26

This approximate form for the effective frequency is especially useful because m/q appears only in the term ω. Thus, at constant magnetic field, the electric fields caused by space charge and the trapping voltages shift all cyclotron frequencies lower by an equal amount. This constant frequency shift and linear dependence on space charge was subsequently experimentally demonstrated.[51]

For ICR signals acquired under the same conditions the above equation leads to the simple calibration relationship

$$\omega_+ = \frac{qB}{m} - \frac{2V_T G_T}{B} - \frac{q\rho G_i}{\varepsilon_0 B} \equiv \frac{qB}{m} - Y \tag{1.6.v}$$

$$\frac{m}{z} = \frac{ML1}{(\omega_+ + ML2)} \tag{1.6.vi}$$

where the calibration constants *ML1* and *ML2* represent the effect of the magnetic field and electric field, respectively. The errors associated with using the approximate form for the effective cyclotron frequency (first term of the Taylor expansion) decreases with increasing magnetic field strength, for example the denominator of the next term in the series would include a B^{-3} term.

As will be shown later, using a 9.4 T magnet the above calibration relationship is sufficiently accurate to provide negligible mass errors (under 1 ppm). Under normal 'external calibration' operation, the values of *ML1* and *ML2* are determined using a known standard sample. These parameters are then applied to the spectra obtained for the sample experiment and the mass accuracies calculated. Owing to the presence of space charge, the total ion intensities of the calibration and sample experiments need to be matched as closely as possible to obtain consistently accurate data.

A more accurate account of the space-charge shifts can be obtained through the use of an internal calibrant, in which the standard sample is present in the cell at the same time as the unknown sample. Alternatively, as all cyclotron frequencies are shifted by an approximately equal amount, an internal lock mass may be used to correct for differential space-charge shifts between the calibration and sample experiments[52]. The magnetic field, and hence *ML1*, can be considered constant over a relatively short time period, for example 1 day. Therefore, any the mass shifts are due to the electric fields present in the cell and can be accounted for using *ML2* alone. As these frequency shifts are approximately constant[51], a single known ion can be used to calibrate the entire spectrum. This was the method of choice for tandem mass spectrometry experiments.

The other commonly used ICR calibration relationship, which does not use the Taylor approximation, was developed by Ledford *et al.*[123] and includes a frequency-squared term

$$\frac{m}{z} = \frac{ML1}{\omega} + \frac{ML2}{\omega^2} \qquad (1.6.\text{vii})$$

As has been found with the 9.4 T instrument at Warwick,[12] and recently reported by Marshall and workers for a 9.4 T and a 5.6 T instrument, "the Ledford or Francl frequency-to-mass conversion formulas yield comparable mass accuracy."[124]
The importance of a good calibration, specifically the amount of space charge, was recently highlighted by Easterling *et al.* who demonstrated that the measured masses of ions using an FTICR mass spectrometer could change over a range of 200 ppm depending on upon trapped ion population size.[51]

More recently still, Smith and workers demonstrated that owing to the multiply charged nature of the protein ions produced by ESI, an FTICR mass spectrum of a protein (or

any other species that produces ions in a range of charge states, *e.g.* a polymer) can be calibrated without standards and without prior knowledge of the identity of the protein.[125] Only if the calibration is correct will the deconvoluted spectrum (each charge state converted to a singly charged species) of each individual charge state overlap. Through maximizing the agreement between each charge state's deconvoluted spectrum the spectrum of an unknown species can be calibrated.

The comparison of calibration equations by Marshall and workers referred to above also demonstrated that mass accuracy decreased with increasing dynamic range. There are several reasons for this finding. If the most intense ions are much more abundant than the least intense (high dynamic range), to be able to detect all ions simultaneously requires many ions to be trapped in the ICR cell. The assumption of a quadrupolar electric field term used in the derivation of the calibration relationships[12, 121-123] is invalidated at high ion densities, basically coulombic repulsion can shift and broaden mass spectral peaks by pushing like charges into regions of different applied external electric or magnetic field.[39, 126] Other mechanisms that can lead to decreased mass accuracy at high ion densities include mass shifts from positive and negative peak overlap[127], the number of data points that describe a peak decreasing with decreasing intensity, and ion cloud deformation during the excitation / detection event.[114, 128] The paper by Peurrung and Kouzes provides a good example of the non-linear effects that can occur in an FTICR cell when many ion packets are present.[129]

The net result is to increase average mass errors. For example, the comparison of calibration relationships referred to above reported that simply fitting the Francl and Ledford calibration relationships to a poly(ethyleneglycol) bis(carboxymethyl) ether mass spectrum obtained using a 9.4 T FTICR mass spectrometer produced average mass errors of $\approx$ 3 ppm in both cases[124].

1.7. Ion isolation and tandem mass spectrometry

Most samples produce more than one ionic species. As a result, to obtain tandem mass spectrometry data the ion to be fragmented must first be isolated (or at least the *m/z* range where the fragment ions are to be produced must be cleared). With FTICR this is commonly achieved with one of three techniques.

i) Correlated sweep excitation (COSE)[39]. In this technique multiple (depending on the number of ions to be isolated) frequency sweeps are applied across the mass ranges to be cleared. In-between these sweeps lie the ions to be isolated. Generally a frequency safety belt, which is not excited and contains the ion to be isolated, is used to prevent off-resonance excitation. The frequency sweeps are used to excite the unwanted ions out of the FTICR cell (and into the cell walls).

ii) Stored waveform inverse Fourier transform (SWIFT) excitation.[111, 112] As explained earlier SWIFT allows the user to apply any excitation waveform, consequently an excitation waveform that excites every ion other than the parent ion can be generated. Like COSE, SWIFT isolates the parent ion(s) by exciting all other ions out of the cell.

iii) Quadrupoler excitation axialization (QEA).[130] As a result of the trapping electrodes that are used to keep the ions in the FTICR cell, the radial motion has two components, ion cyclotron motion and magnetron motion.[39, 105] The energy of the cyclotron motion increases with increasing radii whilst that of the magnetron radius decreases.[39, 105] In the presence of a collision gas both motions are relaxed, such that whilst the cyclotron orbit decreases that of the magnetron motion increases. Consequently, in the presence of a collision gas ions are ultimately lost due to the expansion of the magnetron motion. However if a quadrupolar electric field is applied at the unperturbed cyclotron frequency of the ion to be isolated, rapid interconversion between the two radial

motions occurs that results in the ions being axialized.[130] Consequently, through the

application of a quadrupolar RF field of a specific frequency an ion may be axialized

whilst those ions that are not irradiated expand to the edge of the cell where they are

lost. This isolation technique[131] differs from the two above in that the ion that is kept

is irradiated.

Broadband axialization can be achieved through the use of frequency sweeps or SWIFT

excitation.[132] This technique has permitted ion remeasurement with greater than 99.5

% efficiency.[133] Furthermore, QEA can be applied during a fragmentation experiment

to improve the detection efficiency of tandem mass spectrometry experiments.[134]

Finally, Pastor and Wilkins demonstrated that low-voltage on-resonance excitation, in

the presence of a collision gas, can be used to axialize ions.[135]

In cell, ion fragmentation can be achieved with radiation, electron or collision based

techniques. The first two techniques simply use the ICR cell to contain the ions whilst

an external agent is applied.

The radiation techniques include infrared multiphoton dissociation[42] (IRMPD),

ultraviolet photodissociation[41] (UVPD), blackbody infrared radiative dissociation[43]

(BIRD) and Focused RAdiation for Gaseous Multiphoton ENergy Transfer[44]

(FRAGMENT). Robert Dunbar, one of the pioneers of this field, recently published a

personal perspective on the evolution and scope of trapped ion photodissociation

methods and applications.[136]

Electron capture dissociation (ECD), in which low energy electrons are caught by a

positively charged macromolecular ion (typically a protein) was first reported by

Zubarev *et al.* and has been shown to be a nonergodic reaction that can provide valuable

structural information.[33, 45, 137]

Collisional activation has been achieved through collisions with neutral gas atoms / molecules or collisions with a surface. In cell surface-induced dissociation (SID) has been achieved though the use of a target surface positioned inside one of the cell's trapping plates.[138] A recent modelling study suggests SID could be performed by accelerating the ions into the excitation / detection electrodes.[139] However, collisions with neutral gas molecules account for the majority of tandem mass spectrometry experiments performed on FTICR mass spectrometers.

Using the expression for an ion's radius after excitation, equation 1.5.ii, the kinetic energy of an ion after excitation can be estimated.

$$K.E._{post-excitation} = \frac{mv^2}{2} = \frac{m\omega_c^2 r^2}{2} = \frac{q^2 E_0^2 \left(T_{excite}\right)^2}{8m} \qquad (1.7.i)$$

An ion of mass 100 Da, excited for 1 ms by a 1 V_{p-p} RF voltage applied to infinitely – extended parallel flat electrodes 2 cm apart has a final kinetic energy of 1.2 keV[39]. Thus using on-resonance excitation it is relatively easy to generate high collision energies. Collisions with neutral gas molecules can then to lead fragmentation.[140] Arguably the most common CID technique is sustained off-resonance irradiation (SORI) CID. Off-resonance excitation results in the periodic excitation / de-excitation of the ion's cyclotron motion[141]. As the ions are periodically excited / de-excited the field can be applied for prolonged periods of time. Multiple low energy collisions throughout this excitation then leads to the slow heating[142] of the ion and ultimately fragmentation[143]. The frequency of the periodicity is determined by the difference between the frequency of the applied field and the cyclotron frequency of the ion in question. This frequency dependence is observed as a mass dependence that has been

used to radially separate ions, the innermost of which were selectively photodissociated[144].

The fragments produced by a fragmentation technique depend on the internal energy content of the parent ion after excitation, the time scale of the reaction, and the fragmentation pathway itself.[35] Several approaches have been reported for obtaining energy resolved measurements using a Fourier transform ion cyclotron resonance mass spectrometer, including on-resonance excitation[145-147], surface induced dissociation[138] and sustained off-resonance irradiation[145].

1.8. Summary

Electrospray ionisation in conjunction with Fourier transform ion cyclotron resonance mass spectrometry provides a sensitive instrument that is able to provide accurate mass measurements as well as high resolution for every stage of mass spectrometry for a wide variety of analytes. Furthermore, many different fragmentation techniques are available to the investigator owing to the inherent ability of FTICR to contain the ion for prolonged periods of time, to accelerate the ions for collision induced dissociation, to smash the ions into surfaces as well as the inherent fragmentation techniques afforded by an ESI source. When performed with sufficient control the in cell fragmentation techniques can be used to obtain information regarding the energetics of the reactions[138, 145-147]. In addition to these strengths, it has proved possible to couple ESI-FTICR mass spectrometers to external separation techniques such as GPC[26], LC[148, 149], CE[50] and CIEF[50].

It is for all of the above reasons that FTICR mass spectrometry continues to enjoy wide interest from the analytical, biological and physical sciences.

1.9. Aims

The initial aim of the PhD was to help initiate a new field of research, reaction dynamics, through building and using an ion imaging spectrometer to study the dynamics of small molecule photodissociation. Initial experiments were to be performed and were performed in collaboration with Prof. David Parker, University of Nijmegen, the Netherlands. Unfortunately, six months into this project my reaction dynamics supervisor, Prof. Albert J R Heck, was offered his current job in Utrecht and he subsequently left the university. As there was no other academic in this field, the project was to help initiate a new field of research, for the remainder of my PhD the focus was changed to the characterisation of polymers using FTICR mass spectrometry, under the supervision of Prof. Peter J. Derrick. The reaction dynamics results obtained in Nijmegen are reported in chapter 6.

The aim of the ESI FTICR project was to develop the technique for polymer characterisation such that completely unknown polymer systems could be analysed. This required a thorough understanding of the factors affecting peak precision and ion biases during ion formation / transport / detection as well as developing new methods for the analysis of the results. Chapters 4 and 5 detail the results of this investigation. As the propensity for MSAD increases rapidly with the amount of space charge stored in the hexapole ion trap and polymer analysis requires high ion populations to be trapped, it was recognised that MSAD is potentially a major limiting factor for ESI polymer analysis, especially for large polymer systems. Consequently, a theoretical investigation of the energy of ions in the hexapole ion trap was also undertaken, this is reported in chapter 3.

The mass spectral investigations concerned developing the methodology for polymer analysis as well as in depth study of a potential source of bias.

(1)   Hoffman, E. d.; Charette, J.; Stroobant, V. *Mass Spectrometry*; Wiley: New York, 1996.

(2)   Fenn, J. B.; Yamashita, M. *J. Phys. Chem.* **1984**, *88*, 4671-4675.

(3)   Kebarle, P. *J. Mass Spectrom.* **2000**, *35*, 804-817.

(4)   Zenobi, R.; Knochenmuss, R. *Mass Spectom. Rev.* **1998**, *17*, 337-366.

(5)   Loo, J. A. *Mass Spectrom. Rev.* **1997**, *16*, 1-23.

(6)   Pócsfalvi, G.; Landa, G. D.; Ferranti, P.; Ritieni, A.; Randazzo, G.; Malorni, A. *Rapid Comm. Mass Spectrom.* **1997**, *11*, 265-272.

(7)   Chazin, W.; Veenstra, T. D. *Rapid Comm. Mass Spectrom.* **1999**, *13*, 548-555.

(8)   Konermann, L.; Collings, B. A.; Douglas, D. J. **1997**.

(9)   Pastor, S. J.; Wilkins, C. L. *Int. J. Mass Spectrom. Ion Proc.* **1998**, *175*, 81-92.

(10)   Montaudo, G.; Garozzo, D.; Montaudo, M. S.; Puglisi, C.; Samperi, F. *Macromolecules* **1995**, *28*, 7983-7989.

(11)   Montaudo, M. S.; Samperi, F. *Eur. J. Mass Spectrom.* **1998**, *4*.

(12)   Palmblad, M.; Hakansson, K.; Hankansson, P.; Feng, X.; Cooper, H.; Giannakopulos, A. E.; Green, P. S.; Derrick, P. J. *Eur. J. Mass Spectrom.* **2000**, *6*, 267-275.

(13)   O'Conner, P. B.; Duursma, M.; Rooij, G. J. v.; Heeren, R. M. A.; Boon, J. J. *Analytical chemistry* **1997**, *69*, 2751-2755.

(14)   Suddaby, K. G.; Hunt, K. H.; Haddleton, D. M. *Macromolecules* **1996**, *29*, 8642-8649.

(15)   Shi, S. D. H.; Hendrickson, C. L.; Marshall, A. G.; Simonsick, W. J.; Aaserud, D. J. *Analytical chemistry* **1998**, *70*, 3220-3226.

(16)   Scrivens, J. H.; Jackson, A. T. *Int. J. Mass Spectrom.* **2000**, *200*, 261-276.

(17)   Maziarz III, E.; Baker, G. A.; Mure, J. V.; Wood, T. D. *Int. J. Mass Spectrom.* **2000**, *202*, 241-250.

(18)   Maziarz III, E. P.; Baker, G. A.; Wood, T. D. *Macromolecules* **1999**, *32*, 4411-4418.

(19)   Maziarz III, E. P.; Baker, G.; Lorenz, S. A.; Wood, T. *J. Am. Soc. Mass Spectrom.* **1999**, *10*, 1298-1304.

(20)   Koster, S.; Duursma, M. C.; Boon, J. J.; Heeren, R. M. A. *J. Am. Soc. Mass Spectrom.* **2000**, *11*, 536-543.

(21)   Koster, S.; Duursma, M. C.; Boon, J. J.; Nielen, M. W. F.; Koster, C. G. d.; Heeren, R. M. A. *J. Mass Spectrom.* **2000**, *35*, 739-748.

(22)   Hunt, S. M.; Sheil, M. M.; Belov, M.; Derrick, P. J. *Anal. Chem.* **1998**, *70*, 1812-1822.

(23)   Easterling, M. L.; Amster, I. J.; van Rooij, G. J.; Heeren, R. M. A. *J. Am. Soc. Mass Spectrom.* **1999**, *10*, 1074-1082.

(24)   Danis, P. O.; Kerr, D. E.; Westmoreland, D. G.; Piton, M. C.; Christie, D. I.; Clay, P. A.; Kable, S. H.; Gilbert, R. G. *Macromolecules* **1993**, *26*, 6684-6685.

(25)   Chen, R.; Zhang, N.; Tseng, A. M.; Li, L. *Rapid Comm. Mass Spectrom.* **2000**, *14*, 2175-1281.

(26)   Aaserud, D. J.; Prokai, L.; Simonsick Jr, W. J. *Anal. Chem.* **1999**, *71*, 4793-4799.

(27)   Botrill, A. R.; Giannakopulos, A. E.; Millichope, A.; Lee, K. S.; Derrick, P. J. *Eur. J Mass Spectrom.* **2000**, *6*, 225-232.

(28)   Sze, T.-P. E.; Chan, T.-W. D. *Rapid Commun. Mass Spectrom.* **1999**, *13*, 398-406.

(29)   Wong, S. F.; Meng, C. K.; Fenn, J. B. *J. Chem. Phys.* **1988**, *92*, 546-550.

(30)   Yan, W.; Ammon Jr, D. M.; Gardella Jr, J. A.; Maziarz III, E. P.; Hawkridge, A. M.; Grobe III, G. L.; Wood, T. D. *Eur. J. Mass Spectrom.* **1998**, *4*, 467-474.

(31) Zubarev, R. A.; Horn, D. M.; Fredricksson, E. K.; Kelleher, N. L.; Kruger, N. A.; Lewis, M. A.; Carpenter, B. K.; McLafferty, F. W. *Anal. Chem.* **2000,** *72,* 563-573.

(32) Kendall, G.; Cooper, H.; Heptinstall, J.; Derrick, P. J.; Walton, D. J. *Anal. Biochem. Biophys.* , in press.

(33) Kelleher, N. L.; Zubarev, R. A.; Bush, K.; Furie, B.; Furie, B. C.; McLafferty, F. W.; Walsh, C. T. *Anal. Chem.* **1999,** *71,* 4250-4253.

(34) Green, P. S.; Giannakopulos, A. E.; Derrick, P. J. .

(35) Vékey, K. *J. Mass Spectrom.* **1996,** *31,* 445-463.

(36) Futrell, J. H. *Int. J. Mass Spectrom.* **2000,** *200,* 495-508.

(37) Cooper, H. J.; Gallagher, R. T.; Greenwood, P. F.; Vulpius, T.; Derrick, P. J. *J. Chem. Soc. Chem. Commun.* **1995,** 1459-1460.

(38) March, R. E. *J. Mass Spectrom.* **1997,** *32,* 351-369.

(39) Marshall, A. G.; Hendickson, C. L.; Jackson, G. S. *Mass Spectrom. Rev.* **1998,** *17,* 1-35.

(40) Cooks, R. G. *J. Mass Spectrom.* **1995,** *30,* 1215-1221.

(41) Bowers, W. D.; Delbert, S.-S.; Hunter, R. L.; McIver Jr, R. T. *J. Am. Chem. Soc.* **1984,** *106,* 7288-7289.

(42) Little, D. P.; Spier, J. P.; Senko, M. W.; O'Connor, P. B.; McLafferty, F. W. *Anal. Chem.* **1994,** *66,* 2809-2815.

(43) Price, W. D.; Schnier, P. D.; Williams, W. R. *Anal. Chem.* **1996,** *68,* 859-866.

(44) Freitas, M. A.; Hendrickson, C. L.; Marshall, A. G. *Rapid Commun. Mass Spectrom.* **1999,** *13,* 1639-1642.

(45) Zubarev, R. A.; Kelleher, N. L.; McLafferty, F. W. *J. Am. Chem. Soc.* **1998,** *120,* 3265-3266.

(46) Wingrath, T.; Kirsch, D.; Kaufmann, R.; Stahl, W.; Sies, H. *Meth. Enzymol.* **1999,** *299,* 390-408.

(47) Schneider, B. B.; Douglas, D. J.; Chen, D. D. Y. *Rapid Comm. Mass Spectrom.* **2001,** *15,* 249-257.

(48) Van-Dongen, W. D.; Van-Wijk, J. I. T.; Green, B. N.; Heeren, W.; Haverkamp, J. *Rapid Comm. Mass Spectrom.* **1999,** *13,* 1712.

(49) Sannes-Lowery, K.; Griffey, R. H.; Kruppa, G. H.; P, S. J.; Hofstadler, S. A. *Rapid Comm. Mass Spectrom.* **1998,** *12,* 1957-1961.

(50) Smith, R. D. *Int. J. Mass Spectrom.* **2000,** *200,* 509-544.

(51) Easterling, M. L.; Mize, T. H.; Amster, I. J. *Anal. Chem.* **1999,** *71,* 624-632.

(52) Burton, R. D.; Matuszak, K. P.; Watson, C. H.; Eyler, J. R. *J. Am. Soc. Mass Spectrom.* **1999,** *10,* 1291-1297.

(53) Heck, A. J. R.; Derrick, P. J. *Anal. Chem.* **1997,** *69,* 3603-3607.

(54) Gaskell, S. J. *J. Mass Spectrom.* **1997,** *32,* 677.

(55) Bruins, A. P. *J. Chromatogr. A* **1998,** *794,* 345-357.

(56) Cole, R. B. *J. Mass Spectrom.* **2000,** *35,* 763-772.

(57) Mann, M. *Org. Mass Spectrom.* **1990,** *25,* 575-587.

(58) Vekey, K. *Mass Spectrom. Rev.* **1995,** *14,* 195-225.

(59) Amad, M. a. H.; Cech, N. B.; Jackson, G. S.; Enke, C. G. *J. Mass Spectrom.* **2000,** *35,* 784-789.

(60) de la Mora, J. F.; Van Berkel, G. J.; Enke, C. G.; Cole, R. B.; Martinez-Sanchez, M.; Fenn, J. B. *J. Mass Spectrom.* **2000,** *35,* 939-952.

(61) Drahos, L.; Heeren, R. M. A.; Collette, C.; De Pauw, E.; Vékey, K. *J. Mass Spectrom.* **1999,** *34,* 1373-1379.

(62) Fenn, J. B.; Russell, J.; Meng, C. K. *J. Am. Soc. Mass Spectrom.* **1997,** *8,* 1147-1157.

(63) Enke, C. G. *Anal. Chem.* **1997,** *69,* 4885-4893.

(64) Gamero-Castaño, M.; de la Mora, J. F. *J. Mass Spectrom.* **2000,** *35,* 790-803.

(65) Tang, K.; Smith, R. D. *J. Am. Soc. Mass Spectrom.* **2001,** *12,* 343-347.

(66) Van Berkel, G. J. *J. Mass Spectrom.* **2000,** *35,* 773-783.

(67) Zhou, S.; Cook, K. D. *J. Am. Soc. Mass Spectrom.* **2001,** *12,* 206-214.

(68) Zhou, S.; Cook, K. D. *Anal. Chem.* **2000,** *72,* 963-969.

(69) Zhou, S.; Edwards, A. G.; Cook, K. D.; Berkel, G. J. V. *Anal. Chem.* **1999,** *71,*
769-776.

(70) Mack, L. L.; Kralic, P.; Rehude, A.; Dole, M. *J. Chem. Phys.* **1970,** *52,* 4977-
4986.

(71) Dole, M.; Mack, L. L.; Hines, R. L.; Mobley, R. C.; Ferguson, L. D.; Alice, M.
B. *J. Chem. Phys.* **1968,** *49,* 2240-2249.

(72) Yamashita, M.; Fenn, J. B. *J. Phys. Chem.* **1984,** *88,* 4451-4459.

(73) Gienic, J.; Mack, L. L.; Nakamae, K.; Gupta, C.; Kumar, V.; Dole, M. *Biomed.
Mass Spectrom.* **1984,** *11,* 259-268.

(74) Alexandrov, M. L.; Gall, L. N.; Krasnov, M. V.; Nikolaev, V. I.; Pavelenko, V.
A.; Shkurov, V. A. *Dokl. Akad. Nauk SSSR* **1984,** *277,* 379-383.

(75) Blades, A. T.; Ikonomou, M. G.; Kebarle, P. *Anal. Chem.* **1991,** *63,* 2109-2114.

(76) Evans, C. A.; Hendricks, C. D. *Rev. Sci. Instrum.* **1972,** *43,* 1527.

(77) Kebarle, P.; Tang, L. *Anal. Chem.* **1993,** *65,* 972-986.

(78) Smith, D. P. *IEEE Trans. Ind. Appl.* **1986,** *IA-22,* 527-535.

(79) Wilm, M.; Mann, M. *Anal. Chem.* **1996,** *68,* 1-8.

(80) Wilm, M. S.; Mann, M. *Int. J. Mass Spectrom. Ion Proc.* **1994,** *136,* 167-180.

(81) Emmet, M. R.; Caprioli, R. M. *J. Am. Soc. Mass Spectrom.* **1994,** *5,* 605-613.

(82) Feng, X.; Agnes, G. R. *J. Am. Soc. Mass Spectrom.* **2000,** *11,* 393-399.

(83) ESI special issue *Anal. Chim. Acta* **2000.**

(84)   Iribarne, J. V.; Thomson, B. A. *J. Chem. Phys.* **1976**, *64*, 2287.

(85)   Thomson, B. A.; Iribarne, J. V. *J. Chem. Phys.* **1979**, *71*, 4451.

(86)   Schmelzeisen-Redeker, G.; Buttering, L.; Röllgen, F. W. *Int. J. Mass Spectrom. Ion Proc.* **1989**, *90*, 139.

(87)   Ikonomou, M. G.; Blades, A. T.; Kebarle, P. *Anal. Chem.* **1991**, *63*, 1989.

(88)   Fenn, J. B.; Mann, M.; Meng, C. K.; Wong, S. F.; Whitehouse, C. M. *Science* **1989**, *246*, 64.

(89)   Sjöberg, P. J. R.; Bökman, C. F.; Bylund, D.; Markides, K. E. *Anal. Chem.* **2000**, *73*, 23.

(90)   Gatlin, C. L.; Turacek, F. *Anal. Chem.* **1994**, *66*, 712.

(91)   Hofstadler, S. A.; Beu, S. C.; Laude, D. A. *Anal. Chem.* **1993**, *65*, 312-316.

(92)   Tolmachev, A. V.; Udseth, H. R.; Smith, R. D. *Rapid Comm. Mass Spectrom.* **2000**, *14*, 1907-1913.

(93)   Hakansson, K.; Axelsson, J.; Palmblad, M.; Hakansson, P. *J. Am. Soc. Mass Spectrom.* **2000**, *11*, 210-217.

(94)   Sannes-Lowery, K. A.; Hofstadler, S. A. *J. Am. Soc. Mass Spectrom.* **2000**, *11*, 1-9.

(95)   McDonnell, L. A.; Giannakopulos, A. E.; Tsybin Y.; Håkansson P.; Derrick, P. J. *submitted to Eur. J. Mass Spectrom.*

(96)   Gerlich, D. In *State-selected and state-to-state ion-molecule reaction dynamics. Part 1. Experiment*; Ng, C.-Y., Baer, M., Eds.; Wiley: New York, 1992; Vol. LXXXII, pp 1-176.

(97)   Hägg, C.; Szabo, I. *Int. J. Mass Spectrom. Ion Proc.* **1986**, *73*, 295-312.

(98)   Hägg, C.; Szabo, I. *Int. J. Mass Spectrom. Ion Proc.* **1986**, *73*, 237-275.

(99)   Szabo, I. *Int. J. Mass Spectrom. Ion Proc.* **1986**, *73*, 197-235.

(100) Miller, P. E.; Denton, M. B. *Int. J. Mass Spectrom. Ion Proc.* **1986**, *72*, 223-238.

(101) Wang, Y.; SHi, S. D. H.; Hendrickson, C. L.; Marshall, A. G. *Int. Journal Mass Spectrom.* **2000,** *198*, 113-120.

(102) Huang, Y.; Guan, S.; Kim, H. S.; Marshall, A. G. *Int. J. Mass Spectrom. Ion Proc.* **1996,** *152*, 121-133.

(103) Kofel, P.; Alleman, M.; Kellerhals, H.; Wanczek, K.-P. *Int. J. Mass Spectrom. Ion Proc.* **1986,** *72*, 53-61.

(104) Belov, M. E.; Gorshkov, M. V.; Udseth, H. R.; Anderson, G. A.; Smith, R. D. *Anal. Chem.* **2000,** *72*, 2271-2279.

(105) Amster, I. J. *J. Mass Spectrom.* **1996,** *31*, 1325-1337.

(106) Marshall, A. G.; Verdun, F. R. *Fourier tranforms in NMR, optical, and mass spectrometry: a user's handbook*; Elsevier: Amsterdam; Oxford, 1990.

(107) Halliday, D.; Resnick, R.; Walker, J. *Fundamentals of Physics*, 4th ed.; Wiley: New York, 1993.

(108) Comisarow, M. B. *J. Chem. Phys.* **1978,** *69*, 4097-4104.

(109) Marshall, A. G.; Roe, D. C. *J. Chem. Phys.* **1980,** *73*, 1581-1590.

(110) Comisarow, M. B.; Marshall, A. G. *Chem. Phys. Lett.* **1974,** *26*, 489-490.

(111) Marshall, A. G.; Wang, T.-C.; Ricca, T. L. *J. Am. Chem. Soc.* **1985,** *107*, 7893-7897.

(112) Guan, S.; Marshall, A. G. *Int. J. Mass Spectrom. Ion Proc.* **1996,** *157/158*, 5-37.

(113) Kelly, P. C.; Horlick, G. *Anal. Chem.* **1973,** *45*, 518-527.

(114) Guan, S.; Wahl, M. C.; Marshall, A. G. *Anal. Chem.* **1993,** *65*, 3647-3653.

(115) Gorshkov, M. V.; Marshall, A. G.; Nikolaev, E. N. *J. Am. Soc. Mass Spectrom.* **1993,** *4*, 855-868.

(116) Naito, Y.; Inoue, M. *Int. J. Mass Spectrom. Ion Proc.* **1996,** *157*, 85-96.

(117) He, F.; Hendrickson, C. L.; Marshall, A. G. *Anal. Chem.* **2001,** *73*, 647-650.

(118) Sommer, H.; Thomas, H. A.; Hipple, J. A. *Phys. Rev.* **1951,** *82*, 697.

(119) Guan, S.; Marshall, A. G. *Int. J. Mass Spectrom. Ion Proc.* **1995,** *146*, 261-296.

(120) Hunter, R. L.; Sherman, M. G.; McIver, R. T. *Int. J. Mass Spectrom. Ion Proc.* **1983,** *50*, 259-274.

(121) Jeffries, J. B.; Barlow, S. E.; Dunn, G. H. *Int. J. Mass Spectrom. Ion Proc.* **1983,** *54*, 169-187.

(122) Francl, T. J.; Sherman, M. G.; Hunter, R. L.; Locke, M. J.; Bowers, W. D.; McIver, R. J. *Int. J. Mass Spectrom. Ion Proc.* **1983,** *54*, 189-199.

(123) Ledford Jr, E. B.; Rempel, D. L.; Gross, M. L. *Anal. Chem.* **1984,** *56*, 2744-2748.

(124) Shi, S. D.-H.; Drader, J. J.; Frietas, M. A.; Hendrickson, C. L.; Marshall, A. G. *Int. J. Mass Spectrom.* **2000,** *195/196*, 591-598.

(125) Bruce, J. E.; Anderson, G. A.; Brands, M. D.; Pasa-Tolic, L.; Smith, R. D. *J. Am. Soc. Mass Spectrom.* **2000,** *11*, 416-421.

(126) Wang, T.-C. L.; Marshall, A. G. *Int. J. Mass Spectrom. Ion Proc.* **1986,** *68*, 287-301.

(127) Wang, M.; Marshall, A. G. *Int. J. Mass Spectrom. Ion Proc.* **1988,** *86*, 31-51.

(128) Nikolaev, E. N.; Miluchihin, N. V.; Inoue, M. *Int. J. Mass Spectrom. Ion Proc.* **1995,** *148*, 145-157.

(129) Peurrung, A. J.; Kouzes, R. T. *Int. J. Mass Spectrom. Ion Proc.* **1995,** *145*, 139-153.

(130) Guan, S.; Kim, H. S.; Marshall, A. G.; Wahl, M. C.; Wood, T. D. *Chem. Rev.* **1994,** *8*, 2161-2182.

(131) Wood, T. D.; Ross III, C. W.; Marshall, A. G. *J. Am. Soc. Mass Spectrom.* **1994,** *5*, 900-907.

(132) Guan, S.; Wahl, M. C.; Marshall, A. G. *J. Chem. Phys.* **1994,** *100*, 6137.

(133) Pitsenberger, C. C.; Easterling, M. L.; Amster, I. J. *Anal. Chem.* **1996,** *68*, 3732-3739.

(134) Guan, S.; Marshall, A. G. *Anal. Chem.* **1994,** *66*, 1363-1367.

(135) Paster, S. J.; Wilkins, C. L. *Anal. Chem.* **1998,** *70*, 213-217.

(136) Dunbar, R. C. *Int. J. Mass Spectrom.* **2000,** *200*, 571-589.

(137) Zubarev, R. A.; Kruger, N. A.; Fridriksson, E. K.; Lewis, M. A.; Horn, D. M.; Carpenter, B. K.; McLafferty, F. W. *J. Am. Chem. Soc.* **1999,** *121*, 2857-2862.

(138) Rakov, V. S.; Futrell, J. H.; Denisov, E. V.; Nikolaev, E. N. *Eur. J. Mass Spectrom.* **2000,** *6*, 299-317.

(139) Danell, R. A.; Glish, G. L. *J. Am. Soc. Mass Spectrom.* **2000,** *11*, 1107-1117.

(140) Sheil, M. M.; Guilhaus, M.; Derrick, P. J. *Org. Mass Spectrom.* **1990,** *25*, 671-680.

(141) Heck, A. J. R.; Koning, L. J. d.; Pinkse, F. A.; Nibbering, N. M. M. *Rapid Commun. Mass Spectrom.* **1991,** *5*, 406-414.

(142) McLuckey, S. A.; Goeringer, D. E. *J. Mass Spectrom.* **1997,** *32*, 461-474.

(143) Gauthier, J. W.; Trautman, T. R.; Jacobsen, D. B. *Anal. Chim. Acta* **1991,** *246*, 211-225.

(144) Shin, S. K.; Han, S.-J. *J. Am. Soc. Mass Spectrom.* **1997,** *8*, 86-89.

(145) Laskin, J.; Byrd, M.; Futrell, J. *Int. J. Mass Spectrom.* **2000,** *195/196*, 285-302.

(146) Bensimon, M.; Houriet, R. *Int. J. Mass Spectrom. Ion Proc.* **1986,** *72*, 93-98.

(147) Beyer, M.; Bondybey, V. E. *Rapid Commun. Mass Spectrom.* **1997,** *11*, 1588-1591.

(148) Quenzer, T. L.; Emmett, M. R.; Hendrickson, C. L.; Kelly, P. H.; Marshall, A. G. *Anal. Chem.* **2001,** *73*, 1721-1725.

(149) Emmet, M. R.; White, F. M.; Hendrickson, C. L.; Shi, S. D.-H.; Marshall, A. G. *J. Am. Soc. Mass Spectrom.* **1998,** *9*, 333-340.

2 Experimental

2.1. Instrumentation

All experiments were performed on the commercially available Bruker BioAPEX - 94e Fourier transform ion cyclotron resonance (FTICR) mass spectrometer[1] equipped with a passively shielded 9.4 T central-field superconducting (Nb_3Sn) magnet (Magnex Ltd, UK), a 6 cm diameter cylindrical INFINITY™ cell[2], and an electrospray ionisation (ESI) ion source (Analytica, Branford, CT, USA, model # 103426-1).

The ion source consisted of an inlet Pyrex capillary (15cm length and 0.5mm i.d.) with nickel capping at both ends, a skimmer and an RF-only hexapole ion trap. As can be seen in figure 2.1.1., the skimmer acted as one of the trapping electrodes of the ion trap and collimated the ion beam prior to the hexapole. Ions were accumulated in the hexapole ion-trap for a user-defined time ($D1$), after which the ions were pulsed into the spectrometer by changing the potential on the other trapping electrode (trap) from the trapping value (V_{trap}) to the extract value ($V_{extract}$) for a user-defined duration ($P2$).

The ions were generated by electrospray ionisation[3] using either the nanospray[4] or microspray[5] modifications. The experiments were performed using nanospray and microspray to minimise any potential contamination risks. The lower flow rates of nanospray (and microspray) as opposed to regular electrospray, ~ 0.15 μl min^{-1} and 1.1 μl min^{-1} respectively, introduced less sample into the mass spectrometer. Moreover, as a result of a finer needlepoint and being situated closer to the entrance to the capillary, nanospray (and microspray) were more sensitive than regular electrospray, consequently lower sample concentrations could be used[5].
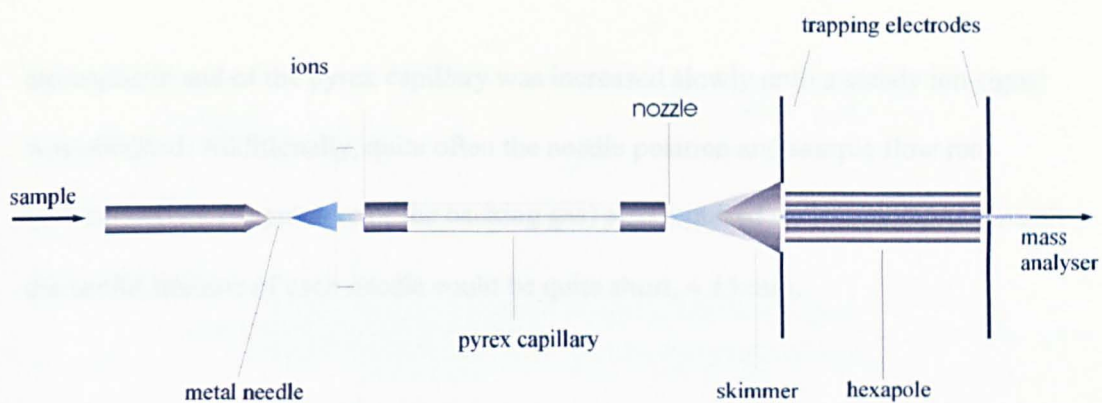
Figure 2.1.1. Schematic of the Analytica ESI source.

Initially all experiments (and most reported here) were performed by nanospray using the supplied nanospray holder and a small-aperture stainless steel cap for the pyrex capillary, see figure 2.1.2.
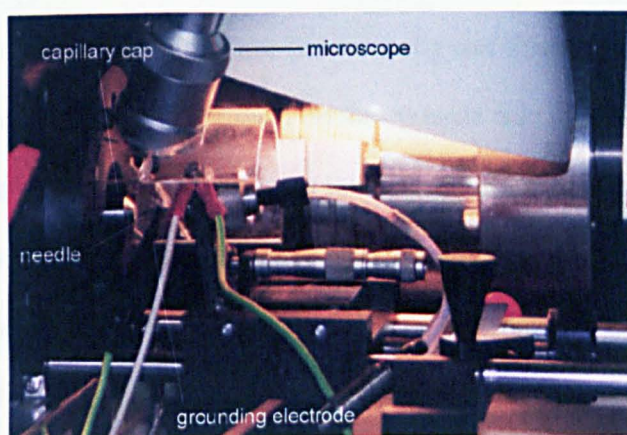
Figure 2.1.2. The nanospray source

The needles used (Protana, medium nano ES spray capillaries) required opening prior to use by gently touching the capillary cap, which protected the capillary during this procedure, with the needle end. A gentle gas pressure, ≈ 6 psi, applied to the back of the nanospray needle was used to push the sample through the needle. Grounding of the needle was achieved through the use of a clip grounding-electrode, see above figure.

A disadvantage of nanospray compared to electrospray was the shorter lifetime of the needle and hence the experiment. Typically approximately 8 µl of the sample was placed into the needle, the needle tip was broken and the potential applied to the

45

atmospheric end of the pyrex capillary was increased slowly until a steady ion signal was obtained. Additionally, quite often the needle position and sample flow rate (determined by the pressure of the backing gas) also required optimisation. As a result the useful lifetime of each needle could be quite short, ≈ 15 min.

To permit longer experiments to be performed a microspray ion source was constructed using commercially available components and an in-house sleeve incorporating a sunken screw that allowed the ion source to be held securely using the available nanospray holder (see figure 2.1.3). The microspray needle was a commercially available needle cut to about 4 cm, see diagram for details. This was placed in a short Teflon tube jacket for structural support such that the ends of each (non-tapered end of needle) were aligned. The small dead volume between the sheathed needle and Teflon tubing on the opposite side of the grounded zero dead-volume (ZDV) union where the liquid was in contact with the union's body provided the required sample grounding. Using the microspray ion source a steady ion signal could be obtained for > 5 hrs, allowing longer experiments to be performed. A Cole-Palmer 74900 series syringe pump was used to control sample infusion for the microspray experiments (not shown on diagram).

Tapered tip
(New Objective, TT360-50-50-CE5)

In-house nanospray sleeve with
sunken screw to secure union

sample

zero dead volume (ZDV) union
(Anachem, part # U-322)

Teflon tubing (Upchurch scientific, part # 1549)
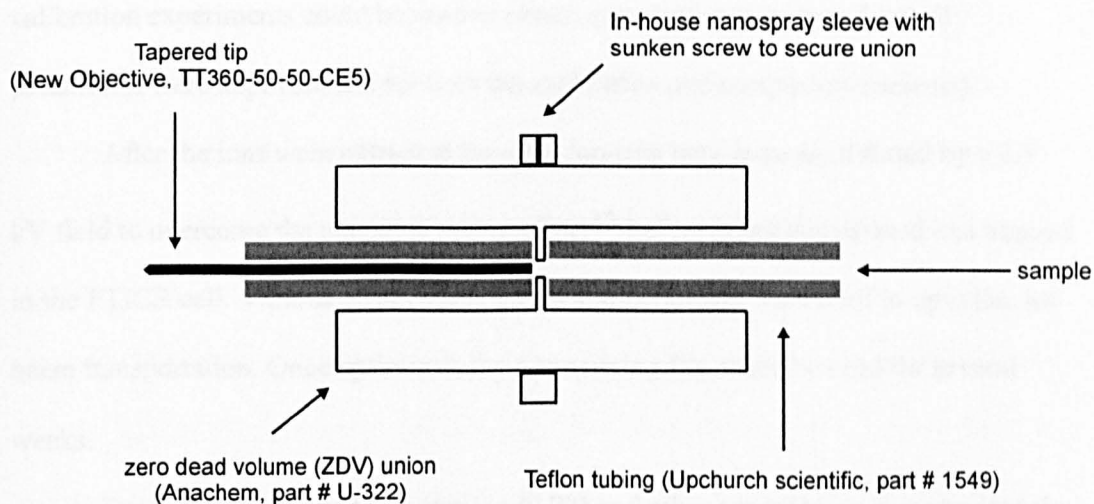
Figure 2.1.3. Schematic of the microspray ion source constructed using mostly commercially available components.

Once ions were produced they were transported through the pyrex capillary into the first vacuum chamber, the nozzle-skimmer region (capillary exit – skimmer), where they were accelerated by an electrostatic field. After collimation the ions entered the RF-only hexapole ion-trap and were accumulated. For an ion to be detected it had to be successfully trapped. Furthermore, for the relative intensities of the detected ion signals to reflect accurately the numbers of each ion, the trapping efficiency needed to be uniform across the desired mass (m/z) range. However, owing to bias effects including ion dependent trapping efficiency, radial stratification in the multipole ion trap[6,7], fragmentation reactions (including charge stripping, nozzle – skimmer[8] collision induced dissociation (CID) and multipole storage assisted dissociation[9-11]), and biases arising from the supersonic expansion of the seeded bath gas[12], such uniformity was not possible. Nevertheless, with careful tuning of the ion source a broad range of ions of different m/z could be trapped. Provided these windows were sufficiently wide to trap all ions of interest, although the relationship between the observed signal intensity and the number of ions might not have been uniform across the m/z window, previous

calibration experiments could be used to obtain quantitative data (provided all parameters were kept constant for both the calibration and sample experiments).

After the ions were extracted from the ion-trap they were accelerated by a 2.5 kV field to overcome the magnetic mirror effect[13] before being decelerated and trapped in the FTICR cell. Various electrostatic lenses and deflectors were used to optimise ion beam transportation. Once optimised, the same tuning file could be used for several weeks.

For collision-induced dissociation (CID) and other experiments that required the introduction of a gas, two computer-controlled solenoid valves (General Valve) were used to inject the gas into the FTICR cell via the ion optic transfer-line. By opening the inlet valve connecting the cell and a volume of collision gas (e.g. N_2 at a pressure of ≈ 100 mbar) for ≈ 0.5 - 1ms, the pressure in the cell was raised to the required level. Under normal operating CID conditions the pulsed valve was opened such that the pressure read by the ion gauge peaked at $\approx 10^{-7}$ mbar. However, as can be seen in figure 2.1.4, the cell pressure was read by an ion gauge that was situated away from the cell and directly above a cryogenic pump. Furthermore, the collision gas inlet was also situated directly above the cryopump and away from the cell.

Figure 2.1.4. Schematic of the cell, pump, pressure gauge, and gas inlet assembly
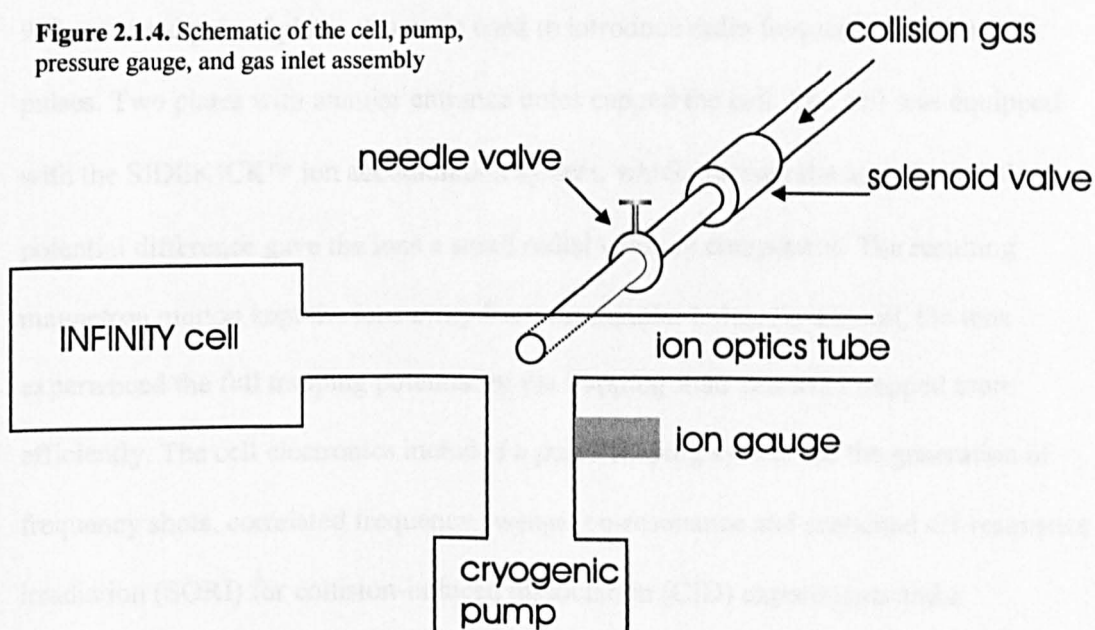
Although the pressure in the cell was sufficient to perform CID experiments, under standard conditions the pressure in the cell was not steady. After rapidly rising with the opening of the pulsed valve the pressure would decrease as the collision gas was pumped away. Moreover, the fact that the gas inlet was situated closer to the cryopump (and pressure gauge) and the gas was introduced in a single short pulse, a pressure differential was expected to exist between the cell and the pump (and pressure gauge). As a result, under such circumstances the actual pressure in the cell during CID experiments was neither steady nor known (with any accuracy). Although the standard CID experiments permitted structurally important fragments to be obtained and were used for the experiments reported here, to obtain information regarding a fragmentation channel's activation energy the cell pressure would need to be known accurately and remain constant for the duration of the activation pulse ($\approx$ 0.5 s for sustained off-resonance irradiation (SORI) CID). Such a thorough investigation was recently carried out by Futrell and workers from which they obtained the internal energy distributions obtained using SORI-CID[14].

The INFINITY™ cell[2] consisted of one pair of detection plates and, offset by 90°, a second pair of plates that were used to introduce radio frequency excitation pulses. Two plates with annular entrance holes capped the cell. The cell was equipped with the SIDEKICK™ ion accumulation system, which through the use of a radial potential difference gave the ions a small radial velocity component. The resulting magnetron motion kept the ions away from the annular holes. As a result, the ions experienced the full trapping potential of the trapping field and were trapped more efficiently. The cell electronics included a pulse-shaping system for the generation of frequency shots, correlated frequency sweeps, on-resonance and sustained off-resonance irradiation (SORI) for collision-induced dissociation (CID) experiments and a

preamplifier and detection electronics for direct and heterodyne-mode (frequency mixing) detection.

The instrument was differentially pumped using three cryogenic pumps, a 250 L s^{-1} turbomolecular pump and a rotary pump. The normal operating pressure of the cell was $\approx 2 \times 10^{-10}$ mbar, that of the hexapole region of the source was $\approx 6 \times 10^{-6}$ mbar and that of the forepumping region was $\approx 10^{-2}$ mbar. As indicated in figure 2.1.1., the forepumping region of the ion source used the turbomolecular and rotary pumps and the hexapole region sat atop a cryogenic pump. The ion transfer line and cell each had dedicated cryogenic pumps to achieve the ultra-high vacuum required. A gate valve separated the cell and transfer line of the vacuum system from the source side allowing ion source changes or maintenance to be performed without disturbing the ultra-high vacuum (a valve was also situated between the source cryopump and the main source housing to allow the ion source to be changed whilst the cryopump was still running).

Data were acquired through a 12-bit fast (10 MHz, broadband mode) digitiser with a 1 Mb acquisition memory and then transferred to an Indy workstation via a dedicated Ethernet connection. The workstation was equipped with a second Ethernet connection for external communication. Secondary workstations were used for data analysis and processing, thus maximising the data acquisition time of the FTICR facility. A PC-based HP 8010e CD-RW was used for long-term data storage. The instrument was controlled by and data retrieved and analysed using the Bruker XMASS™ software package. The software was run under IRIX 6.3.

2.2. Data acquisition

The electrospray ionisation (ESI) FTICR results reported here were obtained mostly in one of two types of experiment, a simple "detect all ions" experiment and SORI-CID[15,16] experiments that involved isolation of the parent ions prior to ion activation and dissociation. As can be seen below, figure 2.2.1., all of the experimental procedures present in the simple experiment were also present in the more complex SORI-CID experiment. Furthermore, the central section of the SORI-CID experiment (the ion-isolation and activation block) could be looped to perform higher stages of tandem mass spectrometry.
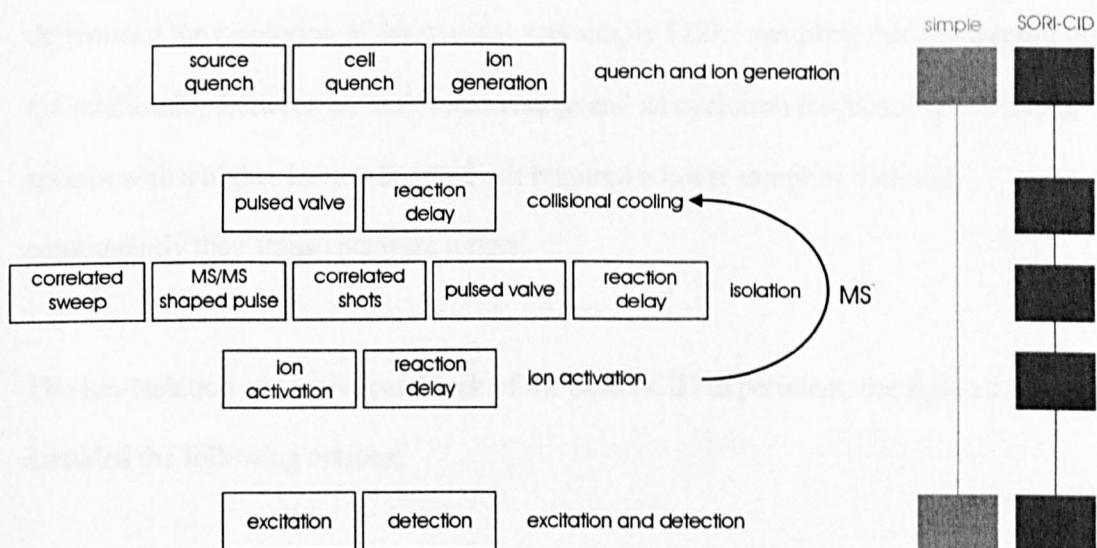
Figure 2.2.1. Schematic of the experimental sequences used.

Briefly, for the simple experiment, the cell and source were first quenched of all ions using a pulsed electrostatic field, after which the ions were allowed to accumulate in the hexapole ion trap for a user-defined period (typically 2 – 4s). The contained ions were then 'generated' by pulsing the ions into the FTICR cell, where they were excited to detectable radii. The current produced between the detector plates was then sampled and the resulting transients transferred to the INDY workstation for accumulation and Fourier transformation. In all cases the ions were excited using a frequency sweep[17],

the highest frequency being determined by the smallest ion ($f \propto z / m$). The frequency sweep consisted of many individual excitation pulses, separated by a user-defined step-size (XBB), each of user-defined intensity and duration. For a specific step-size the intensity and duration were optimised for optimum peak shape. Once optimised the same excitation profile could be used for several weeks. After excitation (the excitation and detection events were temporally distinct), the detected signal was amplified and sampled at twice the frequency of the highest detected frequency[18] (the Nyquist criterion). Most spectra included here were obtained with 512k data points, that is the transients were sampled 512k times. Accordingly the length of the transient (which determined the resolution of the spectra) was simply 512k / sampling rate. As a result of the relationship between an ion's mass/charge and its cyclotron frequency ($f \approx 1/(m/z)$), spectra with a higher lowest-detected m/z required a lower sampling rate and consequently their transients were longer.

The ion-isolation and activation block of the SORI-CID experiment, see figure 2.2.1, included the following options:

Pulsed valve: controlled the duration for which the solenoid valve was opened. Each pulsed valve icon represented a single 'gas shot.' The pressure in the cell, more specifically the pressure indicated by the ion gauge situated above the cryogenic pump, was a complex function of pumping speed, initial cell pressure, collision-gas backing pressure, solenoid valve duration and needle valve position (there was a leak valve situated between the solenoid valve and the gas inlet port, see figure 2.1.5). Typically the collision-gas storage vessels were filled to ≈ 100 mbar, and the solenoid valve duration altered to obtain a peak cell-pressure of about 10^{-7} mbar. Fine-tuning of the peak pressure-reading could then be made using the needle valve. A reaction delay at

the end of the isolation activation sequence ensured subsequent scans began with approximately equal cell pressures.

Reaction delay: set user-defined delays.

Correlated sweep: set the parameters used to isolate the parent ion(s). A frequency sweep of user-defined intensity and duration was swept across the user-defined mass range (by default this was equal to the upper and lower limits detected), except for a region determined by the frequency of the desired parent ion and the safety belt. The correlated sweep consisted of two 'chirp' excitation profiles (frequency sweeps) separated by the safety belt, with the parent ion lying in the centre of the safety belt. Due to off-resonance excitation[16], the parent ion intensity could be reduced. However, careful optimisation of the safety belt and of the ejection-field intensity and duration permitted parent-ion isolation with little intensity loss.

MS/MS shaped pulse: allowed the user to use one of the shaped excitation pulses provided with XMASS.

Correlated shots: could be used to eject specifically chosen ions, any unwanted ions remaining after a correlated sweep or those produced by fragmentation of the parent ion during / after the correlated sweep. Off-resonance excitation during the frequency sweep could result in some fragments being produced through CID when the collision gas was injected. Correlated shots allowed the user to eject specifically these unwanted ions (as with the correlated sweep the mass of the parent-ion was used to ensure it was not excited). Again the intensity and the duration of the correlated shots were user-defined.

Ion activation: was used to excite the ions for CID experiments. On-resonance and off-resonance excitation could be achieved by setting a user-defined offset to zero for the former, and any non-zero value for the latter. The non-zero offset for SORI-CID experiments could be either positive or negative for off-resonance excitation at higher or lower frequencies, respectively. For an on-resonance CID experiment the offset was set to zero.

At the end of an isolation and activation sequence, a reaction delay of 4 – 6 seconds was used to allow the cell pressure to return to excitation-detection levels and to give the ions a time in which to fragment. The subsequent isolation and excitation sequences permitted further stages of tandem mass spectrometry to be performed.

The software reported the RF field strength as the attenuation of the applied RF voltage in decibels, namely *attenuation* (dB) = -20 $\log_{10}$ ($V_{applied}$ / $V_{reference}$), where $V_{applied}$ and $V_{reference}$ were the applied and reference RF voltages respectively. This was related to the applied RF field strength, E_0 (Vm^{-1}), by the formula

$$E_0 = 2000e^{-0.1118A} \qquad (2.2.i)$$

where A is the RF field attenuation (dB) reported by the software and reported herein.

For all FTICR data acquisition routines, the complete acquisition sequences, or scans, were looped and the transients obtained accumulated a set number of times (the number of scans). The resulting transient was then ready for processing. As $S/N \propto$ *(number of scans)*$^{1/2}$, a larger number of scans permitted weaker ion signals to be detected. The longer times required by a larger number of scans was the principal reason the microspray ion source was constructed.

2.3. Data processing and Fourier transformation.

Before Fourier transformation, the experimental transients could be processed in a wide variety of ways including addition / subtraction of transients, multiplication / division by a constant factor, apodization and zero-filling[19] (sometimes referred to as padding). The data reported here include transformed unprocessed transients, apodized transients and zero-filled transients. The transients of the apodized spectra were weighted using a $\sin^2$ *(at)* function, where *a* was a parameter that ensured the nodes of the $\sin^2$ function were situated at the beginning and end of the transient, and zero-filled spectra were padded once only (final data-set size = 1Mb).

A fast Fourier transformation[20] of the transients provided the frequency domain data. The Fourier transformation of digitized time-domain transient yielded two frequency-domain spectra, $R(v)$ and $I(v)$, which were the real and imaginary parts of the complex spectrum[21]. In general, $R(v)$ and $I(v)$ were related to the desired absorption and dispersion spectra, $A(v)$ and $D(v)$ respectively, through

$$A(v) = R(v)\, cos\phi - I(v)\, sin\phi \qquad D(v) = R(v)\, cos\phi + I(v)\, sin\phi \qquad (2.3.\text{i})$$

by a phase, ϕ, which as a result of the pulsed nature of the excitation, was a complex function of cyclotron frequency and time. As this phase was not known, the spectra were displayed in magnitude mode (also known as absolute-value spectra)[22].

$$M(v) = \left[(A(v))^2 + (D(v))^2 \right]^{\frac{1}{2}} \qquad (2.3.\text{ii})$$

The frequency spectrum was converted to the *m/z* domain using the following calibration relationship

$$m/z = \frac{ML1}{v + ML2} \qquad (2.3.\text{iii})$$

where *ML1* and *ML2* are calibration constants determined by recording a spectrum of a known calibrant sample and minimising the difference (least squares) between experiment and theory. The XMASS™ software also permitted the data to be calibrated using the relationship

$$v = \frac{ML1}{m/z} + \frac{ML3}{(m/z)^2} + ML2 \qquad (2.3.\text{iv})$$

However the simpler first relationship was found to describe the frequency shifts more than adequately, provided the intensities of the calibration and sample experiments were as close as possible. Furthermore, as the second relationship does not include any intensity dependent factors, equal care with matching the ion densities during the calibration and experimental scans was still required to obtain consistently accurate spectra.

Several peak-picking algorithms were included in the supplied software package. If the peak was sharp and symmetrical, e.g. the Lorentzian expected from the Fourier transformation of a damped transient[23], the APEX option was used, if not the CENTROID option was chosen. The APEX option uses 3-point expressive interpolation at the maximum whilst the latter calculates a "number-average"

$$\left(m/z\right)_{centroid} = \frac{\sum \left(m/z\right)_i \times I_i}{\sum I_i} \qquad (2.3.\text{v})$$

where I_i is the relative intensity of the ith data point.

Finally, theoretical *m/z* values were determined using the isotopic masses determined by Audi *et al*[24] and the molecular calculators built into XMASS.

2.4. Sample preparation

As a general rule-of-thumb all samples were made up at 50 μM sample, 2.5 mM salt (NaOH, NH_4OAc, NaI, KI...) in the required solvent. The samples using ammonium acetate also had 1 % v/v acetic acid added. Bigger polymers were found to require more concentrated solutions, for example the peg 8000 results reported later used 75 μM samples. The solvent system depended on the polymer in question and will be detailed in the relevant chapters.

2.5. Measurement of excitation profiles

The excitation profiles were measured using a "wave-detect" experiment in which the current induced in the detector plates by the excitation sequence was sampled, accumulated and transformed. During these experiments the excitation field strength was reduced considerably to avoid saturation of the detector. Additionally, the number of data points (which determined the transient length) was such that one complete excitation profile was recorded. Finally, to ensure the complete excitation profile was recorded the detection range enclosed the excitation range.

1)Palmblad, M.; Häkansson, K.; Häkansson, P.; Feng, X.; Cooper, H.; Giannakopulos, A. E.; Green, P. S.; Derrick, P. J. *Eur. J. Mass Spectrom.* **2000**, *6*, 267-275.

2)Caravati, P.; Alleman, M. *Org. Mass Spectrom.* **1991**, *26*, 514.

3)Fenn, J. B.; Mann, M.; Meng, C. K.; Wong, S. F.; Whitehouse, C. M. *Science* **1989**, *246*, 64-71.

4)Wilm, M.; Mann, M. *Anal. Chem.* **1996**, *68*, 1-8.

5)Emmet, M. R.; Caprioli, R. M. *J. Am. Soc. Mass Spectrom.* **1994**, *5*, 605-613.

6)Tolmachev, A. V.; Udseth, H. R.; Smith, R. D. *Anal. Chem.* **2000**, *72*, 970-978.

7)Tolmachev, A. V.; Udseth, H. R.; Smith, R. D. *Rapid Comm. Mass Spectrom.* **2000**, *14*, 1907-1913.

8)Van-Dongen, W. D.; Van-Wijk, J. I. T.; Green, B. N.; Heeren, W.; Haverkamp, J. *Rapid Comm. Mass Spectrom.* **1999**, *13*, 1712.

9)Sannes-Lowery, K.; Griffey, R. H.; Kruppa, G. H.; P, S. J.; Hofstadler, S. A. *Rapid Comm. Mass Spectrom.* **1998**, *12*, 1957-1961.

10)Sannes-Lowery, K. A.; Hofstadler, S. A. *J. Am. Soc. Mass Spectrom.* **2000**, *11*, 1-9.

11)Häkansson, K.; Axelsson, J.; Palmblad, M.; Håkansson, P. *J. Am. Soc. Mass Spectrom.* **2000**, *11*, 210-217.

12)Hunt, S. M.; Sheil, M. M.; Belov, M.; Derrick, P. J. *Anal. Chem.* **1998**, *70*, 1812-1822.

13)Chen, F. F. *Introduction to plasma physics and controlled fusion*; 2nd ed.; Plenum Press: New York, 1984; Vol. 1.

14)Laskin, J.; Byrd, M.; Futrell, J. *Int. J. Mass Spectrom.* **2000**, *195/196*, 285-302.

15)Gauthier, J. W.; Trautman, T. R.; Jacobsen, D. B. *Anal. Chim. Acta* **1991**, *246*, 211-225.

16)Heck, A. J. R.; Koning, L. J. d.; Pinkse, F. A.; Nibbering, N. M. M. *Rapid Comm. Mass Spectrom.* **1991**, *5*, 406-414.

17)Marshall, A. G.; Roe, D. C. *J. Chem. Phys.* **1980**, *73*, 1581-1590.

18)Kelly, P. C.; Horlick, G. *Anal. Chem.* **1973**, *45*, 518-527.

19)Comisarow, M. B.; Melka, J. D. *Anal. Chem.* **1979**, *51*, 2198-2203.

20)Brigham, E. O. *The fast Fourier transform*; Prentice-Hall, Inc.: Englewood Cliffs, New Jersey, 1974.

21)Comisarow, M. B.; Marshall, A. G. *Chem. Phys. Lett.* **1974**, *25*, 283.

22)Craig, E. C.; Santos, I.; Marshall, A. G. *Rapid Commun. Mass Spectrom.* **1987**, *1*, 33-37.

23)Marshall, A. G.; Comisarow, M. B.; Parisod, G. J. *J. Chem. Phys.* **1979**, *71*, 4434-4444.

24)Audi, G.; Wapstra, A. H. *Nucl. Phys. A* **1995**, *595*, 409.

Chapter 3

Simulations of ion motion inside an RF-only hexapole ion trap: further support for a collisionally activated mechanism for multipole storage – assisted dissociation.

3.1. Introduction

Relatively recently a new in-source fragmentation technique was developed in which ions are accumulated inside the multipole of an electrospray ionization source. Multipole storage-assisted dissociation (MSAD) was first reported by Sannes-Lowery *et al.*[1] Subsequent investigations[2, 3] have agreed that the charge density contained in the hexapole is of primary importance.

The proposed mechanism is one of space – charge initiated collision-activated dissociation (CAD), in which the space - charge forces the ions to oscillate to higher amplitudes and thereby reach higher kinetic energies. Collisions with neutral gas molecules at these higher energies instigate fragmentation.

As the accumulation of ions in the multipole ion trap is dependent on the kinetic energy of the incoming ion, the rate of charge-density accumulation and hence the onset of MSAD will be a function of the incoming ion's kinetic energy (which is determined by the characteristics of the ESI source), the ion's collision frequency, the identities of the colliding species and characteristics of the multipole ion-trap (namely the frequency and magnitude of the applied RF potential, the polarity and magnitude of the axial trapping potential, the number of poles and its physical dimensions). Furthermore, collisions with background gas molecules will serve to dampen the ion's motion inside the multipole. Clearly, any process that can alter the damping constant and / or the trapping efficiency will alter the average kinetic energy of a trapped ion (at time, *t*) and hence the onset of MSAD.

Factors that have been shown to be important to the onset of MSAD are the ion's initial energy, the pressure, the storage time and the characteristics of the hexapole

60

trap[1-3]. Clearly an ion's initial energy (translational and internal) will influence both the onset of fragmentation (any internal energy remaining after nozzle-skimmer activation may serve as a "head start" for any subsequent collision-induced fragmentation processes)[2] as well as the trapping probability. The pressure will help determine the transmission of ions to the hexapole, their kinetic energy on entering the hexapole as well as their collision frequency. The collision frequency in turn will help determine the trapping efficiency of the multipole as well as the damping of the trapped ions. Experimentally it has been found that the proportion of fragment ions increased with pressure, suggesting that the increased collision frequency outweighs any increased damping effects[3]. The trend observed for storage time can be interpreted as an increased number of collisions producing more fragments through imparting more internal energy[3]. Finally the finding that the degree of fragmentation increased with RF field strength was interpreted as further proof for the proposed mechanism, namely that for a specific radial position the average kinetic energy of an ion is dependent upon the applied RF potential. Numerical integration of the equations of motion has demonstrated the ion's kinetic energy dependence on radial position[3].

The equations of motion used in the previous study omitted collisional damping as well as space charge. Furthermore, it has recently been suggested that under typical electrospray ionization conditions radial stratification can occur in which the average radial position of an ion is dependent upon its m/z value[5]. As a result, an ion's propensity for MSAD will be affected by the number and identities of the other ions trapped in the multipole ion trap. The same approach used to predict radial stratification, the adiabatic approximation[6, 7], can also be used to demonstrate that the average KE of an ion is independent of the magnitude of the applied RF field (in contradiction to experimental results[3]). Building on the extensive work already reported, the results

from a potential – array model of a hexapole ion trap that incorporates collisions and approximates the effects of space charge are presented here.

3.2 Method

The ideal equations of motion for a hexapole are coupled[6, 8, 9]. Ion motion perpendicular to the main axis of the hexapole (commonly labeled the z – axis) depends on both its x and y coordinates. As a result the equations of motion in the x and y directions have to be solved simultaneously by numerical integration.

All calculations were performed using the widely used commercial simulation package SIMION 3D (Idaho National Engineering Laboratory, version 6.0)[10]. Apart from a skimmer being replaced with a flat electrode identical to the trap electrode, the simulated hexapole ion trap has the same physical dimensions as the hexapole used in the Analytica ESI source of the Bruker BioAPEX FTICR mass spectrometer. This source has been used by previous MSAD investigators and at the University of Warwick.[11]

The previous experimental studies[1-3] showed MSAD to be a general multipole phenomenon. Such generality suggests that, provided the space charge is sufficient, most ions contained in the trap should display trajectories characteristic of MSAD. Accordingly the approach employed was to choose typical initial conditions and to investigate the effects of collisions and space charge on the calculated ion trajectories.

A user program was written to simulate the RF field. When programs with RF potentials are incorporated, SIMION 6 uses a fast refining method that involves the superposition of 3D potential arrays[10]. Unless otherwise stated the RF field in these simulations was identical to that applied under normal operating conditions in the Analytica ESI source of the Bruker BioAPEX FTICR at Warwick, namely 600 V_{p-p} at 5.2MHz.

In order to simulate space charge an extra 3D potential array was used that satisfied the Laplace equation with boundary conditions $V = V_0$ at $r = 0$ and $V = 0$ at the electrode surfaces (1.7 mm away). This approach was used as Szabo and workers[12] demonstrated that the shape of an ion beam in a hexapole ion guide remains almost cylindrical even if it is operating close to the upper limit of stability. Application of Gauss's law to a cylindrical charge density leads to the relationship.

$$E = \gamma / 2\pi\varepsilon_0 r \qquad\qquad (3.2.i)$$

γ is the charge per unit length, r is the radius of the cylinder of ions and ε_0 is the permittivity of free space.

The charge per unit length was determined in the following manner:-

1) Using preliminary experiments the volume within which an ion was successfully contained was estimated. As the axial motion of an ion was progressively damped, the estimate of the trapping volume was made by determining the average radial position and the maximum axial distribution for which an ion was successfully contained.

2) An ion current of 10 – 50 pA was used[13].

The potentials applied to the space charge array, 0.0 - 0.5 V, corresponded to a total charge contained in the hexapole of $0 - 5.9 \times 10^{-13}$ C, respectively. As a rough guide, a hexapole containing 5.9×10^{-13} C of charge would have trapped between $5.9/t$ and $1.2/t$ % of incoming ions for a 10 and 50 pA ion current, respectively, where t is the accumulation time.

It has been shown that the energy distributions of ions already trapped in a multipole can be described by a weighted sum of Maxwell-Boltzmann distributions[6]. In the likely event that the characteristic temperature (or any of the characteristic temperatures) of the ions is different from the temperature of the bath gas, it is possible to use a weighted average temperature to determine the relative velocity[6]

$$T_{rel} = \mu(T_i/m_i + T_b/m_b) \qquad\qquad\qquad (3.2.\text{ii})$$

where i and m refer to the ion and background gas, respectively, and μ is the reduced

mass given by $\mu = m_i m_b/(m_i + m_b)$. Consequently, using appropriate weightings and

effective temperatures a value for a <u>contained</u> ion's mean free path can be obtained

$$v_{rel}(T_{rel}) = (8kT_{rel}/\pi\mu)^{1/2} \qquad v(T_i) = (8kT_i/\pi m)^{1/2} \qquad (3.2.\text{iii})$$

Clearly, the characteristic temperatures and their weightings will depend on

many factors including accumulated space charge, RF potential, RF frequency and the

identities of the ions and the background gas themselves[6]. Nevertheless, in principle a

combination of temperatures can be assigned to a particular case study and an average

mean free path obtained. Consequently, the effects of collisions were approximated by a

user-defined mean free path and a kinetic energy loss per collision. Reflecting the

random nature of collisions, the percentage kinetic energy loss per collision was chosen

randomly between 0 and a user – defined upper limit. For a specific set of conditions,

the maximum mean free path used was determined through trial and error, until no ions

were trapped in 200 attempts.

Reflecting the generality of MSAD, the majority of simulations were run using a

singly charged positive ion of mass 1000 amu with both trapping electrodes set at 10 V.

The initial conditions for the simulations were 0.375 mm off-axis (at the outer edge of

one trapping electrode) with an initial kinetic energy of 65 eV and a velocity parallel to

the principal axis. The skimmers present in most ESI sources will ensure that the

velocity perpendicular to the principal axis is small (relative to the parallel velocity).

The kinetic energy of 65 eV was chosen as a compromise of the many factors

affecting an ion's entrance speed into the hexapole. The velocity distribution of an ion

entering the hexapole is a function of the pressures in the different regions of a

differentially pumped ion source[14], the collision cross-section, the potential difference between the capillary exit and the skimmer, the relative dimensions of the nozzle – skimmer region (mach disk[15, 16]), the temperature of the pseudoreservoir[15] and the size of the velocity slip[16]. The estimate used for the initial kinetic energy of the singly charged ion was half the value a singly charged ion would possess if no collisions occurred under routine operating conditions (capillary $\approx$ 130 V, skimmer $\approx$ 1 V), namely 65 V.

The difficulty in obtaining an accurate estimate of the kinetic energy of the ions as they pass into the hexapole ion trap is clear from the above discussion. Furthermore, it will be highly instrument dependent. Although a different value for this energy would alter the upper limit of the damping constant, the trends observed should not be altered.

Unless otherwise stated, the position, velocity and energy were sampled every microsecond, as well as at each collision. This sampling frequency provided the best compromise between simulation time, file size, processing time and accuracy. As will be shown shortly, no spikes of considerably greater kinetic energy were present in the kinetic energy profiles (variation of KE with time). Furthermore, the 1 MHz sampling rate was much greater than the collision frequency. Accordingly, the average kinetic energy profiles obtained using the 1 MHz sampling rate will be an accurate representation of the average kinetic energy encountered during a collision.

It was recently reported that for identical conditions, the radial position of an ion contained in a hexapole guide is dependent upon the mass of the ion[5]. This conclusion came as a direct result of the need for balance at the ion's equilibrium position between the field due to space charge, E_{sc}, and the effective RF field, E^* (derived from the

effective potential of the adiabatic approximation[6, 7]). In the absence of collisions, the cloud radius, as a function of the total linear charge, Q_L, is given by[5]

$$R_q = a(Q_L / q_3 Q_{max})^{1/4} \; ; \; q_3 = 12qV_{RF}/m\omega^2a^2 \; ; \; Q_{max} = 3\pi\varepsilon_0V_{RF}/2 \qquad (3.2.iv)$$

q_3 is the hexapole stability parameter[6], q is the charge of the ion, V_{RF} is the RF potential, m is the mass of the ion, ω is the angular frequency of the RF field and a is the field radius of the hexapole (defined as the minimum distance from the hexapole axis to an electrode surface). Therefore under identical conditions

$$R_q \propto m^{1/4} \qquad (3.2.v)$$

In the adiabatic approximation the average kinetic energy of the fast oscillatory motion is given by[7]

$$KE = q \, (q/m) \times (3V_{RF} / 2a\omega)^2 \times (r / a)^4 \qquad (3.2.vi)$$

Substituting equation (3.2.v) for r in equation (3.2.vi), it is readily seen that under identical conditions the ion's kinetic energy is predicted to be mass independent. The same approach can be used to study the effects of varying the RF potential. Under otherwise identical conditions

$$R_q \propto (1/V_{RF})^{1/4}$$

Therefore the average kinetic energy of the ion is also predicted to be independent of the RF potential.

At the ion densities used for typical ESI experiments, the degree of smearing due to thermal motion is expected to be small enough to ensure some degree of stratification remains.[5] The results reported here, both calculated and experimental, support the incidence of radial stratification during ion accumulation in a hexapole ion trap. Additionally the average kinetic energy and the collision frequency (the combination of which determine the collisional activation potential) of an ion as a function of mean free path, ion mass, RF field amplitude, and space charge are presented.

All experimental results were obtained using a 9.4 T Bruker BioAPEX II FTICR mass spectrometer and an external ESI source (Analytica), which has been described in detail elsewhere[11].

3.3 Results and discussion

Comparison of the simulation results with experimentally determined transport criteria and previously published hexapole simulation results

Using the supplied RF values, 600 V_{p-p} at 5.2Mz, the hexapole ion guide in the Analytica ion source is specified to provide high transmission for ions of m/z 100 – 3000. The transport efficiency of the simulated ion guide was first tested by setting the trapping potentials to zero and recording the proportion of ions of a specific m/z that were transported successfully. Through repeating this process for a range of ions the simulated ion guide was shown to provide equivalent transmission.

Space charge free collisionally damped simulations

To enhance further the statistical reliability of the profiles obtained, (the multiple collisions experienced by the ions during each simulation will confer a significant degree of statistical reliability) the kinetic energy profiles (variation of kinetic energy with time) detailed below were the average of at least 12 individual trajectories. The kinetic energy profiles for ions with mean free paths of 2, 8 and 14 mm entering a space – charge free hexapole array (standard conditions, 50 % max. KE loss) are shown in figure 3.3.1. It is apparent that the shorter mean free path led to increased damping.

67

space charge free kinetic energy profiles
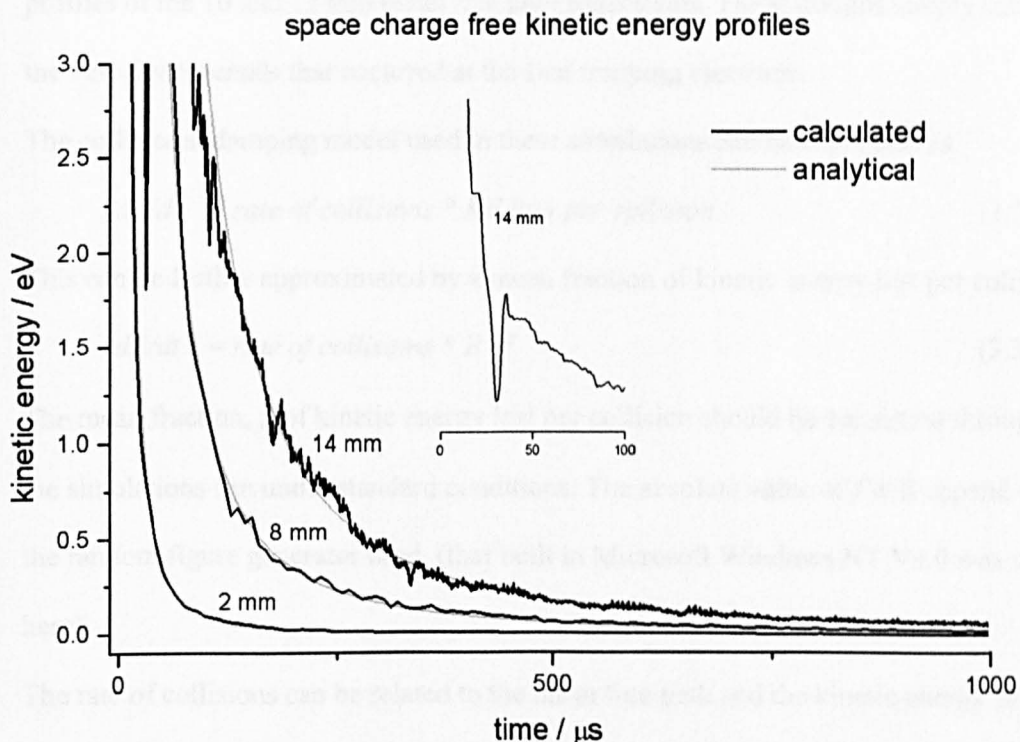
Figure 3.3.1. Kinetic energy profiles for space – charge free simulations using standard conditions (see method). The upper, middle and lower curves correspond to mean free paths of 14, 8 and 2 mm respectively. The simulated results are shown in black and the analytical curves in light grey. The 2 mm experimental and analytical curves are almost superimposable

As a result of a smaller number of collisions (decreased damping) the kinetic

energy variation of the 14 mm profile was greater than that for the 2 mm profile.

Although not shown, the kinetic energy profiles for mean free paths 4 – 12 mm

displayed the same pattern, i.e. less efficient damping allowed the local maxima to be

more pronounced for longer mean free paths. Nevertheless, even when the trapping

efficiency of the hexapole was small (the trapping efficiency for 14 mm mean free path

simulations was approximately 2 %), the ions lost the majority of their initial KE within

the first millisecond.

Inspection of figure 3.3.1 revealed a trough in the kinetic energy profile for the

14mm mean free path. The troughs were evident whenever an ion was damped to

kinetic energies below 10eV (trapping requirement) and the axial component of the

velocity (initial velocity) was still dominant. The troughs were also apparent in the KE

68

profiles of the 10 and 12 mm mean free path trajectories. These troughs simply reflected the velocity reversals that occurred at the first trapping electrode.

The collisional damping model used in these simulations can be expressed as

$$dE/dt = rate\ of\ collisions * KE\ loss\ per\ collision \qquad (3.3.i)$$

This can be further approximated by a mean fraction of kinetic energy lost per collision.

$$dE/dt = rate\ of\ collisions * E * f \qquad (3.3.ii)$$

The mean fraction, f, of kinetic energy lost per collision should be consistent throughout the simulations run under standard conditions. The absolute value of f will depend on the random figure generator used, (that built in Microsoft Windows NT V4.0 was used here).

The rate of collisions can be related to the mean free path and the kinetic energy of the ions, so that the change in kinetic energy became

$$dE/dt = v/\lambda \times E \times f = \{[sqrt(2E/m)]/\lambda\} \times E \times f = [(2/m)^{1/2}/\lambda] \times E^{3/2} \times f \qquad (3.3.iii)$$

v is the velocity, m is the mass of the ion and λ is the mean free path. Using the boundary condition that $KE = E_0$ at time $t = 0$ gives the following equation.

$$1/sqrt\ (E_t) - 1/sqrt\ (E_0) = (2/m)^{1/2} \times f \times t/\lambda \qquad (3.3.iv)$$

As can be seen in figure 3.3.1 (analytical curves) this expression could describe the calculated damping. In each case the value of f was 0.145.

Multipole storage – assisted dissociation simulations

Under collisionless conditions it has been shown[9] that the change in kinetic energy in a hexapole is proportional to r^3 and that, for unstable trajectories, this radial dependence causes an avalanche-like increase of the amplitude of radial oscillations until the ion is lost[8]. Clearly, highly energetic ions will participate in MSAD only if they are retained. While space – charge free and collisionless simulations have demonstrated that the

69

kinetic energies of trapped ions increased rapidly with radial position, the ions will be damped in the presence of collisions.

As stated earlier the effects of previously acquired charge density was approximated by an extra array. The kinetic energy profiles for a range of mean free paths and charge densities were calculated.

For any specific simulation, the average kinetic energy of the incoming ion remained fairly constant after a few milliseconds. Figure 3.3.2 shows the kinetic energy profile of an ion (standard conditions, space charge = 3.54×10^{-13} C, mean free path = 10 mm) where the trajectory was sampled at twice the frequency of the RF field, so that any resonant motion was accurately recorded[17]. As can be seen a kinetic energy band spanning $0 - 0.1$ eV was obtained. Closer inspection revealed that the kinetic energy band consisted of many localized maxima and minima (subharmonic motion). Further closer inspection revealed harmonic fine structure, however in no instance did the harmonic fine structure lead to kinetic energy spikes of significantly greater kinetic energy.
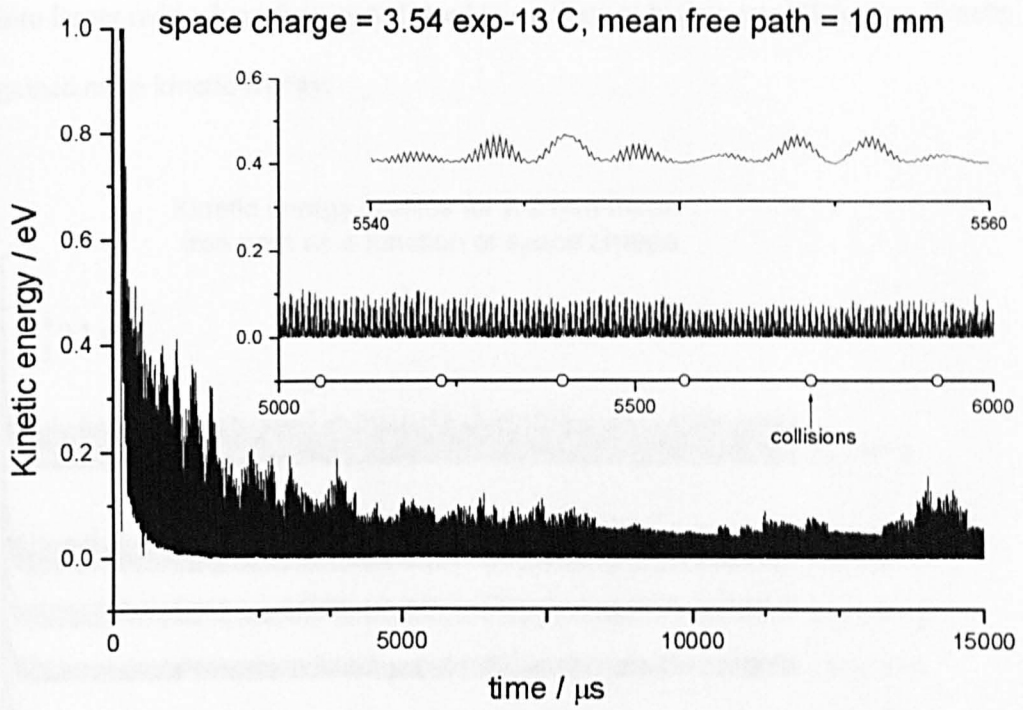
Figure 3.3.2. Kinetic energy variation with time for a space charge = 3.54×10^{-13} C and mean free path = 10 mm simulation (other conditions as standard, see method) that was sampled at twice the frequency of the applied RF field. The close-ups reveal the fine structure contained in the kinetic energy profile.

Also included in figure 3.3.2 are the collisions the ion experienced. It is readily apparent that the collision frequency was much less that of the fine (harmonic) structure and the subharmonic structure. Furthermore, the average time between collisions (≈ 177 μs for this simulation) was much greater than the standard sampling time interval of 1 μs. As the smallest interval between collisions recorded was greater than 20 μs the 1 MHz sampling rate was more than sufficiently accurate to record any trends pertinent to collisional activation and was sufficient to describe fully the subharmonic oscillations.

The same kind of kinetic energy band shown above was also observed in all other simulations. The kinetic energy profiles for a 2 mm mean free path as a function of charge are shown in figure 3.3.3. It is readily apparent that the kinetic energy band of the ion increased from $0 - 0.01$ eV to $0 - 0.1$ eV as the space charge increased from 0 to 5.9×10^{-13} C. In every case calculated, mean free path = $2 - 14$ mm, the kinetic energy band of the ion increased as space charge increased. As expected the ions were repelled

71

into larger radii where they were forced to oscillate at higher amplitudes and thereby gained more kinetic energy.

Kinetic energy profiles for a 2 mm mean free path as a function of space charge
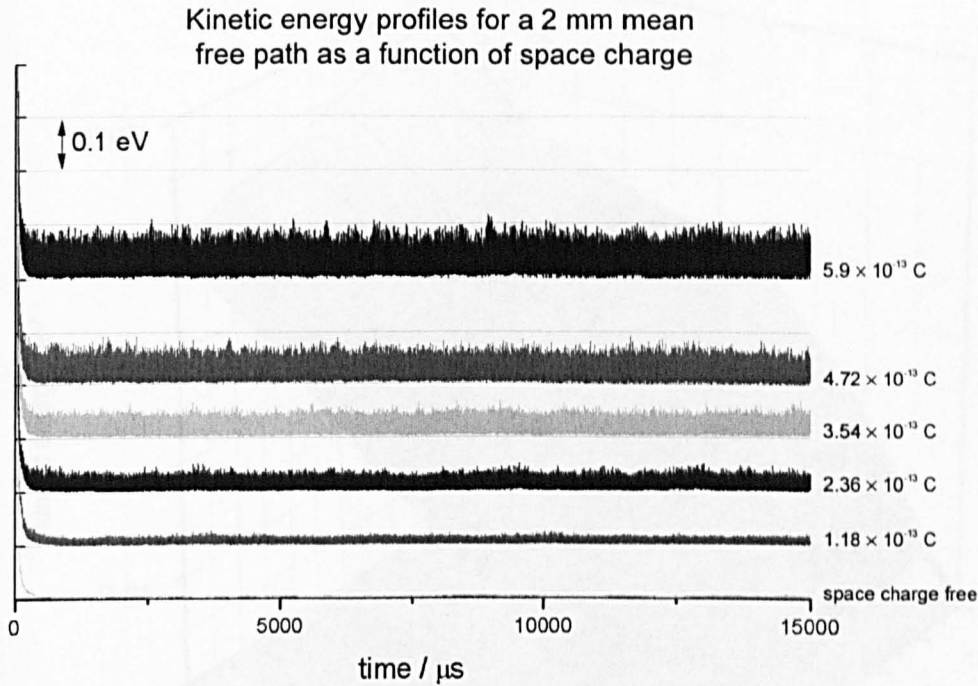
Figure 3.3.3. Kinetic energy profiles a 2 mm mean free path as a function of space charge, all other conditions as standard (see method).

In addition to the finding that the width of the kinetic energy band increased with space charge, it was also found that the width of the band increased slowly with an increasing mean free path. For example the average kinetic energy for a 12 mm mean free path was about 50 % larger than that for a 2 mm mean free path. Decreased damping allowed the ions to gain more kinetic energy.

These trends to wider kinetic energy bands for both increasing space charge and an increasing mean free path would manifest themselves as an increase in the average kinetic energy of the ion as experienced during an average collision. The average kinetic energy of the trapped ion as a function of space charge and mean free path is shown in figure 3.3.4. To omit the contribution from the ion's initial kinetic energy the average

72

kinetic energy was determined between 2 500 and 15 000 μs. As a result the graph was

independent of trapping efficiency and the ion's initial conditions.
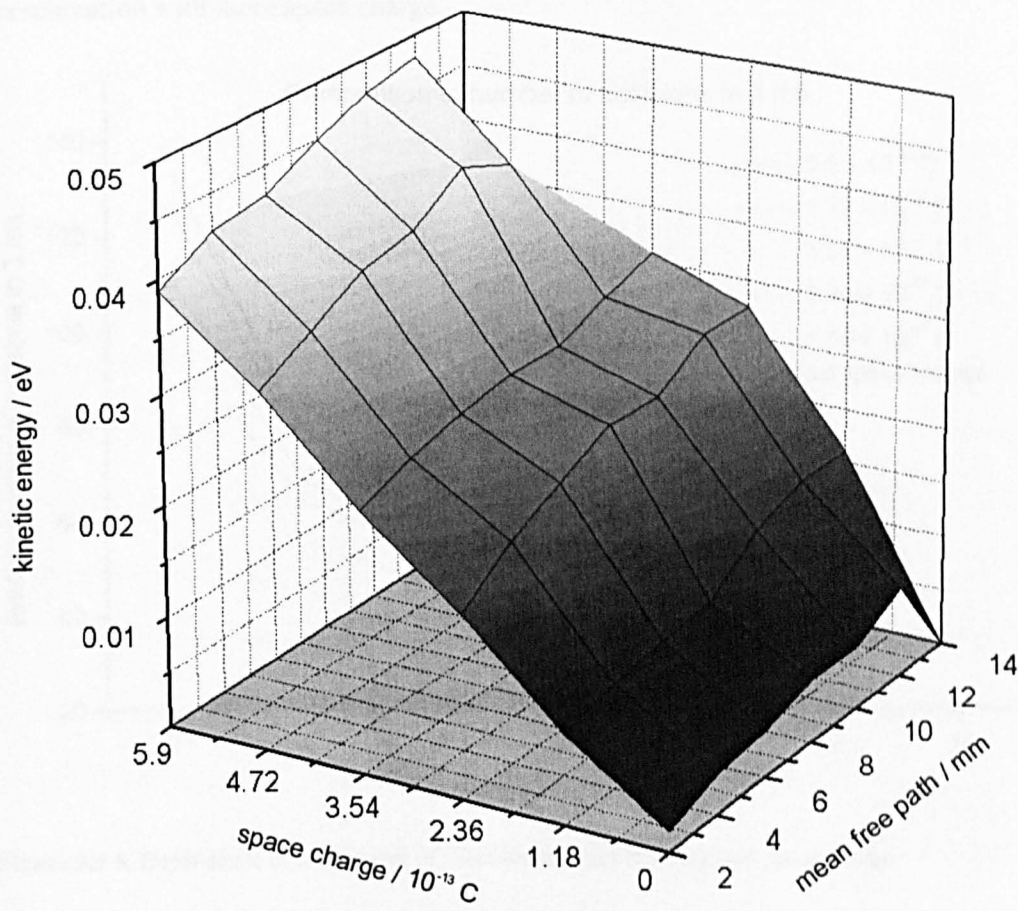
Figure 3.3.4. Mean kinetic energy surface of trapped ions as a function of mean free path and space charge obtained using standard conditions (see method). To omit the contribution from the ion's initial energy the average kinetic energy was determined between 2500 and 15000 μs.

As can be seen, the average kinetic energy of an ion increased rapidly with space

charge and slowly with an increasing mean free path. Using the mean kinetic energy

surface and the observation that the local maxima were more intense for longer mean

free paths (decreased damping), the appearance of the kinetic energy profiles for

conditions not calculated specifically can be qualitatively predicted.

With regard to collisional activation the trend to higher kinetic energies for

longer mean free paths would be offset by the fact that ions with a smaller mean free

path experienced more collisions. As can be seen in figure 3.3.5 the number of

73

collisions increased with decreasing mean free-path and with increasing space charge. Furthermore, the increase was much more rapid for a smaller mean free path in combination with more space charge.
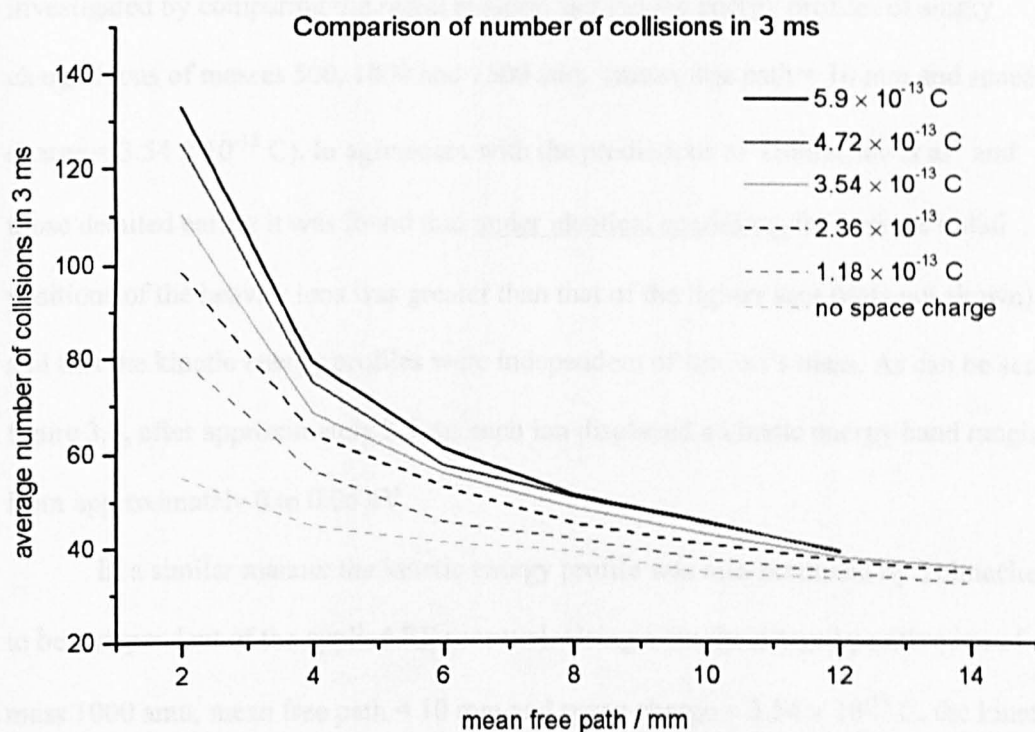
Figure 3.3.5. Dependence of the number of collision on mean free path and space charge

Although ions with a shorter mean free path acquired less kinetic energy (see figure 3.3.4), under higher space conditions (e.g. total charge contained = 5.9×10^{-13} C) the rapid increase in collision frequency with decreasing mean free path was more pronounced. As a result, once space charge is significant, slow heating collisional activation[18] could increase with a decreasing mean free path because the higher number of collisions would outweigh the decrease in the ion's kinetic energy. This finding is in agreement with previous experimental results, in which the degree of fragmentation was found to increase with an increased background gas pressure[2, 3].

Kinetic energy and radial position profile dependence on mass, charge and rf potential

Radial stratification and the kinetic energy dependence upon mass was investigated by comparing the radial position and kinetic energy profiles of singly charged ions of masses 500, 1000 and 1500 amu (mean free path = 10 mm and space charge = 3.54×10^{-13} C). In agreement with the predictions of Tolmachev et al[5] and those detailed earlier it was found that <u>under identical conditions</u> the average radial positions of the heavier ions was greater than that of the lighter ions (data not shown) and that the kinetic energy profiles were independent of the ion's mass. As can be seen figure 3.6, after approximately 2.5 ms each ion displayed a kinetic energy band ranging from approximately 0 to 0.06 eV.

In a similar manner the kinetic energy profile was also predicted by Tolmachev to be independent of the applied RF potential. Using a singly charged positive ion of mass 1000 amu, mean free path = 10 mm and space charge = 3.54×10^{-13} C, the kinetic energy dependence on RF potential was investigated. As can also be seen 3.3.6, the RF potential independence was also observed.

Whilst it was predicted that the kinetic energy was independent of mass and RF potential, the same approach predicted that the kinetic energy of the ion is directly proportional to the number of charges on the ion. The results of simulations using ions of 10 times the molecular mass but the same *m/z* entering the hexapole at the same speed (m = 10 000 amu, z = 10e, KE_0 = 650 eV, mean free path = 10 mm and space charge = 3.54×10^{-13} C) are shown in figure 3.3.7. After the ions have been damped (2500 μs), the width of the kinetic energy band of the '10 times' ion was about 10 times that of the singly charged ion. Also in agreement with predictions, the average radial position of the ion is independent of the ion's charge state. It is dependent only on the mass / charge ratio (figure 3.3.7.).
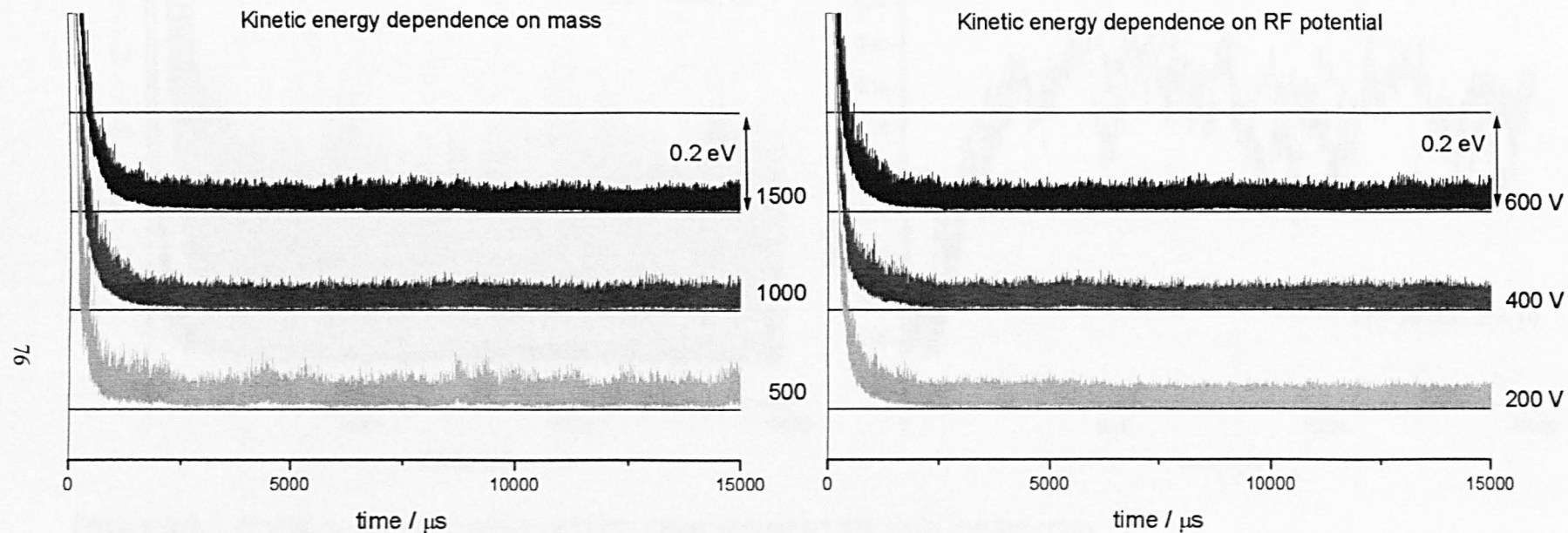
Figure 3.3.6. Kinetic energy dependence on the ion's mass and the applied RF potential.
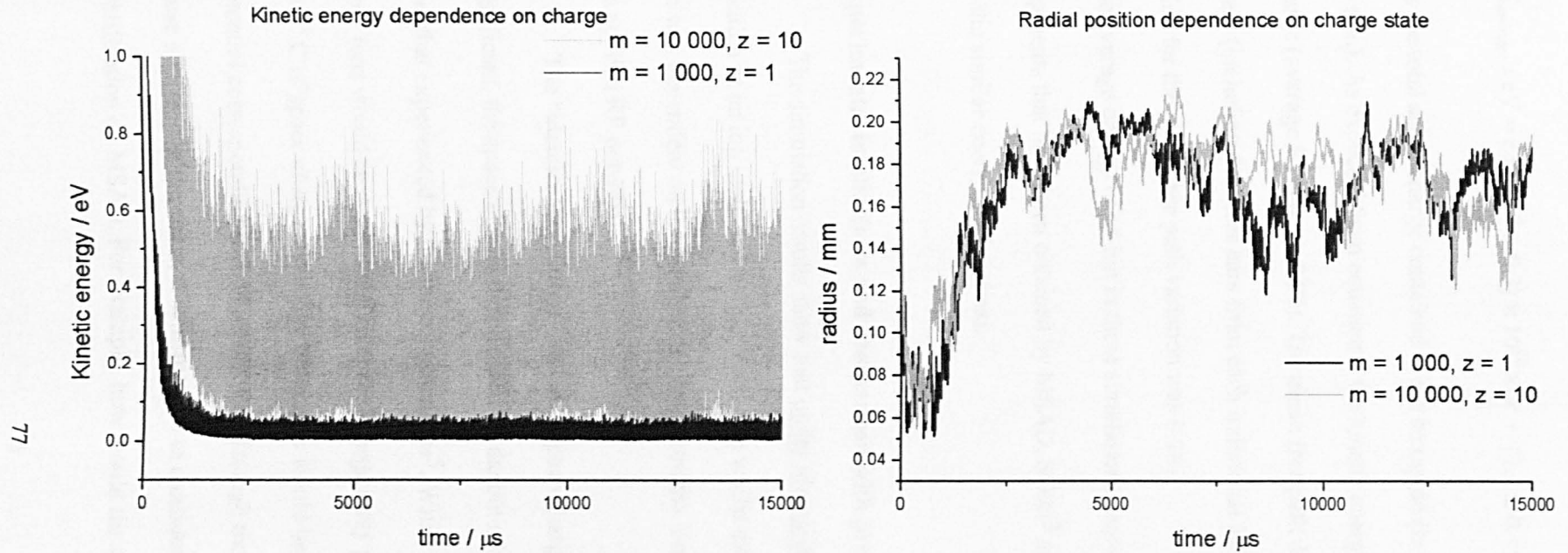
Figure 3.3.7. Kinetic energy and radial position dependence on the ion's charge state. In agreement with the adiabatic approximation predictions, the radial position was dependent on m/z only whereas the kinetic energy was directly proportional to the ion's charge state. The simulations were run using a 10 mm mean free path and 3.54×10^{-13} C of space charge.

For the conditions used here, the average kinetic energy (in eV) of an ion was given by

$$KE_{average} / \text{eV} = z \times [(6.7 \pm 0.3) \times 10^{10} \times \gamma + (1.4 \pm 0.1) \times 10^{-3} \times \lambda - 10^{-4}] \qquad (3.3.\text{v})$$

γ is the total space charge contained in the hexapole (in C) and λ is the mean free path (in mm). As expected from equation 2 the kinetic energy increased linearly with space charge (average R^2 value = 0.99). The mean free path dependence also appeared to be linear (including the error bars from each individual KE vs space charge plot, the R^2 value for the mean free path variation was 0.98).

The average energy of an ion in these simulations was $\approx 0.025 \times z$ eV. Thus the similar fragments that have been obtained by MSAD, SORI[3] and IRMPD[19] can be explained by the similar energetics involved.

Experimental implications and comparison with previous results

The simulation results show that under identical conditions the average radial position of an ion increased with m/z and that whilst the average kinetic energy of the ion was dependent on the number of charges on the ion, it was independent of mass and the applied RF potential.

The "identical conditions" included space charge. If radial stratification were significant, the space charge experienced by the outer heavier ions would be greater than that experienced by the inner lighter ions[5]. With regard to these simulations the inner ions would be described by a space charge array potential corresponding to 2.36×10^{-13} C of space charge whilst the outer ions would be described by a space charge potential corresponding to 3.54×10^{-13} C. Although the onset of fragmentation would cause a mixing of the strata, it is instructive to consider the possible effects of radial stratification on MSAD. For example, how would the radial dependence on m/z

influence the fragmentation of proteins, where the lower charge states would be located further away from the principal axis?

A broadband non-MSAD spectrum of reduced mono-nitrated hen egg-white lysozyme[20, 21] showing parent ions in the 9+ – 16+ charge states is shown in figure 3.3.8b. It is readily apparent that under non-MSAD conditions the 13+ charge state was the most intense. However, after MSAD, figure 3.3.8a, the only remaining parent ions were those of the 14+ ions, despite the 13+ charge state having been more intense previously. Radial stratification inside the hexapole could explain the counter – intuitive result that under prolonged residence time inside the hexapole the lower charge states of mono-nitrated lysozyme were preferentially fragmented, despite intramolecular space charge causing the higher charge states to have a lower fragmentation threshold[22]. As the lower charge states would have been located at larger radial positions the space charge they would have experienced would be greater. The simulations reported above showed that as a result of increased space charge the lower charge states would have a higher average kinetic energy and would have collided more often. Consequently, the collisional activation of the lower charge states would be greater. This observation that the lower charge states of mono-nitrated lysozyme fragmented preferentially is all the more startling as the simulations also demonstrate that under identical conditions the higher charge states would possess more kinetic energy. Moreover, the ion mobility results of Clemmer and workers showed that the higher charge states of reduced lysozyme have larger cross-sections[23]. Radial stratification provides an explanation to reconcile these experimental results with theoretical expectations.

79
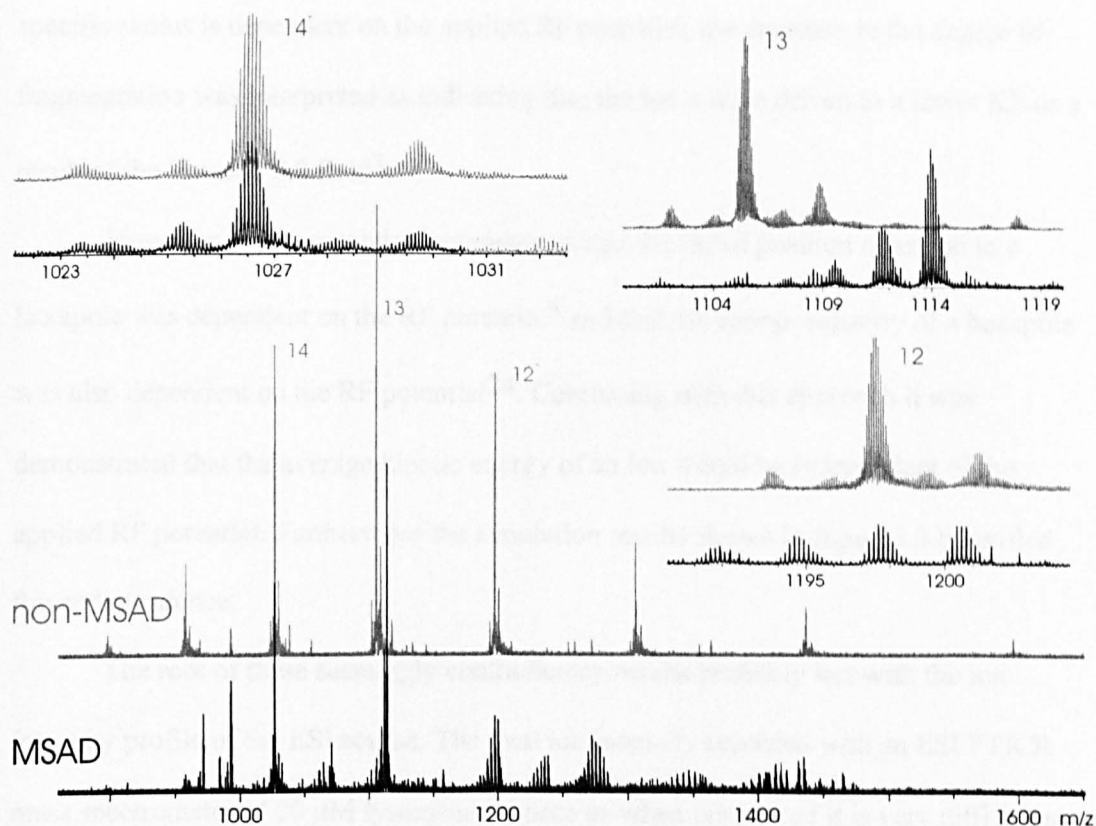
Figure 3.3.8 a) microspray spectrum of mono-nitrated lysozyme (20μM in 1:1 water : acetonitrile, 1 % formic acid). Data were obtained using typical microspray conditions and the instrument tuned for maximum ion transmission, $d1$ = 4 s. After a 20 s accumulation time (b) MSAD fragments were obtained.

The insensitivity of the kinetic energy profiles to a change in RF potential over the range 200 – 600 $V_{p\text{-}p}$ is in stark contrast to experimental results[3]. It was found[3] that once MSAD was in operation (accumulation period = 3 s) the degree of fragmentation decreased with a decreasing RF potential (600 – 400 $V_{p\text{-}p}$). Reflecting the prominent role of charge density in the MSAD mechanism, it was recognized[3] that any changes to the ion storage capability of the hexapole would affect the onset of MSAD. However, it was found[3] that prior to the onset of MSAD (accumulation period = 1 s) the total ion intensity remained constant for this range of RF potentials. Only at lower potentials did the signal intensity start to decrease. This was taken[3] as demonstrating that in the potential range 600 – 400 V_{p-p} the ion storage capability of the hexapole was unaffected by the decrease in RF potential. As the potential experienced by an ion at a

specific radius is dependent on the applied RF potential, the decrease in the degree of fragmentation was interpreted as indicating that the ion's were driven to a lower KE as a result of the lowered RF field[3].

However, it was recently demonstrated that the radial position of an ion in a hexapole was dependent on the RF potential[5] and that the charge capacity of a hexapole was also dependent on the RF potential[24]. Continuing with this approach it was demonstrated that the average kinetic energy of an ion would be independent of the applied RF potential. Furthermore the simulation results shown in figure 3.3.6 verified this independence.

The root of these seemingly contradictory results probably lies with the ion intensity profile of the ESI source. The total ion intensity recorded with an ESI FTICR mass spectrometer of 20 μM lysozyme (chosen as when unreduced it is very difficult to fragment) as a function of accumulation time is shown in figure 3.3.9. As can be seen, for the conditions used there was an approximately 1 s delay before appreciable signal intensity was observed (no ion signals were observed for an accumulation time under 0.6s). The ion intensity profile displayed a sigmoidal pattern, the upper limit of which corresponded to the working charge capacity of the ion trap.

The sigmoidal line shape is indicative of a low initial trapping efficiency that increases with the number of trapped ions before tailing off as the ions leak out. The sigmoidal profiles shown in figure 3.3.10 clearly demonstrate that after a small accumulation time the measured ion intensity would be relatively insensitive to a moderate change in the charge capacity of the hexapole. After a short accumulation period the small decrease in total ion intensity accompanying such a decrease could have been within the boundaries of experimental uncertainty (see experimental scatter in figure 3.3.9). However after a longer accumulation time the reduced charge capacity would become more pronounced, see figure 3.3.10. As a result, the fact that the

81

measured ion intensity was experimentally insensitive to RF potential after 1 s does not mean that it was insensitive after 3 s (MSAD experiment accumulation time).

Total ion intensity dependence on accumulation time
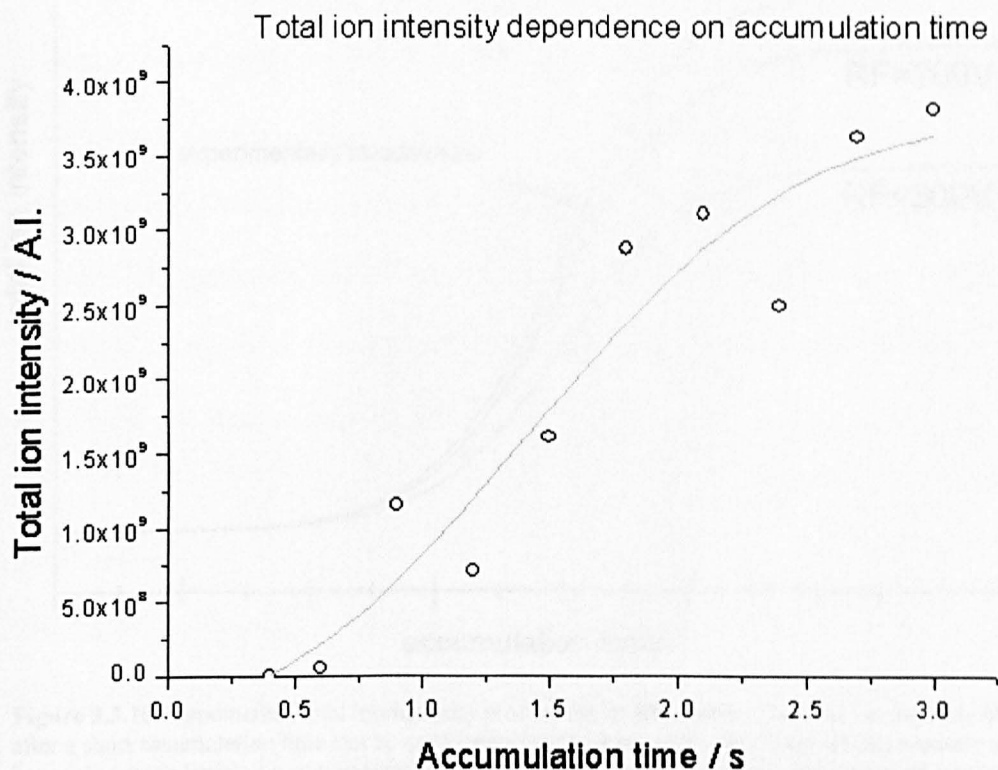
Figure 3.3.9. Total ion intensity dependence on hexapole accumulation time. The broadband spectra, 512k, were obtained using regular ESI, 20 μM lysozyme in 1:1 water : acetonitrile + 1 % (v / v) formic acid. Unreduced lysozyme was used as it is difficult to fragment.

The accumulation time required for an experimentally measurable decrease in ion intensity would be smaller for a greater reduction in the charge capacity of the hexapole, see figure 3.3.10. The observation that the ion signal, after a 1 s accumulation period, was found to decrease for $V_{RF} < 400$ V but not for $V_{RF} = 400 - 600$ V can be explained in terms of the former having been experimentally observable whereas the latter was not.[3] Therefore, the observation that the degree of fragmentation decreased with RF potential (accumulation time = 3 s) could be due to a reduction in the charge capacity of the hexapole and not to a reduction in the average kinetic energy of the ion, in agreement with the results presented here.
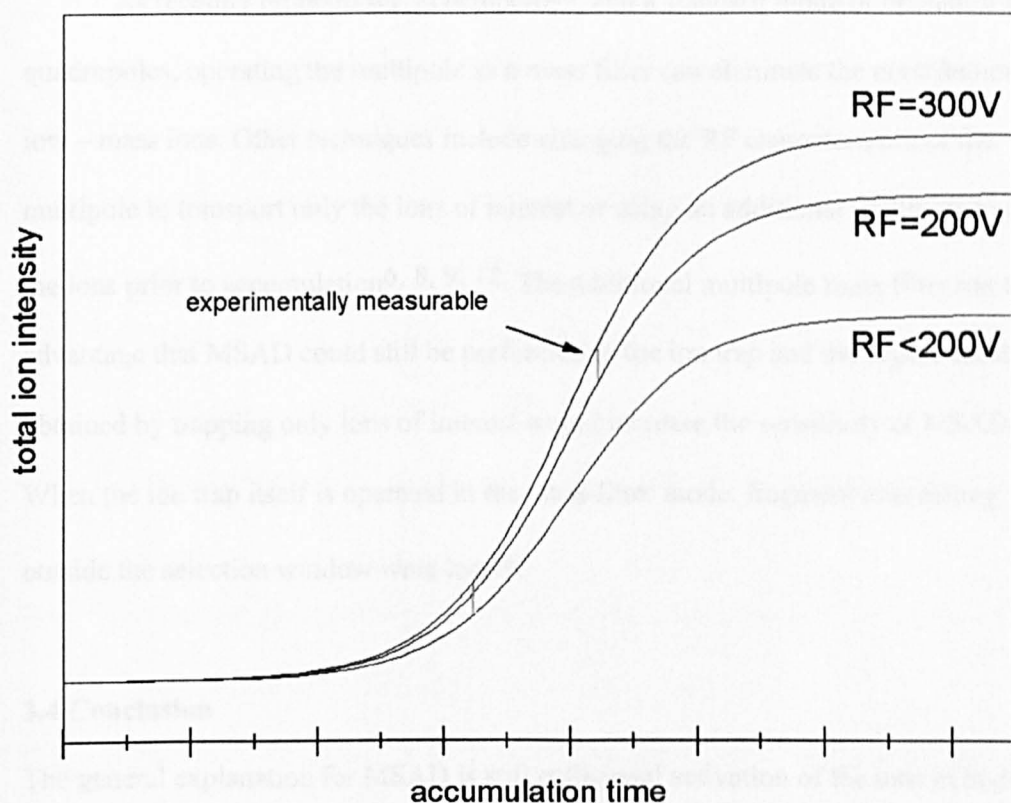
Figure 3.3.10. Hypothetical total ion-intensity profiles for an ESI source. The total ion intensity obtained after a short accumulation time can be quite insensitive to modest changes in the charge capacity of the hexapole (upper-limit). An experimentally measurable decrease in ion signal is observed at lower accumulation times for a larger decrease in charge capacity.

Finally, in the light of preferential fragmentation as a result radial stratification, the words of caution offered by Sannes-Lowery and Hofstadler[2] with regard to the analysis of solutions containing significant amounts of contaminants and / or ionizable buffering agents, are particularly apt. "..it is important to minimize, or eliminate, space charge contributions from species outside the molecular weight range of interest..." The space charge from low mass ions, perhaps not trapped or detected in the FTICR cell but contained nevertheless in the hexapole ion trap, could result in the preferential fragmentation of the high-mass ions of interest. This would be especially true for the detection of non-covalently bound protein dimers[25], protein-peptide adducts[26] and aggregates[27].

As recently reported for an octopole[28], and a standard mode of operation for quadrupoles, operating the multipole as a mass filter can eliminate the contribution from low – mass ions. Other techniques include changing the RF characteristics of the multipole to transport only the ions of interest or using an additional multipole to filter the ions prior to accumulation[6, 8, 9, 12]. The additional multipole mass filter has the advantage that MSAD could still be performed in the ion trap and the higher sensitivity obtained by trapping only ions of interest would increase the sensitivity of MSAD. When the ion trap itself is operated in the mass-filter mode, fragment ions falling outside the selection window were lost[28].

3.4 Conclusion

The general explanation for MSAD is still collisional activation of the ions in higher energy trajectories as a result of space-charge repulsion. The simulations demonstrated that the kinetic energy of the trapped ions correlated strongly with the charge density and more weakly with the collision frequency – however, longer mean free paths allowed more pronounced kinetic energy fluctuations to occur, which could contribute significantly to collisional activation. The kinetic energies obtained were of the order $0.025 \times z$ eV, where z is the elementary charge of the ion. This value is similar to the energy of a single IR photon and the kinetic energy ions possess during SORI excitation[19]. The similar energies involved explain the similar fragments that have been obtained using MSAD, SORI, and IRMPD[3, 19].

At high space charge the collisional activation might be greater at smaller mean free paths as the increase in the number of collisions would be greater than the decrease in mean kinetic energy (re figures 3.4 and 3.5).

Under the conditions simulated the trapped ion's average kinetic energy was independent of its mass and the applied RF potential but was directly proportional to its

charge state. Whilst under certain conditions radial stratification could result in ions of higher m/z experiencing a larger space charge field. The resulting m/z dependence of the ion's kinetic energy could lead to the preferential fragmentation of the lower charge states of proteins, despite intramolecular space-charge favouring the opposite.

(1)   Sannes-Lowery, K.; Griffey, R. H.; Kruppa, G. H.; P, S. J.; Hofstadler, S. A. *Rapid Comm. Mass Spectrom.* **1998**, *12*, 1957-1961.

(2)   Sannes-Lowery, K. A.; Hofstadler, S. A. *J. Am. Soc. Mass Spectrom.* **2000**, *11*, 1-9.

(3)   Häkansson, K.; Axelsson, J.; Palmblad, M.; Häkansson, P. *J. Am. Soc. Mass Spectrom.* **2000**, *11*, 210-217.

(4)   Hofstadler, S. A.; Beu, S. C.; Laude, D. A. *Anal. Chem.* **1993**, *65*, 312-316.

(5)   Tolmachev, A. V.; Udseth, H. R.; Smith, R. D. *Rapid Comm. Mass Spectrom.* **2000**, *14*, 1907-1913.

(6)   Gerlich, D. In *State-selected and state-to-state ion-molecule reaction dynamics. Part 1. Experiment*; Ng, C.-Y., Baer, M., Eds.; Wiley: New York, 1992; Vol. LXXXII, pp 1-176.

(7)   Dehmelt, H. G. *Adv. Atomic and Mol. Phys.* **1967**, *3*, 53-72.

(8)   Hägg, C.; Szabo, I. *Int. J. Mass Spectrom. Ion Proc.* **1986**, *73*, 237-275.

(9)   Szabo, I. *Int. J. Mass Spectrom. Ion Proc.* **1986**, *73*, 197-235.

(10)   Dahl, D. *Int. J. Mass Spectrom.* **2000**, *200*, 3-25.

(11)   Palmblad, M.; Häkansson, K.; Häkansson, P.; Feng, X.; Cooper, H.; Giannakopulos, A. E.; Green, P. S.; Derrick, P. J. *Eur. J. Mass Spectrom.* **2000**, *6*, 267-275.

(12)   Hägg, C.; Szabo, I. *Int. J. Mass Spectrom. Ion Proc.* **1986**, *73*, 295-312.

(13)   Analytica ; personal communication.

(14)   Fenn, J. B. *Int. J. Mass Spectrom.* **2000,** *200,* 459-478.

(15)   Anderson, J. D. *Modern compressible flow: with historical perspective,* 2 ed.; McGraw-Hill: New York, 1990.

(16)   Hunt, S. M.; Sheil, M. M.; Belov, M.; Derrick, P. J. *Anal. Chem.* **1998,** *70,* 1812-1822.

(17)   Kelly, P. C.; Horlick, G. *Anal. Chem.* **1973,** *45,* 518-527.

(18)   McLuckey, S. A.; Goeringer, D. E. *J. Mass Spectrom.* **1997,** *32,* 461-474.

(19)   Gauthier, J. W.; Trautman, T. R.; Jacobsen, D. B. *Anal. Chim. Acta* **1991,** *246,* 211-225.

(20)   Richards, P. G.; Coles, B.; Heptinstall, J. *Enzyme Microbial Tech.* **1994,** *16,* 795-801.

(21)   Richards, P. G.; Walton, D. J.; Heptinstall, J. *J. Biochem.* **1996,** *315,* 473-479.

(22)   Rockwood, A. A.; Busman, M.; Smith, R. D. *Int. J. Mass Spectrom. Ion Proc.* **1991,** *111,* 103-129.

(23)   Valentine, S. J.; Anderson, J. G.; Ellington, A. D.; Clemmer, D. E. *J. Phys. Chem. B* **1997,** *101,* 3891-3900.

(24)   Tolmachev, A. V.; Udseth, H. R.; Smith, R. D. *Anal. Chem.* **2000,** *72,* 970-978.

(25)   Lafitte, D.; Heck, A. J. R.; Hill, T. J.; Jumel, K.; Harding, S. E.; Derrick, P. J. *Eur. J. Biochem.* **1999,** *261,* 337-344.

(26)   Hill, T. J.; Lafitte, D.; Wallace, J. I.; Cooper, H. J.; Tsvetkov, P. O.; Derrick, P. J. *Biochem.* **2000,** *39,* 7284-7290.

(27)   Kilbinger, A. F. M.; Cooper, H. J.; McDonnell, L. A.; Feast, W. J.; Derrick, P. J.; Schenning, A. P. H. J.; Meijer, E. W. *Chem. Commun.* **2000,** 383-384.

(28)   Wang, Y.; Shi, S. D. H.; Hendrickson, C. L.; Marshall, A. G. *Int. J. Mass Spectrom.* **2000,** *198,* 113-120.

4. Characterisation of complex polymer mixtures

4.1. Introduction

In Fourier transform mass spectrometry the average mass accuracy with which the components present in a sample can be measured is, among other things, dependent on the dynamic range of the ion signals measured. If the most intense ions are much more abundant than the least intense (high dynamic range) many ions need to be trapped in the ICR cell for all ions to be detected simultaneously. In addition to increased space charge shifts[1-4], other processes conspire to decrease the average mass accuracy of a measurement. At high ion densities intermolecular coulombic repulsion forces ions into different regions of the cell, consequently the fields they experience are different. The resulting space – charge peak broadening[5] reduces the precision with which a peak can be measured, as a result the accuracy with which an ion's mass can be measured (reliably) is diminished. Additionally, mass shifts from peak overlap[6] (especially if a weak signal is situated near an intense signal), the measurement precision decreasing with decreasing signal-to-noise ratio[7], ion cloud deformation during the excitation / detection event[8] and the complicated coupled gyrator phenomena reported by Peurrung and Kouzes[9] all combine to increase the average mass error. For example, in 2000 Marshall and workers reported that simply fitting the Francl and Ledford calibration relationships to a poly(ethyleneglycol) bis(carboxymethyl) ether 9.4 T FTICR mass spectrum produced average mass errors of ≈ 3 ppm for both calibration equations[10].

Nevertheless, as will be shown shortly even for spectra displaying a high dynamic range, the accurate mass measurements performed using a 9.4 T FTICR mass spectrometer for both basic and tandem mass spectrometry, when combined with the information provided by other techniques regarding functionality, has permitted the

87

chemical formulae and structures of previously <u>unknown</u> samples to be identified. Furthermore, FTICR mass spectrometry allowed the identification of all the components detected in a complex polymeric system without the need for prior separation.

The example studied was a blue polymeric dye named "reactint® blue" produced by Milliken[11]. When used as part of a polyurethane a blue ink can be produced that has many favourable characteristics, including water-fastness (no thumb marks). Additionally, as the dye is contained in a liquid polymer there are no potentially obstructive particulates.

As an example of the scarcity of information regarding reactint® blue prior to its analysis, it was discovered during the initial sample preparation that the samples provided consisted mostly of a volatile solvent and just 5% (w/w) of the sample contained the involatile polymeric species.

4.2. Spectroscopic results

To help identify the components of reactint® blue nuclear magnetic resonance (NMR) and ultraviolet (UV) / visible absorption spectra were obtained and compared with standards. The UV / visible spectra of the dye and a diaminoanthraquinone chromophore are shown below. Note that the concentrations of the reactint® blue sample (see figure 4.2.1) were estimated using the mass spectrometry results.

As can be seen in figure 4.2.1. the diaminoanthraquinone (AQ) chromophore is an almost perfect match for reactint® blue. The polymeric dye consisted of a chromophore and a polymer. An estimate of the effective concentration of AQ in the dye was obtained by comparing the extinction coefficients of the AQ standard and the dye.

88
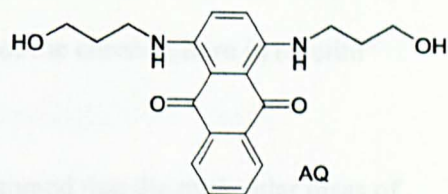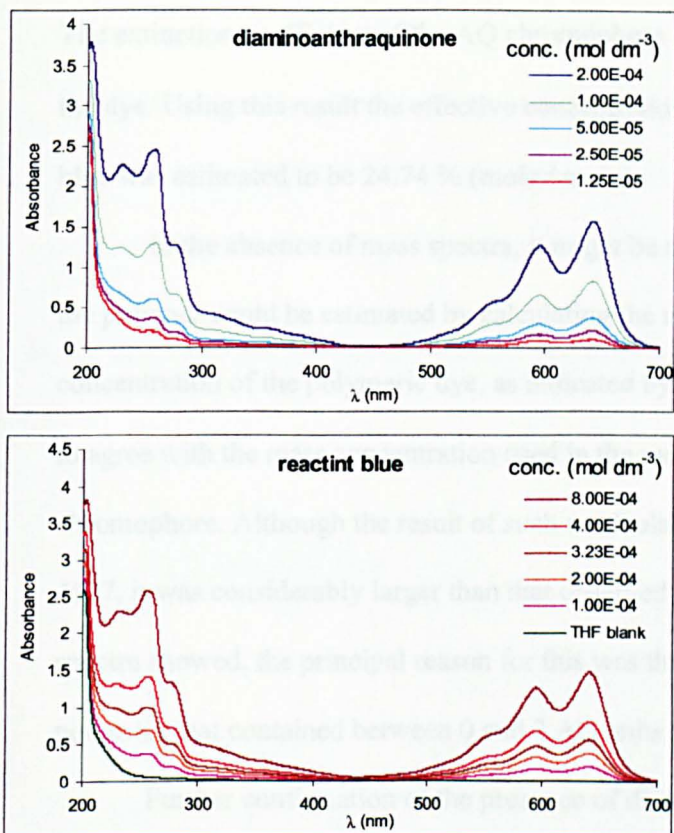
Figure 4.2.1. UV / visible absorption spectra of diaminoanthraquinone (a) and reactint® blue (b). The samples were prepared in THF and obtained using a Carey 1E UV/Visible spectrophotometer and a 0.5 cm cell.

To prevent interference from THF absorption at low wavelengths (although the spectra were referenced from a THF blank), the extinction coefficients were determined at 595 nm. The plots of absorbance versus concentration are shown in figure 4.2.2. As can be seen a linear dependence was observed.
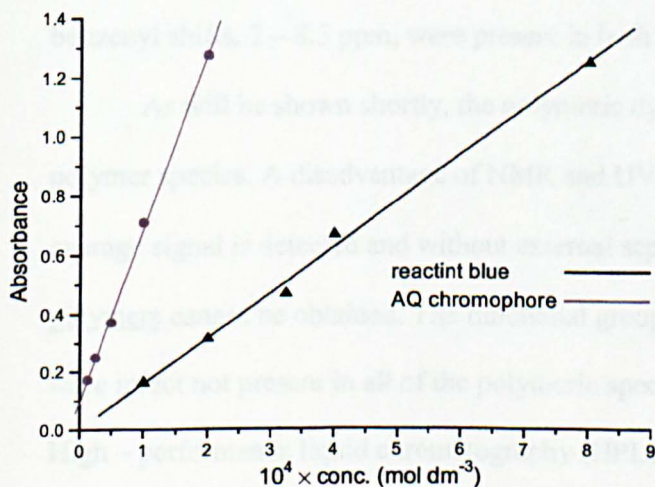
$\varepsilon_{reactint\ blue} = 3136\ mol^{-1}\ dm^3\ cm^{-1}$

$\varepsilon_{AQ} = 12722\ mol^{-1}\ dm^3\ cm^{-1}$

Figure 4.2.2. Determination of the extinction coefficients for reactint® blue and the AQ chromophore.

89

The extinction coefficient of the AQ chromophore was approximately 4 times that of the dye. Using this result the effective concentration of the chromophore in reactint® blue was estimated to be 24.74 % (mole / mole).

In the absence of mass spectra, it might be assumed that the molecular mass of the polymer could be estimated by calculating the mass required for the molar concentration of the polymeric dye, as indicated by comparison with the AQ standard, to agree with the mass concentration used in the sample assuming one polymer per chromophore. Although the result of such a calculation was a sensible figure, Mn = 4507, it was considerably larger than that observed in the mass spectra. As the mass spectra showed, the principal reason for this was the dye sample consisted of many polymers that contained between 0 and 2 AQ units per molecule.

Further confirmation of the presence of diamino anthraquinone chromophore was obtained using NMR. Shown below are proton NMR spectra of reactint® blue and diaminoanthraquinone (note the spectra have different scales). The dye ^{1}H NMR spectra was obtained in CDCl$_3$ using the automated Bruker 300 MHz Departmental service instrument, and the diamino anthraquinone spectrum was supplied by Avecia (run on a Bruker DPX 300 in D$_6$ – DMSO). As can be seen in figure 4.2.3. the three expected benzenyl shifts, 7 – 8.5 ppm, were present in both the dye sample and the AQ sample.

As will be shown shortly, the polymeric dye consisted of many individual polymer species. A disadvantage of NMR and UV/visible spectroscopy is that an average signal is detected and without external separation the signals from individual polymers cannot be obtained. The functional groups identified in the UV/ Vis spectra were infact not present in all of the polymeric species subsequently identified in the dye. High – performance liquid chromatography (HPLC) of the polymeric dye was attempted and although many individual signals were obtained, the mass spectrum of only one of the fractions contained a signal present in the unfractionated sample.

90

However, armed with the information provided by UV/Vis and NMR spectroscopy, ESI-FTICR mass spectrometry permitted the identification of all of the components of reactint® blue without external separation. Furthermore, using tandem mass spectrometry the structures of the more intense polymers were determined.

Figure 4.2.3. NMR spectra of reactint® blue, and diaminoanthraquinone
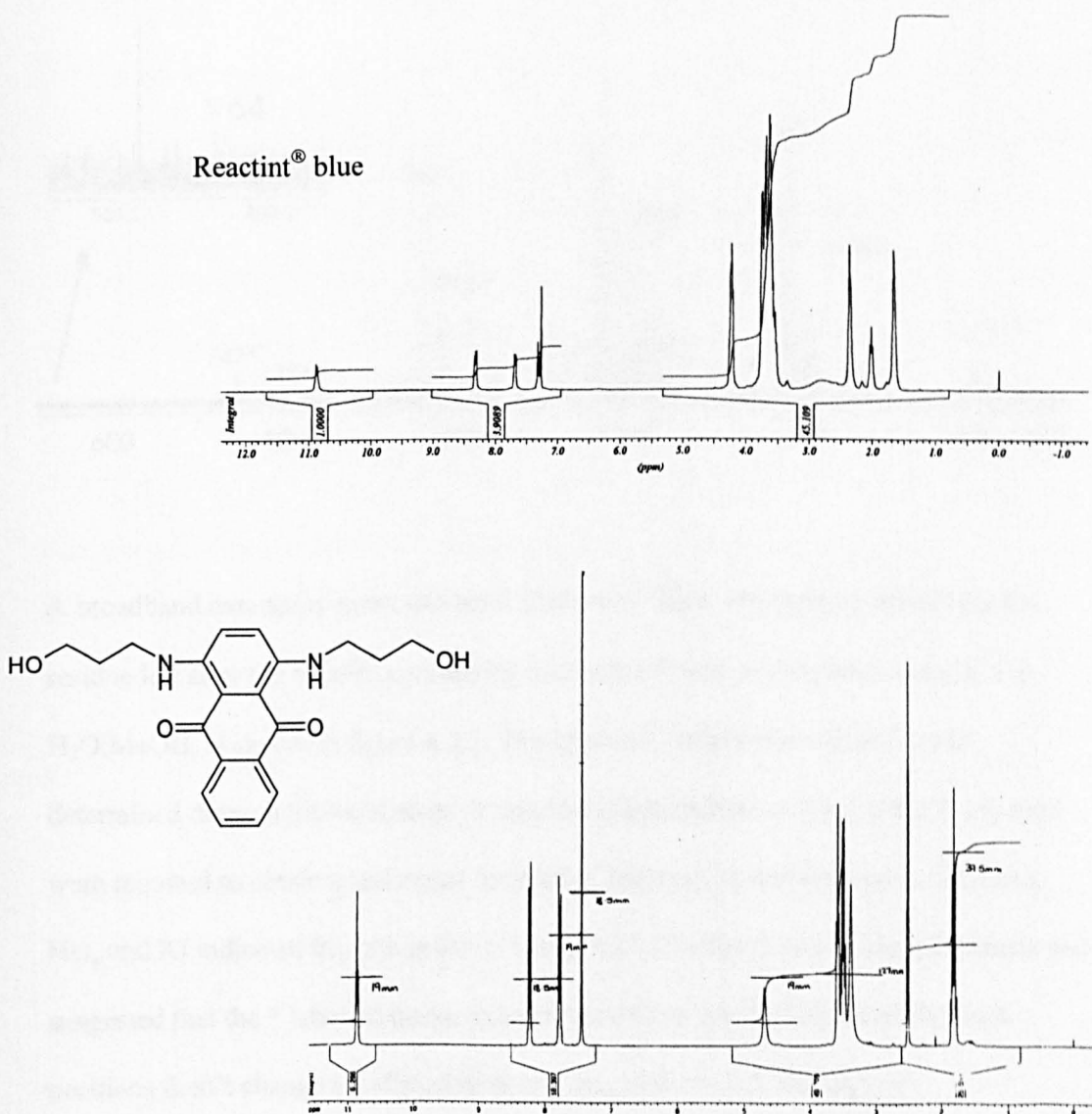
4.3 Reactint® blue mass spectrometry

Figure 4.3.1. Nanospray FTICR mass spectrum of reactint blue
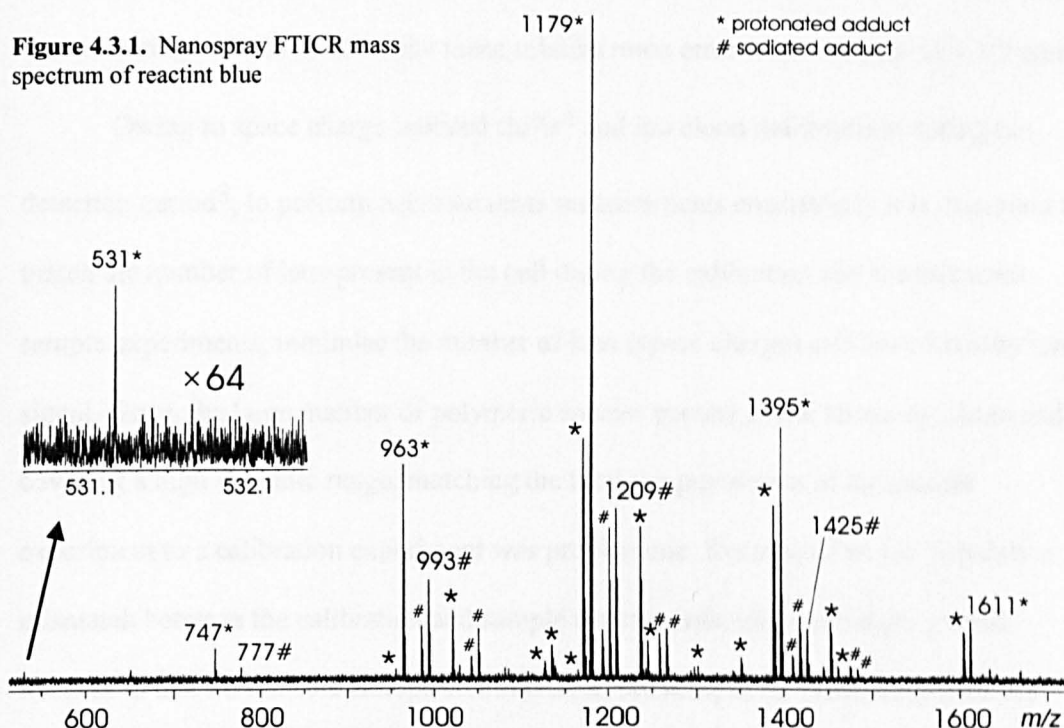
A broadband nanospray mass spectrum of reactint® blue, obtained by dissolving the residue left after the volatile component had been allowed to evaporate away in 1:1 H_2O:MeOH, is shown in figure 4.3.1. The optimum sample concentration was determined through trial-and-error. It was found that neither acid nor salts of any kind were required to obtain good signal intensities. Doping experiments using NH_4OAc, NaI, and KI indicated that the peaks in figure 4.3.1 labelled # were sodiated adducts and suggested that the * labelled peaks were protonated molecules (although the peak positions didn't change a sodiated molecule was observed 22 Da higher).

As can be seen the mass spectrum of the dye was dominated by a series of peaks beginning at $m/z = 531$ with a repeat unit of 216 Da. In addition to this dominant species the spectrum also contained several other polymer series. Finally, the relative intensities

of the ions varied greatly. For example, the most intense peak at m/z = 1179 was 70 times more intense than that at m/z = 1165. As will be shown later, the effect of the high dynamic range was to increase the mean relative mass error from < 1 ppm to ≈ 2.2 ppm.

Owing to space charge induced shifts[4] and ion cloud deformation during the detection period[8], to perform accurate mass measurements consistently it is important to match the number of ions present in the cell during the calibration and the unknown sample experiments, minimise the number of ions (space charge) and have a steady ion signal. Given the large number of polymeric species present in the above spectrum and covering a high dynamic range, matching the total ion population of the sample experiment to a calibration experiment was problematic. Because of an ion population mismatch between the calibration and sample experiments, initial attempts proved fruitless in that no sensible isotope combinations had acceptable mass accuracies. As will be shown, once one of the polymer series was identified conclusively the space-charge shift in the above spectra was estimated accurately by using the known polymer series as an internal calibrant. The more accurate results so obtained were used to determine the identities of the other polymers present in the dye.

Accordingly, the next step was to perform accurate mass measurements of the first two oligomers of the main polymer species. In addition to obtaining an accurate measurement of the polymer's repeat unit, the lowest-mass oligomers provide the most direct and accurate information about the polymer's end groups. As a result of the relationship between an ion's mass and its cyclotron frequency, the absolute accuracy with which an ion's m/z can be determined is greater for ions of smaller masses. Consequently, after removing the required number of repeat units (which is unknown for an unknown sample), the endgroup mass estimates will also be more accurate.

Reflecting the need for ions to be excited to an identical radius (otherwise the space charge experienced by the different ion packets would vary) the chirp excitation profile used was altered from that used previously to make it more uniform over the detected mass range. The frequency – sweep step size was decreased from 5196 to 625 Hz and the excitation – frequency range altered such that it was twice that detected. As can be seen in figure 4.3.2, which displays the excitation profiles, both changes served to produce a flatter excitation profile <u>over the desired mass range</u>.

Figure 4.3.2. Excitation profiles for a 5196 Hz (black) and 625 Hz (red) frequency sweep step size.
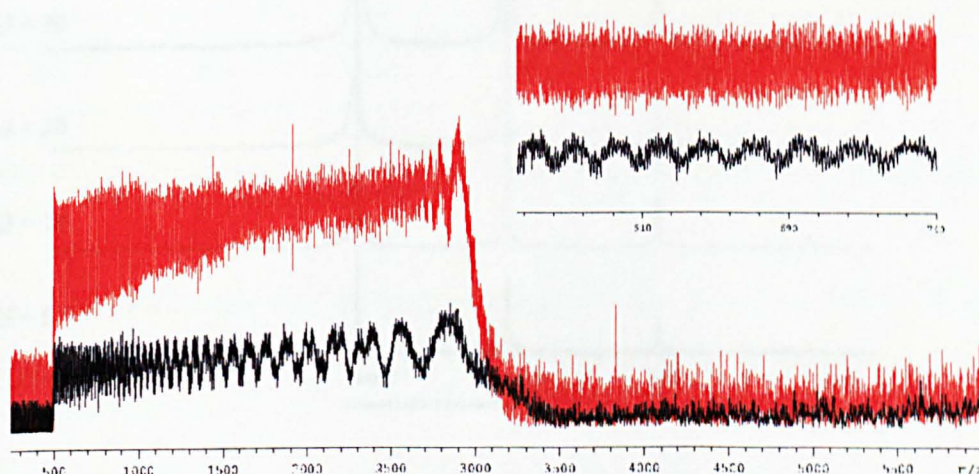
Furthermore, as a result of more individual excitation pulses the relative intensity of the shorter step – size excitation profile was greater than that of the longer step – size. Consequently, the excitation duration and RF field strength required reoptimisation. This was achieved by minimising the mean mass error for a calibrant spectrum. The peak shapes obtained using an excitation duration, $p3$, of $5 – 30$ µs and an excitation field attenuation of 2.57 dB are shown in figure 4.3.3a. It is clear that the peaks became broader for longer ion activation periods, consequently the mean mass error (of poly ethyleneglycol, $Mn = 1500$) increased (figure 4.3.3b). Finally, the instrument was tuned

to transfer only ions near the desired *m/z* range. As a result space charge from other ions

was minimised.

Figure 4.3.3. a) peak shape dependence on excitation duration, *p3*, and b) the resulting relative mass errors

a)

p3 = 30

p3 = 20

p3 = 10

p3 = 5

1443.0   1444.0   1445.0   1446.0   1447.0   m/z
liam041099/22/pdata/1
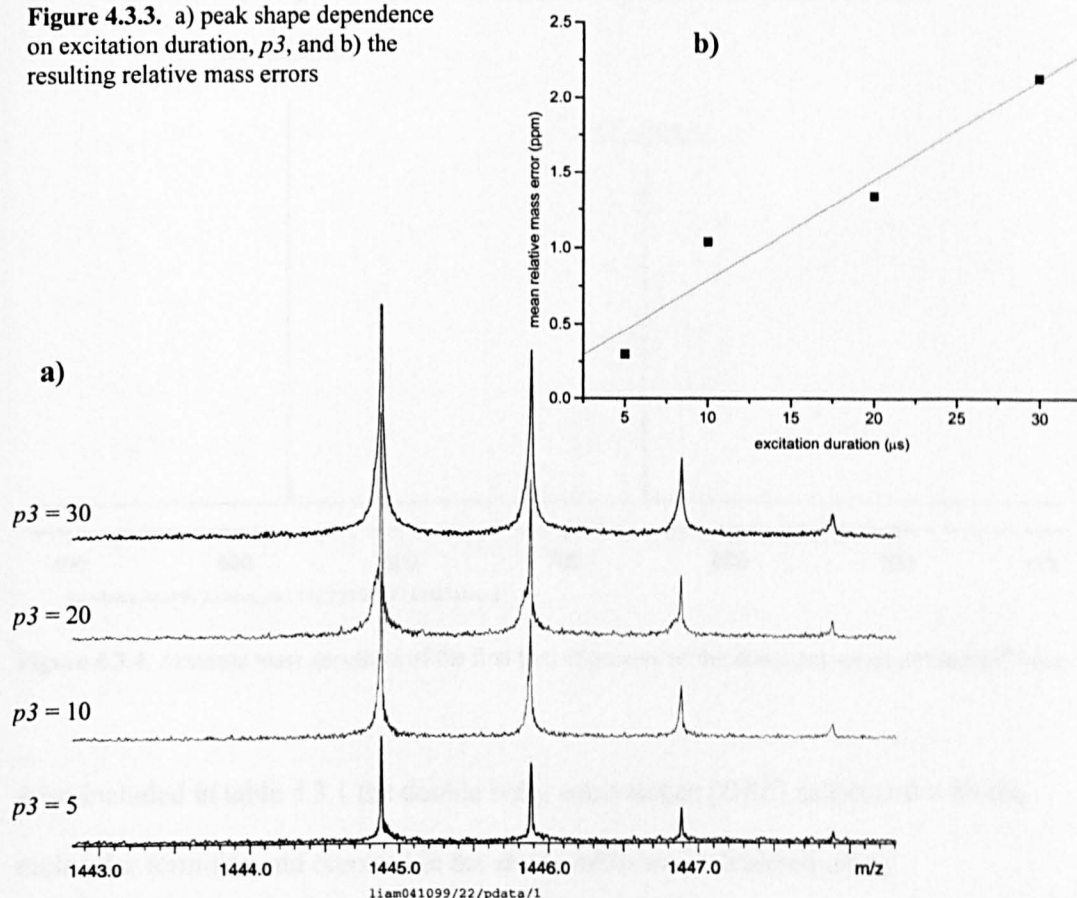
The accurate mass spectrum of the first two oligomers of the dominant series in

reactint® blue is shown in figure 4.3.4. The high mass-accuracies obtained permitted

mass analysis of the ion peaks to determine their isotopic content. Bruker's XMASS

software included a macro that determined all possible combinations of user – defined

isotopes that have a total mass within a user – defined mass tolerance. The number of

combinations satisfying these criteria increases rapidly with the number of possible

isotopes, the mass tolerance (acceptable mass error) and the mass of the ion. The high

mass – accuracies obtainable with FTICR mass spectrometry minimised the mass

tolerance, whilst a preliminary study of the ion's isotopic envelope was used to rule out

the presence of halogen atoms and the analysis was performed on the smallest

oligomers detected. Table 4.3.1. details the results from mass analysis of the $m/z = 531$

mono-isotopic ion peak (531.269565) shown in figure 4.3.4, where the possible isotopes

were limited to ^1H, ^{12}C, ^{16}O, and ^{14}N using a maximum error of ± 0.005 m/z.

/u/data/mary/liama_calib_251099/10/pdata/1
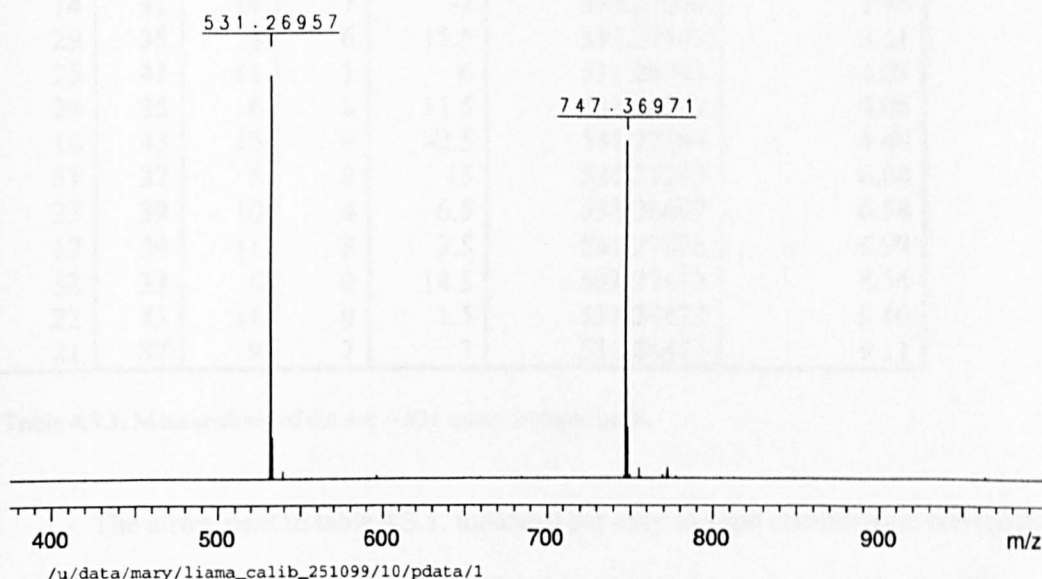
Figure 4.3.4. Accurate mass spectrum of the first two oligomers of the dominant series of reactint® blue.

Also included in table 4.3.1 the double bond equivalence (*DBE*) associated with the

molecular formulae and reported in the above table was calculated using

$$DBE = 0.5 \times \left[2 + \sum_i N_i(V_i - 2) \right] \qquad (4.3.i)$$

N_i is the number of atoms i of valance V_i. The charge carriers (protons) were also

included in the calculation of the double bond equivalence. The extra hydrogen atom

caused the double bond equivalence to be reduced by 0.5 (conversely, an anion formed

by proton abstraction would have a *DBE* 0.5 greater than that of the neutral species).

96

# ^{12}C	# ^{1}H	# ^{16}O	# ^{14}N	*DBE*	Calculated *m/z*	Error (ppm)
12	39	13	10	-1.5	531.26926	0.58
27	33	3	9	16	531.27009	0.98
28	39	8	2	10.5	531.27009	0.99
26	37	7	5	11	531.26875	1.53
14	41	14	7	-2	531.27060	1.95
29	35	4	6	15.5	531.27143	3.51
25	41	11	1	6	531.26741	4.05
24	35	6	8	11.5	531.26741	4.06
16	43	15	4	-2.5	531.27194	4.48
31	37	5	3	15	531.27277	6.04
23	39	10	4	6.5	531.26607	6.58
17	39	11	8	2.5	531.27328	6.99
33	39	6	0	14.5	531.27412	8.56
22	43	14	0	1.5	531.26473	9.10
21	37	9	7	7	531.26473	9.11

Table 4.3.1. Mass analysis of the *m/z* = 531 mono-isotopic peak.

The arrow next to table 4.3.1. indicates the only isotope combination consistent with the UV absorbance data, namely a diamino anthraquinone based polymer. The mass accuracies for the diamino anthraquinone polymers were 0.98 and 0.21 ppm for the *m/z* = 531 and 747 ions, respectively ($C_{38}H_{55}O_{13}N_2^+$ = 747.3698663 Th). The difference between the two ions, the polymer's repeat unit, was found to be $C_{10}H_{16}O_5$, the mass accuracy of which was 1.7 ppm (determined by comparing the mass difference between the two oligomers with the theoretical mass). The greater mass error associated with the repeat unit was due to it including the mass errors from both measured ion peaks. The lower mass ion had an experimental *m/z* slightly below its theoretical value (- 0.98 ppm) whereas the higher mass ion was observed at slightly greater *m/z* (+0.21 ppm).

The chemical formula of the repeat unit $C_{10}H_{16}O_5$ is consistent with diethylene glycol adipate, the presence of which was confirmed using NMR spectroscopy, see figure 4.3.5 (note: different scales).
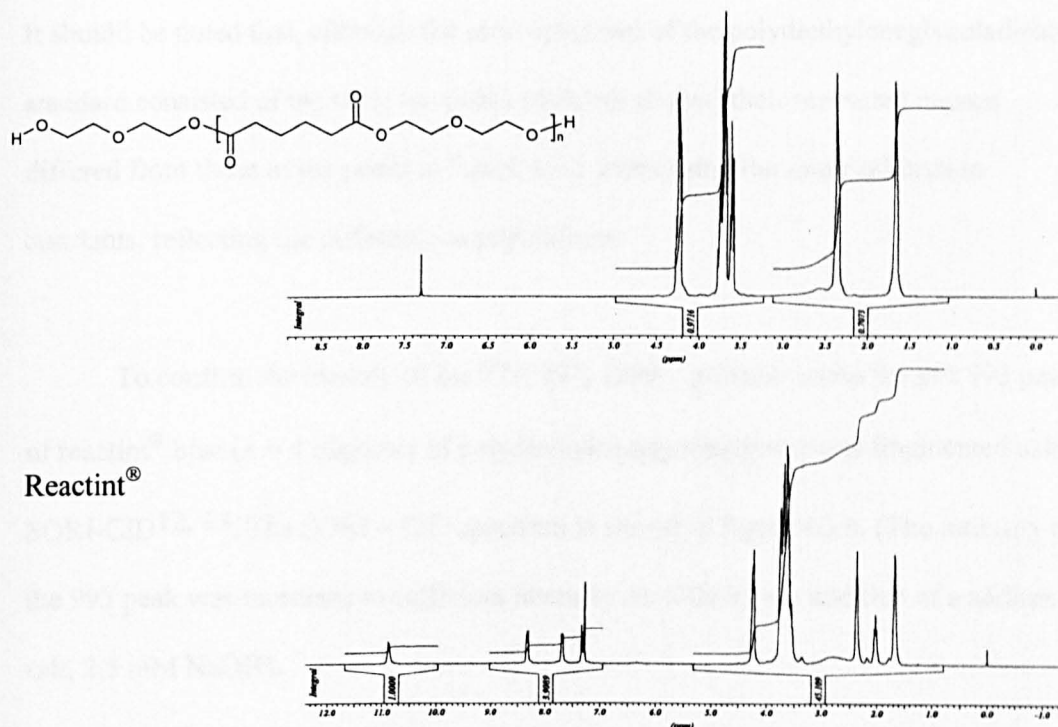
Reactint®

Figure 4.3.5. Comparison of NMR spectra of poly diethylene glycol adipate and reactint® blue. Both spectra were obtained using the automated Bruker 300 MHz service instrument at Warwick, and were run in CDCl₃.

A polymer consistent with the NMR, UV/Visible absorption and mass spectral data is
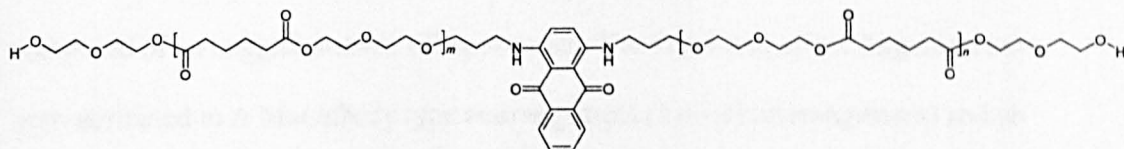
where the ions detected at $m/z = 531$ and 747 correspond to the protonated $n + m = 0$

and $n + m = 1$ adducts, respectively.

Inspection of the mass spectrum of reactint® blue revealed a series of peaks (777, 993,

1209…) consistent with the polydiethyleneglycoladipate standard used for the NMR

experiments (detected ions were sodiated). As can be seen in figure 4.3.1. the intensity

of this polymer series was approximately the same as that of the other minor

components when no additional salts or acid were added.

98

It should be noted that, although the mass spectrum of the polydiethyleneglycoladipate standard consisted of the same ion peaks (data not shown) their measured masses differed from those of the peaks in figure 4.3.1 when using the same calibration constants, reflecting the different ion populations.

To confirm the identity of the 777, 993, 1209...polymer series the *m/z* 993 peak of reactint[®] blue (*n* = 4 oligomer of polydiethyleneglycoladipate) was fragmented using SORI-CID[12, 13]. The SORI – CID spectrum is shown in figure 4.3.6. (The intensity of the 993 peak was increased to sufficient intensity for CID by the addition of a sodium salt, 2.5 mM NaOH).

As can be seen from the figure 4.3.6 the more intense fragments displayed a 88 – 146 – 70 – 146 – 70 ... Da pattern which is consistent with a rearrangement that forms a carboxylic acid and an alkene (see scheme 4.3.1). Weaker fragments displayed a 216 – 106 – 110 – 106... pattern, attributable to shorter oligomers and cyclic polymers composed of an integral number of repeat units. The major and minor fragments have been attributed to A McLafferty type rearrangement (1,4 – H rearrangement) and an intramolecular transesterification, respectively[14, 15].

These mechanisms do not immediately explain the observed charge – carrier dependency reported below. It will be proposed that the major and minor fragments provide examples of charge-induced and charge-remote fragmentation, respectively[16].

Figure 4.3.6. SORI-CID spectrum of the m/z 993 ion of reactint blue. The parent ion was isolated using a correlated sweep (V_{iso} = 39.11 dB, t_{iso} = 4000 ms, 120 Hz safety belt) and fragmented using SORI-CID (V_{SORI} = 28.53 dB, t_{SORI} = 0.5 s, 1000 Hz offset, 4 s reaction delay) with nitrogen as the collision gas. The peak cell pressure was 1×10^{-6} mbar.
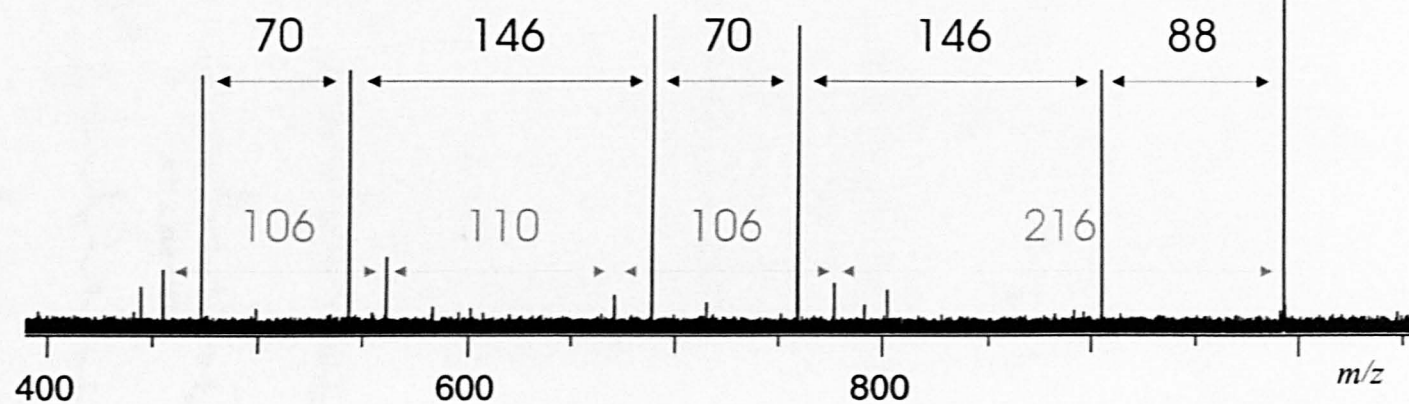
Major fragments (labelled in black)

$n = 4$, $m/z = 993$

$n = 3$, $m/z = 905$

$n = 2$, $m/z = 759$

$n = 3$, $m/z = 689$
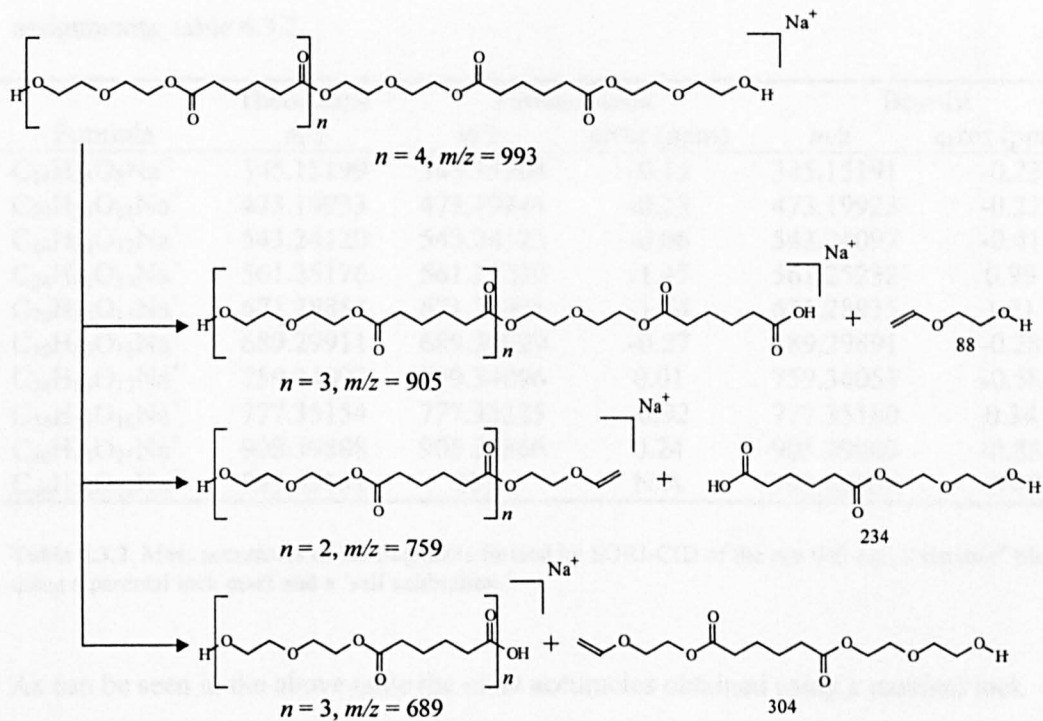
Minor fragments (labelled in grey)

$n = 3$, $m/z = 777$

$n = 3$, $m/z = 671$

$n = 2$, $m/z = 561$

$m = 3$, $m/z = 671$

$m = 2$, $m/z = 455$
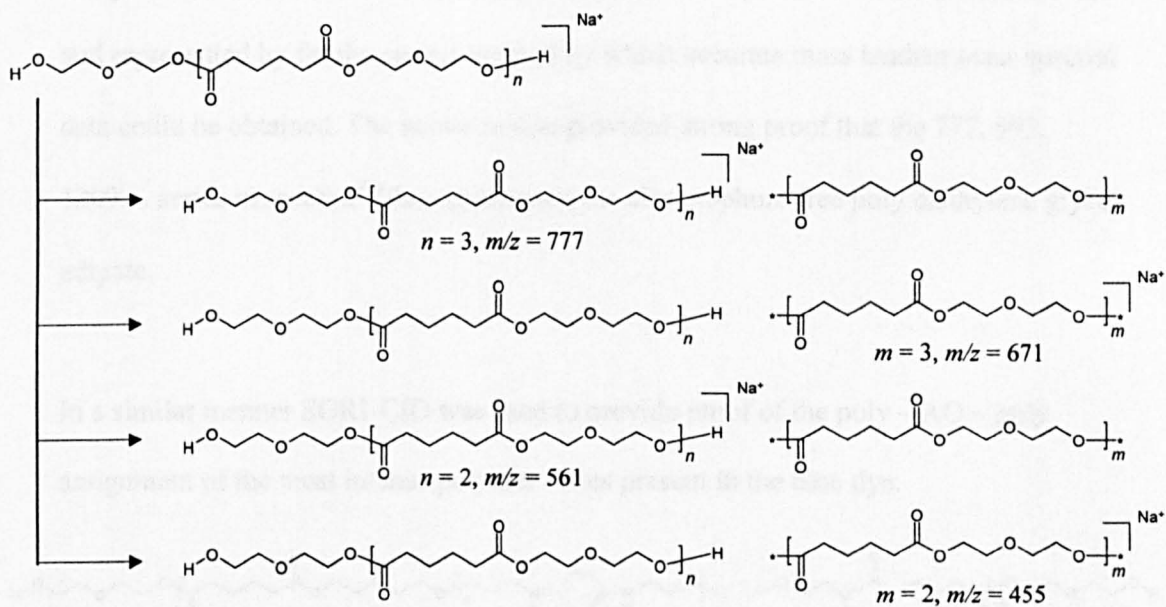
Scheme 4.3.1. The SORI – CID fragments of the m/z 993 ion of reactint blue.

The mass accuracies of the above assignments provided confidence for the above assignments, table 4.3.2.

	Theoretical	Parental-lock		Best-fit	
Formula	m/z	m/z	error (ppm)	m/z	error (ppm)
$C_{14}H_{26}O_8Na^+$	345.15199	345.15204	-0.15	345.15191	-0.23
$C_{20}H_{34}O_{11}Na^+$	473.19933	473.19944	-0.23	473.19923	-0.22
$C_{24}H_{40}O_{12}Na^+$	543.24120	543.24123	-0.06	543.24097	-0.41
$C_{24}H_{42}O_{13}Na^+$	561.25176	561.25259	-1.47	561.25232	0.99
$C_{30}H_{48}O_{15}Na^+$	671.28854	671.28971	-1.74	671.28935	1.21
$C_{30}H_{50}O_{16}Na^+$	689.29911	689.29929	-0.27	689.29891	-0.28
$C_{34}H_{56}O_{17}Na^+$	759.34097	759.34096	0.01	759.34053	-0.58
$C_{34}H_{58}O_{18}Na^+$	777.35154	777.35225	-0.92	777.35180	0.34
$C_{40}H_{66}O_{21}Na^+$	905.39888	905.39866	0.24	905.39809	-0.88
$C_{44}H_{74}O_{23}Na^+$	993.45131	N/A	N/A	993.45064	-0.67

Table 4.3.2. Mass accuracies of the fragments formed by SORI-CID of the m/z 993 ion of reactint® blue using a parental lock mass and a 'self calibration.'

As can be seen in the above table the mass accuracies obtained using a parental lock mass, in which the parent ion is used to fine tune the calibration (see page 28), were comparable to those obtained by fitting the calibration equation to the experimental data and represented by far the easiest method by which accurate mass tandem mass spectral data could be obtained. The above results provided strong proof that the 777, 993, 1209... series in reactint® blue represented the chromophore free poly diethylene glycol adipate.

In a similar manner SORI-CID was used to provide proof of the poly – AQ – poly assignment of the most intense polymer series present in the blue dye.

poly – AQ – poly

$C_{28+10(n+m)}H_{38+16(n+m)}O_{8+5(n+m)}N_2$

102
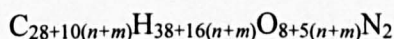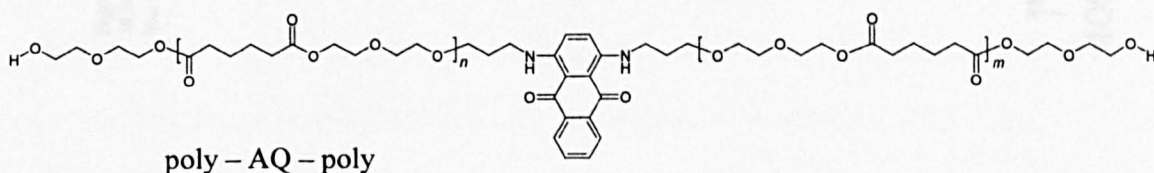
Figure 4.3.7. SORI-CID of the protonated $n+m=3$ oligomer of poly - AQ - poly. (SORI-CID:- V_{SORI} = 28.84 dB, t_{SORI} = 0.5 s, 1000 Hz offset, peak cell pressure = 10^{-6} mbar, 6 s reaction delay; Isolation: - V_{iso} = 34 dB, t_{iso} = 4 ms, 120 Hz safety belt; correlated shots:- V_{shots} = 25 dB, t_{shots} = 0.1 s).
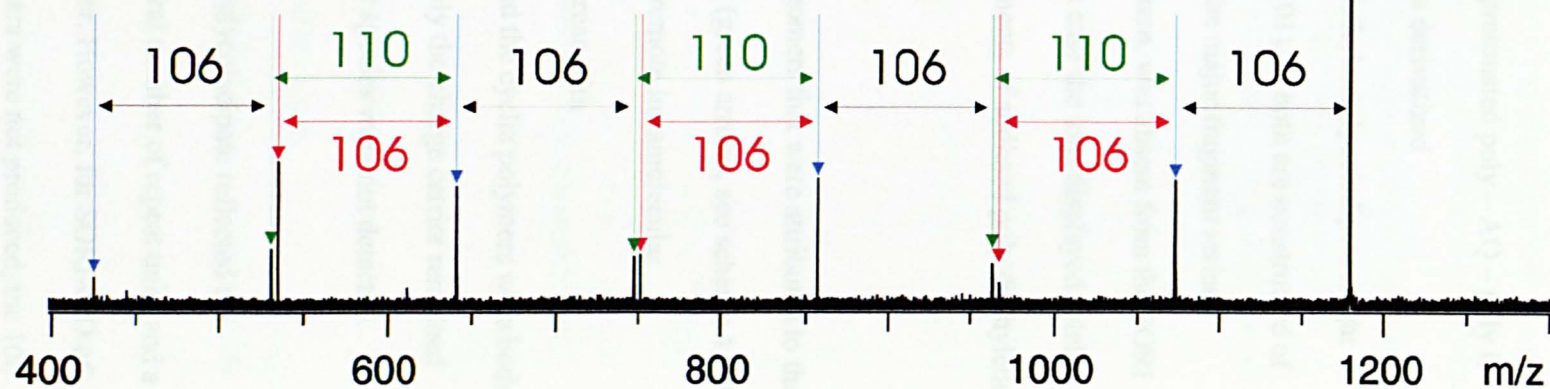
The SORI-CID spectrum of the $n + m = 3$ oligomer of protonated poly – AQ – poly is shown in figure 4.3.7. Although the fragments from this derivatized diethyleneglycoladipate polymer and those from polydiethyleneglycoladipate might have been expected to be similar (see formula on page 101), as both are constructed of the same repeat unit, it was immediately apparent that the major fragment series observed with the latter, the 146 – 70 – 146 – 70 … pattern, was absent from the SORI – CID spectrum of protonated poly – AQ – poly. In this case the ions displayed solely the 106 – 110 – 106 – 110 … pattern of the minor fragments of sodiated poly diethylene glycol adipate.

As with polydiethyleneglycoladipate, the shortened oligomers that were attributed to the loss of an integral number of repeat units were detected (green arrows, see scheme 4.3.2 and figure 4.3.7), presumably through the same charge remote intramolecular transesterification mechanism[15, 17, 18]. However, whereas with polydiethyleneglycoladipate the shortened oligomers and the cyclic polymers were both detected (figure 4.3.6.), with protonated poly – AQ – poly the charge carrier remained on the diamino-anthraquinone substituent and the cyclic species were not detected.

The 106 Da spacings after SORI-CID of polydiethyleneglycoladipate reflected the difference between a cyclic species made up of an integral number of repeat units and a shortened oligomer of the poly diethylene glycol polymer. However, for SORI-CID of poly – AQ – poly, as the cyclic diethylene glycol polymers were not produced, the 106 Da spacings must have had a different origin. Evidence of a different origin was provided by the observation that a fragment ion was produced 106 Da lighter than the parent ion of protonated poly – AQ – poly, but an analogous ion was not observed for sodiated poly diethylene glycol adipate (figure 4.3.6.). The peaks labelled with blue

arrows were due to the loss of one diethylene glycol unit (+ an integral number of repeat units) and those labelled with red arrows, the heavier ion of the doublet, to the loss of a diethylene glycol unit from both arms of poly – AQ – poly (see scheme 4.3.2 and figure 4.3.7. Presumably, the nucleophilic amine groups were responsible for the reaction channels leading to the loss of one or two diethylene glycol units (+ integral number of repeat units).
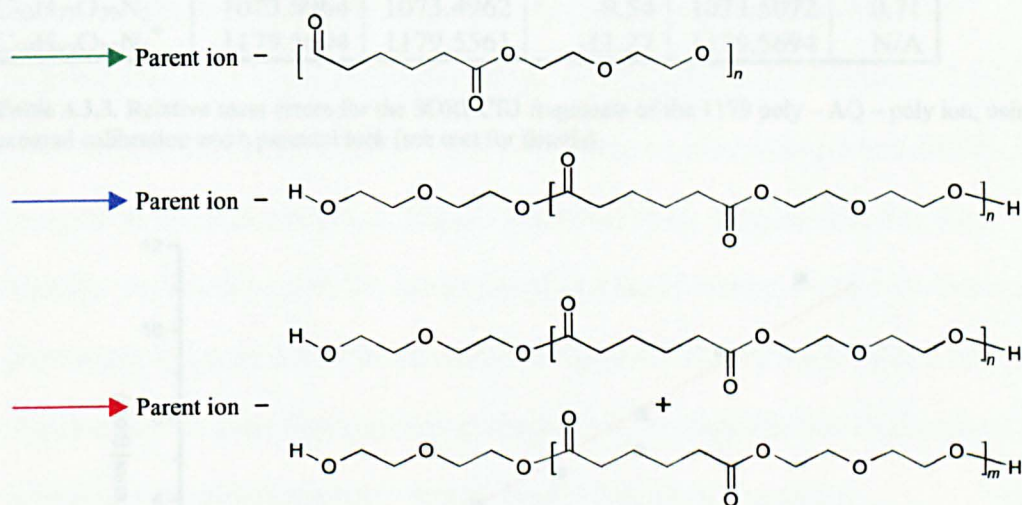
Scheme 4.3.2. The SORI - CID fragments of the m/z 1179 ion of reactint blue (protonated poly – AQ – poly).

The dependence of an ion's effective cyclotron frequency on space – charge could readily be seen when the SORI-CID self-calibration file (best-fit) of polydiethyleneglycoladipate was used to calibrate the SORI-CID spectrum of the 1179 ion of poly – AQ – poly.

The mass accuracies of the assignments, using the previous SORI – CID spectrum as an external calibration(best – fit calibration constants) are shown in table 4.3.3 and displayed as a function of fragment mass in figure 4.3.7.

	Theo.	External calibration		Parental lock	
		Measured	Error	Measured	Error
$C_{24}H_{29}O_5N_2^+$	425.2071	425.2060	-2.58	425.2077	1.48
$C_{28}H_{39}O_8N_2^+$	531.2701	531.2678	-4.26	531.2705	0.81
$C_{30}H_{35}O_7N_2^+$	535.2439	535.2417	-4.00	535.2445	1.11
$C_{34}H_{45}O_{10}N_2^+$	641.3069	641.3038	-4.77	641.3077	1.35
$C_{38}H_{55}O_{13}N_2^+$	747.3699	747.3654	-5.91	747.3708	1.22
$C_{40}H_{51}O_{12}N_2^+$	751.3437	751.3394	-5.61	751.3448	1.56
$C_{44}H_{61}O_{15}N_2^+$	857.4066	857.4009	-6.69	857.4079	1.50
$C_{48}H_{71}O_{18}N_2^+$	963.4696	963.4627	-7.20	963.4716	1.99
$C_{50}H_{67}O_{17}N_2^+$	967.4434	967.4356	-8.07	967.4446	1.17
$C_{54}H_{77}O_{20}N_2^+$	1073.5064	1073.4962	-9.54	1073.5072	0.71
$C_{58}H_{87}O_{23}N_2^+$	1179.5694	1179.5561	-11.27	1179.5694	N/A

Table 4.3.3. Relative mass errors for the SORI-CID fragments of the 1179 poly – AQ – poly ion, using an external calibration and a parental lock (see text for details).
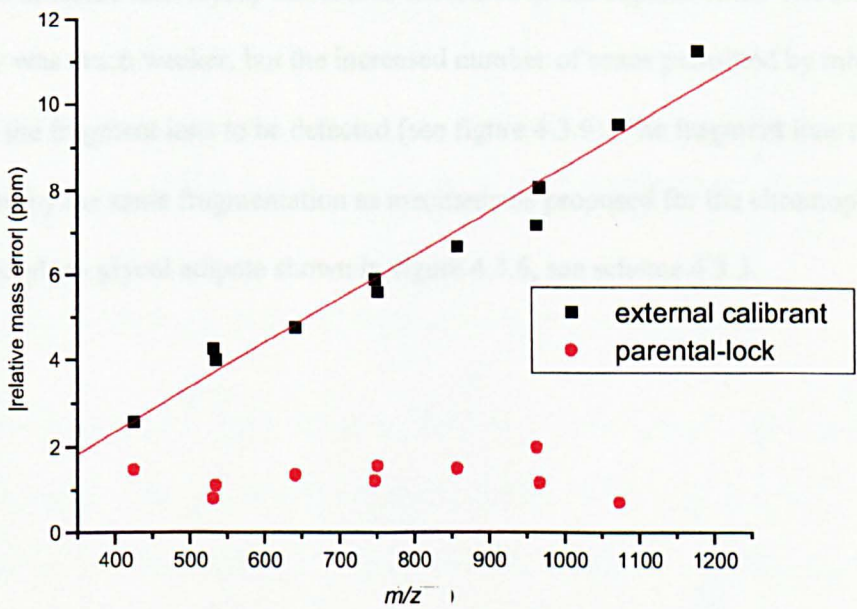
Figure 4.3.8. Comparison of the mass accuracies of the fragments from SORI-CID of the $n = 3$ oligomer of protonated poly – AQ – poly using a SORI-CID spectrum of a polymer of the same repeat unit was used for the external calibration and a parental lock.

As can be seen the mass errors obtained using a SORI-CID experiment of a polymer with the same repeat unit to perform the calibration gave significant mass errors. Furthermore, the relative mass errors increased with m/z. As will be explained in section 4.8 this linear relationship is expected when the ion density present in the cell during the sample experiment is different from that during the calibration experiment.

The absence of the 146 – 70 – 146 ... fragment series (McLafferty rearrangement) for the above SORI-CID spectrum of the protonated dye is attributed to a charge-induced fragmentation. As can be seen in figure 4.3.9, which shows the SORI-CID spectra of the sodiated $n + m = 2$ oligomers of poly –AQ – poly, the fragment ions display the same 88 – 146 - 70 ... pattern observed for the fragments of sodiated polydiethyleneglycoladipate (see figure 4.3.6). To maximise the intensity of the sodiated poly – AQ – poly adduct, the sample was prepared in 1:1 methanol : 5 mM NaI. The resulting sodiated poly – AQ – poly was just sufficient to perform SORI-CID using the in-house microspray ion source described in the experimental. The ion intensity was much weaker, but the increased number of scans permitted by microspray allowed the fragment ions to be detected (see figure 4.3.9). The fragment ions could be explained by the same fragmentation as mechanisms proposed for the chromophore-free poly diethylene glycol adipate shown in figure 4.3.6, see scheme 4.3.3.
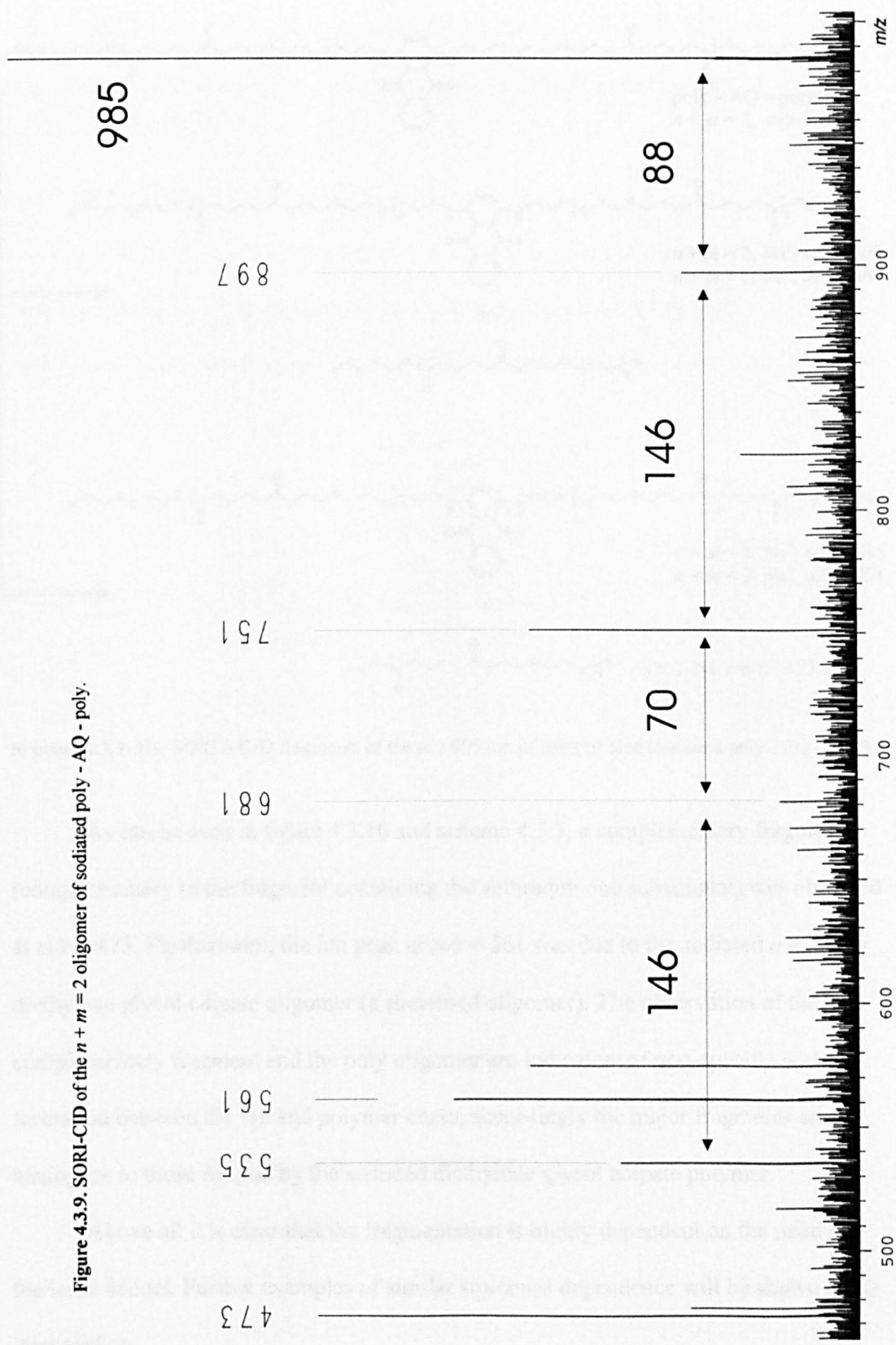
Figure 4.3.9. SORI-CID of the $n + m = 2$ oligomer of sodiated poly - AQ - poly.

985

897

751

681

561

535

473

88

146

70

146

m/z

poly − AQ − poly, Na⁺
$n + m = 2,\ m/z = 985$

$n + m = 2$, Na⁺, $m/z = 897$
$n + m = 1$, Na⁺, $m/z = 681$

+

$n + m = 1$, Na⁺, $m/z = 535$
$n + m = 2$, Na⁺, $m/z = 751$

+

$q = 2$, Na⁺, $m/z = 473$
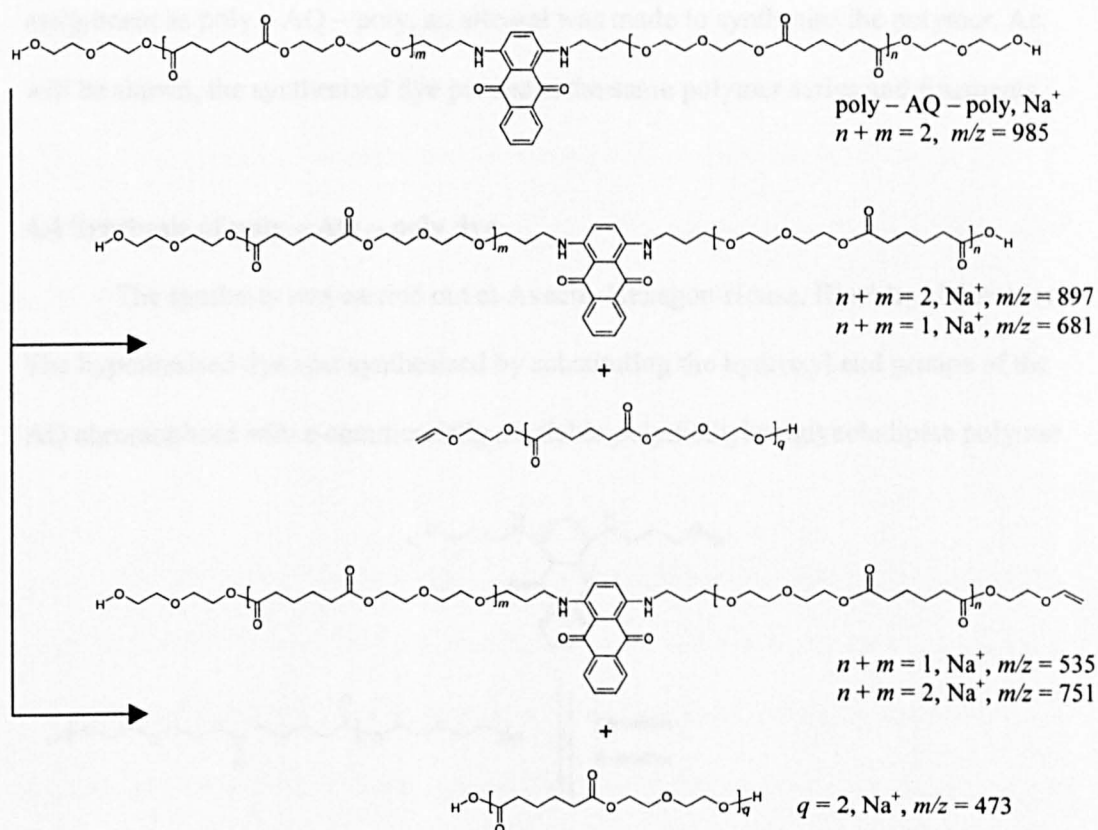
Scheme 4.3.3. The SORI − CID fragments of the m/z 985 ion of reactint blue (sodiated poly - AQ - poly).

As can be seen in figure 4.3.10 and scheme 4.3.3, a complementary fragment (complementary to the fragment containing the anthraquinone substituent) was observed at $m/z = 473$. Furthermore, the ion peak at $m/z = 561$ was due to the sodiated $n = 2$ poly diethylene glycol adipate oligomer (a shortened oligomer). The observation of the complementary fragment and the poly oligomer are indicative of non-specific adduct formation between the ion and polymer chain, accordingly the major fragments are analogous to those formed by the sodiated diethylene glycol adipate polymer.

Above all it is clear that the fragmentation is highly dependent on the nature of the ionic adduct. Further examples of similar structural dependence will be shown in the next section.

Finally, recalling that the contents of reactint® blue were completely unknown prior to the mass spectrometry experiments, for definitive proof of the <u>major</u> ion series'

109

assignment as poly – AQ – poly, an attempt was made to synthesise the polymer. As will be shown, the synthesised dye produced the same polymer series and fragments.

4.4 Synthesis of poly – AQ – poly dye

The synthesis was carried out at Avecia, Hexagon House, Blackley, Manchester. The hypothesised dye was synthesised by substituting the hydroxyl end groups of the AQ chromophore with a commercially available polydiethyleneglycoladipate polymer.
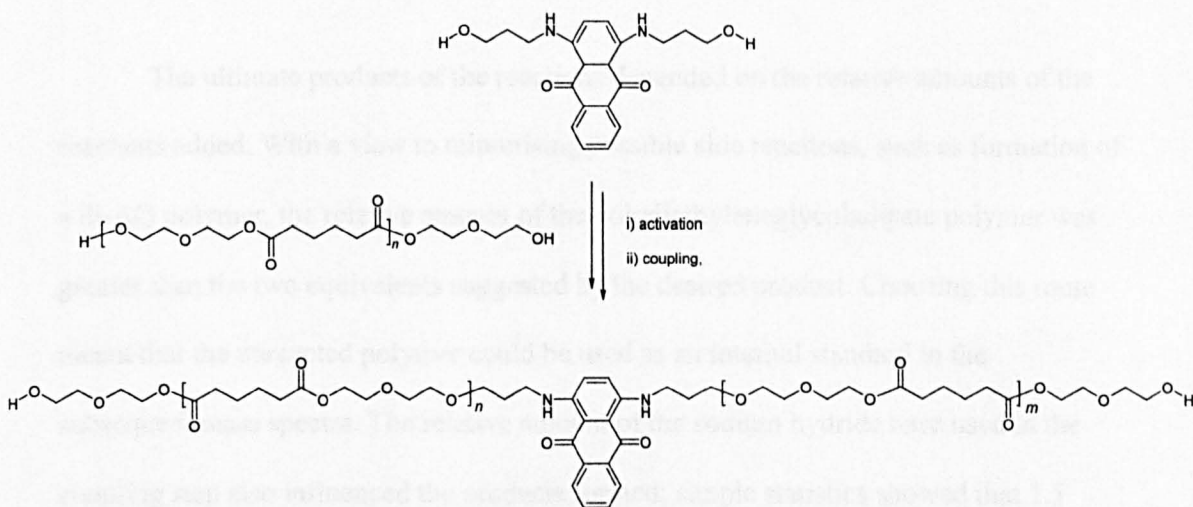
The formation of the ether link between the AQ chromophore and the polymer required either the chomophore's or the polymer's hydroxyl end groups to be activated. So as to avoid self-condensation of the polymer, the chromophore was activated. Activation was achieved by tosylation of the alcoholic end groups. Owing to the slow rate of tosylation reaction a strong base, 4-dimethyl ammonium pyridine (DMAP), was used to deprotonate the chromophore's alcoholic groups prior to its reaction with tosyl chloride.

Finally, coupling was achieved through deprotonation of the polymer to form a polymeric anionic nucleophile, which then displaced the tosylate groups of the activated chromophore. The final coupling reaction was performed under nitrogen in oven-dried glassware as the base used, NaH, and the anions formed were highly moisture sensitive.

110

The diaminoanthraquinone chromophore (AQ) used was synthesised prior to my arrival at Avecia, the purity of which was ascertained by NMR and MALDI-TOF mass spectroscopy. Additionally, as the reactint® blue dye was found to possess only a small number of diethylene glycol adipate repeat units, the smallest commercially available polymer (Mn = 500) was used. A nanospray ESI-FTICR mass spectrum of the polymer confirmed the commercial sample contained the desired polymer.

The ultimate products of the reactions depended on the relative amounts of the reactants added. With a view to minimising possible side reactions, such as formation of a di-AQ polymer, the relative amount of the polydiethyleneglycoladipate polymer was greater than the two equivalents suggested by the desired product. Choosing this route meant that the unreacted polymer could be used as an internal standard in the subsequent mass spectra. The relative amount of the sodium hydride base used in the coupling step also influenced the products formed; simple statistics showed that 1.5 equivalents (with respect to the polymer) would favour the desired product.

Reaction progress was monitored using thin-liquid-chromatography (TLC). Standard safety procedures, rubber gloves, lab coat, safety specs and a fume hood were employed.

The procedure followed for the synthesis of the dye is detailed in the two reaction schemes:

1) Tosylation of anthraquinone chromophore

DMAP (10%)
CH$_2$Cl$_2$
room temperature
TsCl
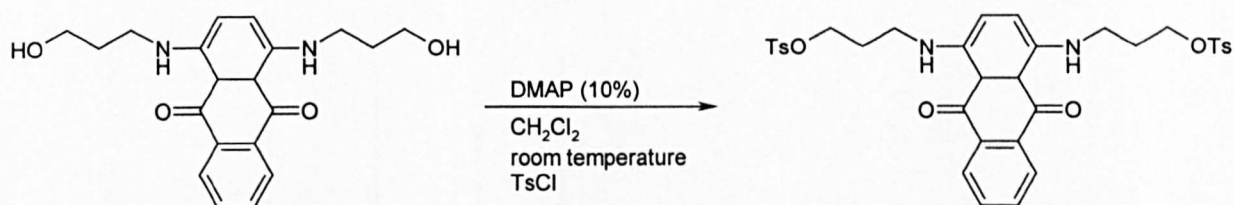
2) Addition of polymer to tosylated diaminoanthraquinone.

NaH
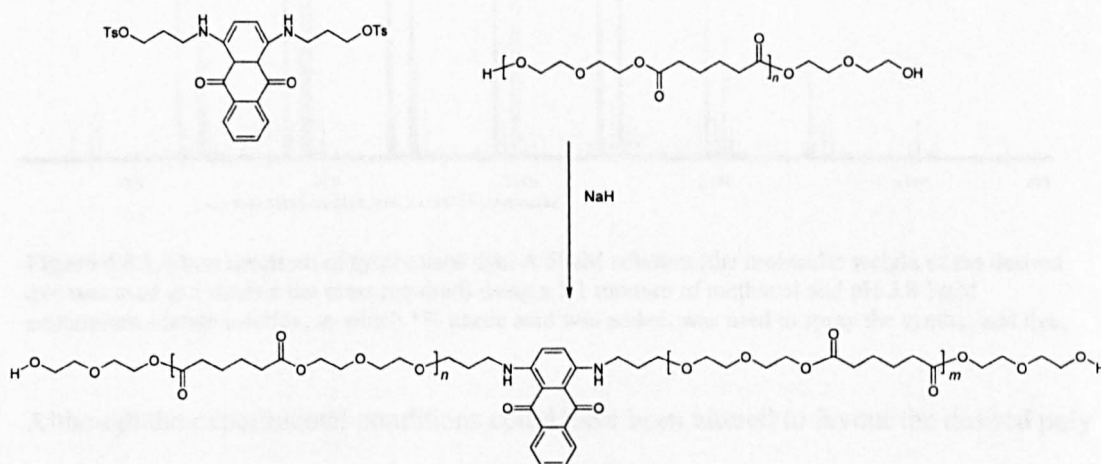
As will be shown shortly the basic conditions led to several side-reactions.

4.5 Synthetic dye mass spectra

As can be seen from the following nanospray ESI FTICR mass spectrum of the synthesised dye, it was clear that there were significant differences between the synthetic and reactint® blue dyes. Perhaps the biggest difference was the presence of at least four distinct intense polymer series (figure 4.5.1), whereas one series dominated reactint® blue's mass spectrum. Using potassium / sodium doping experiments it was found that the mass spectrum of the synthetic dye were dominated by singly charged adducts of hydrogen, sodium or ammonium ions (see sample preparation in figure caption).

/u/data/liam/synth2_int_cal231199/7/pdata/1
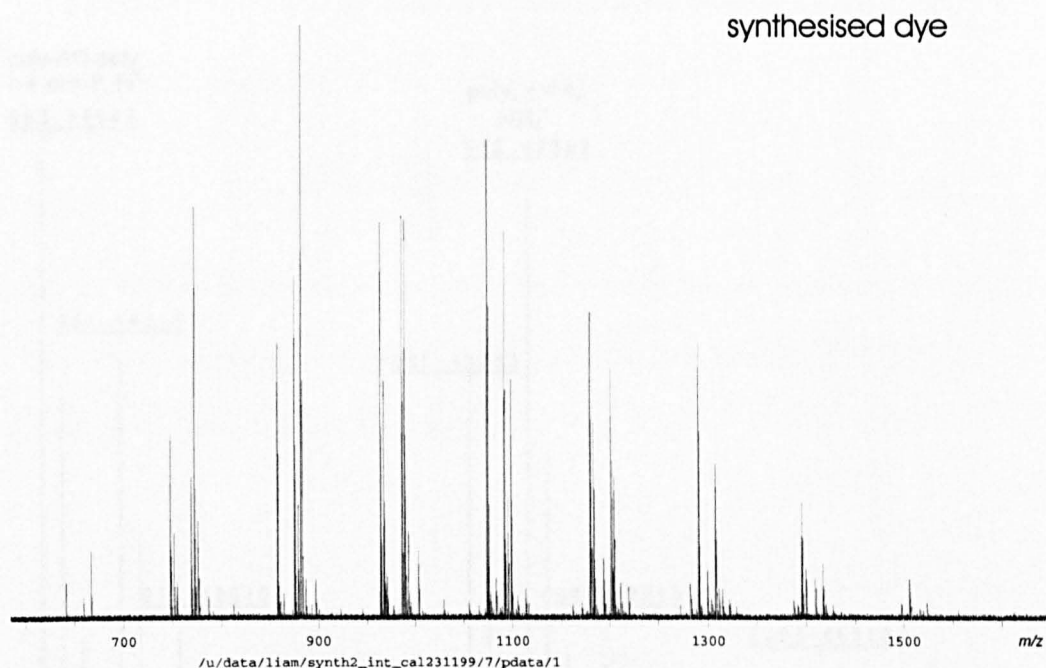
Figure 4.5.1. Mass spectrum of synthesised dye. A 50uM solution (the molecular weight of the desired dye was used to calculate the mass required) using a 1:1 mixture of methanol and pH 5.8 5mM ammonium acetate solution, to which 1% acetic acid was added, was used to spray the synthesised dye.

Although the experimental conditions could have been altered to favour the desired poly – AQ – poly product, it was not necessary. As can be seen in figure 4.5.2., which shows a close up of the *m/z* = 960 – 1000 region of the synthetic dye, both the desired dye and unreacted poly diethylene glycol adipate (referred to as poly) were present, as well as several other species. Using the unreacted polydiethyleneglycoladipate as an internal calibrant the protonated poly-AQ-poly adduct shown below had a mass accuracy of 0.18 ppm. As the starting materials were known and the reaction conditions were controlled, it can be stated confidently that the desired dye was responsible for the *m/z* = 963 ion observed. Further confirmation was achieved using tandem mass spectrometry.

113

poly-AQ-poly
$n + m = 2$, H$^+$
963.46947

967.44325

970.48610

poly, $n = 4$,
NH$_4^+$
988.49562

985.45383

992.47015

1003.46540

970   980   990   1000   m/z

/u/data/mary/synth2_int_cal231199/3/pdata/1
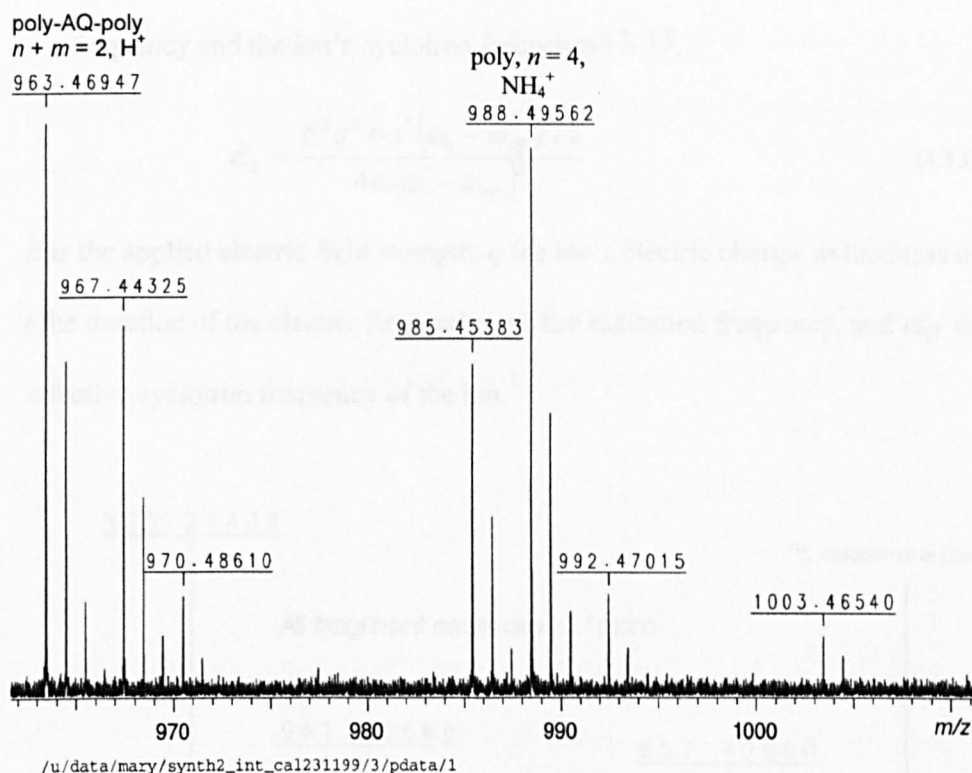
Figure 4.5.2. Mass spectrum of synthetic blue, displaying the presence of both the desired polydiethyleneglycoladipate diaminoanthraquinone (poly-AQ-poly) dye and unreacted polydiethyleneglycoladipate (poly).

The SORI-CID mass spectrum of the m/z=963, $n = 2$, oligomer of the synthetic dye is shown in figure 4.5.3. The signal intensity of the m/z = 963 peak was barely enough for tandem mass spectrometry, here the entire signal intensity of the monoisotopic parent ion has been fragmented and only the $^{13}C_1$ isotopomer remained. As its cyclotron frequency lay close to that of its monoisotopic analogue (the detected frequencies were 149566 and 149722 Hz respectively) the $^{13}C_1$ isotopomer would have also been expected to fragment. The absence of + $^{13}C_1$ fragment peaks can be attributed to two causes: -

1) the much lower signal intensity of the + $^{13}C_1$ parent ion, and

2) under the experimental conditions used, the excitation energy of the $^{13}C_1$ parent ion was lower. The translational energy of an ion during off-resonance irradiation is

inversely proportional to the square of the difference between the excitation

frequency and the ion's cyclotron frequency[12, 13].

$$E_{tr} = \frac{E^2 q^2 \sin^2\left(\omega_0 - \omega_{eff}\right)t/2}{4m\left(\omega_0 - \omega_{eff}\right)^2}$$

(4.5.i)

E is the applied electric field strength, q the ion's electric charge, m the mass of the ion,

t the duration of the electric field pulse, ω_0 the excitation frequency, and ω_{eff} the

effective cyclotron frequency of the ion.

/u/data/james/testLMDext_cal_blue231199/12/pdata/1
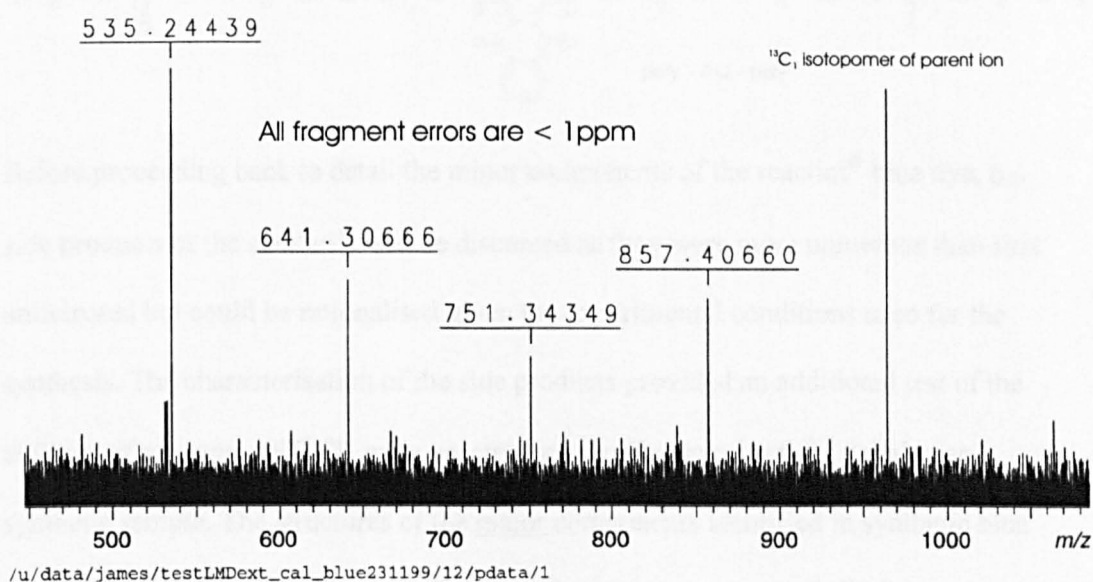
Figure 4.5.3 SORI-CID of $m/z = 963$ oligomer of synthetic dye. An internal lock mass was used to calibrate the spectrum.

The excitation was performed at 1000 Hz greater than that of the monoisotopic peak and

so the excitation frequency was 1156 Hz greater than that of the $+ \, ^{13}C_1$ peak.

Consequently the translational energy of the heavier parent ion was approximately 75%

that of the monoisotopic peak. The absence of fragment peaks and the presence of a $+$

$^{13}C_1$ parent ion peak is attributable to the heavier ions simply not possessing sufficient

internal energy to fragment.

The fragments produced by the synthetic dye were the same as those produced by the reactint blue dye except for the fragment at $m/z = 747$, however as its $(n-1)$ analogue was observed at $m/z = 531$ its absence was probably due to low signal intensity.

In the light of the above results it can be stated with certainty that the polymer adduct responsible for the $m/z = 531, 747, 963, 1179...$ series was the singly protonated poly diethylene glycol adipate diaminoanthraquinone shown below.

poly - AQ - poly
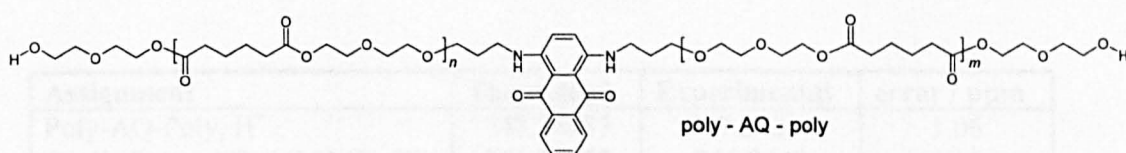
Before proceeding back to detail the minor components of the reactint® blue dye, the side products of the synthesis will be discussed as they were more numerous than first anticipated but could be rationalised given the experimental conditions used for the synthesis. The characterisation of the side products provided an additional test of the abilities of nanospray FTICR mass spectrometry to characterise fully a real-case synthetic sample. The structures of the major components identified in synthetic blue are shown below, as well as a table detailing the mass accuracies of all of the assignments. Included in appendix A.4 are close-ups of the mass spectrum shown previously detailing the assignments.

poly

cyclic poly

cyclic poly-AQ

mono poly-AQ

116
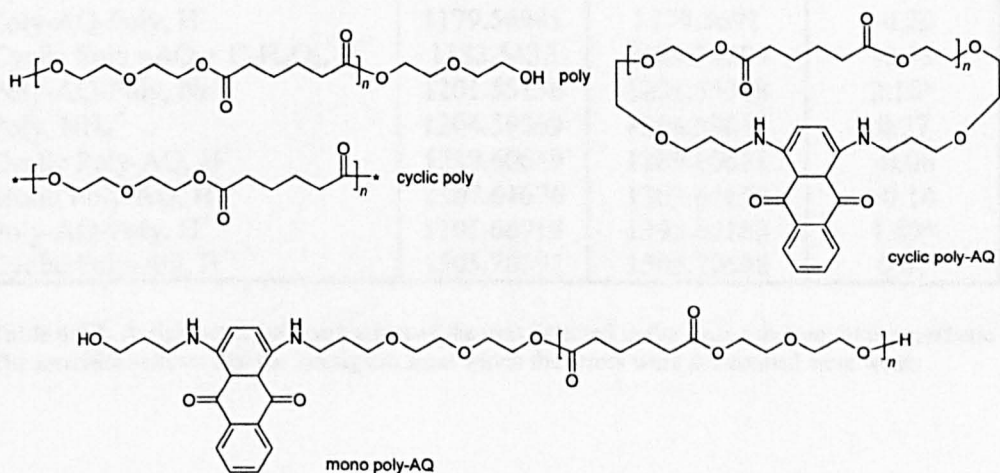
The mass accuracies in table 4.5.1 associated with the assignments were in line with the

performance expected of a 9.4 T FTICR mass spectrometer.[10] The small difference

between theoretical and measured mass permitted the assignments to be made with a

high degree of confidence. Mono-substitution of the tosyl groups (and substitution of

the mono-tosylated anthraquinone) formed the mono poly-AQ and substitution of both

tosylate groups of Ts – AQ – Ts by either end of a poly diethylene glycol adipate

molecule was responsible for the cyclic poly-AQ.

Assignment	Theoretical	Experimental	error / ppm
Poly-AQ-Poly, H^+	747.36987	747.37066	1.06
Cyclic Poly –AQ + $C_6H_6O_2$, H^+	751.34365	751.3449	1.66
Poly-AQ-Poly, Na^+	769.35181	769.35541	4.68*
Poly, NH_4^+	772.39614	772.3963	0.21
Cyclic Poly + $C_6H_6O_2$, NH_4^+	776.36993	776.37113	1.55
Cyclic Poly-AQ, H^+	857.40665	857.40658	-0.08
Cyclic Poly (-H_2O), NH_4^+	864.42236	864.4233	1.09
Mono Poly-AQ, H^+	875.41721	875.41738	0.19
Cyclic Poly-AQ, Na^+	879.38859	879.39106	2.81*
Cyclic Poly, NH_4^+	882.43292	882.43296	0.05
Cyclic Poly, Na^+	887.38832	887.38945	1.27*
Poly-AQ-Poly, H^+	963.46964	963.46947	0.77
Cyclic Poly –AQ + $C_6H_6O_2$, H^+	967.44343	967.44325	-0.18
Poly (-H_2O), NH_4^+	970.48535	970.4861	-0.19
Poly-AQ-Poly, Na^+	985.45158	985.45383	2.28
Poly, NH_4^+	988.49591	988.49562	-0.29
Cyclic Poly + $C_6H_6O_2$, NH_4^+	992.4697	992.47015	0.45
Cyclic Poly-AQ, H^+	1073.50642	1073.50551	-0.85
Mono Poly-AQ, H^+	1091.51698	1091.51762	0.59
Cyclic Poly-AQ, Na^+	1095.48836	1095.48981	1.32*
Cyclic Poly, NH_4^+	1098.53269	1098.53326	0.52
Poly-AQ-Poly, H^+	1179.56941	1179.5691	-0.26
Cyclic Poly –AQ + $C_6H_6O_2$, H^+	1183.5432	1183.54299	-0.18
Poly-AQ-Poly, Na^+	1201.55136	1201.55388	2.10*
Poly, NH_4^+	1204.59569	1204.59614	0.37
Cyclic Poly-AQ, H^+	1289.60619	1289.60611	-0.06
Mono Poly-AQ, H^+	1307.61676	1307.61658	-0.14
Poly-AQ-Poly, H^+	1395.66919	1395.67183	1.89*
Cyclic Poly-AQ, H^+	1505.70597	1505.70698	0.67

Table 4.5.1. Assignments and mass errors of the ions detected in the mass spectrum of the synthetic dye. The asterisks indicate that the ion signals from which the errors were determined were weak.

The cyclic polydiethyleneglycoladipate resulted from a competing nucleophilic pathway

as above

cyclic poly
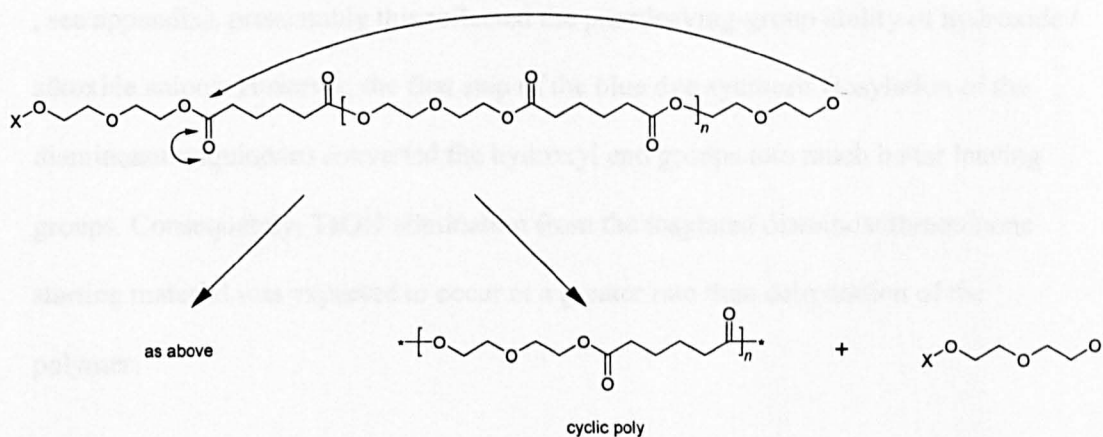
X is either a hydrogen atom or a hydrogen atom plus an integral number of repeat units. Although the above diagram is for an intramolecular reaction, intermolecular reactions would also have occurred, resulting in both chain-shortening and chain-lengthening reactions.

The poly - H_2O species in table 4.5.1 suggested elimination reactions also occurred under the experimental conditions.
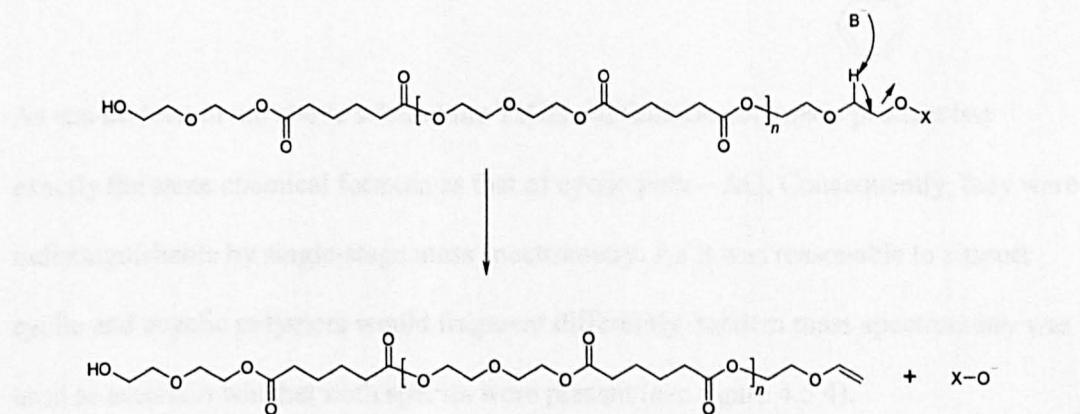
X can represent either a hydrogen or a hydrogen atom plus repeat units – therefore corresponding to loss of water or an integral number of repeat units + water, the latter being indistinguishable from water loss from a smaller oligomer.

118

The poly - H_2O was only a minor product (only one weak ion signal detected at m/z 970 , see appendix), presumably this reflected the poor leaving-group ability of hydroxide / alkoxide anions. However, the first step of the blue dye synthesis (tosylation of the diaminoanthraquinone) converted the hydroxyl end groups into much better leaving groups. Consequently, TsOH elimination from the tosylated diaminoanthraquinone starting material was expected to occur at a greater rate than dehydration of the polymer.
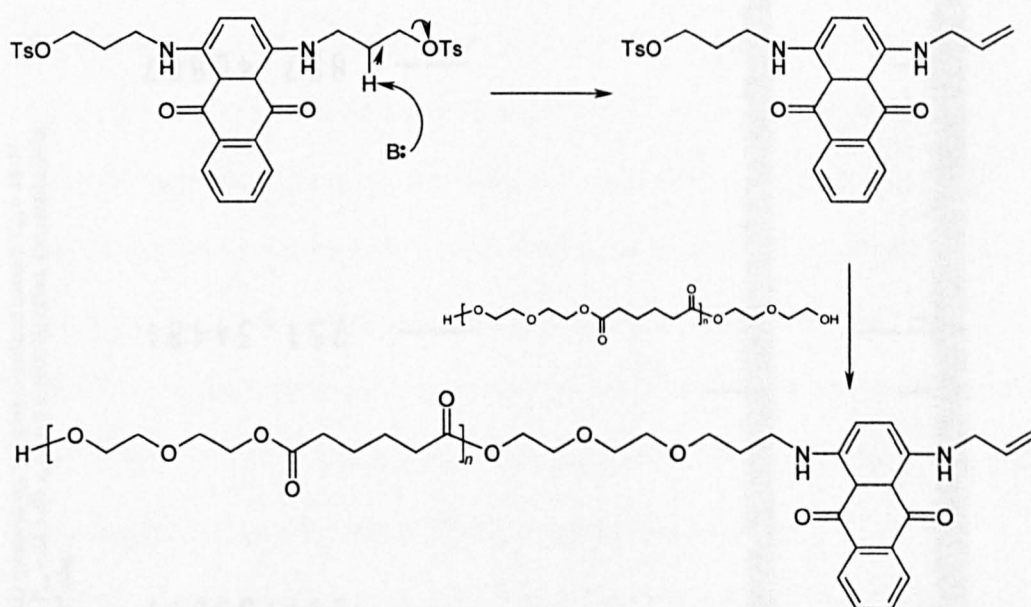
As can be seen in the above scheme the TsOH elimination polymeric product has exactly the same chemical formula as that of cyclic poly – AQ. Consequently, they were indistinguishable by single-stage mass spectrometry. As it was reasonable to suspect cyclic and acyclic polymers would fragment differently, tandem mass spectrometry was used to ascertain whether both species were present (see figure 4.5.4).

Figure 4.5.4. SORI-CID of the cyclic poly – AQ (protonated). Isolation (correlated sweep): V_{iso} = 35.07 dB, t_{iso} = 4 ms, 120 Hz safety belt. Activation: V_{act} = 28.3 dB, t_{act} = 0.5 s, 1000 Hz offset, 4 s reaction delay. Nitrogen collision gas, peak cell pressure ≈ 10^{-6} mbar.
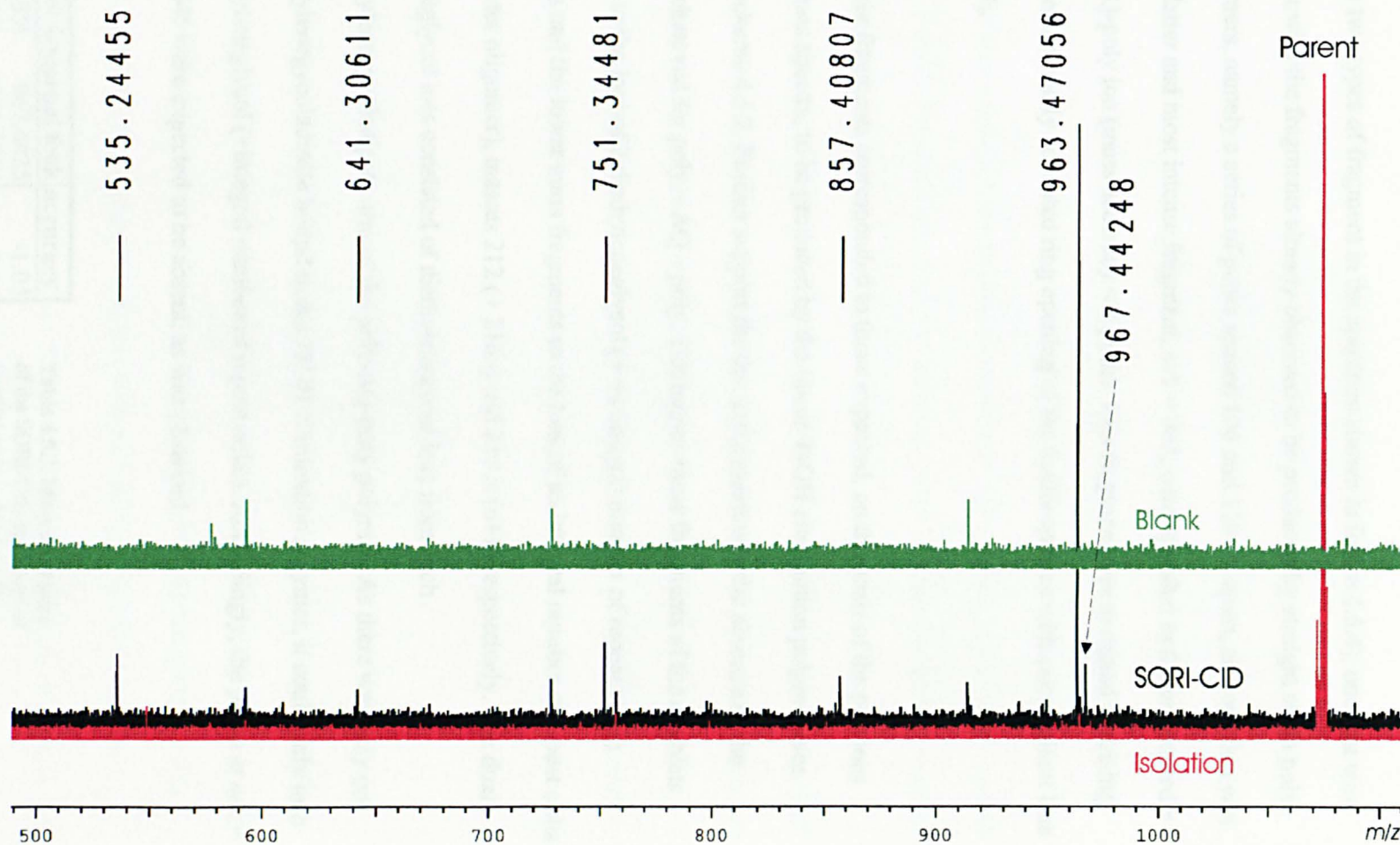
There are two types of fragment in the spectrum shown in figure 4.5.4), one that was consistent with the fragments already observed to be produced by straight chain poly-AQ polymers, namely a series of peaks spaced 106 and 110 Da apart, and one that was not. The latter and most intense fragment, m/z = 963, corresponded to the protonated n = 2 poly-AQ-poly ion (mass accuracy < 1 ppm). This fragment was assigned as arising from the collisionally activated ring opening of the cyclic species with concomitant loss of $C_6H_6O_2$.

The weaker fragments corresponded to those expected, on the basis of the previous tandem mass spectra, to be produced by the linear TsOH elimination polymer (see reaction scheme 4.3.2. Further support for this assignment was the absence of the doublets observed for poly – AQ – poly. The higher-mass fragments of the doublets were due to the loss of 2 diethyleneglycol (+ an integral number of repeat units) molecules and the lower mass fragments to the loss of an integral number of repeat units (*i.e.* a shorter oligomer), masses 212 (+ 216n) and 216 × (n+1) respectively. The dual diethyleneglycol loss consisted of diethylenegycol loss from each polydiethylenegycoladipate arm of the poly-AQ-poly polymer. As there was only one polydiethylenegycoladipate bound to the TsOH elimination polymer, it could only lose one diethyleneglycol (+integral number of repeat units). Accordingly, the peaks at m/z = 861 and 645 were expected to be absent, as was observed.

Theoretical	external lock	accuracy
967.4435	967.4425	-1.05
963.4696	963.4706	0.95
857.4067	857.4081	1.60
751.3437	751.3448	1.48
641.3069	641.3061	-1.23
535.2439	535.2446	1.21

Table 4.5.2. Mass accuracies of the SORI-CID spectrum of 'cyclic' poly – AQ (n = 2)

The final calibration technique, and the one used to produce the spectrum in figure 4.5.4, used the isolation experiment as an external lock mass. After altering *ML2* such that the measured mass of the isolation experiment matched the theoretical mass, the calibration constants were applied to the SORI-CID spectrum. The mass accuracies obtained are only slightly greater than those obtained using the parent ion of the SORI-CID spectrum as an internal lock (all < 1 ppm). As the size of the axial trapping potential (which was kept constant) and the number of ions present in the cell determine the value of *ML2*, this result indicated that most ions were retained during off-resonance collisional activation.

The above SORI-CID spectrum (figure 4.5.4) includes peaks that are unlabelled and were present in a spectrum labelled blank. The latter spectrum, taken as a last resort, was measured with the potentials applied to the atmospheric region of the nanospray source and the pneumatic gas used to push the sample out of the needle both switched off, using precisely the same pulse program. Thus these peaks were not due to the sample.

There was circumstantial evidence for TsOH elimination. In table 4.5.1 are species labelled as cyclic poly + $C_6H_6O_2$ and cyclic poly-AQ + $C_6H_6O_2$ It was very difficult to assign structures to these species without invoking a TsOH elimination product.

The high mass-accuracy obtainable using FTICR mass spectrometry permitted molecular formulae to be assigned to these peaks with a high degree of confidence (table 4.5.3).

Peak	Error / ppm	Empirical formula	DBE
751	1.66	$C_{40}H_{51}O_{12}N_2^+$	17
967	0.18	$C_{50}H_{67}O_{17}N_2^+$	19
1183	0.18	$C_{60}H_{83}O_{22}N_2^+$	21

Table 4.5.3. Mass accuracies of cyclic – poly + $C_6H_6O_2$ peaks

These chemical formula are identical to those for cyclic poly – AQ plus $C_6H_6O_2$. The

only sub species that $C_6H_6O_2$ could rationally be was

$C_6H_6O_2$, 110 Da
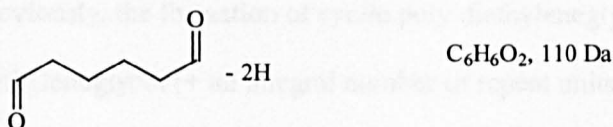
It was difficult to insert this species into the cyclic poly – AQ polymer. Opening the

cyclic species and adding $C_6H_6O_2$ would produce a species that had two unbound ends,

required two hydrogen atoms to be removed and two double bond equivalents to be

added to achieve agreement with the accurate mass measurements.
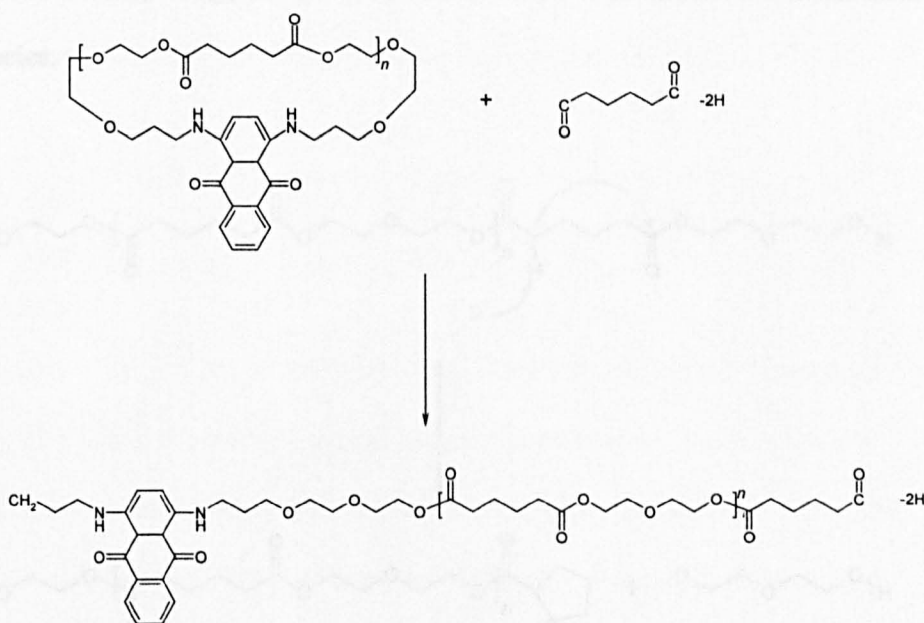
Based on the <u>above</u> structure, the only species that could satisfy the mass accuracy

criteria would possess two concentric rings. The strain involved would be prohibitive

for the polymers in question ($n = 1$–3). However, the TsOH elimination polymer

(pictured immediately below) had the same chemical formula as the cyclic structure

123
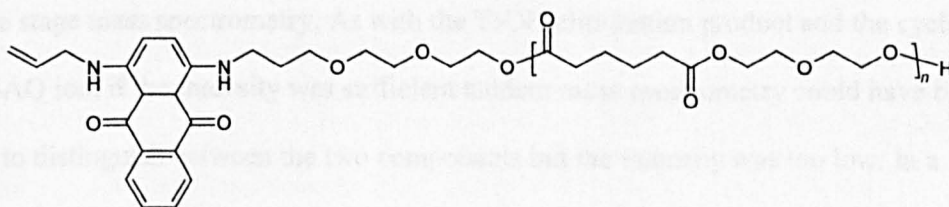
Addition of $C_6H_6O_2$ is equivalent to the loss of diethyleneglycol from the next higher oligomer. As shown previously, the formation of cyclic poly diethyleneglycol adipate involved the loss of diethyleneglycol (+ an integral number of repeat units) from its straight chain precursor. To perform such a cyclisation a nucleophile is required. The remaining nucleophilic possibility was the enolate resulting from the abstraction of the relatively acidic carbonyl α-hydrogen. As can be seen below for poly diethyleneglycol adipate, nucleophilic attack at the position marked with an asterisk would result in the effective loss of diethyleneglycol and the product has the same chemical formula as the cyclic species.
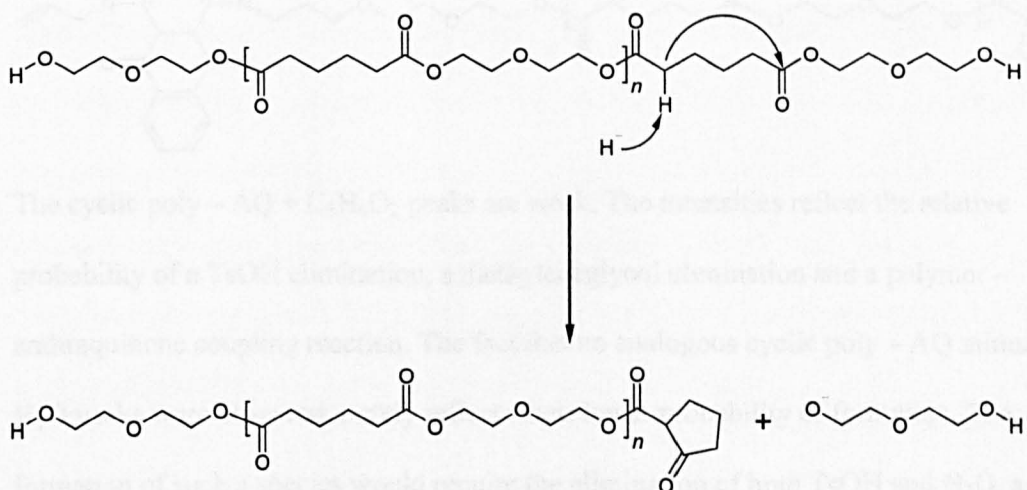
The above compound, the result of a single enolate initiated ring formation reaction, is indistinguishable from the other cyclic poly diethylene adipate shown previously by single stage mass spectrometry. As with the TsOH elimination product and the cyclic poly-AQ ion, if the intensity was sufficient tandem mass spectrometry could have been used to distinguish between the two components but the intensity was too low. In a similar manner the peak labeled cyclic poly + $C_6H_6O_2$ in table 4.5.1. resulted from the

formation of two five membered rings by the above reaction. Its low intensity and

singular appearance reflected its low probability of formation.

With regard to the formation of a five-membered ring, although other sized rings can

and will be formed studies have shown the rate of formation of a five membered ring

can be 10^6 times that of an 8 membered ring, [19, 20] the next ring size available using

the chemistry illustrated.

A product that satisfies the mass accuracy results for poly-AQ $+ C_6H_6O_2$ is that formed

by a combination of a TsOH elimination, a diethylene glycol elimination (by the above

mechanism) and a polymer anthraquinone coupling reaction, namely...
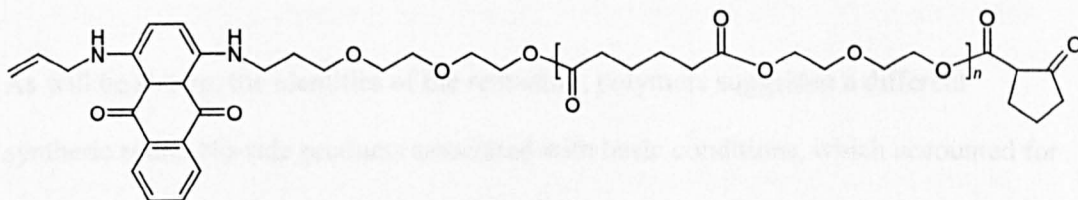
The cyclic poly $- AQ + C_6H_6O_2$ peaks are weak. The intensities reflect the relative

probability of a TsOH elimination, a diethyleneglycol elimination and a polymer –

anthraquinone coupling reaction. The fact that no analogous cyclic poly $- AQ$ minus

H_2O peaks were observed merely reflects their lower probability of formation. The

formation of such a species would require the elimination of both TsOH and H_2O, as

well as an anthraquinone polymer coupling reaction. As explained earlier, the low

probability of the dehydration step was suggested by the observation of only one small

peak for the dehydrated polymer itself.

Although the synthesis was unspecific it did serve its purpose of providing confirmation

of the $m/z = 531, 747, 963, 1179...$ series' assignment. Moreover, the lack of specificity

provided an additional stern test for the abilities of FTICR-MS to identify the

components of a complex polymeric mixture. To this end, through high mass-accuracy

125

mass spectrometry and tandem mass spectrometry, the components present in the synthetic dye were identified without the need for prior separation.

4.6   Reactint blue continued...

A theme running through the heart of the previous section is how knowledge of experimental conditions can allow educated guesses to be made regarding the identity of side-products. Although no information about synthetic blue's synthesis was available, and at the time of writing is still not available, a similar approach helped to identify all of the remaining components of the unknown reactint® blue polymeric dye.

As will be shown, the identities of the remaining polymers suggested a different synthetic route. No-side products associated with basic conditions, which accounted for almost all of synthetic blue's side products, were found in reactint® blue. The only common polymers were the two already identified (poly – AQ – poly and poly diethylene glycol adipate). The remaining polymers point to a synthesis involving the production of amine terminated poly diethylene glycol adipate.

The broadband mass spectrum of synthetic blue highlighting the polymer series present in reactint® blue is shown in figure 4.6.1, immediately followed by diagrams and tables detailing those assignments and their mass accuracies.
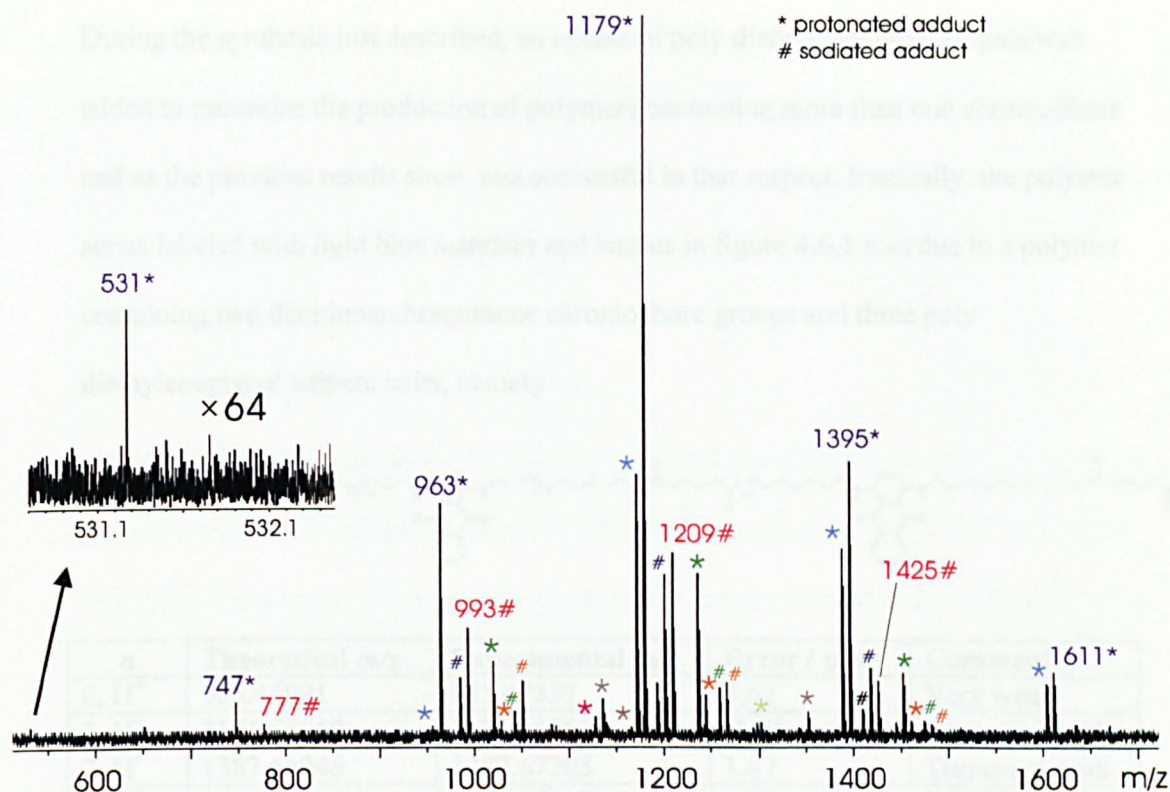
Figure 4.6.1. Broad band mass spectrum (previously shown) of reactint® blue detailing the different polymer series. The peak positions of the two series already assigned are included for clarity.

Each colour represents a different polymer series, an asterisk a protonated adduct and a hash a sodiated adduct. The series for which the nominal masses are given are the previously assigned protonated poly-AQ-poly (22 *m/z* units to higher mass is its sodiated adduct, labelled with an asterisk coloured the same blue as the figures) and sodiated polydiethyleneglycoladipate.

There are at least 7 additional polymers present in reactint blue, many of which are detected as both protonated and sodiated adducts, the former being more intense if present. As will be shown, all of the protonated species possessed a basic amino group.

During the synthesis just described, an excess of poly diethyleneglycol adipate was added to minimize the production of polymers containing more than one chromophore and as the previous results show was successful in that respect. Ironically, the polymer series labeled with light blue asterisks and hashes in figure 4.6.1 was due to a polymer containing two diaminoanthraquinone chromophore groups and three poly diethyleneglycol adipate units, namely
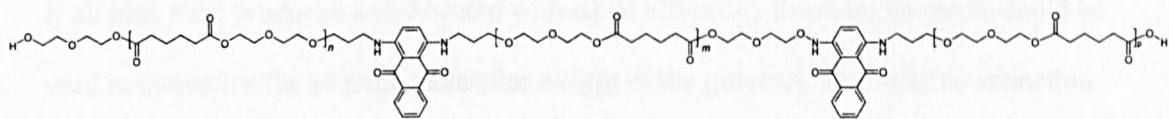
n	Theoretical m/z	Experimental m/z	Error / ppm	Comment
0, H^+	955.46991	955.47337	3.62	Very weak
1, H^+	1171.56969	1171.56851	-1.01	Truncated peak
2, H^+	1387.66946	1387.67205	1.87	Truncated peak
3, H^+	1603.76924	1603.77018	0.59	Truncated

Table 4.6.1. Mass accuracies of poly – AQ – poly – AQ – poly

This polymer can be envisaged as being produced by the poly-AQ-poly mono-chromophore dye acting as the basic polydiethyleneglycoladipate polymer (or derivatised polymer depending on the synthetic route used) during the synthesis. The extinction coefficient of this bi-chromophoric polymer was expected to be considerably greater than that of the mono-chomophoric poly – AQ – poly. Although there were two chromphoric centres, the extinction coefficient of the former would not simply be twice that of the latter. The bound polymers act to dilute the chromophores. In poly – AQ – poly there are 2 polymer units per diaminoanthraquinone chromophore, whereas for poly-AQ-poly-AQ-poly there are 1.5. Assuming the two chromophores of the bi-chromophoric polymer act independently, then depending on the average masses of the polymers the extinction coefficient of the above compound would lie between 1.5 and 2 times that of poly-AQ-poly. In the unlikely scenario that the mass of the chromophore » the mass of the polymer then $\varepsilon_{bi} \approx 2 \times \varepsilon_{mono}$. Alternatively, if the mass of the polymer

was much bigger than that of the chromophore $\varepsilon_{bi} \approx 1.5 \times \varepsilon_{mono}$. A quick look at the above tables or the mass spectra shows that neither limiting scenario is in effect. The average mass of the polymer is comparable to that of the chromophore and the relative extinction coefficient of the bi-chromophoric polymer will depend on the polymer's average molecular weight.

If all ions were produced and detected with equal efficiency the mass spectrum could be used to determine the average molecular weight of the polymer. The relative extinction coefficient of the bi-chromophoric polymer could then be estimated. However, it is clear that biases are present as all polymer distributions show a maximum at $m/z \approx 1200$ despite this corresponding to the $n = 3$ oligomer of poly-AQ-poly and $n = 1$ of poly-AQ-poly-AQ-poly. The highest signal intensities were generally obtained for the 963, 1179 peaks of the mono-chromophore polymer, corresponding to 2 and 3 repeat units, respectively.

Further evidence for the above di-chromophore assignment was twofold, the first being the absence of analogous peaks below $m/z = 955$ ($n + m = 0$). Additionally, the height of the poly-AQ-poly-AQ-poly polymer relative to that of the nearby poly-AQ-poly peak, for example 955 relative to 963, gradually increased with increasing m/z, which is behaviour indicative of a polymer possessing a much heavier 'end' group.

The next three assigned polymer series provided evidence for a synthetic route different to that used to produce synthetic blue. Derivatised polydiethyleneglycoladipate species, not used to produce nor detected in synthetic blue, were observed in reactint® blue. For example the green series in the above spectra was due to the mono propylaminated poly-AQ-poly shown below
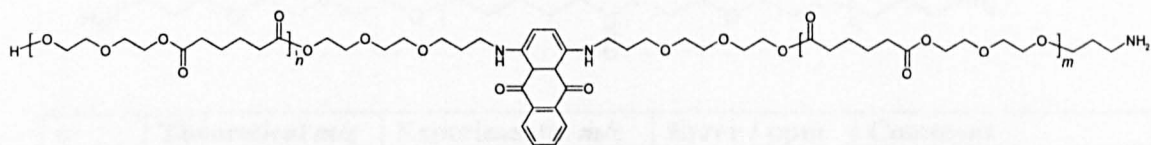
n	Theoretical m/z	Experimental m/z	Error / ppm	Comment
2, H^+	1020.52749	1020.52443	-3.0	truncated peak
2, Na^+	1042.50943	1042.50922	-0.2	truncated peak
3, H^+	1236.62726	1236.62437	-2.3	truncated peak
3, Na^+	1258.60921	1258.60981	0.5	truncated peak
4, H^+	1452.72704	1452.72272	-3.0	truncated peak

Table 4.6.2. Mass accuracies of mono-propyl aminated poly – AQ – poly. Truncated refers to a peak that is described by too few data points and the top of which is flat, this occurs with weak ion signals.

The propylamine group was identical to that attaching polydiethyleneglycoladipate to the anthraquinone chromophore. Another two propylaminated poly diethylene glycol adipate polymers were found in reactint® blue, polymers that were be expected if the polymers were aminated prior to addition to the anthraquinone chromophore. The orange series corresponded to the mono-propylaminated polymer shown below
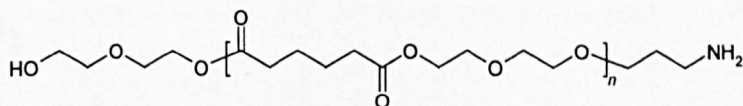
n	Theoretical m/z	Experimental m/z	error / ppm	Comment
4, H^+	1028.52721	1028.53141	4.08	very weak
4, Na^+	1050.50916	1050.50600	-3.01	weak, truncated
5, H^+	1244.62699	1244.62139	-4.5	weak, truncated
5, Na^+	1266.60893	1266.61483	4.66	weak, truncated
6, H^+	1460.72676	1460.73261	4	weak, truncated
6, Na^+	1482.70871	1482.71568	4.7	weak, truncated

Table 4.6.3. Mass accuracies of mono-propyl aminated polydiethyleneglycoladipate.

and the single light green asterisked peak corresponded to the bis-propyl aminated polymer shown below
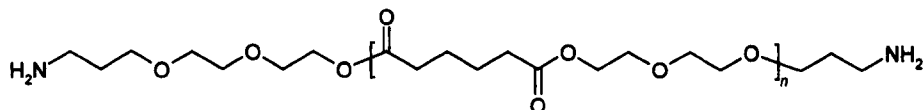
n	Theoretical *m/z*	Experimental *m/z*	Error / ppm	Comment
5, H$^+$	1301.68484	1301.68098	-2.97	Very weak, truncated

Table 4.6.4. Mass accuracy of the bis-propyl aminated polydiethyleneglycoladipate peak.

In light of the fact that there were no side-products induced by bases, as observed in synthetic blue, and the derivatised polydiethyleneglycoladipate species were observed, it was concluded that a different synthetic route was used to produce reactint® blue. The above derivatised polymers were not due to in-source fragmentation of larger polymers as no similar peaks were observed if synthetic blue was sprayed under identical conditions. Additionally, the source conditions were gentle (low capillary-exit voltage and low skimmer voltage, ≈ 120 V and 1 V, respectively) such that few highly energetic ions were produced and trapped (the skimmer acts as one of the hexapole's trapping electrodes[21]).

Finally, three minor components were present that can be attributed to a minor contaminant in the diethyleneglycol used to synthesize the polydiethyleneglycoladipate. Polydiethyleneglycoladipate polymers missing one ethyleneglycol unit were observed. For example the peak labeled with the brown asterisk in figure 4.6.1 was due to polydiethyleneglycoladipate missing one ethylene glycol unit, namely
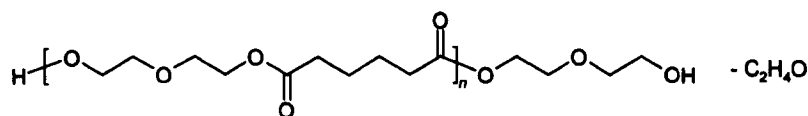
n	Theoretical *m/z*	Experimental *m/z*	Error / ppm	Comment
5, Na$^+$	1165.52487	1165.53208	-0.6	weak, truncated

Table 4.6.5. Mass accuracy of the polydiethyleneglycoladipate missing one ethylene glycol unit peak.

Reflecting the greater intensities of the poly – AQ – poly peaks, the poly – AQ – poly species missing an ethyleneglycol unit were significantly more intense and more numerous than the polydiethyleneglycoladipate – C_2H_4O signals described above. The two peaks labeled with black asterisks in figure 4.6.1 corresponded to poly-AQ-poly missing an ethyleneglycol unit. Namely
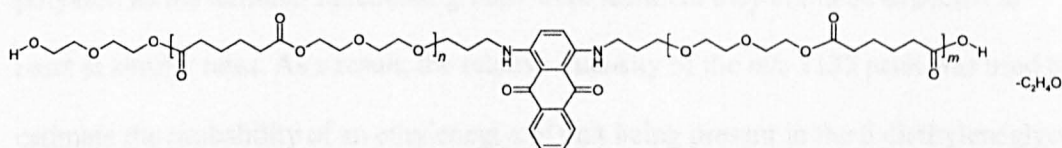
n	Theoretical *m/z*	Experimental *m/z*	Error / ppm	Comment
3, H$^+$	1135.54320	1135.53839	-4.2	Very weak, truncated
4, H$^+$	1351.63661	1351.64297	-4.7	Very weak, truncated

Table 4.6.6. Mass accuracy of the poly – AQ – poly missing an ethyleneglycol unit peaks.

Finally, the solitary peak labelled with a pink asterisk corresponded to the analogous di-chromophoric polymer missing an ethyleneglycol unit, namely
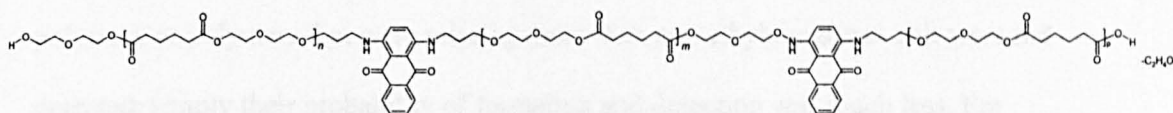
n	Theoretical *m/z*	Experimental *m/z*	Error / ppm	Comment
1, H$^+$	1127.54347	1127.54280	-0.6	Very weak, truncated

Table 4.6.7. Mass accuracy of the poly – AQ – poly – AQ – poly missing an ethyleneglycol unit peak.

The most probable cause of the polymers missing an ethyleneglycol unit was a minor contaminant in the diethyleneglycol used to produce the polydiethyleneglycoladipate. A minor ethyleneglycol contaminant would have resulted in the polymers detected. The relative intensity of the *m/z* 1135 ethyleneglycol light poly-AQ-poly oligomer, with

respect to the complete poly-AQ-poly oligomer at m/z 1179, was used to estimate the proportion of ethyleneglycol in the diethyleneglycol used to produce the polyester. Any ion transfer bias between the two ions was expected to be small. The instrument was tuned such that the ions, which were separated by m/z 44, were situated in the center of the ion distribution. Any ion formation bias was also expected to be small as both ions were structurally and chemically very similar. As will be shown in the next chapter, for a specific charge state of a specific polymer, the relative ionization efficiency was a smooth function of the polymer size. With regards to formation of the poly – AQ – poly polymer, as the terminal functional groups were identical they could be expected to react at similar rates. As a result, the relative intensity of the m/z 1135 peak was used to estimate the probability of an ethyleneglycol unit being present in the 5 diethyleneglycol units present in the m/z 1179 ion, and the relative concentration (more correctly, relative rate of reaction) of the ethyleneglycol present in the diethyleneglycol sample.

The relative intensity of the m/z = 1135 peak, with respect to the m/z = 1179 peak, was 0.073. Accordingly the proportion of ethyleneglycol in the diethyleneglycol was estimated to be 0.014. It is readily apparent why ethyleneglycol light propylaminated polymers or polymers that were missing more than one ethyleneglycol unit were not detected: simply their probability of formation and detection was much less. For example, the n = 3 poly-AQ-poly polymer having two ethyleneglycol units instead of two diethylene glycol units was calculated to be approximately 500 times less intense than poly – AQ – poly.

Summarizing - reactint® blue consisted of nine (detected) polymers based on a diethyleneglycoladipate repeat unit and a diaminoanthraquinone chromophore, the signals from which covered a high dynamic range. Anthraquinone based dyes are well established and several mass spectrometric studies have been published, however these

have been principally concerned with sulphonated dyes that were not bound to a polymer chain[22, 23].

Under the experimental conditions used the dominant species was poly – AQ – poly. The following minor polymeric adducts were detected: the bi-chromophoric polymer poly – AQ – poly – AQ – poly, basic polydiethyleneglycoladipate, and both the propylaminated and ethyleneglycol-light analogues of poly – AQ – poly, poly – AQ – poly – AQ – poly and polydiethyleneglycoladipate. The chemical structures of the nine polymers found in reactint® blue are

134
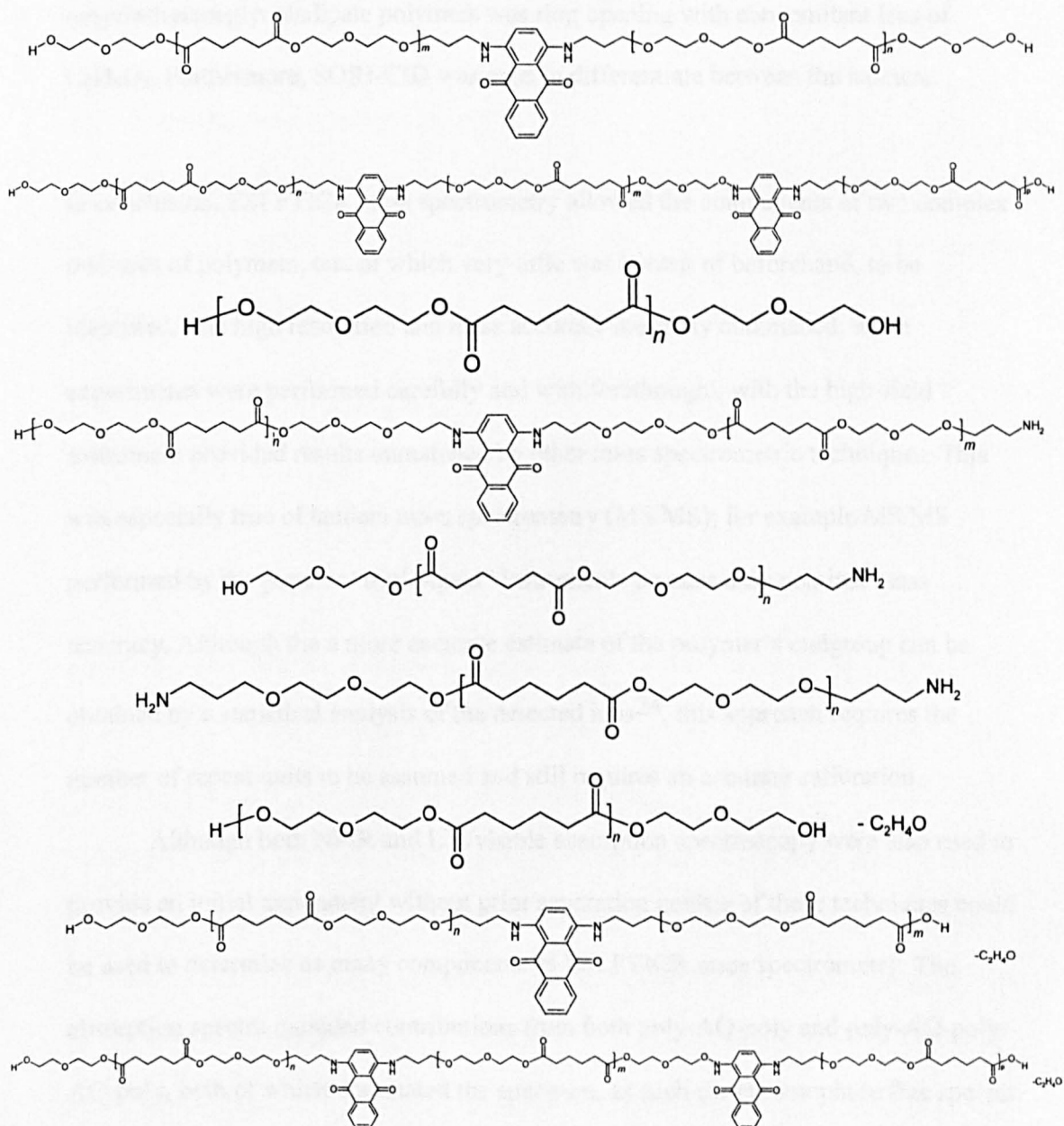
The fragments produced by SORI-CID confirmed the two-armed structure of poly –AQ – poly. Furthermore, the fragments obtained were dependent on the nature of the adduct formed. In each the production of shortened oligomers could be described by a charge remote mechanism[16] and, when the adduct involved a non-specific charge site, a fragmentation could be described by a charge-induced McLafferty rearrangement[15].

Finally, the characterization of the 'cyclic' poly – AQ produced in the synthesis provided the finding that the overwhelming fragmentation pathway followed by cyclic polydiethyleneglycoladipate polymers was ring opening with concomitant loss of $C_6H_6O_2$. Furthermore, SORI-CID was used to differentiate between the isomers.

In conclusion, ESI FTICR mass spectrometry allowed the components of two complex mixtures of polymers, one of which very little was known of beforehand, to be identified. The high resolution and mass accuracy routinely obtainabed, when experiments were performed carefully and with forethought, with the high-field instrument provided results unmatched by other mass spectrometric techniques. This was especially true of tandem mass spectrometry (MS/MS); for example MS/MS performed by the popular "triple-quad" instruments possess only nominal mass accuracy. Although the a more accurate estimate of the polymer's endgroup can be obtained by a statistical analysis of the detected ions[24], this approach requires the number of repeat units to be assumed and still requires an accurate calibration.

Although both NMR and UV/visible absorption spectroscopy were also used to provide an initial assignment without prior separation neither of these techniques could be used to determine as many components as ESI FTICR mass spectrometry. The absorption spectra included contributions from both poly-AQ-poly and poly-AQ-poly-AQ-poly, both of which dominated the spectrum, as such the chromophore free species

could not be detected. Additionally, the ethyleneglycol-missing polymers would be effectively indistinguishable. With regard to NMR, although signals from the chromophore and the repeat unit could be resolved and detected, the chromophore peaks, like the absorption spectrum, included contributions from all chromophore-containing polymers. Moreover, the repeat unit peaks contained contributions from all polymers. Again, the ethyleneglycol missing polymers would be hidden under the main peaks.

Summarizing, ESI FTICR mass spectrometry permitted confident assignment of all detected peaks <u>without the need for prior fractionation</u>.

4.7. Calibration and space charge shifts

For ions of similar intensity, such that they experience similar space charge fields, inter-ion-packet repulsion leads to a reduction of the Lorenz force, which serves to reduce the ion's effective cyclotron frequency by a constant factor, Δv.[1, 25]

As shown on page 26 the *m/z* of an ion is related to its cyclotron frequency through the relationship

$$m/z = \frac{ML1}{(freq. + ML2)} \qquad (4.7.i)$$

where *ML1* and *ML2* are calibration constants that are determined by the magnetic field strength and the static electric field strength (due to the electrostatic axial trapping field and the presence of other ions in the cell), respectively.

If the space charge experienced during the calibration experiment is different to that during the sample experiment the value of *ML2*, the calibration constant that accounts for the frequency shifts due to the presence of other ions and the trapping potential, will be incorrect. As a result, the sample ion's effective cyclotron frequency will be shifted by a constant frequency, defined by the difference between the applied *ML2* value and

its 'true' value. This constant frequency shift between the two experiments will cause the relative mass errors to be larger for ions of larger m/z (lower frequency, larger relative shift).

Using data in the calibration file the relationship between mass and frequency

$$(m/z)_{cal,i} = \left(\frac{ML1_{cal}}{V_{cal,i} + ML2_{cal}} \right) \qquad (4.7.\text{ii})$$

is optimised to yield the mass calibration constants, $ML1_{cal}$ and $ML2_{cal}$. If this equation is then applied to another experiment where the space - charge is different, the difference between the experimentally determined mass and that predicted by the calibration equation is given by

$$(m/z)_{exp} - (m/z)_{pred} = \left(\frac{ML1_{true}}{V_{exp} + ML2_{true}} \right) - \left(\frac{ML1_{cal}}{V_{exp} + ML2_{cal}} \right) \qquad (4.7.\text{iii})$$

$(m/z)_{exp}$ and $(m/z)_{pred}$ are the accurate mass – to – charge ratio of the ions determined by experiment and that predicted by the mass calibration equation, respectively. v_{exp} is the measured cyclotron frequency of the ion. $ML1_{true}$ and $ML2_{true}$ are the 'true' and unknown calibration constants for the ions (true in the sense that they are the values required for the above calibration relationship to estimate the ion's mass correctly). Over the course of several days the magnetic field of a super-conducting magnet could be considered to be constant, consequently the magnetic field term in the above equation, $ML1$, was also constant. Note that $ML1$ was not dependent on space charge, see page 26. Accordingly

$$(m/z)_{exp} - (m/z)_{pred} = ML1 \times \left[\frac{ML2_{cal} - ML2_{true}}{\left(v_{exp} + ML2_{true} \right)\left(v_{exp} + ML2_{cal} \right)} \right] \qquad (4.7.\text{iv})$$

$$= ML1 \frac{\Delta ML2}{\left(v_{exp} + ML2_{true} \right)\left(v_{exp} + ML2_{cal} \right)}$$

Note this equation communicates the internal lock mass method, through minimising

the disagreement between the experimentally determined mass and the theoretical mass

of a known ion, i.e. the parent ion, $\Delta ML2$ and hence the true value of $ML2$ was be

obtained and the entire experiment effectively calibrated. The value of $ML1$ and of

$ML2_{cal}$ was obtained from a standard calibration experiment

As $v_{exp} \gg ML2$ (under typical operating conditions $ML2 \approx 20 - 30$ Hz and the measured

cyclotron frequency, v_{exp}, is 100 KHz or more, for example the measured cyclotron

frequency of the m/z 993 ion was approximately 145 KHz) the above equation reduces

to

$$(m/z)_{exp} - (m/z)_{pred} = ML1 \frac{\Delta ML2}{v_{exp}^2} \qquad (4.7.v)$$

The mass calibration equation can be rearranged and approximated to

$$v_{exp} = \frac{ML1}{m/z} - ML2 \approx \frac{ML1}{m/z} \qquad (4.7.vi)$$

as $ML2$ is still relatively small ($ML1 \approx 144276800$ u e^{-1} Hz, where u and e represent

atomic mass units and elementary charge, respectively) . Therefore

$$\Delta(m/z) = \frac{\Delta ML2}{ML1} \times (m/z)^2 \qquad (4.7.vii)$$

In terms of relative mass errors

$$\frac{\Delta(m/z)}{(m/z)} = \frac{\Delta ML2}{ML1} \times (m/z) \qquad (4.7.viii)$$

This expression accounts for the observed linear dependence (see figure 4.3.8). The

gradient of the best-fit line can be used to estimate the difference in $ML2$ values that

best characterises the calibration and sample experiments. The gradient of the best-fit

line shown in figure 4.3.8 was 1.04×10^{-8} u^{-1} e, leading to a value for $\Delta ML2 = 1.49$ Hz.

Inspection of figure 4.3.8. reveals that the ions of intermediate m/z appeared to follow a linear relationship with a smaller gradient. This can be seen more clearly in figure 4.7.1, which displays the 'individual frequency' errors for each ion. The average frequency errors of the innermost peaks, which displayed the constant frequency errors required for this approach (determined by fitting a straight line through the innermost ions, m/z = 500 – 1000) was 1.18 Hz.
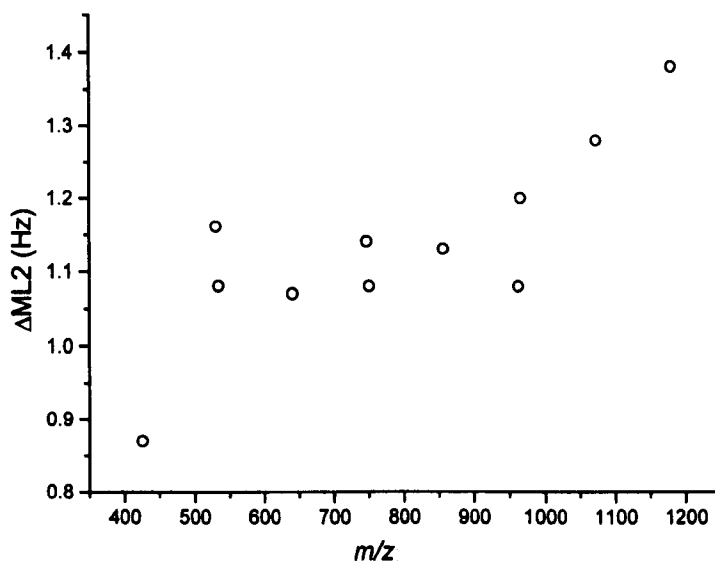
Figure 4.7.1. Individual frequency errors for the innermost peaks of the SORI-CID spectra of poly – AQ – poly shown in figure 4.3.7.

In most cases only the identity of the parent ion can be assumed (or guessed). The parental lock mass method referred to earlier can be used to fine – tune a spectrum through altering $ML2$ such that the parent ion's measured m/z matches the theoretical value. As can be seen in, table 4.3.3. this estimate of $\Delta ML2$ improved the mass accuracies greatly. The value of $ML2$ was decreased by 1.38 Hz.

Nevertheless, the above approach demonstrates that even with a poor calibration (more correctly an incorrect estimate of $ML2$) the mass errors associated with correct assignments will increase with increasing m/z, from which an estimate of $\Delta ML2$ and hence the true value of $ML2$ can be obtained.

Inspection of table 4.3.3 revealed that the relative mass errors of all of the fragment ions was positive, because the 1.38 Hz shift required for the parent ion was greater than that required for the fragments. As can be seen in figure 4.8.1 the individual frequency error for the parent ion was slightly larger than that for most of the fragment ions. As can be seen in table 4.7.1. if $\Delta ML2 = 1.18$ Hz was used, the value obtained from the central individual frequency errors (see page 108), the mass accuracies of the fragment ions were comparable to those obtained from a self-calibration (in which the two calibration constants are varied to minimise mass errors).

	$\Delta ML2 = 1.18$ Hz		Self-calibration	
Theoretical	Measured	Error	Measured	Error
425.2071	425.2075	0.91	425.2074	0.60
531.2701	531.2701	0.10	531.2700	-0.09
535.2439	535.2441	0.39	535.2440	0.21
641.3069	641.3072	0.49	641.3071	0.43
747.3699	747.3700	0.22	747.3701	0.26
751.3437	751.3441	0.55	751.3441	0.61
857.4066	857.4069	0.35	857.4071	0.53
963.4696	963.4703	0.70	963.4706	1.00
967.4434	967.4433	-0.13	967.4436	0.20
1073.5064	1073.5060	-0.41	1073.5061	-0.29
1179.5694	1179.5675	-1.59	1179.5682	-1.01

Table 4.7.1. Mass accuracies obtained by decreasing *ML2* by 1.81 Hz and those obtained using a self-calibration.

The constant frequency shifts required for a parental lock approach require all ions to be of approximately similar intensity. As the space charge experienced by one ion packet is due to the other ions present in the cell, if one ion packet contributes much more than the rest then the space charge it experiences will be different. Nevertheless, an approach such as that undertaken above can be used to investigate whether poor mass accuracies are due to a space charge discrepancy, and then to correct for the discrepancy.

References

(1)   Francl, T. J.; Sherman, M. G.; Hunter, R. L.; Locke, M. J.; Bowers, W. D.; McIver, R. J. *Int. J. Mass Spectrom. Ion Proc.* **1983**, *54*, 189-199.

(2)   Jeffries, J. B.; Barlow, S. E.; Dunn, G. H. *Int. J. Mass Spectrom. Ion Proc.* **1983**, *54*, 169-187.

(3)   Ledford Jr, E. B.; Ghaderi, S.; White, R. L.; Spencer, R. B.; Kulkarni, P. S.; Wilkins, C. L.; Gross, M. L. *Anal. Chem.* **1980**, *52*, 463-468.

(4)   Ledford Jr, E. B.; Rempel, D. L.; Gross, M. L. *Anal. Chem.* **1984**, *56*, 2744-2748.

(5)   Wang, T.-C. L.; Marshall, A. G. *Int. J. Mass Spectrom. Ion Proc.* **1986**, *68*, 287-301.

(6)   Wang, M.; Marshall, A. G. *Int. J. Mass Spectrom. Ion Proc.* **1988**, *86*, 31-51.

(7)   Chen, L.; Cottrell, C. E.; Marshall, A. G. *Chemometrics and Intelligent Lab. Syst.* **1986**, *1*, 51.

(8)   Nikolaev, E. N.; Miluchihin, N. V.; Inoue, M. *Int. J. Mass Spectrom. Ion Proc.* **1995**, *148*, 145-157.

(9)   Peurrung, A. J.; Kouzes, R. T. *Int. J. Mass Spectrom. Ion Proc.* **1995**, *145*, 139-153.

(10)   Shi, S. D.-H.; Drader, J. J.; Frietas, M. A.; Hendrickson, C. L.; Marshall, A. G. *Int. J. Mass Spectrom.* **2000**, *195/196*, 591-598.

(11)   Foucher, D. A.; Sacripante, G. G.; Breton, M. P.; Burns, P. A. ; Xerox Corporation: United states, 1998.

(12)   Heck, A. J. R.; Koning, L. J. d.; Pinkse, F. A.; Nibbering, N. M. M. *Rapid Comm. Mass Spectrom.* **1991**, *5*, 406-414.

(13)   Gauthier, J. W.; Trautman, T. R.; Jacobsen, D. B. *Anal. Chim. Acta* **1991**, *246*, 211-225.

(14)   Koster, S.; Duursma, M.; Boon, J.; Nielen, M.; Koster, C. d.; Heeren, R. ,
        University of Warwick 1999.

(15)   Koster, S.; Duursma, M. C.; Boon, J. J.; Nielen, M. W. F.; Koster, C. G. d.;
        Heeren, R. M. A. *J. Mass Spectrom.* **2000,** *35,* 739-748.

(16)   Gross, M. *Int. J. Mass Spectrom.* **2000,** *200,* 611-624.

(17)   Cohen, L. R. H.; Hercules, D. M.; Karakatsanis, C. G.; Rieck, J. N. *Macromol.*
        1995, *28,* 5601-5608.

(18)   Dua, S.; Bowie, J. H.; Cerda, B. A.; Wesdemiotis, C. *J. Chem. Soc. Perkin
        Trans. 2* **1998,** 1443-1448.

(19)   Galli; Illminati; Mandolini; Tamborra *J. Am. Chem. Soc.* **1977,** *99,* 2591.

(20)   Mandolini, J. *J. Am. Chem. Soc.* **1978,** *100,* 550.

(21)   Palmblad, M.; Hakansson, K.; Hankansson, P.; Feng, X.; Cooper, H.;
        Giannakopulos, A. E.; Green, P. S.; Derrick, P. J. *Eur. J. Mass Spectrom.* **2000,**
        6, 267-275.

(22)   Richardson, S. D.; McGuire, J. M.; Thruston Jr, A. D.; Baughan, G. L. *Org.
        Mass Spectrom.* **1992,** *27,* 289-299.

(23)   Sullivan, A. G.; Gaskell, S. J. *Rapid Comm. Mass Spectrom.* **1997,** *11,* 803-809.

(24)   Koster, S.; Duursma, M. C.; Boon, J. J.; Heeren, R. M. A. *J. Am. Soc. Mass
        Spectrom.* **2000,** *11,* 536-543.

(25)   Easterling, M. L.; Mize, T. H.; Amster, I. J. *Anal. Chem.* **1999,** *71,* 624-632.

5 Polymer distributions and charge state distributions.

5.1. Introduction

In electrospray ionisation (ESI) the final highly charged droplets, from which the gas

phase ions are liberated, result from a cascade of solvent evaporation and droplet

fission[1]. In each droplet fission event the charge-to-mass ratio increases in the offspring

droplets relative to the parent droplet which produced them, but the overall repulsive

force of the like charges near the droplet surfaces is attenuated because the charge is

spread over a larger total surface area[1]. Inter ion repulsion causes the ions to

concentrate near the surface of the droplets and whilst the fission event decreases this

repulsion it also acts to increase the concentration of the ions. In a similar manner,

surface-active analytes are also concentrated and is the cause of the experimental

finding that surface-active compounds give higher signal intensity[1-3].

Accordingly, the electrospray response for an analyte ion in the presence of an

electrolyte has been modelled in terms of a partitioning between the surface layer and

the interior of the droplet. The former ions are those detected in a mass spectrum (if

successfully transferred to the mass analyser)[4]. In keeping with the general consensus

that the yield of gas-phase ions reflects the desorption coefficient and the surface

concentration of ions *in the final small droplets prior to desorption*, Cook and workers

recently extended the model further to include the effects of electrophoretic mobility on

the relative signal intensities of analyte ions[5]. The extended model was able to account

qualitatively for the field dependence of the relative intensities of different

electrophoretic mobilities. Although not stated explicitly, this mechanism provides a

useful explanation of the observation reported by Fenn *et al.* and observed in this

laboratory, that the relative intensities of the charge states of a polymer are dependent

on the value of the applied field.[6]

The partition coefficient, K_A, for the equilibrium between the droplet surface and the droplet interior was shown to be dependent on the applied field, E, and the intrinsic surface activity, $K_{A, sa}$, of the analyte ion.[5]

$$(A^+X^-)_i \rightleftharpoons (A^+)_s + (X^-)_i \qquad K_A = \left. [A^+]_s [X^-]_i \middle/ [A^+X^-]_i \right.$$ (5.1.i)

$$K_A = f_A \left(K_{A, sa} + \frac{a\mu_A Et}{V_s} \right)$$

a is the cross-sectional area of the analyte, μ_A is the ionic mobility, V_s is the volume of the droplet surface layer, t is the time and f_A is the activity coefficient of the ion

$$[A]_i = f_A C_A$$ (5.1.ii)

$[A]_i$ is the effective concentration of A (its activity) and C_A is the bulk concentration of A.

Clearly, the cross-sectional area, the surface layer volume, the field and the concentration of the analyte are not static but complicated functions of time. Not only do solvent evaporation and droplet subdivision occur as the droplet moves away from the needle toward the field - free region near the counter-electrode, but the self-developed coulombic field will change in response to charge separation (which will tend to offset the applied field) and in response to the droplet's changing size.[5] Nevertheless, the parametric dependence (see equation 5.1.iii) for the two-component system agreed qualitatively with experimental results.

$$\frac{C_{A,s}(t)}{C_{B,s}(t)} = \frac{K_A C_A(t)}{K_B C_B(t)} \approx \frac{f_A [V_s K_{A,sa} + a\mu_A Et] C_A(t)}{f_B [V_s K_{B,sa} + a\mu_B Et] C_B(t)}$$ (5.1.iii)

However, Cook and workers based their model on the simpler model of Enke[4] in which the surface concentration of the analyte was assumed to be small compared to the analytical concentration:

$$C_{A,s} = \frac{C_A K_A}{C_A K_A + C_B K_B}[Q]$$

(5.1.iv)

$[Q]$ is the concentration of excess charge in the droplet. When this assumption was not used a more complicated expression was obtained for the equilibrium surface concentration of the analyte

$$C_{A,s}^2\left(\frac{K_A}{K_B}-1\right) - C_{A,s}\left([Q]\left(\frac{K_A}{K_B}-1\right) + C_A\frac{K_A}{K_B} + C_B\right) + C_A[Q]\frac{K_A}{K_B} = 0$$

(5.1.v)

This expression was able to describe the ion signal dependence on concentration that the simpler equation was unable to replicate[4, 7]. Although the function obtained, equation 5.1.iii, was not applicable over as wide a concentration range the effect of the applied field was predicted.

The equation derived for the equilibrium surface concentration of an analyte in a mixture of a three analytes (previous equations were for a two-component mixture) was yet more complicated

$$C_{A,s}^3[K_C - K_A + K_B(1 - K_C/K_A)] + C_{A,s}^2\left[\begin{array}{l} C_A(2K_A - K_B - K_C) + C_C(K_A - K_B) + \\ C_B K_B(1 - K_C/K_A) + [Q](K_A - K_C - K_B(1 - K_C/K_A)) \end{array}\right] -$$

$$C_{A,s}C_A[[Q](2K_A - K_B - K_C) + C_C K_A + C_A K_A + C_B K_B] + C_A^2[Q]K_A = 0$$

(5.1.vi)

When the concentrations of two of the analytes (the third being a background ion) are similar and the surface activities are similar, the equations predict similar ion signal / concentration profiles. Such an example would be two consecutive oligomers of a polymer. Furthermore, these two species (same charge state) would be expected to have

145

similar ionic mobilities. Consequently the electrospray ionization response is expected to be similar for two ionic oligomers (of the same charge) that differ by a single repeat unit, independent of the applied field.

Taking this general result further and given the similarities of the species contained in a polymer distribution, the electrospray response of a polymer (of a single charge state) would be expected to fairly constant across a narrow polymer distribution. Of course the response would change if the charge state of the polymer is not constant across the distribution.

Synthetic polymers can present a challenging scenario for ESI because their solubilities often limit their use to ESI-unfriendly solvents. Despite these problems and the inherent electroneutrality of some polymers, ESI mass spectrometry has been used to study poly (ethylene glycol)[6, 8-11], polyesters[12, 13], poly (methyl methacrylate)[14, 15], polystyrene[16, 17], poly(dimethylsiloxane)[9, 18, 19] and several related polymers[17, 20, 21]. However, the polymer distributions obtained by ESI mass spectrometry (in many instances ESI FTICR mass spectrometry) are frequently narrower than those measured using MALDI-TOF or GPC (the average masses determined using the latter two techniques are also frequently different from each other).[18, 19, 21, 22]

For the ion signals present in the FTICR mass spectra to reflect accurately the ions produced by electrospray ionisation the sampling, storage (in the hexapole ion trap), ion transfer and detection must be uniform across the polymer distribution. Frequently, this is not true. It is widely recognised that the FTICR mass spectra are dependent on the experimental parameters and source design.[23] Mechanisms by which the detected ion signals are changed include charge-stripping[8], MSAD[24-26], radial stratification[27, 28], nozzle-skimmer dissociation[18, 29, 30], time-of-flight effects arising from ion injection from the external ion source[31], ion-focusing[32], as well as ion trapping in the hexapole

ion trap, which are not known (but will resemble the KE dependence of trapping ions in the FTICR cell[33]). Nevertheless, despite these effects and the multiple charging that occurs it has been shown that ESI mass spectrometry can be used to characterise polymers with narrow molecular weight distributions.[15, 19, 21, 22] Finally, Simonsick and workers have shown that external fractionation using gel permeation chromatography (GPC) or in-line GPC ESI can be used to characterise fully polymers of a wider distribution.[20, 21]

Here, after outlining the deconvolution procedure, it is demonstrated that ESI mass spectrometry can be used to obtain the distribution of a copolymer. Finally, the effects of solvent composition on the polymer's charge state and its calculated average molecular weight are presented.

5.2 Results

Many of the studies of polymers using electrospray ionisation have concentrated on polyethyleneglycol (peg).[6, 8-11, 19, 32, 34-36] Although peg is important in the fields of biocongugation and biomembranes as well as membrane, coating and implant technologies (e.g. contact lenses) the principal reason for their use with ESI is their reliability. Stable ion currents and high ion yields are readily obtainable.

In addition to strong stable ion currents, the ions produced by electrospray ionisation of peg span a wide *m/z* range. As can be seen figure 5.2.1 the ions produced by the nanospray ionisation of methoxy polyethyleneglycol (mpeg) 2000 spanned 4 charge states and 1200 *m/z* units. This property proved to be especially useful for signal optimisation and was the diagnostic sample of choice. Note the relative intensities of the ions were dependent on the applied electrospray field (see page 142).
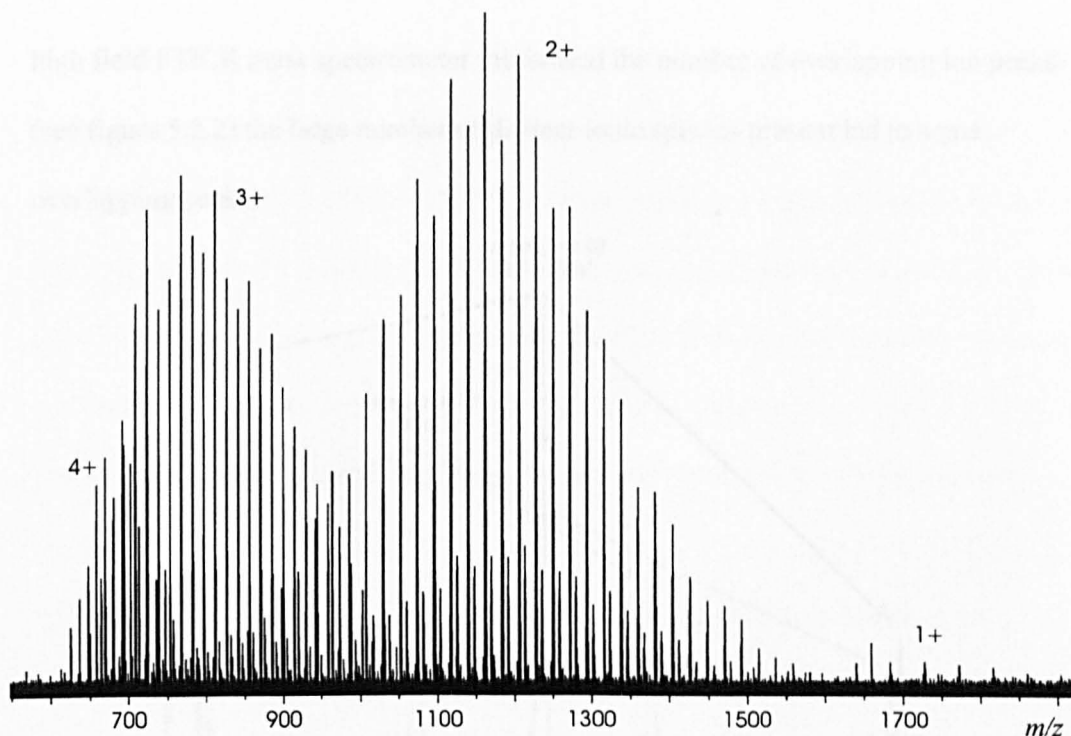
Figure 5.2.1. 512k nano ESI FTICR mass spectrum of 50 μM mpeg 2000 in 1:1 methanol: 5 mM NaOH solution.

The most intense peaks of each charge state were completely sodiated, the detected ions were adducts of the neutral polymer and the respective number of sodium ions, e.g. 4 sodium ions for the 4+ charge state. The satellite peaks that were present in the more intense charge states (3+ and 2+) were due to a mixed adduct in which one sodium ion was replaced by one potassium ion. Even with such a modest polymer, the large number of peaks produced by an oligomer distribution, each of which could be produced in a range of charge states, resulted in many individual ionic species.

In order to obtain quantitative information regarding the distribution of polymeric ions detected, the relative intensity of each ion was required. It has been shown that the heights of ICR peaks correlate directly with the number of ions detected[37] and this is the method normally used to quantify ICR signal intensity (and hence the number of ions). However, overlapping peaks and weak ion signals, where only a few isotopomer peaks were detected, prevented the straightforward approach of simply recording the intensity of each individual ion. Although the high resolution routinely achieved with a

148

high field FTICR mass spectrometer minimised the number of overlapping ion peaks (see figure 5.2.2) the large number of distinct ionic species present led to some overlapping peaks.
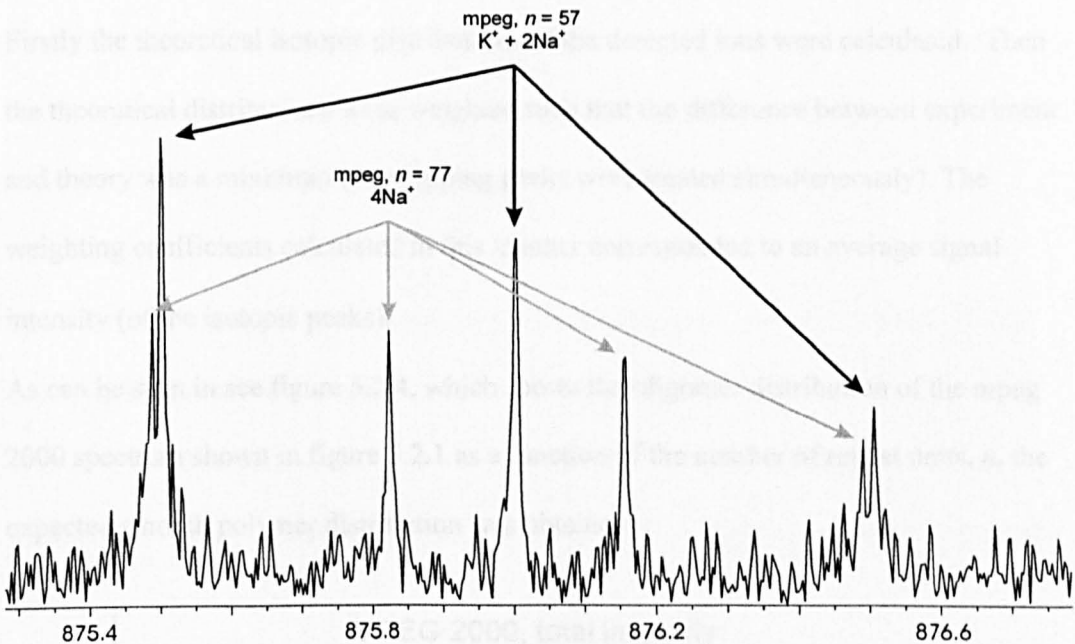
Figure 5.2.2. Close up of broad band spectrum shown in figure 5.2.1.

As a result of the changing isotopic probability across a polymer distribution, it was insufficient to record only the intensity of the monoisotopic (or any other isotopomer) peak of each ionic species. As can be seen in figure 5.2.3 the relative intensity of the monoisotopic peak changed from 1 for the smallest oligomer detected in the spectrum shown in figure 5.2.1. (32 repeat units, 2+ charge state) to 0.582 for the largest oligomer (73 repeat units, 3+ charge state).
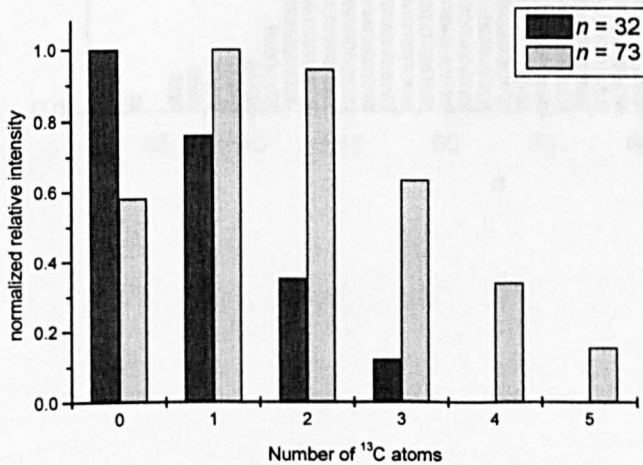
Figure 5.2.3. Comparison of the normalised relative intensities of the isotopomers of the $n = 32$ and $n = 73$ oligomers of peg. Only the isotopomers with a relative intensity ≥ 0.1 are included.

Rather than weight the relative intensity of an isotopic peak according to its probability of formation (such a calculation was vulnerable to noise in the peak chosen), all polymer spectra reported in this chapter were deconvoluted in the following manner. Firstly the theoretical isotopic distributions of the detected ions were calculated. Then the theoretical distributions were weighted such that the difference between experiment and theory was a minimum (overlapping peaks were treated simultaneously). The weighting coefficients calculated in this manner corresponded to an average signal intensity (of the isotopic peaks).

As can be seen in see figure 5.2.4, which shows the oligomer distribution of the mpeg 2000 spectrum shown in figure 5.2.1 as a function of the number of repeat units, n, the expected smooth polymer distribution was obtained.

MPEG 2000, total intensity

$Mn = 2396$
$Mw = 2433$
$Pdi = 1.02$
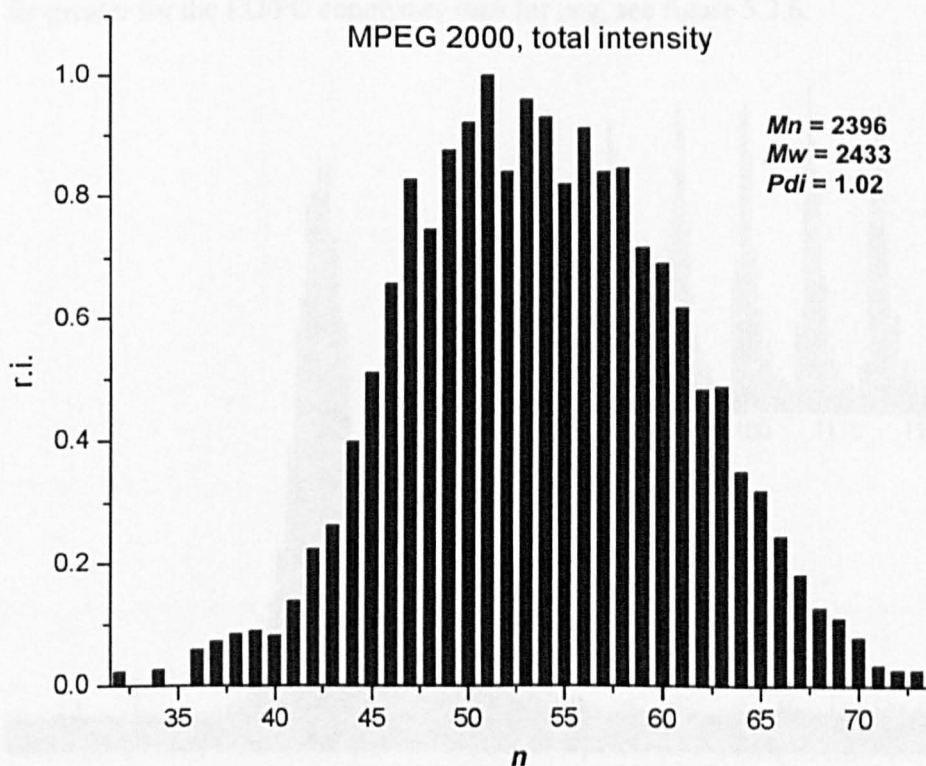
The same analysis was used to obtain the oligomer distribution of an ethylene oxide / propylene oxide (EO/PO) copolymer (Aldrich). In as much as a copolymer is an amalgamation of two polymer distributions, for a specific number of EO repeat units there was a distribution in the number of PO repeat units, there were many more species in the copolymer. As can be seen in figure 5.2.5. the ESI mass spectrum of an EO/PO copolymer, Mn = 2000, (Aldrich) contained many more peaks.

The dominant ions in the EO/PO mass spectrum were ammoniated. It was found that strong stable ion signals could be obtained using the solvent system 1:1 methanol: 5 mM ammonium acetate (pH ≈ 5.1) + 1% acetic acid. As was expected for a sample containing more distinct ionic species, the number of overlapping peaks was potentially far greater for the EO/PO copolymer than for peg, see figure 5.2.6.
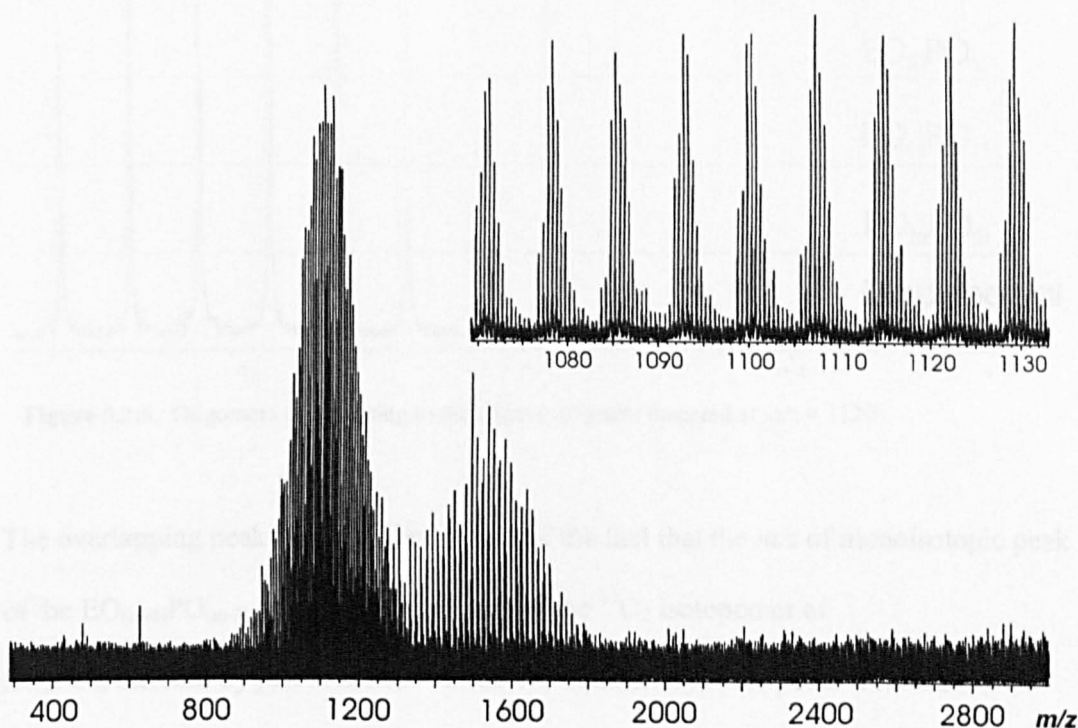
Figure 5.2.5. Nano ESI FTICR mass spectrum of 50 μM solution of an EO/PO block copolymer, Mn = 2000, in 1:1 methanol : 5 mM ammonium acetate (pH ≈ 5.1) + 1% acetic acid.

151

As can be seen in the inset of figure 5.2.5, which shows a close up of the EO/PO

spectrum, the spectrum consisted of clusters of peaks spaced evenly apart (about m/z 7

for the 3+ charge state and m/z 10.5 for the 2+ charge state). These clusters included the

signals from several oligomers. As can be seen in figure 5.2.6 the $EO_{22}PO_{21}$ and

$EO_{26}EO_{18}$ oligomers differed by just two mass units (+4 EO – 3 PO = 2), consequently

their isotopic envelopes overlapped. The next oligomers in this series, $EO_{30}PO_{15}$,

$EO_{34}PO_9$ and $EO_{38}PO_9$ also contributed to the cluster with the relative contribution

decreasing with increasing EO content.
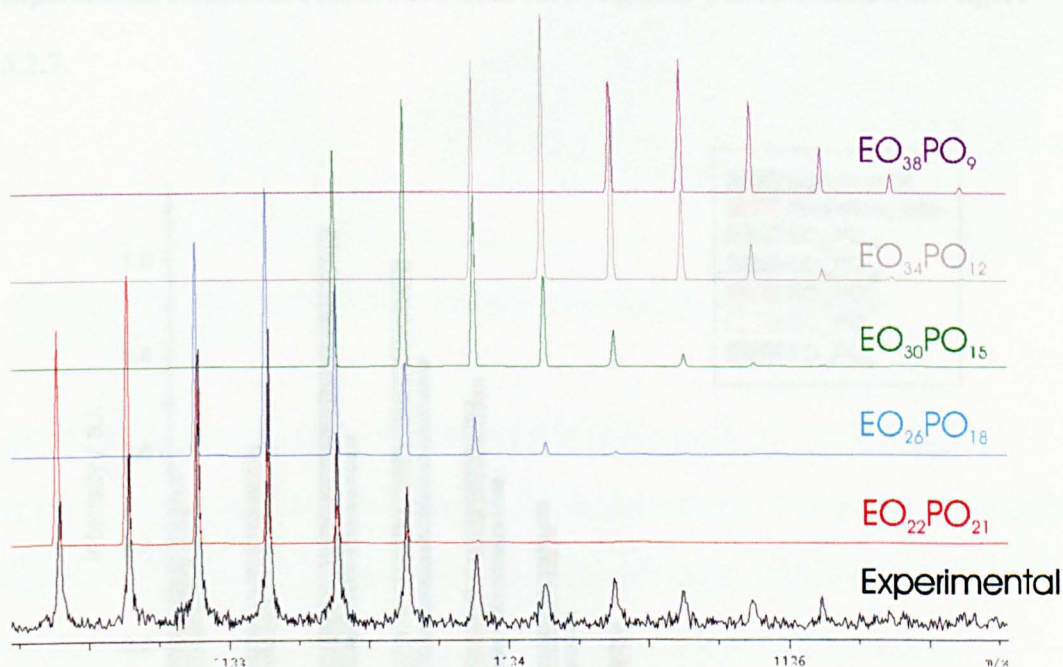
Figure 5.2.6. Oligomers contributing to the cluster-of-peaks detected at $m/z = 1120$

The overlapping peaks were a direct result of the fact that the m/z of monoisotopic peak

of the $EO_{(n+4)}PO_{(m-3)}$ oligomer and the m/z of the $^{13}C_2$ isotopomer of

EO_nPO_m differed by just 0.02 m/z. To resolve completely these peaks a resolution of

100 000 (FWHM) was required. However, as a result of the low-mass limit used to

record the mass spectrum (see figure 5.2.5) the sampling rate was quite high (1 MHz)

and the transient length was relatively short (0.52 s). Consequently the resolution was

insufficient, being about 50 000 at $m/z = 1120$. This value was slightly less than that predicted on the basis of transient length (FFT limit (9.4 T FTICR) = 56 000)[37]. The slight reduction can be attributed to the large number of ions trapped in the FTICR cell (required to detect all species) and the resulting coulombic peak broadening.[38, 39]

Nevertheless, the resolution routinely achievable permitted the complete distribution of the polymer to be determined. Through simultaneously weighting the theoretical distributions and minimising the difference between the total theoretical distribution and experimental results the contribution from each oligomer was determined, see figure 5.2.7.
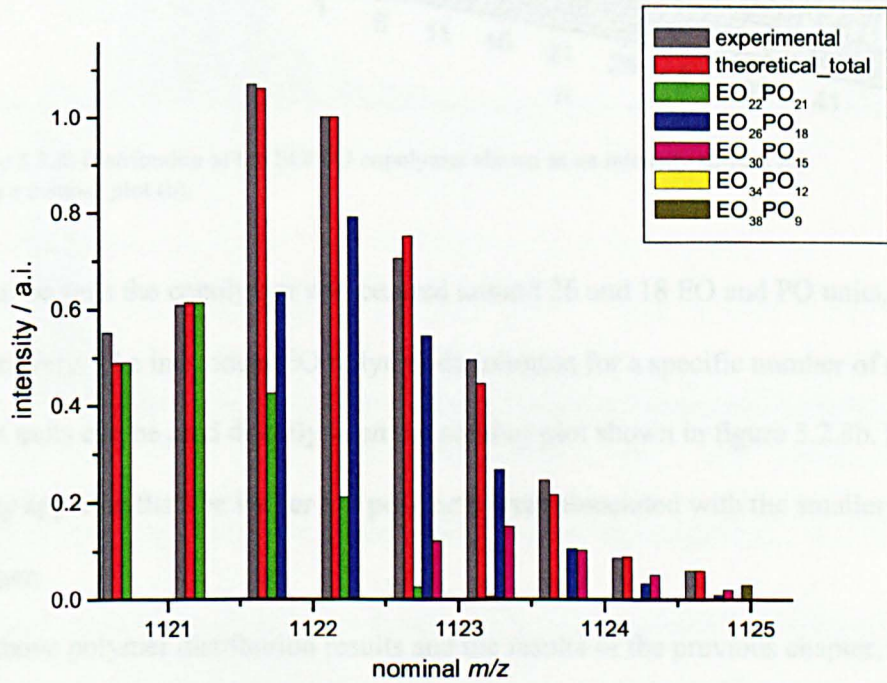
Figure 5.2.7. Deconvolution of the experimental results.

The complete distribution of the copolymer is shown in figure 5.2.8.
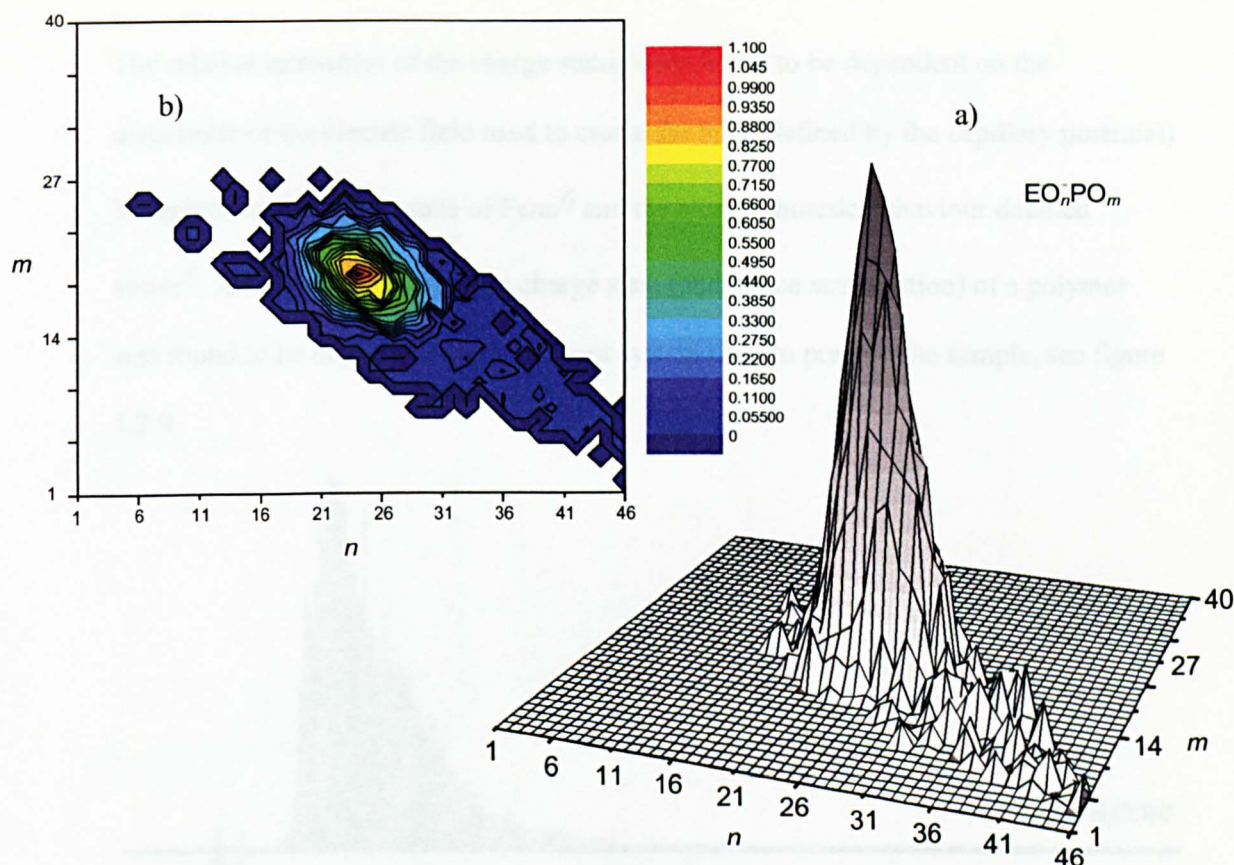
Figure 5.2.8. Distribution of the EO/ PO copolymer shown as an intensity surface (a) and as a contour plot (b).

As can be seen the copolymer was centred around 26 and 18 EO and PO units, respectively. The individual EO polymer distribution for a specific number of repeat PO repeat units can be read directly from the contour plot shown in figure 5.2.8b. It is readily apparent that the longer EO polymers were associated with the smaller PO polymer.

The above polymer distribution results and the results of the previous chapter, namely that the components of a complex polymeric mixture can be identified using accurate-mass mass spectrometry, indicate that high-field FTICR mass spectrometry can permit the complete characterisation of a narrow polymer. Of course care must be taken to minimise effects of the instrumental bias mechanisms detailed in the introduction. The poly alkoxide spectra shown above both showed ion distributions centred near m/z = 1000. Such results were typical when using 1:1 methanol:water as the solvent system.

The relative intensities of the charge states were found to be dependent on the magnitude of the electric field used to create the ions (defined by the capillary potential) in agreement with the results of Fenn[6] and the electrophoretic behaviour detailed above[5]. Additionally the average charge state (and hence m/z position) of a polymer was found to be dependent on the solvent system used to prepare the sample, see figure 5.2.9.
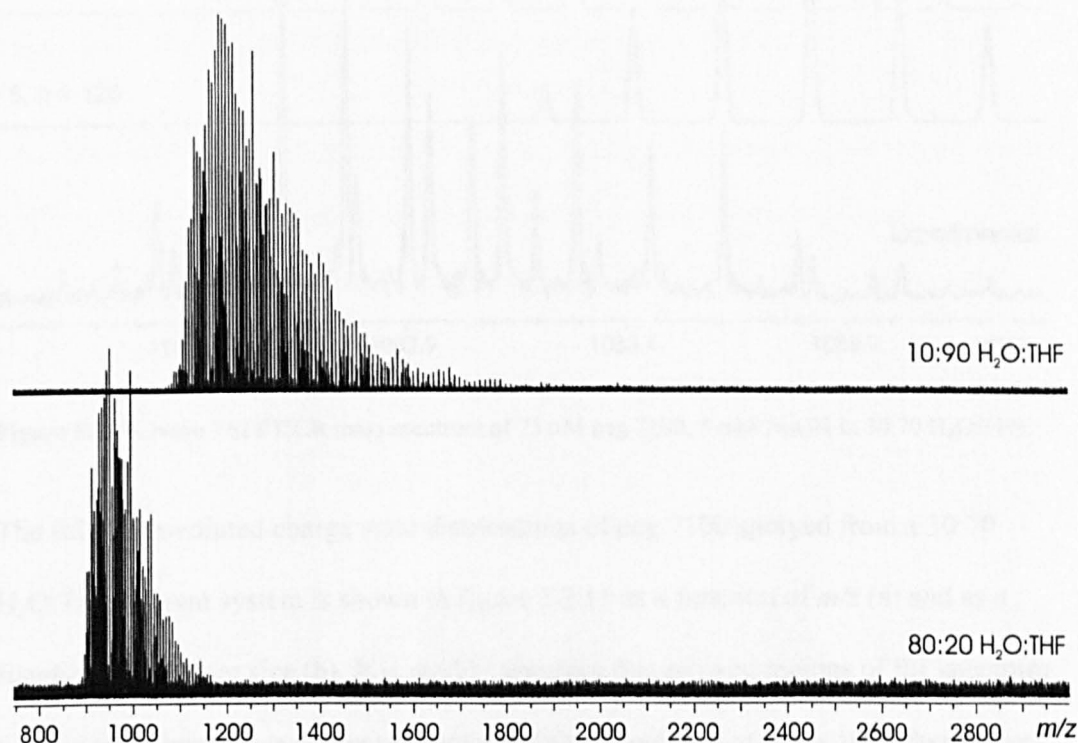
Figure 5.2.9. Nano ESI FTICR mass spectra of 75 µM peg 7100 and 5 mM NaOH. The top spectrum was taken with a 10:90 H₂O:THF solvent system and the bottom with 80:20 H₂O:THF.

As can be seen, the average charge state of the polymer increased with water content (m/z position decreased). The range of charge states produced by ESI of peg 7100 was greater than that for the two smaller polymers described above. As a result there were many distinct ionic species of similar m/z, which in turn meant that many peaks overlapped and many isotopic envelopes were intertwined, see figure 5.2.10. It is for these reasons that most electrospray ionisation polymer studies concern smaller polymer systems.
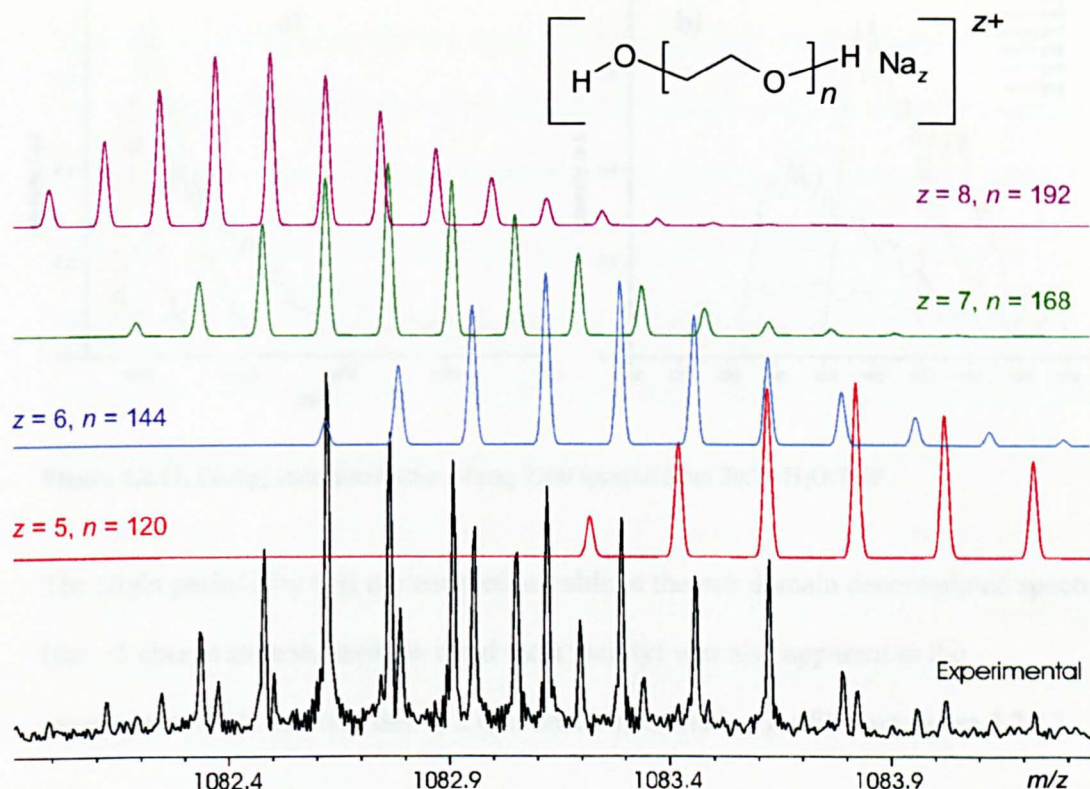
Figure 5.2.10. Nano ESI FTICR mass spectrum of 75 µM peg 7100, 5 mM NaOH in 30:70 H₂O:THF.

The full deconvoluted charge state distributions of peg 7100 sprayed from a 30:70

H₂O:THF solvent system is shown in figure 5.2.11 as a function of m/z (a) and as a

function of polymer size (b). It is readily apparent that in most regions of the spectrum

there were at least three distinct polymer series present, and at $m/z \approx 1075$ there were

four ($z = 5 - 8$ inclusively). It was also clear that the larger oligomers were detected in a

higher charge state, and vice versa, in agreement with previous results.[11]
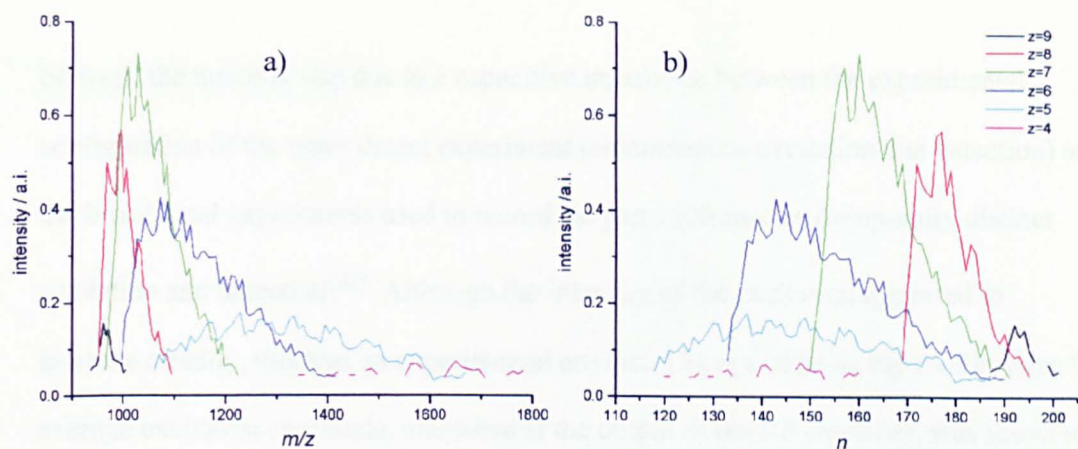
Figure 5.2.11. Charge state distribution of peg 7100 sprayed from 30:70 H_2O:THF.

The slight periodicity that is clearly observable in the *m/z* domain deconvoluted spectra (the +5 charge state showed the trend most lucidly) was also apparent in the experimental data and was due to a non-uniform excitation profile, see figure 5.2.12.

PEG7100 experiment
Exc. 200 - 6000 m/z
Det.. 500 - 3000 m/z
Sweep_width 294118 Hz
AQ-time 0.8913 seconds

Wave detect experiment
Exc. 200 - 6000 m/z
Det.. 100 - 12000 m/z
Sweep_width 1.667 x 10⁶ Hz
AQ-time 0.0393 seconds
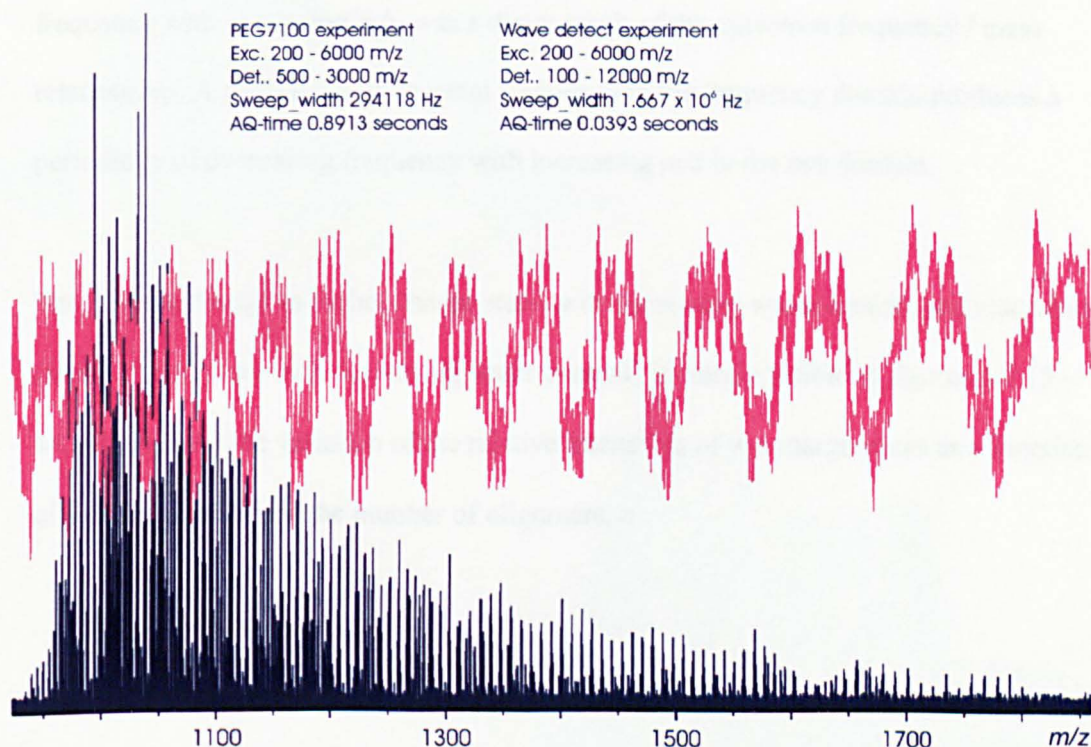
Figure 5.2.12. Comparison of experimental data (30:70 H_2O:THF) and the excitation profile.

The excitation profile (a frequency sweep) was measured by sampling the current induced in the detector plates as the frequency sweep was applied. The slight offset

between the maxima was due to a capacitive imbalance between the experimental configuration of the wave detect experiment (simultaneous excitation and detection) and the broad band experiments used to record the peg 7100 spectra (temporally distinct excitation and detection)[40]. Although the intensity of the excitation appeared to increase steadily, this was an experimental artefact. Using a cathode ray oscilloscope the average excitation amplitude, measured at the output of the RF amplifier, was found to be of constant intensity. Nevertheless, the periodicity in the excitation amplitude would have resulted in a periodic sensitivity. As the signal intensity of an ion is proportional to the ion's cyclotron radius[41], which in turn is determined by the excitation field strength, the minimum number of ions required for a detectable signal (the sensitivity) was also periodic. The apparent changing frequency of the periodicity, namely decreasing frequency with increasing m/z, was a direct result of the cyclotron frequency / mass relationship. A periodicity of constant frequency in the frequency domain produces a periodicity of decreasing frequency with increasing m/z in the m/z domain.

The gradual change to higher charge states with increasing water content and vice versa (lower charge state with decreasing water content) is clearly visible in figures 5.2.13 – 14, which show the variation of the relative intensities of the charge states as a function of solvent content and the number of oligomers, n.

Figure 5.2.13. Charge state distribution dependence on solvent composition.

4+ charge state

5+ charge state

6+ charge state

159
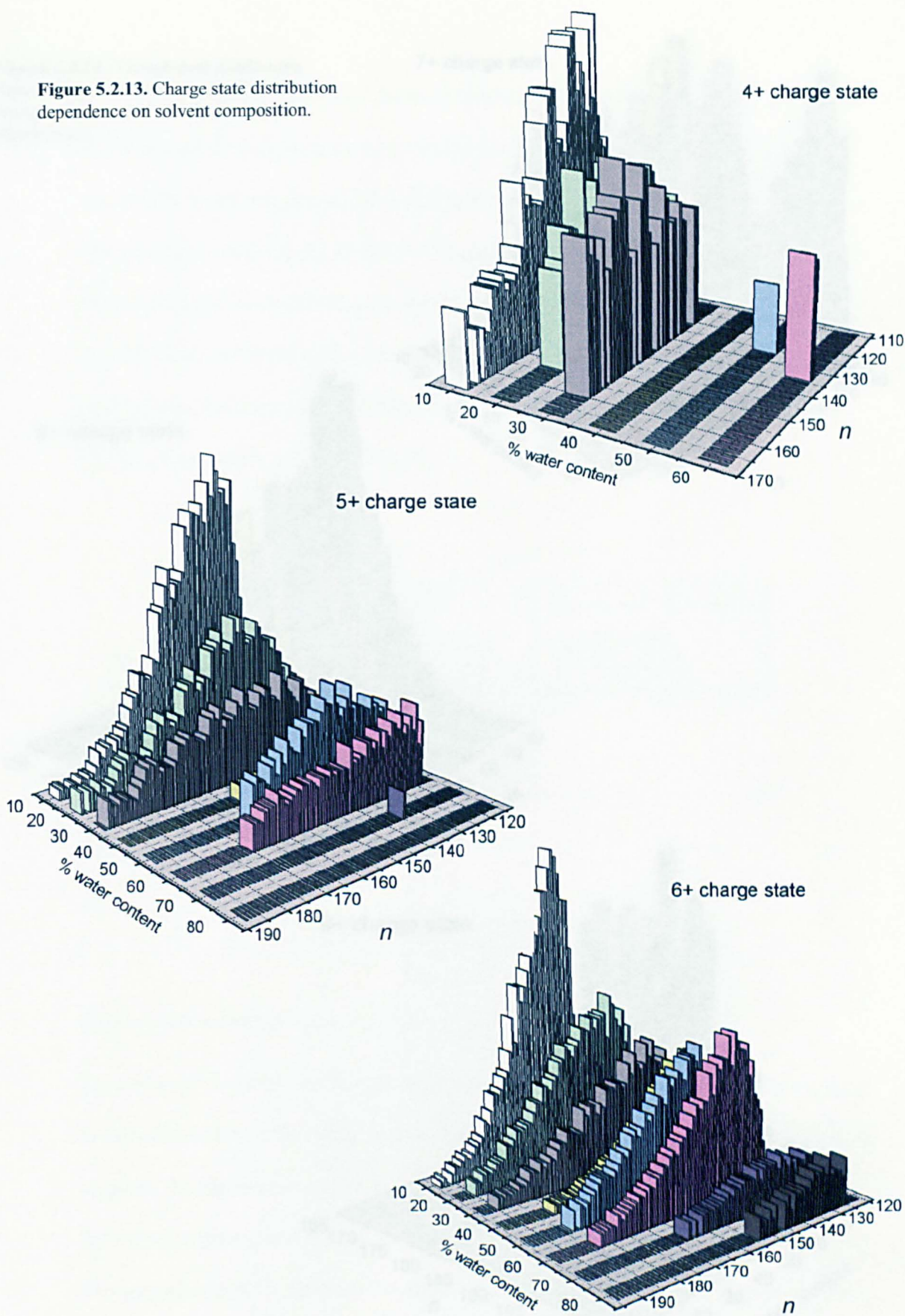
Figure 5.2.14. Charge state distribution dependence on solvent composition. Note change of orientation for the 8+ and 9+ distributions.

7+ charge state

8+ charge state
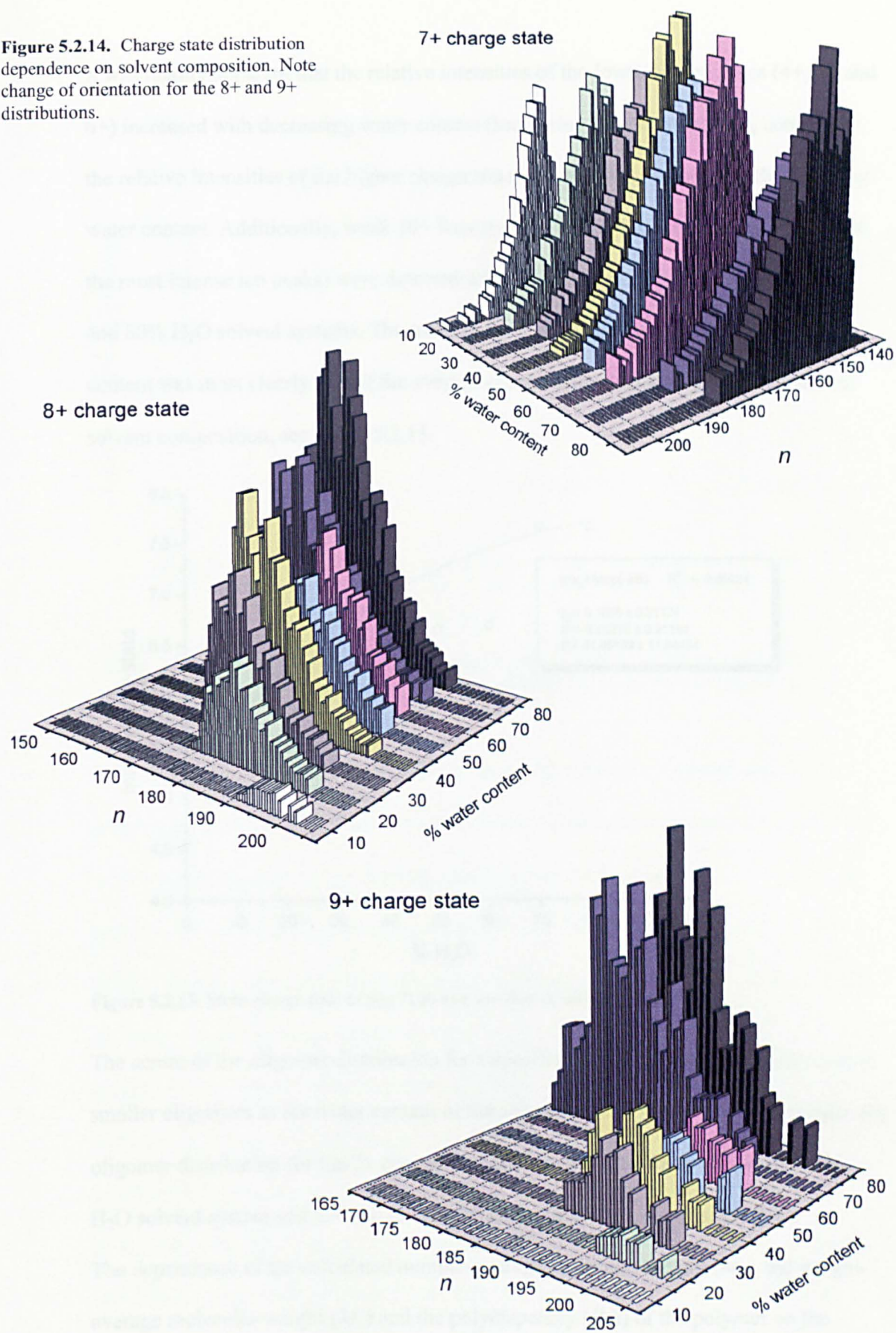
9+ charge state

It was readily apparent that the relative intensities of the lower charge states (4+, 5+ and 6+) increased with decreasing water content (increasing THF content) and, conversely, the relative intensities of the higher charge states (8+ and 9+) increased with increasing water content. Additionally, weak 10+ ions signals (intensities approximately 0.2 % of the most intense ion peaks) were detected when peg 7100 was sprayed from the 70% and 80% H_2O solvent systems. The trend to an increasing charge state with water content was most clearly seen if the average charge state was displayed as function of solvent composition, see figure 5.2.15.
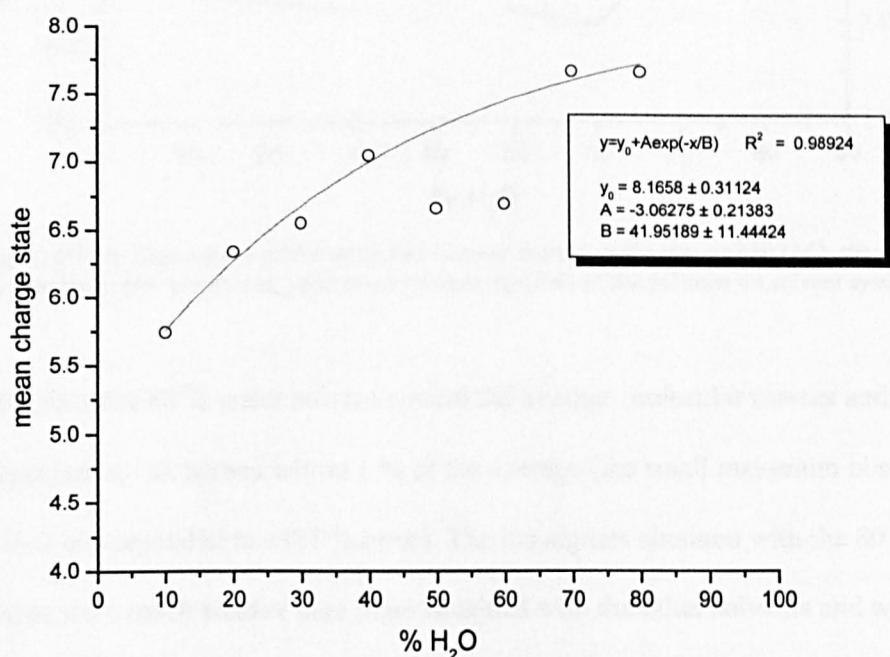
Figure 5.2.15. Mean charge state of peg 7100 as a function of solvent composition.

The centre of the oligomer distribution for a specific charge state was found to move to smaller oligomers as the water content of the solvent system increased. For example, the oligomer distribution for the 7+ charge state was centred about $n = 180$ for the 10% H_2O solvent system and $n = 150$ for the 80% solvent system, see figure 5.2.14. The dependence of the calculated number-average molecular weight (M_n), the weight-average molecular weight (M_w) and the polydispersity (Pdi) of the polymer on the solvent content in shown in figure 5.2.16.

161
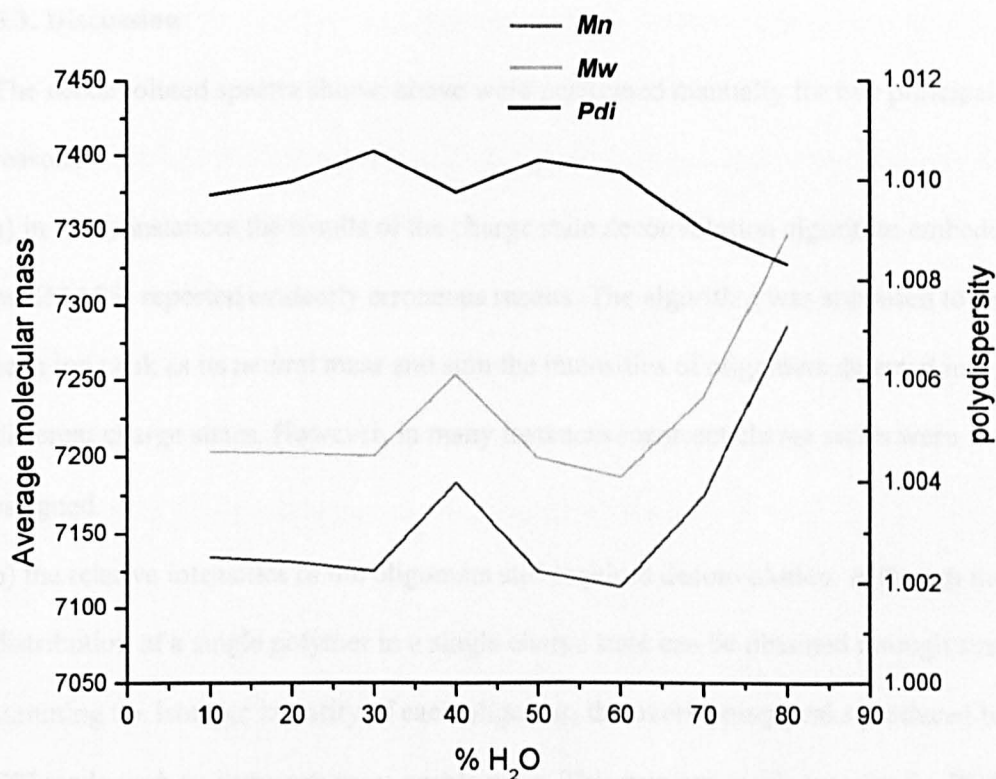
Figure 5.2.18. Dependence of the calculated number average molecular weight (M_n), the weight average molecular weight (M_w) and the polydispersity (Pdi) of the polymer on solvent system.

Other than the 80 % water solvent system the average molecular masses and the polydispersity all agreed within 1 % of the average (the small maximum observed at 40 % H_2O corresponded to a 0.7 % error). The ion signals obtained with the 80 % solvent system were much weaker than those obtained with the other solvents and were less stable. The higher average molecular masses calculated for this solvent system reflected the lower signal intensity / sensitivity associated with it. The *S/N* ratio of the smaller polymers was typically about one tenth of the most intense (see figure 5.2.11). For the 80 % water solvent system these smaller polymers were not detected. Without the contribution of the smaller polymers, which would lower the calculated average molecular mass, the values of M_n and M_w calculated for the 80 % H_2O solvent system were larger. They were in effect the average molecular masses of the more intense component, and did not include the contribution from the low intensity low-mass tail.

5.3. Discussion

The deconvoluted spectra shown above were performed manually for two principal reasons:

a) in many instances the results of the charge state deconvolution algorithm embedded in XMASS reported evidently erroneous results. The algorithm was supposed to report each ion peak as its neutral mass and sum the intensities of oligomers detected in different charge states. However, in many instances incorrect charge states were assigned.

b) the relative intensities of the oligomers still required deconvolution. Although the distribution of a single polymer in a single charge state can be obtained through simply summing the isotopic intensity of each oligomer, the overlapping peaks produced by ESI made such an approach more problematic. This was especially true for the EO/PO copolymer.

Automation of polymer deconvolution was reported by McLafferty and workers for a variety of pegs of average molecular weight 4.3 – 23 kDa.[10] However, the two deconvolution algorithms produced artefact peaks or severe abundance distortions that increased in severity with increasing molecular weight. It is for this reason that many ESI polymer applications have concentrated on relatively small polymers (M_n < 2000). As can be seen above, ESI mass spectrometry can yield the distribution of a narrow copolymer provided the deconvolution is performed correctly.

Two previous studies of the charge state distribution dependence on solvent concerned intrinsic ions (diquaternary ammonium salts) where the lower charge states of which were due to ion pairing.[42, 43], whereas this study was concerned with the formation of polymer : ion adducts. Nevertheless the same qualitative results were apparent. The charge state distribution of the ions was affected by the permittivity of the solvent

system. Some of the physical characteristics of the solvents used here are shown in table 5.3.1. The higher charge states observed with a higher water content are interpreted as reflecting the higher dielectric constant of that solvent system. Similarly, for a specific charge state, the centre of the distribution was seen to move to smaller polymers, presumably the higher dielectric constant permitted the ions to be situated closer together (whilst in the final droplets), see figure 5.2.13 – 14. An approach based on calculating the distance between the cations attached to peg was recently used by Fenn to estimate the charge density on the surface of the droplet.[6]

	Methanol	Tetrahydrofuran	Water
Boiling point / °C	64.6	65	100
Density @ 25 °C / g cm^{-3}	0.813	0.889	1
$\Delta_{vap} H^\circ$ @ 25 °C / kJ mol^{-1}	37.43	31.99	43.98
Viscosity @ 25 °C / mPa s	0.544	0.456	0.89
Relative permittivity	33.0	7.52	80.1
Vapour pressure / kPa	16.9	21.6	
Surface tension / mN m^{-1}	22.55	26.4	72.8

Table 5.3.1. Some physical characteristics of methanol, THF and water. Unless other wise stated the data was obtained from the CRC Handbook of Chemistry & Physics (80th Edition, 2000).

Although it is virtually impossible to change a single solvent parameter while the others are held constant evidence has been provided that some solvent characteristics (surface tension and viscosity) exhibit no obvious influence upon the distribution of analyte charge states[43].

Although the volatility of the solvent system clearly affects the rate of droplet evaporation the trends observed here and in the previous studies[42, 43] oppose that expected solely on the basis of volatility. Fenn has previously proposed that the charge state of an ion increases when the evaporation rate increases[2] (more droplet subdivisions leads to increased charge enrichment). This proposal was supported by experiments wherein the charge state distributions were shifted to higher values when

the droplet evaporation rate was increased through the use of a variable temperature counterflow bath gas. Therefore, if volatility were dominant the charge state of the polymer would be expected to decrease as the proportion of water increased (see table 5.3.1). Clearly this was not the case. This result was in agreement with that of Wang and Cole.[42, 43]

As explained in the introduction a cascade of solvent evaporation / Rayleigh subdivision is supposed to form the smaller satellite droplets with an excess of charge (with respect to the initial droplets)[7]. The size of the droplets formed by the spray[46] (as opposed to the satellite droplets) as well as the size of the droplets that undergo Rayleigh fission depend upon surface tension of the solvent system. As the evaporation rate of the solvent is dependent upon the vapour pressure of the solvent,[7] it is clear that the rate of droplet subdivision (and hence the external field experienced by the droplet) is also solvent composition dependent. Furthermore the processes of solvent fractionation[47] as well as the recently reported physical / chemical separation phenomenon during droplet subdivision[48], make quantification difficult. Nevertheless, the results show that the dielectric constant is of principal importance in determining the number of atomic ions that form an adduct with polyethyleneglycol.

5.4 Conclusion

The charge state of polymer adduct was found to be determined by the permittivity of the solvent. For the H_2O:THF solvent system the charge state of the adduct was found to increase with an increasing water content (higher permittivity, see table 5.3.1). When the signal intensity was sufficient the average molecular masses were insensitive to the solvent system and the polymer's average charge state.

Finally, despite the presence of many overlapping peaks (specifically for the EO/PO copolymer) the deconvolution method described provided accurate polymer

distributions for moderately large and small polymers (peg 7100 and mpeg 2000) as well as an EO/PO copolymer.

(1)   Cole, R. B. *J. Mass Spectrom.* **2000**, *35*, 763-772.

(2)   Fenn, J. B. *J. Am. Soc. Mass Spectrom.* **1993**, *4*, 524-535.

(3)   Tang, L.; Kebarle, P. *Anal. Chem.* **1993**, *65*, 3654.

(4)   Enke, C. G. *Anal. Chem.* **1997**, *69*, 4885-4893.

(5)   Zhou, S.; Cook, K. D. *J. Am. Soc. Mass Spectrom.* **2001**, *12*, 206-214.

(6)   Fenn, J. B.; Russell, J.; Meng, C. K. *J. Am. Soc. Mass Spectrom.* **1997**, *8*, 1147-1157.

(7)   Kebarle, P.; Tang, L. *Anal. Chem.* **1993**, *65*, 972-986.

(8)   Maziarz III, E. P.; Baker, G.; Lorenz, S. A.; Wood, T. *Journal of the American society of mass spectrometry* **1999**, *10*, 1298-1304.

(9)   Maziarz III, E.; Baker, G. A.; Mure, J. V.; Wood, T. D. *Int. J. Mass Spectrom.* **2000**, *202*, 241-250.

(10)   O'Conner, P. B.; McLafferty, F. W. *Jounral of the American chemical society* **1995**, *117*, 12826-12831.

(11)   Wong, S. F.; Meng, C. K.; Fenn, J. B. *J. Chem. Phys.* **1988**, *92*, 546-550.

(12)   Koster, S.; Duursma, M.; Boon, J.; Nielen, M.; Koster, C. d.; Heeren, R. , University of Warwick 1999.

(13)   Koster, S.; Duursma, M. C.; Boon, J. J.; Nielen, M. W. F.; Koster, C. G. d.; Heeren, R. M. A. *J. Mass Spectrom.* **2000**, *35*, 739-748.

(14)   Haddleton, D. M.; Feeney, E.; Buzy, A.; Jasieczek, C. B.; Jennings, K. R. *Chemical communications* **1996**, 1996.

(15)   McEwen, C. N.; Simonsick, W. J.; Larsen, B. S.; Ute, K.; Hatada, K. *Journal of the American society for mass spectrometry* **1995**, *6*, 906-911.

(16) Deery, M. J.; Jennings, K. R.; Jasieczek, C. B.; Haddleton, D. M.; Jackson, A. T.; Yates, H. T.; Scrivens, J. H. *Rapid Comm. Mass Spectrom.* **1997**, *11*, 57-62.

(17) Scrivens, J. H.; Jackson, A. T. *Int. J. Mass Spectrom.* **2000**, *200*, 261-276.

(18) Maziarz III, E. P.; Baker, G. A.; Wood, T. D. *Macromolecules* **1999**, *32*, 4411-4418.

(19) Yan, W.; Ammon Jr, D. M.; Gardella Jr, J. A.; Maziarz III, E. P.; Hawkridge, A. M.; Grobe III, G. L.; Wood, T. D. *Eur. J. Mass Spectrom.* **1998**, *4*, 467-474.

(20) Shi, S. D. H.; Hendrickson, C. L.; Marshall, A. G.; Simonsick, W. J.; Aaserud, D. J. *Analytical chemistry* **1998**, *70*, 3220-3226.

(21) Aaserud, D. J.; Prokai, L.; SImonsick Jr, W. J. *Anal. Chem.* **1999**, *71*, 4793-4799.

(22) Hunt, S. M.; Sheil, M.; Derrick, P. J. *European mass spectrometry* **1998**, *4*.

(23) Collette, C.; Drahos, L.; Pauw, E. D.; Vekey, K. *Rapid Comm. Mass Spectrom.* **1998**, *12*, 1673.

(24) Sannes-Lowery, K.; Griffey, R. H.; Kruppa, G. H.; P, S. J.; Hofstadler, S. A. *Rapid Comm. Mass Spectrom.* **1998**, *12*, 1957-1961.

(25) Sannes-Lowery, K. A.; Hofstadler, S. A. *J. Am. Soc. Mass Spectrom.* **2000**, *11*, 1-9.

(26) Hakansson, K.; Axelsson, J.; Palmblad, M.; Hakansson, P. *J. Am. Soc. Mass Spectrom.* **2000**, *11*, 210-217.

(27) Tolmachev, A. V.; Udseth, H. R.; Smith, R. D. *Rapid Comm. Mass Spectrom.* **2000**, *14*, 1907-1913.

(28) Tolmachev, A. V.; Udseth, H. R.; Smith, R. D. *Anal. Chem.* **2000**, *72*, 970-978.

(29) Schneider, B. B.; Douglas, D. J.; Chen, D. D. Y. *Rapid Comm. Mass Spectrom.* **2001**, *15*, 249-257.

(30) Van-Dongen, W. D.; Van-Wijk, J. I. T.; Green, B. N.; Heeren, W.; Haverkamp, J. *Rapid Comm. Mass Spectrom.* **1999,** *13*, 1712.

(31) O'Conner, P. B.; Duursma, M.; Rooij, G. J. v.; Heeren, R. M. A.; Boon, J. J. *Analytical chemistry* **1997,** *69*, 2751-2755.

(32) Hunt, S. M.; Sheil, M. M.; Belov, M.; Derrick, P. J. *Anal. Chem.* **1998,** *70*, 1812-1822.

(33) Hofstadler, S. A.; Beu, S. C.; Laude Jr, D. A. *Anal. Chem.* **1993,** *65*, 312-316.

(34) Palmblad, M.; Hakansson, K.; Hankansson, P.; Feng, X.; Cooper, H.; Giannakopulos, A. E.; Green, P. S.; Derrick, P. J. *Eur. J. Mass Spectrom.* **2000,** *6*, 267-275.

(35) Koster, S.; Duursma, M. C.; Boon, J. J.; Heeren, R. M. A. *J. Am. Soc. Mass Spectrom.* **2000,** *11*, 536-543.

(36) Miyabayashi, K.; Naito, Y.; Miyake, M.; Tsujimoto, K. *Eur. J. Mass Spectrom.* **2000,** *6*, 251-258.

(37) Marshall, A. G.; Hendickson, C. L.; Jackson, G. S. *Mass Spectrom. Rev.* **1998,** *17*, 1-35.

(38) Gorshkov, M. V.; Marshall, A. G.; Nikolaev, E. N. *J. Am. Soc. Mass Spectrom.* **1993,** *4*, 855-868.

(39) Wang, T.-C. L.; Marshall, A. G. *Int. J. Mass Spectrom. Ion Proc.* **1986,** *68*, 287-301.

(40) Schmidt, E. G.; Fiorentino, M. A.; Arkin, C. R.; Laude, D. A. *Anal. Chem.* **2000,** *72*, 3568-3572.

(41) Dunbar, R. C. *Int. J. Mass. Spectrom. Ion Proc.* **1984,** *56*, 1-9.

(42) Wang, G.; Cole, R. B. *J. Am. Soc. Mass Spectrom.* **1996,** *7*, 1050-1058.

(43) Cole, R. B.; Harrata, A. K. *J. Am. Soc. Mass Spectrom.* **1993,** *4*, 546-556.

(44) Thomson, B. A.; Iribarne, J. V. *J. Chem. Phys.* **1979,** *71*, 4451.

(45)   Iribarne, J. V.; Thomson, B. A. *J. Chem. Phys.* **1976,** *64*, 2287.

(46)   Fernandez de la Mora, J.; Rossel-Liompart, J. , Nashville, TN 1991; 441.

(47)   Zhou, S.; Cook, K. D. *Anal. Chem.* **2000,** *72*, 963-969.

(48)   Tang, K.; Smith, R. D. *J. Am. Soc. Mass Spectrom.* **2001,** *12*, 343-347.

6 HCl (2+1) Resonance enhanced multi-photon ionization studied by ion imaging

6.1. Introduction

The fragments reported in chapters 2 and 3, namely those due to multipole storage assisted dissociation[1] (MSAD) and sustained off-resonance irradiation collision-induced dissociation[2] (SORI CID), were both due to slow collisional-activation of the parent ion. This slow heating causes the internal (vibrational) energy of the molecule to increase and ultimately to the production of fragments[3]. This process is distinct from that reported in many reaction dynamics studies, in which the molecule is excited to a different electronic state from which the fragments are produced, e.g. ultraviolet photodissociation.

The distribution of excited states accessed and the behaviour of those excited states constitutes the basis of a complete field of chemistry, namely reaction dynamics.

The majority of gas-phase reaction dynamics studies focus on the asymptotic properties of the reaction, measuring product branching ratios, product quantum states (electronic, vibrational and rotational) and/or velocities (speed and angular distributions). It is desirable to simultaneously measure all these quantities so that correlated quantities can be determined, *e.g.*, the velocities of the fragments correlated with a particular quantum state. Prior to the development of the technique used in this study, ion imaging, simultaneous measurement was extremely difficult.

6.2. Ion imaging

Ion imaging[4-10] is a relatively new technique used to study gas-phase uni- and bimolecular reactions at the molecular level. Simultaneous (or multiplex) detection of rotational, vibrational, electronic and translational energy distributions is achieved by

combining two more established techniques. The spectroscopic state-specific technique

resonance-enhanced multi-photon ionisation (REMPI) is used to determine product

quantum state distributions, and two-dimensional time-of-flight mass spectroscopy

(using position sensitive detectors) gives velocity (speed and angular) distributions.

Many ion imaging experiments have investigated the photodissociation dynamics of a

small molecule, *e.g.* O_2[11-13], H_2[14], CD_3I[15], CH_3SH[16], H_2S[16], ICl[17], $HNCO$[18] and

N_2O[19, 20].

Relatively recently John Eland and workers used what is in essence a dual ion imaging

spectrometer, one for positive ions and the other for negative ions, to simultaneously

measure the distributions of both ions and so study ion pair formation[21].

As with all chemical reactions, photodissociations are governed by the potential energy

surfaces the reactions evolve on. Figure 6.2.1 shows a schematic representation of the

potential energy surfaces involved in a 'simple' photodissociation of a molecule ABC.
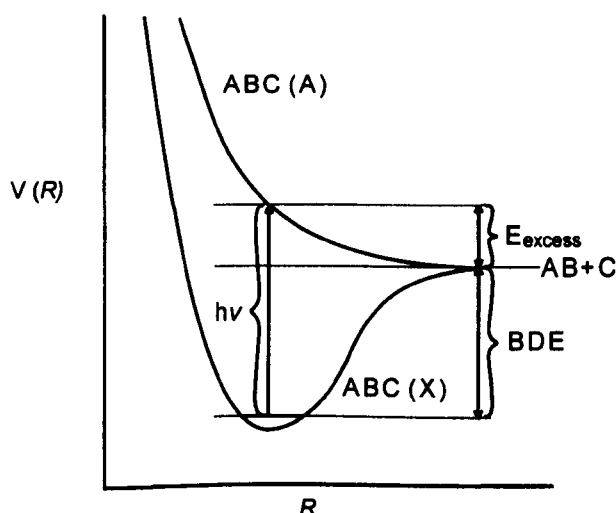
Figure 6.2.1. Schematic representation of the photodissociation of a triatomic molecule (ABC), R is the distance between atom C and the AB molecular fragment, BDE the bond dissociation energy and $h\nu$ the energy of the photon.

The ground-state potential energy surface is termed X and the excited state A, R is the

internuclear distance between atom C and the AB and $h\nu$ is the energy of the laser

photon. The ground state potential is bound and evolves at long AB-C internuclear

distances to AB + C (both in their ground states) fragments. The energy difference

between the two AB and C ground state fragments and the ground state of the ABC

molecule is the bond dissociation energy (BDE). Following absorption of a photon, the

molecule is excited from the ground state (X) to a repulsive excited state (A).

Depending on the nature the repulsive excited state, the molecule will dissociate

promptly, or more slowly, into the fragments AB + C.

The excess energy, the difference between the photon energy and the bond dissociation

energy, can be distributed among all available degrees of freedom of the nascent

photofragments, i.e., translational, electronic, rotational and vibrational. The release of

kinetic energy causes the fragments to move away from the point in space where they

were generated. The proportion of the excess energy released as kinetic energy and the

masses of the fragments determine their recoil speeds. The residual excess energy is

divided over the other available degrees of freedom. State-selective REMPI is used to

determine this distribution whilst two-dimensional time-of-flight mass spectroscopy is

used to record their recoil velocities (speed and direction). The experiment described in

this report concerns (2+1) REMPI of HCl and differs from the one-photon case in that

the total energy supplied to a molecule is $3h\nu$; the selection rules and consequently the

angular distributions of the product photofragments also differ.

6.3. Resonance-enhanced multiphoton ionisation (REMPI)

The ionisation potential of most small molecules is above 8 eV; therefore highly

energetic photons are required to induce photoionisation through regular one-photon

absorption. Highly energetic photons can be produced by traditional line sources such as

He (I) and Ne (I), which provide radiation of a fixed energy. Synchrotron sources and

vacuum (VUV) lasers may provide tuneable radiation. In a direct one-photon ionisation

process there is little state selectivity, i.e., ionisation of several vibrational and rotational

levels of the electronic ground state occurs to give several electronic, vibrational and rotational states of the ion, determined mostly by the Frank-Condon factors between the initial and final states and conservation of angular momentum. However, most common lasers produce less energetic photons. Visible light lasers (*e.g.,* dye lasers) produce photons of an energy ranging between ~1 and 4 eV. The laser photon energy can be extended to higher energies by frequency doubling the initial laser light using non-linear crystals (*e.g.* β-barium borate). These photon energies are still insufficient to ionise most molecules. However, the available photon flux of a pulsed dye laser is generally high enough to induce multi-photon absorption. Figure 6.3.1 shows a schematic diagram of several energy levels of a diatomic molecule AX. The first process, a), shows the one-photon ionisation of AX by a high energy photon.
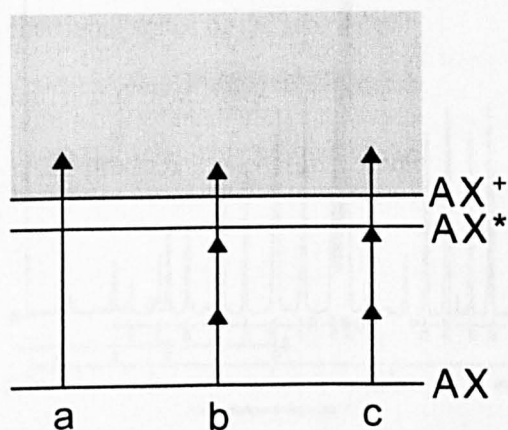
Figure 6.3.1. (a) Ionisation *via* direct one-photon absorption, (b) non-resonant multiple photon ionisation and (c) resonance enhanced multiphoton ionisation (REMPI). Process (c) is an example of (2+1) REMPI; two photons are required to excite the molecule AX to a resonant excited intermediate state AX* and one more to ionise AX*.

The second process (b) shows the ionisation of the same molecule by simultaneous absorption of three photons. As all three photons have to be absorbed simultaneously this is statistically far less likely and will only occur if the laser flux is sufficiently high. In process (c) the energy of the laser photons are matched to be resonant, at the two-photon level, with an excited state of the neutral molecule. The lifetime associated with the resonant state is generally long enough such that only two photons need to be absorbed simultaneously, making the process much more likely than (b). Ionisation *via* a resonant state has been named 'resonance-enhanced multi-photon ionisation'[22]. The

173

process shown in (c) is termed (2+1) REMPI, in which the first integer describes the number of photons required to reach the resonant level and the second integer the number to reach the ionisation continuum from the resonance level. A particularly useful feature of REMPI is that the resonance wavelength is often different for different quantum states. Therefore, using REMPI each rovibrational level of a molecule can be ionised individually by varying the wavelength of the laser. To illustrate the state selectivity of this technique, figure 6.3.2. shows the rotationally resolved structure of the $^3\Delta_2$ (2)($v' = 0$) state of HCl[23]. The spectrum was obtained by recording the total electron signal as the wavelength was scanned.
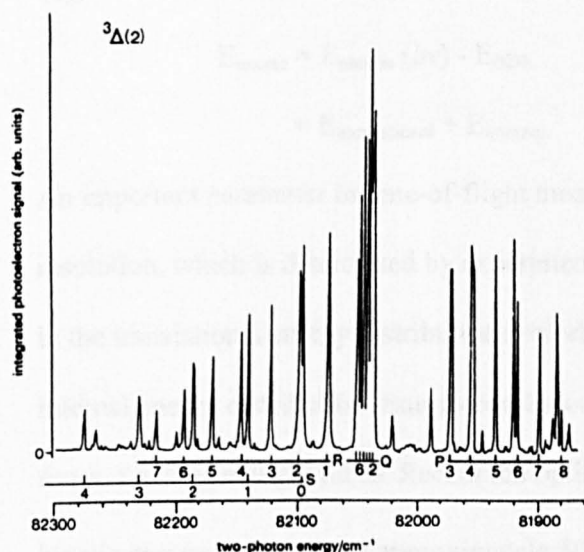
Figure 6.3.2. The total photoelectron signal of HCl as a function of two-photon energy in the region 81 860 – 82 300 cm⁻¹. A rotationally resolved wavelength spectrum of the $^3\Delta_2$ ($v=0$) is shown in this energy region. Diagram obtained from reference 23. P, Q, R and S have the usual spectroscopic meaning.

6.4. Photofragment time-of-flight spectroscopy

In addition to the internal energy distribution another observable of interest that can be measured following a molecular dissociation or chemical reaction is the product's velocity (speed and angular) distribution. A common route to determine a fragment's velocity is photofragment time-of-flight (TOF) spectroscopy[22], measuring the distribution of times taken for particle fragments to traverse a well-defined distance to a detector. In measurement of photofragment velocities we can distinguish two different observables, the speed and angular distributions.

174

Speed distribution: Following molecular dissociation the photofragments start to recoil away from the point where they were generated. Measurement of the speed distributions of photofragments will reveal directly the proportion of the excess energy that is deposited in the translational degrees of freedom. Through conservation of energy and momentum the speed of the two concomitant fragments are related, and thus by measurement of the speed of one of the fragments we can determine the total kinetic energy released to both fragments. If the photolysis energy is known the translational energy distribution can also be used to determine the energy released into the other degrees of freedom:

$$E_{excess} = E_{photon} (hv) - E_{BDE} \qquad (6.4.i)$$

$$= E_{translational} + E_{internal} \qquad (6.4.ii)$$

An important parameter in time-of-flight measurements is the energy or velocity resolution, which is determined by experimental parameters. Detection of fine structure in the translational energy distributions correlates directly to fine structure in the internal energy distribution. Energy resolution generally increases with increasing flight times, *i.e.* longer flight tubes. Recent ion optical improvements have led to achievable kinetic energy resolution of approximately 50 meV at a kinetic energy of 1 eV[11, 12].

Angular distributions: When the dissociation is initiated by absorption of a linearly polarised photon and the dissociation is fast the angular distribution of the photofragments is likely to be anisotropic as the velocities of the fragments are correlated with the laser polarisation vector. Angular recoil distributions depend on the direction of the laser polarisation vector and the symmetries of the electronic states involved in the absorption process. To appreciate the source of this anisotropy we need to recall that absorption of light occurs through the interaction of the electric vector of

the radiation, ε, and the transition dipole moment of the molecule, μ. For an ensemble of random rotating molecules the transition dipole moments μ have a random orientation with respect to the laser's electric field vector, ε. The probability of absorption, P (v), is proportional to $|\varepsilon.\mu|^2$, where

$$\mu.\varepsilon = |\mu| |\varepsilon| \cos(\theta) \qquad (6.4.\text{iii})$$

and θ is the angle between the transition dipole moment and the electric field vector, ε^{22}. Therefore, since

$$P(v) \propto |\mu.\varepsilon|^2 \propto |\mu|^2 |\varepsilon|^2 \cos^2(\theta) \qquad (6.4.\text{iv})$$

the probability for molecules to absorb photons will follow a $\cos^2(\theta)$ pattern about μ.

For linearly polarised radiation, the electric vector, ε, defines a fixed axis in the laboratory frame that absorption will follow a $\cos^2(\theta)$ pattern about.

So far we have not considered the relationship between the transition dipole of the molecule, μ, and its structure. As fragments are formed by stretching an internuclear axis, provided the dissociation is fast, the relationship between the molecular axis and μ will determine in which directions the fragments recoil. We consider two limiting cases. Absorption through a parallel transition in which μ is directed parallel to the molecular axis is schematically shown in figure 6.4.1A. Absorption *via* a perpendicular transition in which μ is directed perpendicular to the molecular axis is shown in figure 6.4.1B. In case A, a parallel transition, the photofragments recoil primarily along the polarisation vector. In case B, a perpendicular transition, they move away perpendicular to the laser polarisation vector.
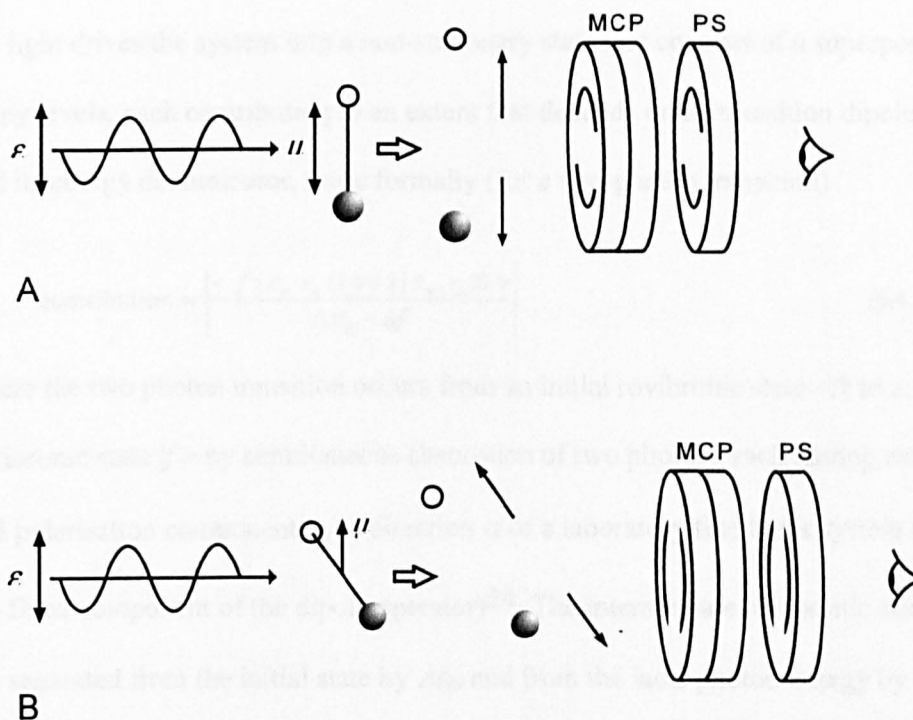
Figure 6.4.1. Photodissociation of a diatomic molecule *via* (a) a parallel and (b) a perpendicular transition. For a parallel and perpendicular transitions the transition dipole moments, μ, lie parallel and perpendicular to the molecular axis respectively. The photofragments recoil along the direction of the stretching molecular axis and, consequently, photofragments are produced parallel and perpendicular to μ. As the laser's electric vector defines a laboratory fixed axis frame, provided the dissociation is fast the photofragments will have anisotropic distributions. As described in more detail in the text, the speed and angular distributions are measured using a position-sensitive detector consisting of a pair of microchannel plates (MCP) coupled to a phosphor screen (PS).

More generally, for one-photon dissociation, the anisotropy function will have the form

$$I(\theta) = (4\pi)^{-1} [\, 1 + \beta P_2 (\cos \theta)] \qquad\qquad (6.4.\text{v})$$

where β has been termed the anisotropy parameter and P_2 is the second Legendre polynomial [$P_2 (\cos \theta) = \frac{1}{2} (3\cos^2 (\theta) - 1)$]. For the limiting cases, pure parallel and perpendicular transitions, β takes the values +2 and –1 respectively. An isotropic angular distribution is characterised by $\beta = 0$, *i.e.* independent of θ.

The angular distribution expected from multi-photon processes reflect the combined angular distribution of each 'one-photon' step, each being dependent on the states accessed, the electric vector of the radiation, ε, the transition dipole moment, μ, and the relationship between the transition dipole moment and the molecular axis. In practice

177

the light drives the system into a non-stationary state that consists of a superposition of

many levels, each contributing to an extent that depends on its transition dipole moment

and its energy denominator, more formally (for a two-photon transition)

$$\text{contribution} \propto \left| \frac{< f \mid \varepsilon_\alpha \; r_\alpha \mid i >< i \mid \varepsilon_\alpha \cdot r_\alpha \mid 0 >}{\Delta\varepsilon_{0i} - hf} \right| \qquad (6.4.\text{vi})$$

where the two photon transition occurs from an initial rovibronic state $<0\mid$ to a final

rovibronic state $\mid f>$ by simultaneous absorption of two photons each having energy hv

and polarisation component ε_α in direction α of a laboratory fixed axis system (r_α is the

lab fixed component of the dipole operator)[24]. The intermediate rovibronic states $\mid i >$

are separated from the initial state by $\Delta\varepsilon_{0i}$ and from the laser photon energy by $(\Delta\varepsilon_{0i} -$

$hv)$. It is clear form equation (7.6) that a simple one-parameter expression for the

angular distribution of the photofragments generated by a two-photon process is

inadequate. In general, for an n photon transition the angular distribution can be

described by

$$I(\theta) \propto 1 + \sum_{m=1}^{n} \beta_{2m} P_{2m}(\cos\theta) \qquad (6.4.\text{vii})$$

where n is the number of photons absorbed, β_{2m} are anisotropy parameters which

depend on the details of the excitation and decay of the molecule and P_{2m} are Legendre

polynomials. Product velocities are three dimensional vector properties. The angular

distributions depend on the alignment between the transition dipole moment and the

direction of the electric field. To measure these three-dimensional velocity distributions

we ideally would like to have a three dimensional time-of-flight detector. An ion

imaging spectrometer records the two-dimensional representation of the full three-

dimensional velocity distribution by accelerating the recoiling fragments in one

direction only and recording how the fragments impinge onto a two-dimensional

position sensitive detector. Clearly care must be taken to ensure that the accelerating

fields do not deflect the fragment ions. The following experimental overview describes how this is achieved.

6.5. The ion imaging spectrometer

Figure 6.5.1. shows schematically the basic features of a conventional spectrometer. The photolyte (neat or seeded in a carrier gas) is expanded supersonically through a pulsed valve and introduced into the first stage of a differentially pumped vacuum chamber. One or more skimmers collimate the molecular beam before entering the reaction and detection regions, located in the second stage of the vacuum chamber. A few centimetres downstream the molecular beam passes through a hole in a repeller plate. Between the repeller and extractor plates the molecular beam is intersected by one or more linearly polarised laser beams. The usually short ($\approx$3 ns), and focused laser pulse provides a well-defined starting point for the experiment in both time and space.

Extractor
Ionization Laser
Molecular Beam
Skimmer
Pulsed Beam Valve
Repeller
Product Ions
TOF Tube
Position-sensitive Detector
CCD Camera
Photolysis Laser
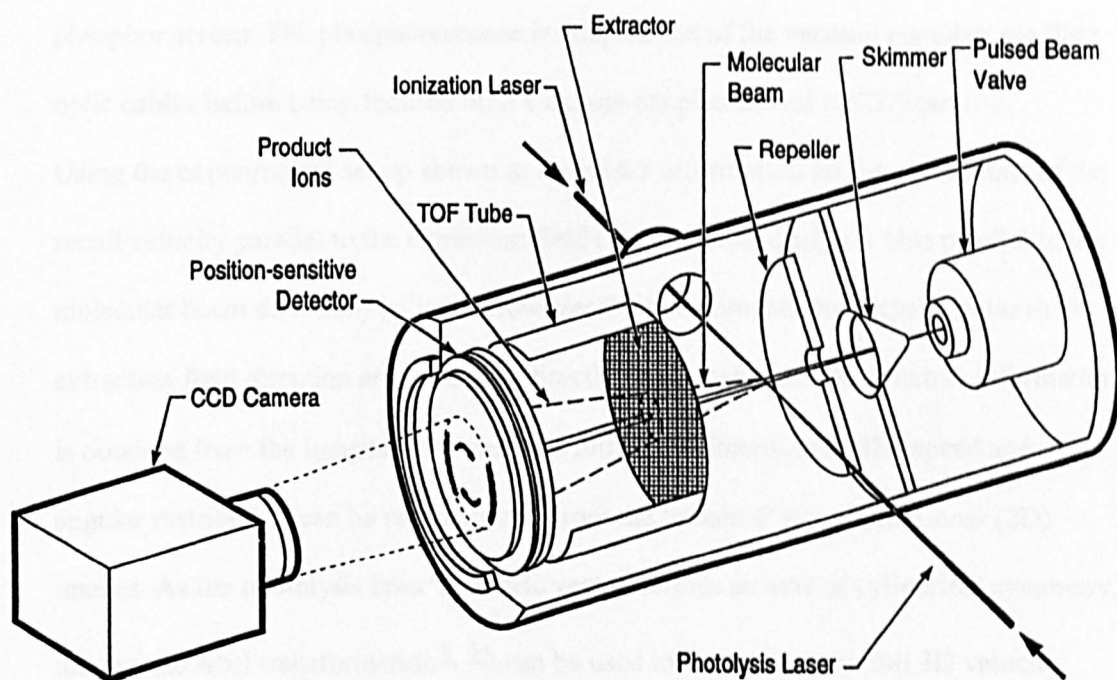
Figure 6.5.1. Schematic diagram of a photofragment imaging apparatus.

Following photolysis the fragments start to recoil away from the point where they where

generated. The products of interest are then state-selectively ionised using REMPI. The

expanding ion spheres are then accelerated by a one-direction only uniform electric

field, the extraction field, toward a field free time-of-flight tube. Typical fragment recoil

speeds are around 1 kms^{-1}, which means that following a time-of-flight delay of 10 μs

the spheres have expanded to measurable sizes. The flight times of the fragment ions,

and thus the sizes of the images, can be adjusted experimentally by varying the

magnitudes of the extraction field. At the end of the time-of-flight region the ions

impinge upon the position sensitive detector. The detector consists of a pair of chevron-

type microchannel plates coupled to a fast phosphor screen. In order to detect ions

mass-selectively the front plate of the microchannel plate is briefly pulsed upon arrival

of the ions of interest, thus ensuring maximum gain through the detector. The ions

generate an electron signal on the MCP channel they impinge on, these electron signals

180

are then amplified through the MCP assembly and induce phosphorescence on the phosphor screen. The phosphorescence is coupled out of the vacuum chamber *via* fibre optic cables before being focused onto a charge-coupled device (CCD) camera.

Using the experimental set up shown in figure 6.5 information on the co-ordinate of the recoil velocity parallel to the extraction field (which in this design is also parallel to the molecular beam direction) is 'lost.' However the two components perpendicular to the extraction field direction are measured directly on the detector. Quantitative information is obtained from the images only when the full three-dimensional (3D) speed and angular distribution can be reconstructed from the 'crushed' two-dimensional (2D) images. As the photolysis laser's electric vector defines an axis of cylindrical symmetry, the inverse Abel transformation[5, 25] can be used to reconstruct the full 3D velocity distribution from the crushed 2D image (provided the plane of the position-sensitive detector is parallel to the laser polarisation vector). Figure 6.5.2. illustrates idealised images for a hypothetical one-photon dissociation producing fragments of a single speed.
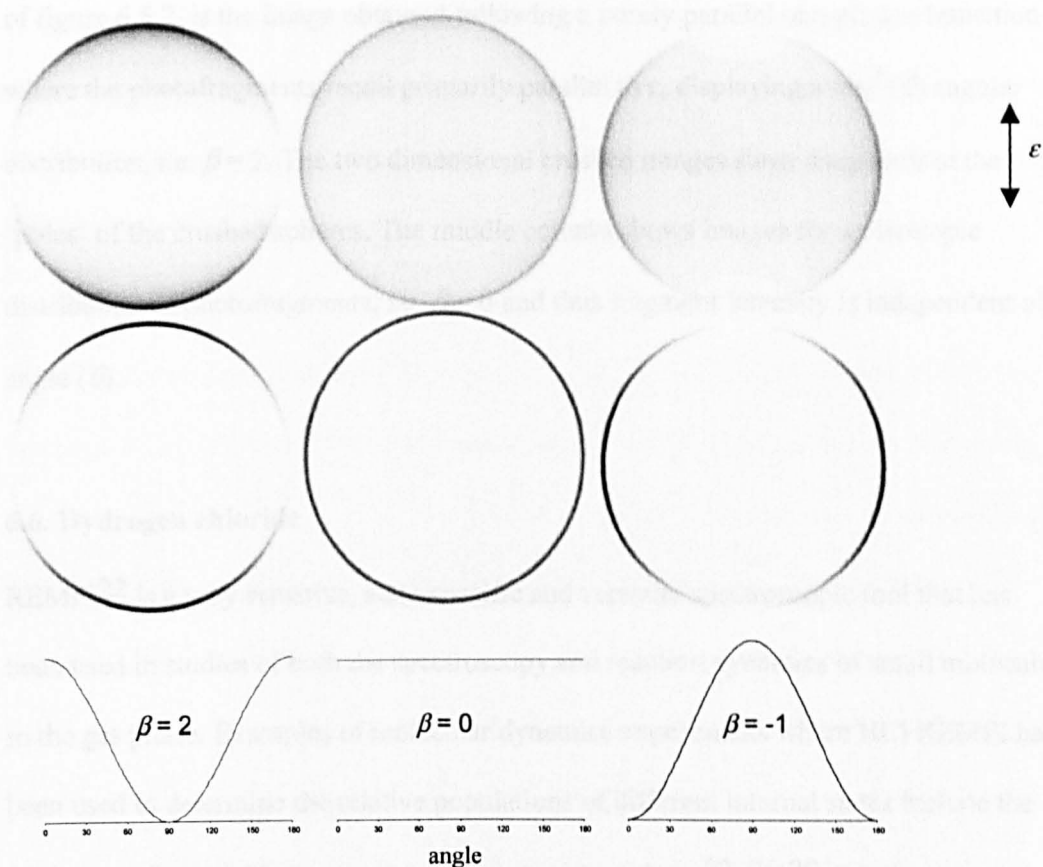
Figure 6.5.2. The top row shows simulated two-dimensional images corresponding to anisotropy parameters β_2 = 2, 0, and -1. The arrow indicates the direction of the laser field's polarisation. In the middle row the intensity distributions of the photofragments through the centre of the image are shown derived from the inverse Abel transformed images. Rotation of these slices around the laser polarisation vector provides the full three dimensional photofragment distribution.

On the right-hand-side of figure 6.5.2. a simulated image is shown for a purely perpendicular transition (β = -1). The photofragments recoil direction is primarily perpendicular to laser polarisation vector. A perpendicular transition produces a distribution of photofragments about the 'equator' of a sphere, where the polarisation vector lies parallel to the line joining the 'poles of the sphere.' As a result of the perpendicular relationship between the transition dipole moment and the molecular axis, the fragment distribution follows a $\cos^2(\theta+90)$ which is equivalent to $\sin^2(\theta)$. The corresponding Abel transformed reconstructed images are generally displayed by taking a slice through the full three-dimensional distribution. The full 3-D distribution is then obtained by rotating the slice around the laser polarisation vector. On the left-hand-side

of figure 6.5.2. is the image obtained following a purely parallel one-photon transition where the photofragments recoil primarily parallel to ε, displaying a $\cos^2 (\theta)$ angular distribution, *i.e.* $\beta = 2$. The two dimensional crushed images show fragments at the 'poles' of the crushed spheres. The middle column shows images for an isotropic distribution of photofragments, *i.e.* $\beta = 0$ and thus fragment intensity is independent of angle (θ).

6.6. Hydrogen chloride

REMPI[22] is a very sensitive, state-specific and versatile spectroscopic tool that has been used in studies of both the spectroscopy and reaction dynamics of small molecules in the gas phase. Examples of molecular dynamics experiments where HCl REMPI has been used to determine the relative populations of different internal states include the reactions between chlorine atoms and small hydrocarbons[22, 26-29]. In contrast to the more frequently employed method of laser-induced fluorescence (LIF), although more sensitive and versatile, the use of REMPI to determine state distributions is problematic[30-33]. In part, the determination of populations requires care because of the ease of saturating the resonant transition, which can cause the dependence of the ionisation rate on the laser power to vary from level to level[34]. In addition, previous studies have shown that many of the resonantly excited states are perturbed; such perturbations can have large effects on the rotational intensity factors[30, 33]. This is quite likely to occur in REMPI detection because of the high density of electronic states at energies reached by the absorption of two or three UV photons. Lastly, dissociation may compete with ionisation of either the intermediate or a superexcited state, and both parent and fragment ions can be produced[23, 24]. For some states (2+1) REMPI of HCl the fragment ion yield exceeds the molecular ion yield; this leads to further

complications in converting ion signals to relative internal state populations[32, 35].

Since it is difficult to calculate quantitatively the effects of all these factors on the

magnitude of an ion signal, it is useful to calibrate the REMPI signal strengths by using

a known internal state distribution, such as a Boltzmann distribution at a known

temperature[30, 32, 35, 36].

The HCl molecule provides a very good example of the complications in REMPI

detection as well as providing a stern challenge in trying to understand the competing

processes. In the case of resonant multiphoton excitation, the selection of intermediate

states of known symmetry and angular momentum governs the opening of the

competitive channels[37]. The resonant states participating in these pathways include

Rydberg states and valence electron excited states as well as multiply excited states.

Excitation through Rydberg, valence and / or ion-pair states can be used to probe

superexcited states which are generally defined as molecular states whose energy is

greater than the first ionisation potential[23, 37-45]. At such high energies, the

superexcited states can dissociate, predissociate as well as electronically and

vibrationally autoionise. Previous experimental studies on the dynamics of HCl REMPI

include photoelectron spectroscopy[23] (PES), zero-kinetic-energy photoelectron

spectroscopy[23, 46] (ZEKE-PES), dispersed fluorescence[23, 43, 46], time-of-flight[30,

33, 47-50], pulsed-field ionisation[51] and velocity-aligned Doppler spectroscopy[24, 52]

(VADS). However, none of the previous studies could distinguish simultaneously the

different reaction pathways and the angular distributions. REMPI-PES studies by de

Beer *et al.*[51] have shown that HCl^+ is formed in all energetically allowed vibrational

levels and in both spin-orbit states, *i.e.* $^2\Pi_{3/2}$ and $^2\Pi_{1/2}$. In addition, they detected

electrons originating from the excited atoms H*(n = 2), Cl* (*$3p^4 4s\ ^2P_{3/2}$*) and Cl* (*$3p^4 4p$*

$^2D_{5/2}, ^2D_{3/2}$ and *$^2S_{1/2}$*) for some intermediate resonant states. The threshold for formation

of these excited atoms requires three photons in the energy range studied ($hv \approx 5$ eV)

and so ionisation of the excited atoms constitutes a four-photon process. Ionisation of

the excited atoms is saturated even at low laser intensities and consequently, the REMPI

signal will still show the three-photon power dependence expected for (2+1) REMPI.

VADS experiments by Gordon et al.[24, 52] detecting Cl atoms showed evidence for

predissociation of states at the two-photon level, i.e. a two-photon process. The various

mechanisms in operation in HCl (2+1) REMPI are summarised in table 6.6.1.

Table 6.6.1. Competing mechanisms for photodissociation and photoionisation of HCl

Two-photon processes		
Excitation to a Rydberg / valence state:	$HCl + 2hv \rightarrow HCl^*$	R(1)
Predissociation:	$HCl^* \rightarrow H + Cl$	R(2)
Three-photon processes		
Direct ionisation:	$HCl^* + hv \rightarrow HCl^+$	R(3)
Population of a superexcited state:	$HCl^* + hv \rightarrow HCl^{**}$	R(4)
Autoionisation:	$HCl^{**} \rightarrow HCl^+$	R(5)
Dissociation to produce excited atoms:	$HCl^{**} \rightarrow H^* + Cl$	R(6)
	$HCl^{**} \rightarrow H + Cl^*$	R(7)
Fluorescence to produce ground state atoms:	$H^* \rightarrow H + hv$	R(8)
	$Cl^* \rightarrow Cl + iv$	R(9)
Four-photon processes		
Ionisation of excited atoms	$H^* + hv \rightarrow H^+$	R(10)
	$Cl^* + hv \rightarrow Cl^+$	R(11)

REMPI time-of-flight studies by Wallace and workers[47-50] have shown that fragments

are generated by all rovibrational levels associated with the V and E $^1\Sigma^+$ (0^+) states and

that there is strong interaction between the vibrational levels of the E and V $^1\Sigma^+$ (0^+)

states. This latter point was further enhanced by the work of Kvaran et al.[53] and of

Liyanage et al.[54]

6.7. Experimental

The (2+1) REMPI of HCl experiments were performed at the University of Nijmegen

(The Netherlands) in collaboration with Prof. David Parker and Bernard Bakker.

The ion imaging spectrometer used for the experiments follows the design of the conventional spectrometer described in the introduction bar one important difference. The ion imaging spectrometer used modified ion optics that focused ions according to their velocities. The conventional ion-imaging spectrometer uses a parallel electric field to extract the ions and accelerate them into a time-of-flight region. Fine wire grids are used to ensure parallel field lines. At first sight this seems ideal, as the projected radius is a direct measure of the fragment velocity. However, parallel field lines also project the ionisation volume (defined by the crossing of the laser and molecular beams) onto each point of the detector. Furthermore, the grids themselves cause further distortions in the image by deflecting the ions from their initial trajectories. Combined these two effects lead to resolution problems in conventional ion imaging. Eppink and Parker[11, 12] removed the grids from the electrodes leaving open holes and found that by setting the voltages of the latter two electrodes to a set ratio, the electrode manifold acts as an immersion lens (see figure 6.7.1. for a schematic of the velocity mapping spectrometer). The lens was found to map all ions of the same velocity onto the same position of the microchannel plate detector irrespective of where the ion was formed in the ionisation volume, thus deblurring the image. Using this velocity mapping set up the instrument was able to record photoelectron images as well as ion images even though the instrument was not designed for electron detection. None of the extensive measures (μ-metal shields, graphite coatings, non-magnetic materials, etc) required in modern angle-resolved photoelectron spectroscopy was used, and yet images comparable to those of regular ions were obtained.
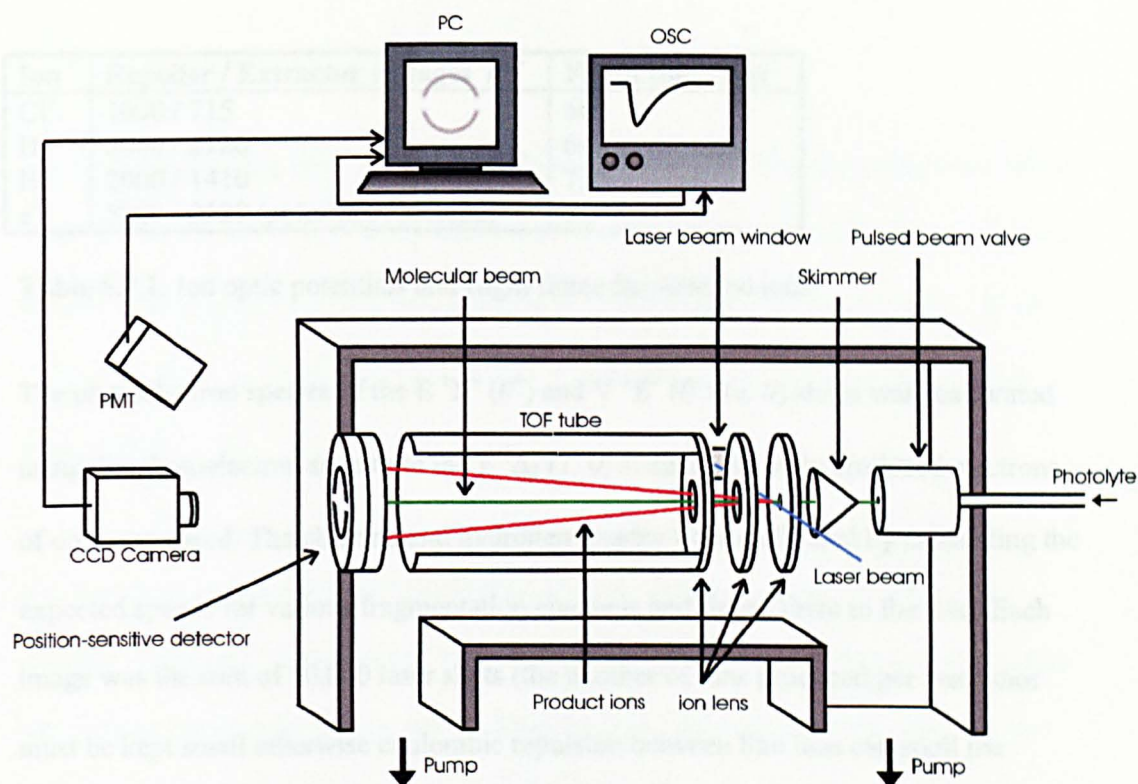
Figure 6.7.1. Schematic of the ion imaging spectrometer used to record the HCl (2+1) REMPI spectra.

A beam of ≈ 8 % HCl seeded in a 1 bar pulsed expansion of He was passed through a

1mm skimmer then a 1 mm hole in the repeller plate, as a result the beam size at the

laser crossing was limited to a diameter of ≈1.1 mm. The output from a frequency

tripled Nd:Yag pumped dye laser using Coumarin 460 dye was frequency doubled in a

BBO (β-bariumborate) crystal. The doubled light (≈ 0.5 mJ / pulse, 5 ns pulselength,

and 0.8 cm^{-1} bandwidth) was focused with a 19 cm lens onto the molecular beam. The

cylindrical symmetry necessary for reconstruction of the 3D distribution from the 2D

image was retained with the polarisation vector of the laser standing parallel to the

detector face. The flight times and voltages of the ion optics are given in table 6.7.1

Mass selective detection of an ion was achieved by pulsing the gain of the front channel

plate as the ion of interest arrived.

Ion	Repeller / Extractor voltages / V	Flight times / ns
Cl^+	1000 / 715	605
H^+	3000 / 2120	640
H^+	2000 / 1410	770
e^-	5000 / 3520 (polarities reversed)	58

Table 6.7.1. Ion optic potentials and flight times for detected ions.

The photoelectron spectra of the E $^1\Sigma^+$ (0^+) and V $^1\Sigma^+$ (0^+) (v, 0) states were calibrated using the photoelectron spectra of the F $^1\Delta_2$ (1, 0) state as this state produced electrons of only one speed. The chlorine and hydrogen images were calibrated by calculating the expected speeds for various fragmentation channels and fitting them to the data. Each image was the sum of 50,000 laser shots (the number of ions produced per laser shot must be kept small otherwise coulombic repulsion between like ions can spoil the images).

6.8 HCl (2+1) REMPI results

The velocity mapping spectrometer was able to acquire photoelectron images as well as 'regular' ion images of the fragment cations. Accordingly, for each REMPI transition up to three images (H^+, Cl^+ and e^-) were recorded. The three ion images for the V $^1\Sigma^+$ (0^+)($v = 15$) ($J = 1$) $\leftarrow \leftarrow$ X $^1\Sigma^+$ (0^+) ($v = 0$) ($J = 1$) transition, $\lambda = 231.5$ nm are shown in figure 6.8.1.

It is readily apparent that the photoelectron images were the sharpest and that the chlorine ion images were the least well resolved. The different resolution of the images was a direct result of the image sizes. Using the flight times indicated in table 6.2 and their calculated recoil speeds the diameter of the photoelectron image that impinged upon the MCP detector for the transition shown in figure 6.8 was calculated to be approximately 160 times greater than the diameter of the chlorine image. Although optical lenses situated between the CCD camera and the phosphor screen were used to magnify the chlorine ion image and so reduce the image size discrepancy, as fewer electron channels of the MCP assembly and fewer pixels of the CCD camera were used to measure the chlorine ion images, the resolution obtainable was less.

The higher resolution of the photoelectron images was necessary, as it was readily apparent that the photoelectron images contained many more rings than the hydrogen and chlorine ion images. The extra photoelectrons were due to the formation of HCl^+ in a wide variety of vibrational and spin orbit states.

Figure 6.8.1. HCl (2+1) REMPI @ 231.5 nm V(*15*) Q(*1*)

Chlorine atoms
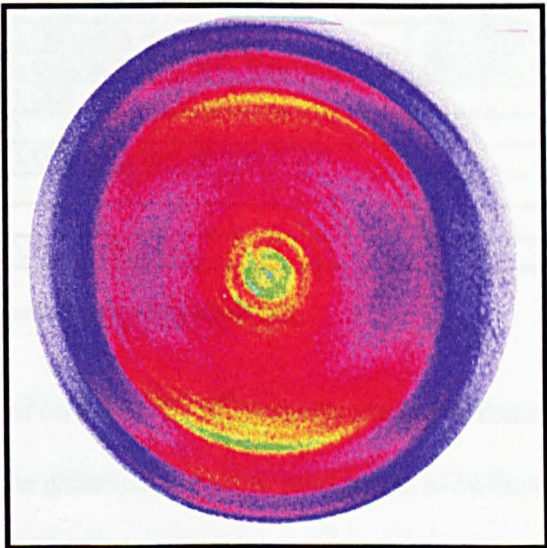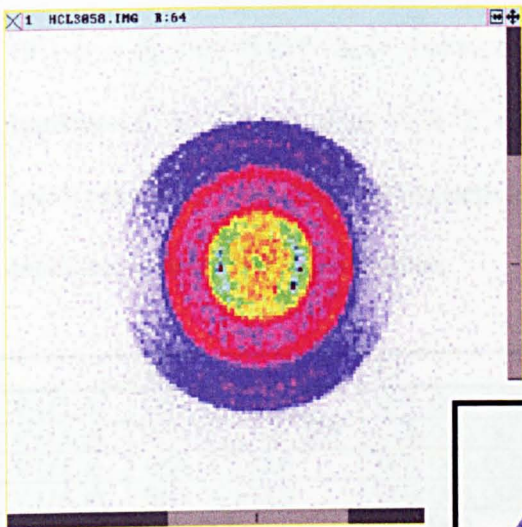
H atoms

photoelectrons
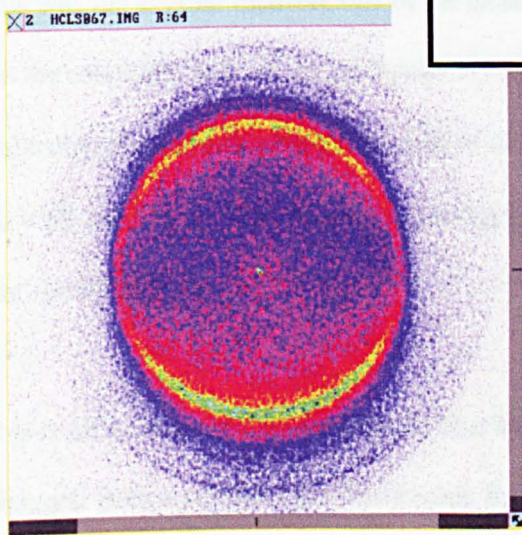
The images obtained of the ionic photofragments and photoelectrons are summarized in Table 6.8.1. V (v, 0) refers to the two-photon transition V $^1\Sigma^+$ (0^+)($v = v$) $\leftarrow \leftarrow$ X $^1\Sigma^+$ (0^+) ($v = 0$), F (v, 0) to F $^1\Delta_2$ ($v = v$) $\leftarrow \leftarrow$ X $^1\Sigma^+$ (0^+) ($v = 0$) and E (v, 0) to the transition E $^1\Sigma^+$ (0^+) ($v = v$) $\leftarrow \leftarrow$ X $^1\Sigma^+$ (0^+) ($v = 0$). As is conventional the labels O, Q and S refer to ΔJ = -2, 0 and +2 respectively, and the initial rotational state of the HCl molecule is described in parenthesis.

	H$^+$	Cl$^+$	e$^-$
V (12, 0)	Q(0), Q(2)	Q(0), Q(1), Q(2), S(0), S(1)	Q(0), Q(2)
V (13, 0)	Q(0), Q(1), S(0), S(1)	Q(0), Q(1), Q(2), Q(3), S(0), O(2)	Q(0), Q(1), Q(2), S(0)
V (15, 0)	Q(0), Q(1), Q(2)	Q(0), Q(1), Q(2), Q(3), Q(4), S(0), S(1), O(2), O(3)	Q(0), Q(1), Q(2)
V (16, 0)	Q(0), Q(1), Q(2)	Q(0), Q(1), Q(2)	
V (17, 0)	Q(0), Q(2)	Q(0), Q(2)	
g (0,0)		Q(0), Q(1), Q(2), Q(3), Q(4), S(0), S(1), S(2)	
F (1, 0)			Q(2)
E (1, 0)	Q(1)		Q(1)
E (0,0)		Q(0), Q(1), Q(2), S(0), S(1)	

Table 6.8.1. A summary of the images obtained for (2+1) REMPI of HCl.

As can be seen the results concentrated on the V $^1\Sigma^+$ (0^+) valence state. The reason for this was the angular distributions of the chlorine fragments were found to be dependent on the rotational state of the molecule. This behaviour was first observed whilst recording the chlorine photofragments of the Q (J) V $^1\Sigma^+$ (0^+) ($v = 15$) $\leftarrow \leftarrow$ X $^1\Sigma^+$ (0^+) ($v = 0$), transitions. The chlorine ion images of the Q (0) and Q (1) V (15, 0) transitions are shown in figure 6.8.2.

It is readily apparent that the angular distribution of the two innermost channels changed from a parallel type distribution for the Q (0) transition to a perpendicular type transition for the Q (1) transition.

Q(0)

Q(1)

ε
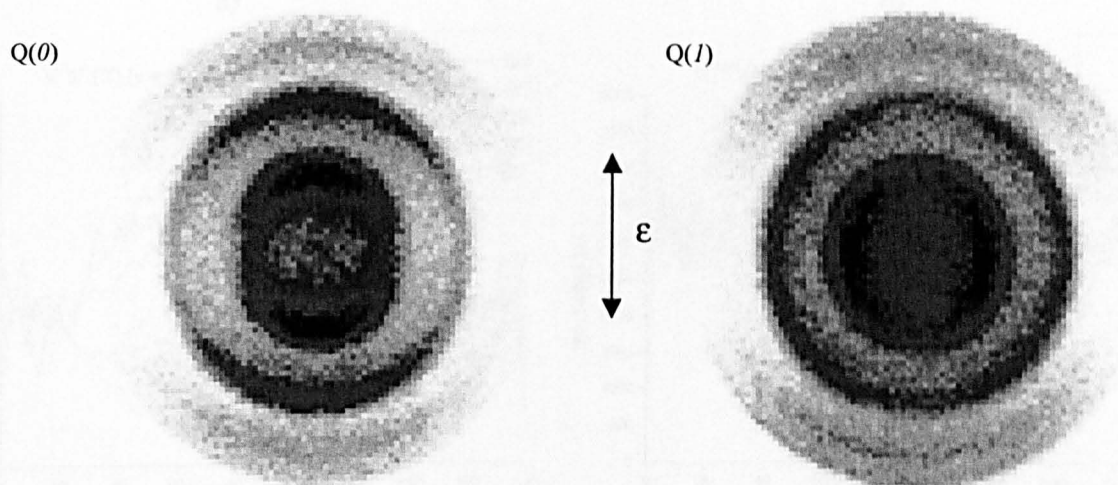
Figure 6.8.2. Chlorine ion images of the Q (*0*) and Q (*1*) V (*15, 0*) transitions.

The angular distribution of the inner channels of all of the Q (*J>0*) V (*15, 0*) transitions displayed a perpendicular type distribution. Furthermore, despite the fact that both transitions progressed through the same resonant state, V $^1\Sigma^+$ (0^+) (*v = 15, J = 2*), the two inner channels of the S (*0*) transition displayed a parallel type distribution (like Q (*0*)) and not the perpendicular distribution of the Q (*2*) transition. This behaviour is more clearly seen after Abel inversion of the images. The angular distribution of the middle and outer chlorine channels, after Abel inversion, for the Q (*J*) V $^1\Sigma^+$ (0^+) (*v = 15*) transitions is shown in figure 6.8.3a and 6.8.3b, respectively. It is readily evident that unlike the inner two channels the outermost channel was insensitive to *J* and *ΔJ* (S, Q, O) and remained parallel for all of the transitions through the V $^1\Sigma^+$ (0^+) (*v = 15*) state investigated.
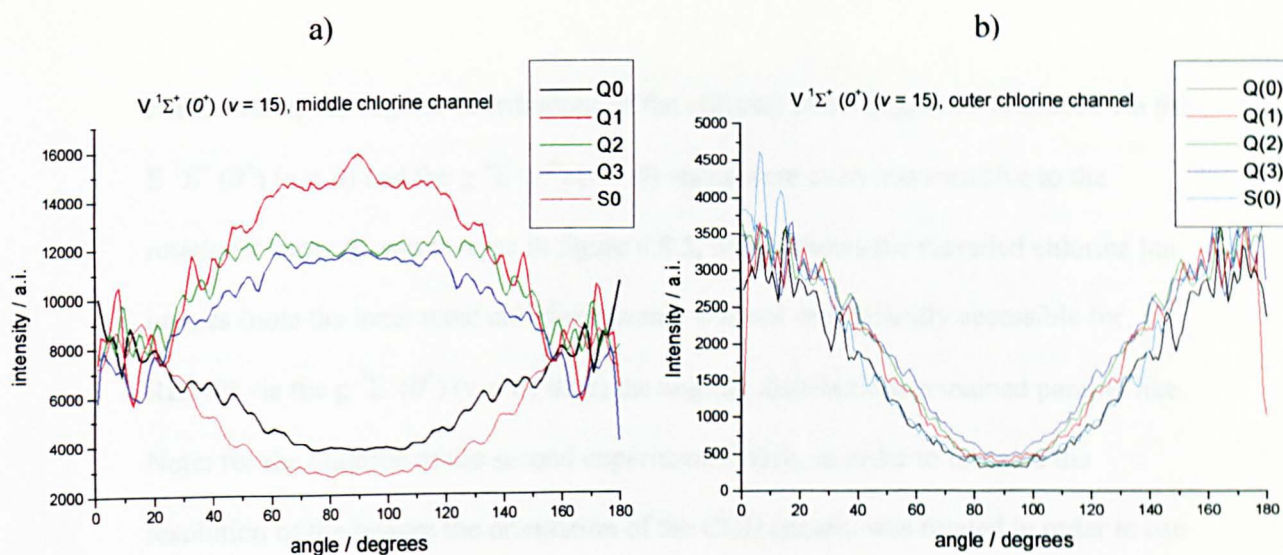
Figure 6.8.3. Angular distributions of the middle (a) and outer (b) chlorine channels of the Abel inverted chlorine ion image of the $V \, ^1\Sigma^+ \, (0^+) \, (v = 15) \leftarrow \leftarrow X \, ^1\Sigma^+ \, (0^+) \, (v = 0)$ transitions.

Whilst the chlorine ion images of the Q (J) V (v = 12) transitions displayed similar switching behaviour (the inner two chlorine channels switched from a parallel distribution to a perpendicular distribution), the images obtained of the Q (J) V (v = 13) transitions displayed a noticeably less dramatic angular distribution behaviour. Instead of switching to a perpendicular type distribution, for Q (J>0) transitions the ions displayed an almost isotropic distribution. This is clearly visible in figure 6.8.4, which shows the angular distributions of the Abel inverted chlorine images of the Q (J) V (v = 13) transitions.
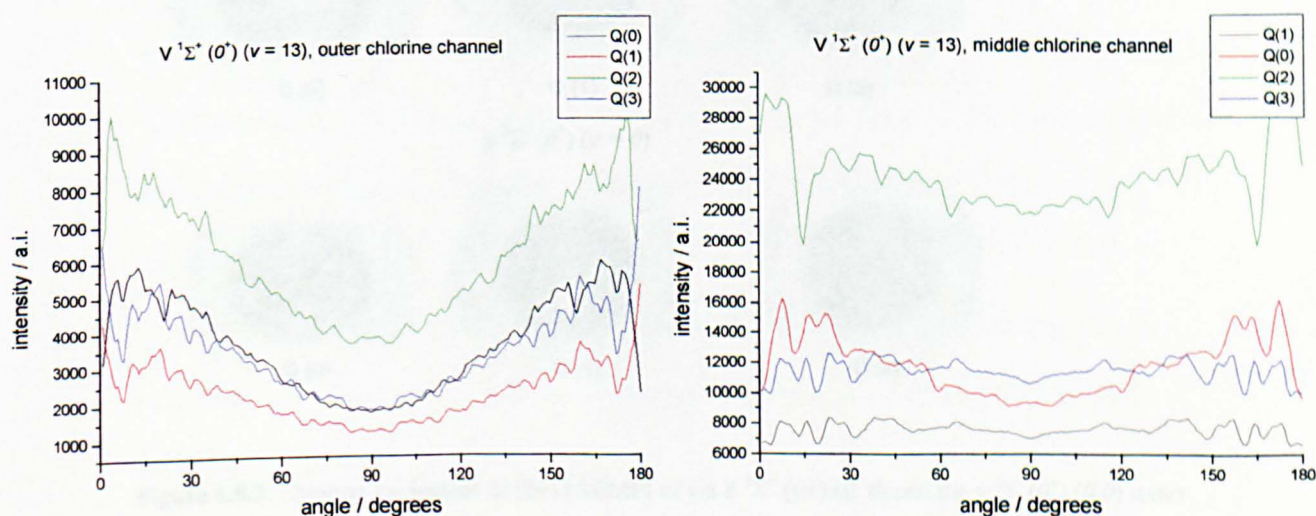
Figure 6.8.4. Angular distributions of the middle and outer rings of the Abel inverted chlorine ion images.

Furthermore, the angular distributions of the chlorine photofragments produced via the E $^1\Sigma^+$ (0^+) ($v = 0$) and the g $^3\Sigma^-$ (0^+) ($v = 0$) states were even less sensitive to the rotational state. As can be seen in figure 6.8.5, which shows the recorded chlorine ion images (note the inner most chlorine channel was not energetically accessible for REMPI via the g $^3\Sigma^-$ (0^+) ($v = 0$) state) the angular distributions remained parallel like. Note: for the duration of the second experimental visit, in order to increase the resolution of the images the orientation of the CCD camera was rotated in order to use as many of the cameras pixels as possible (the camera had a rectangular field-of-vision). Furthermore, the time-of-flight region had been lengthened between the two visits. Although this modification permitted larger chlorine images to be obtained (increased resolution) a drawback was that many of the electron signals present in the photoelectron images would not have been detected (the electrons would have simply moved too far in the increased time-scale of the experiment). As a result the photoelectron images of the E Σ^+ (0^+) ($v = 0$) and the g $^3\Sigma^-$ (0^+) ($v = 0$) states were not recorded.
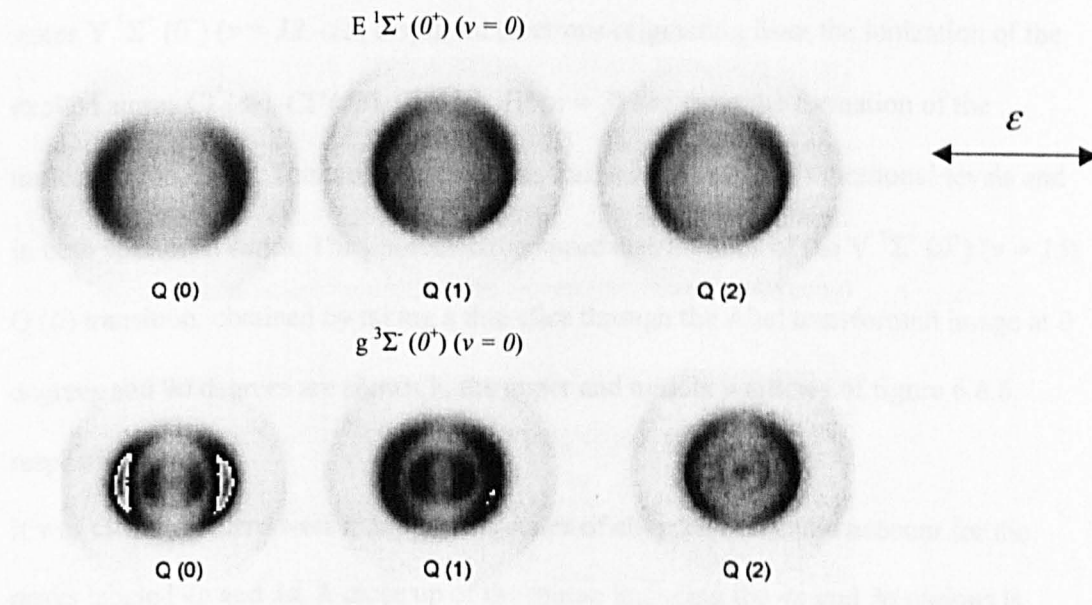
Figure 6.8.5. Chlorine ion images of (2+1) REMPI of via E $^1\Sigma^+$ ($0+$) ($0, 0$) and the g $^3\Sigma^-$ (0^+) ($0,0$) states

An advantage of recording the photoelectron image as well as the fragment ion image was that the channels forming the atomic ions were visible in both images, thus the images could be 'tied' together and the origin of each reaction channel could be assigned more confidently. The single image of the F $^1\Delta_2$ ← ← X $^1\Sigma^+$ (0^+) (*1, 0*) transition was recorded for calibration purposes. REMPI photoelectron spectroscopy (PES) studies by de Beer *et al*[51] had already demonstrated that REMPI *via* the F $^1\Delta_2$ (*2*) Rydberg state produced electrons of one speed only that corresponded to formation of the molecular ion, HCl^+ ($\Delta v = 0$). The photoelectron image of the F $^1\Delta_2$ (*2*) state, since electrons of one known speed were produced, was used to calibrate the other photoelectron images. As the mass of the ions were much greater than that of the electron, the photoelectron speeds were assumed to be determined solely by the kinetic energy release of the photolysis event (kinetic energy release = $n^*h\nu$ – ionization energy – internal energy of ion).

As was seen in figure 6.8.1. the photoelectron images obtained via the V $^1\Sigma^+$ (0^+) (*v*) valence states displayed much structure. The photoelectron images from the valence states V $^1\Sigma^+$ (0^+) (*v = 12 –15*) displayed electrons originating from the ionization of the excited atoms Cl^*(*4s*), Cl*(*4p*), Cl*(*3d*), H*(*n = 2*) and from the formation of the molecular ion, HCl^+. The molecular ion was formed in a range of vibrational levels and in both spin-orbit states. The photoelectron speed distributions of the V $^1\Sigma^+$ (0^+) (*v = 15*) Q (*0*) transition, obtained by taking a thin slice through the Abel transformed image at 0 degrees and 90 degrees are shown in the upper and middle windows of figure 6.8.6, respectively.

It was clear that there were many atomic states of chlorine that could account for the peaks labeled *4p* and *3d*. A close up of the region including the *4p* and *3d* regions is shown in figure 6.8.7.
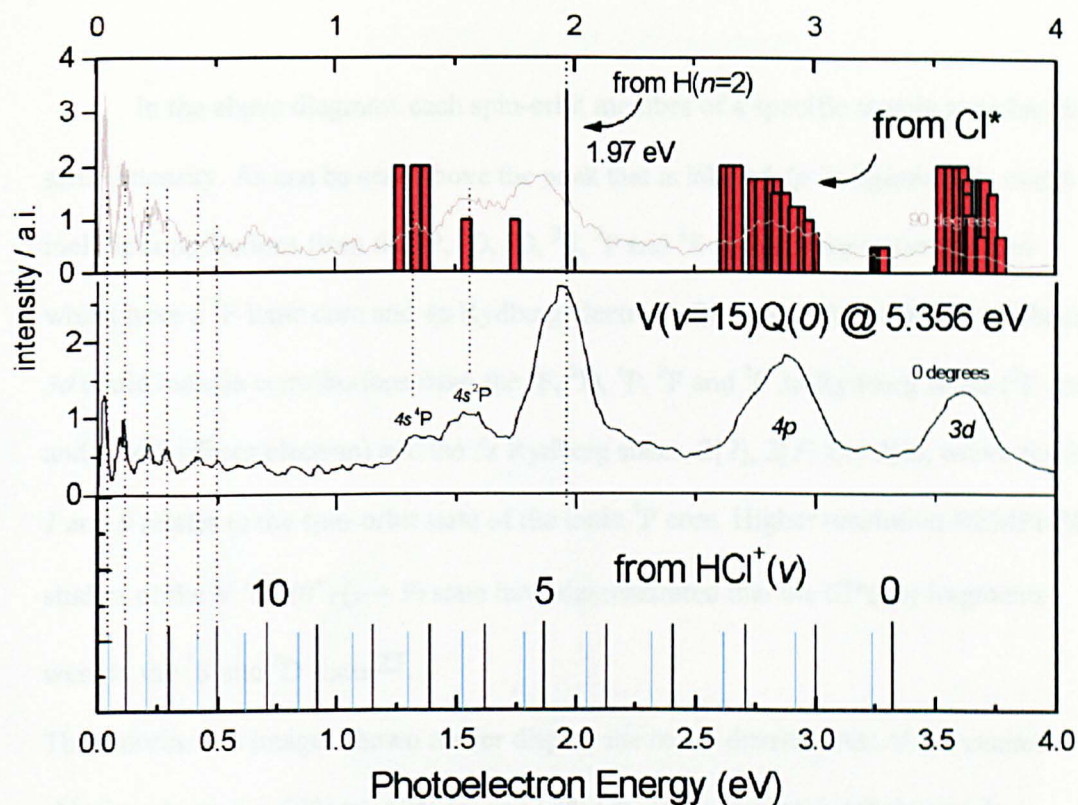
Figure 6.8.6. Photoelectron speed distributions of the Q (*0*) V (*v* = *15*) (2+1) REMPI transition, the upper and middle kinetic energy profiles were taken at 90 and 0 degrees, respectively.
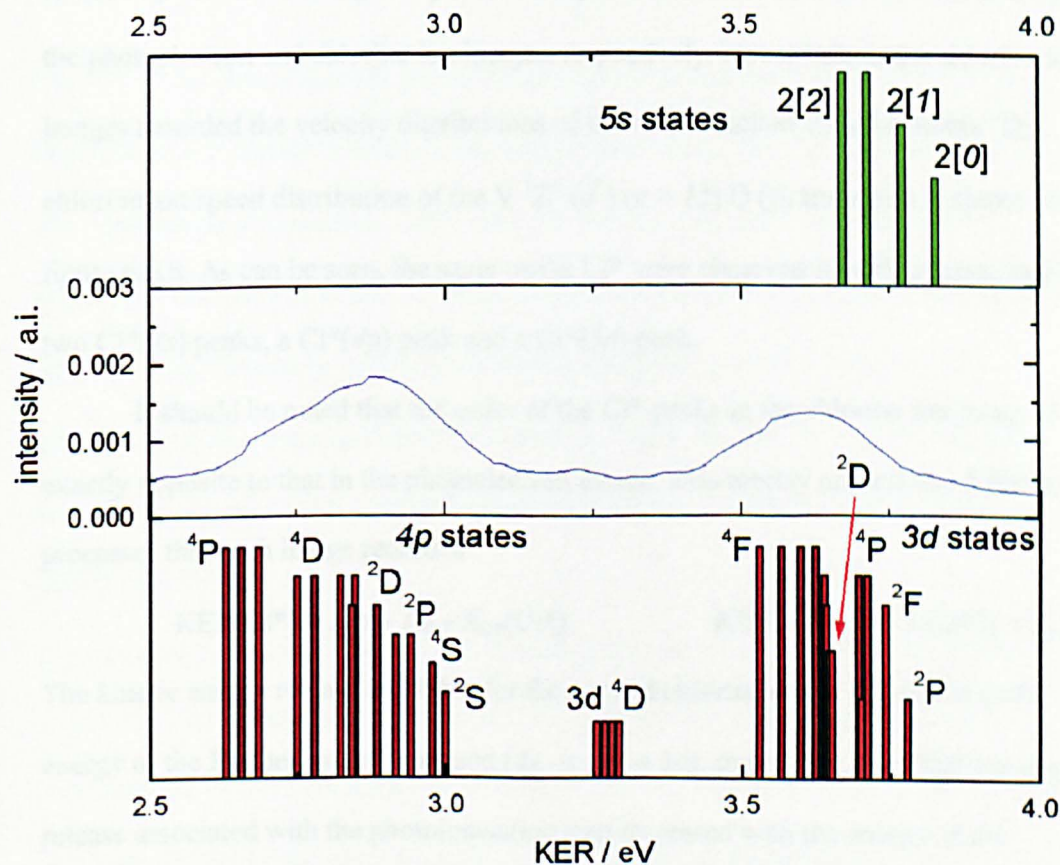
Figure 6.8.7. Close up of the photoelectron speed distribution (at 90°) of the Q (*0*) V (*v* = *15*) (2+1) REMPI transition and the atomic states in the appropriate energy regime.

In the above diagrams each spin-orbit member of a specific atomic state has the same intensity. As can be seen above the peak that is labeled *4p* in figure 6.8.6. could include contributions from the ^4P, ^4D, ^2D, ^2S, ^2P and ^4S *4p* Rydberg states (each of which have a ^3P ionic core and *4p* Rydberg electron). Similarly, the peak that is labeled *3d* could include contributions from the ^4F, ^2D, ^4P, ^2F and ^2P *3d* Rydberg states (^3P cores and a *3d* Rydberg electron) and the *5s* Rydberg states, 2[*2*], 2[*1*] and 2[*0*], where the *2*, *1* and *0* relates to the spin-orbit state of the ionic ^3P core. Higher resolution REMPI-PES studies of the V $^1\Sigma^+$ (0^+) (*v* = *9*) state have demonstrated that the Cl*(*4p*) fragments were in the ^2S and ^2D states[23].

The chlorine ion images shown earlier display the recoil distributions of the excited chlorine atoms, i.e. Cl*(*4s*), Cl*(*4p*) and Cl*(*3d*). These Rydberg states were then ionized by the UV laser light to produce the photoelectrons and chlorine ions detected in the photoelectron and chlorine ion images, respectively. Nevertheless, the chlorine ion images recorded the velocity distributions of the of the excited chlorine atoms. The chlorine ion speed distribution of the V $^1\Sigma^+$ (0^+) (*v* = *15*) Q (*0*) transition is shown in figure 6.8.8. As can be seen, the same peaks Cl* were observed in both images, namely two Cl*(*4s*) peaks, a Cl*(*4p*) peak and a Cl*(*3d*) peak.

It should be noted that the order of the Cl* peaks in the chlorine ion image is exactly opposite to that in the photoelectron image. This merely reflects the different processes that each image recorded

$$\text{KER(Cl*)} = 3h\upsilon - D_0 - E_{int}\text{(Cl*)} \qquad\qquad \text{KER(e}^-\text{)} = h\upsilon - \text{I.E.(Cl)} + E_{int}\text{(Cl*)}$$

The kinetic energy release available for the excited chlorine atoms decreased as the energy of the Rydberg state increased (*4s* → *4p* → *3d*). In contrast, the kinetic energy release associated with the photoionisation step increased with the energy of the Rydberg state, as less energy was required to ionize the excited atoms.
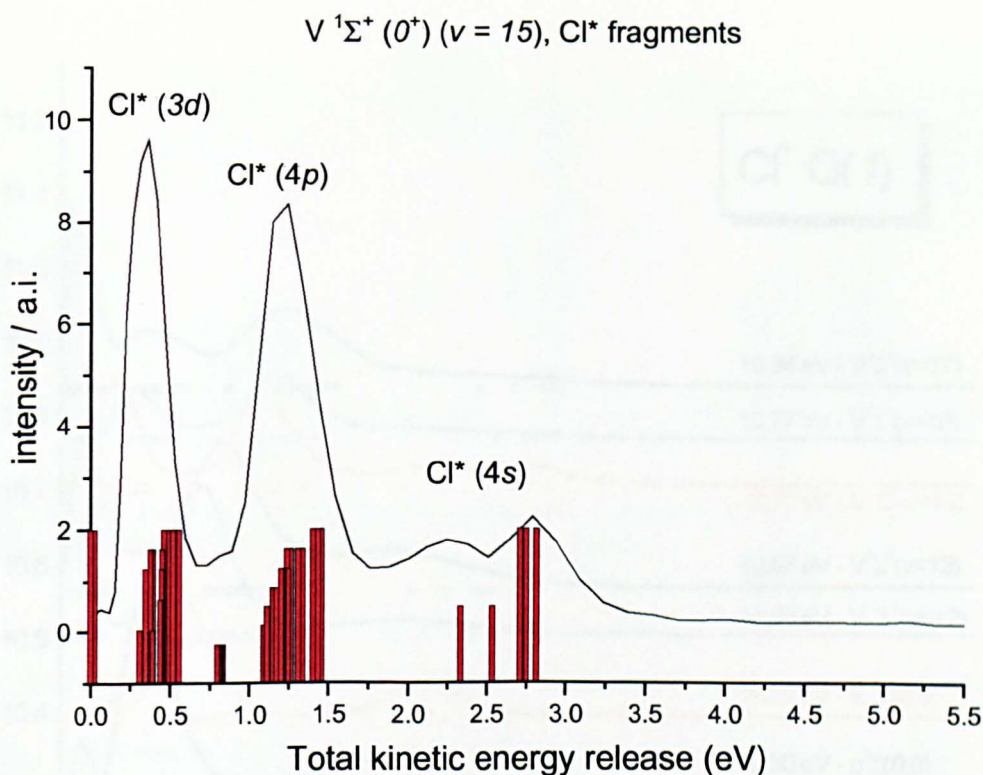
Figure 6.8.8 Chlorine ion speed distribution of the V $^1\Sigma^+$ (0^+) ($v = 15$) Q (0) transition.

The Cl* states detected in the photoelectron image did not include all of the states energetically accessible (infinitely separated atom limit). The ^{4}P $5p$ Rydberg state was also energetically accessible, KER ≈ 0.1 eV, however no such chlorine ions or photoelectrons were detected. At larger photolysis energies another chlorine channel was observed. Similarly, at lower photolysis energies some of the reaction channels detailed above were energetically inaccessible. The KER and the number of peaks detected in the chlorine ion images for each electronic – vibrational state studied is shown figure 6.8.9.

As expected the recoil energy of the fragments increased as the photolysis energy increased. The threshold energy of the Cl*($3d$) fragment was estimated by linear extrapolation of the peak apex until the kinetic energy release was zero. The value obtained, 91 000 $\pm$ 500 cm^{-1}, suggesting the majority of the $3d$ fragment intensity was due to the ^{2}D state (91 127 cm^{-1}).
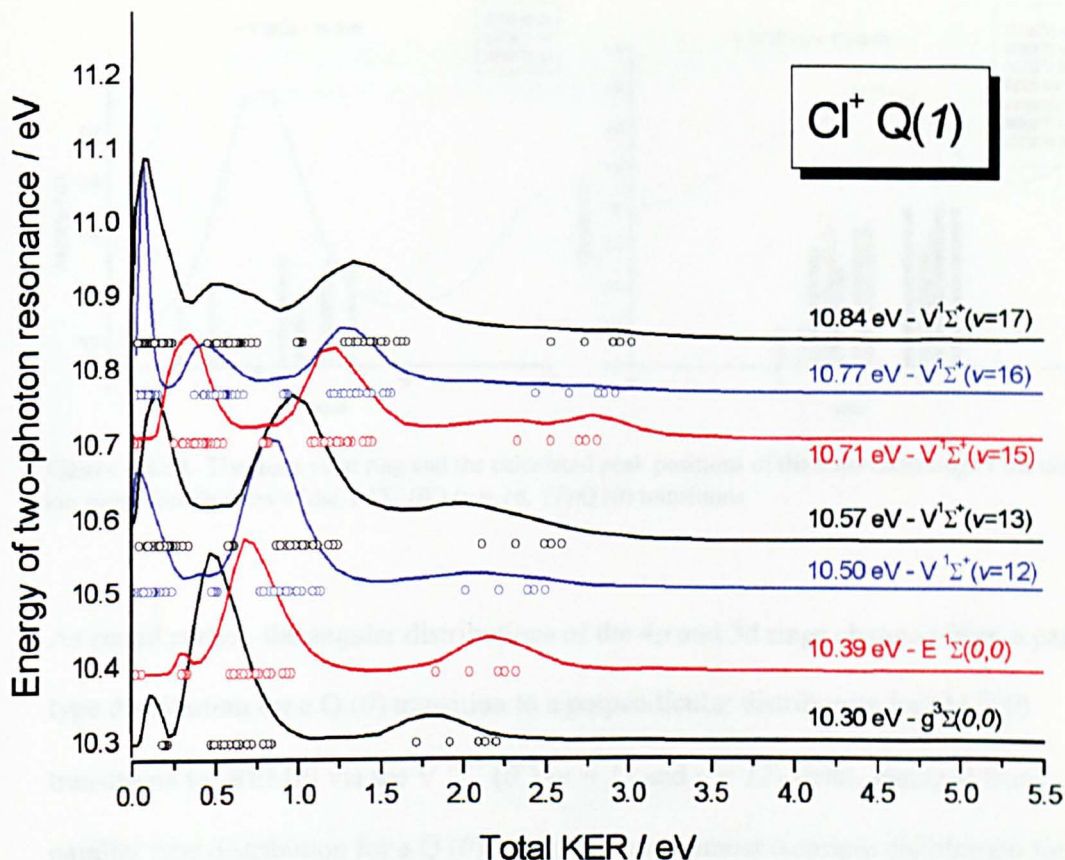
Figure 6.8.9. Chlorine atom speed distributions for each electronic – vibrational state sampled. The circles represent the calculated kinetic energy release associated with the energetically accessible fragments, re figures 6.8.8 and 6.8.10.

The speed distributions and the calculated peak positions of the inner most peaks for the Q (0) V $^1\Sigma^+$ (0^+) (v = 16 and v = 17) transitions are shown in figure 6.8.10. It would appear that another reaction channel has opened on passing from the v = 16 state to the v = 17 state (the shoulder visible in the v = 17 distribution was present in both v = 17 chlorine ion images recorded and absent in the three v = 16 images recorded).
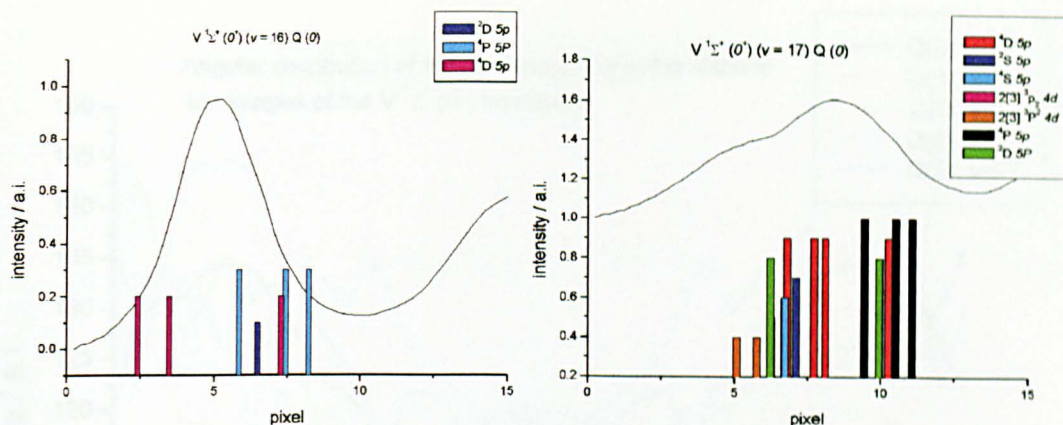
Figure 6.8.10. The inner most ring and the calculated peak positions of the inner most ring of the chlorine ion speed distributions of the V $^1\Sigma^+$ (0^+) (v = 16, 17) Q (0) transitions.

As stated earlier, the angular distributions of the 4p and 3d rings changed from a parallel type distribution for a Q (0) transition to a perpendicular distribution for Q (J>0) transitions for REMPI via the V $^1\Sigma^+$ (0^+) (v = 15 and v = 12) states, changed from a parallel type distribution for a Q (0) transition to an almost isotropic distribution for Q (J>0) transitions for REMPI via the V $^1\Sigma^+$ (0^+) (v = 13), and remained parallel like for Q (J) transitions via the E $^1\Sigma^+$ (0^+) (v = 0) and g $^3\Sigma^-$ (0^+) (v = 0) states. The angular distributions of the outer three 4s, 4p and 3d channels of the Q (J) V $^1\Sigma^+$ (0^+) (v = 16 and 17) transitions resembled that of the Q (J) V $^1\Sigma^+$ (0^+) (v = 13) transitions, namely the 4s channel was always parallel like whereas the 4p and 3d changed from a parallel like to an almost isotropic distribution. Although the innermost rings of the Q (J) V $^1\Sigma^+$ (0^+) (v = 16, 17) were very small and consequently the angular distributions were erratic, the angular distribution did not display the same J dependent behavior. Rather, like the 4s channel, the innermost ring retained a parallel type distribution, see figure 6.8.11.
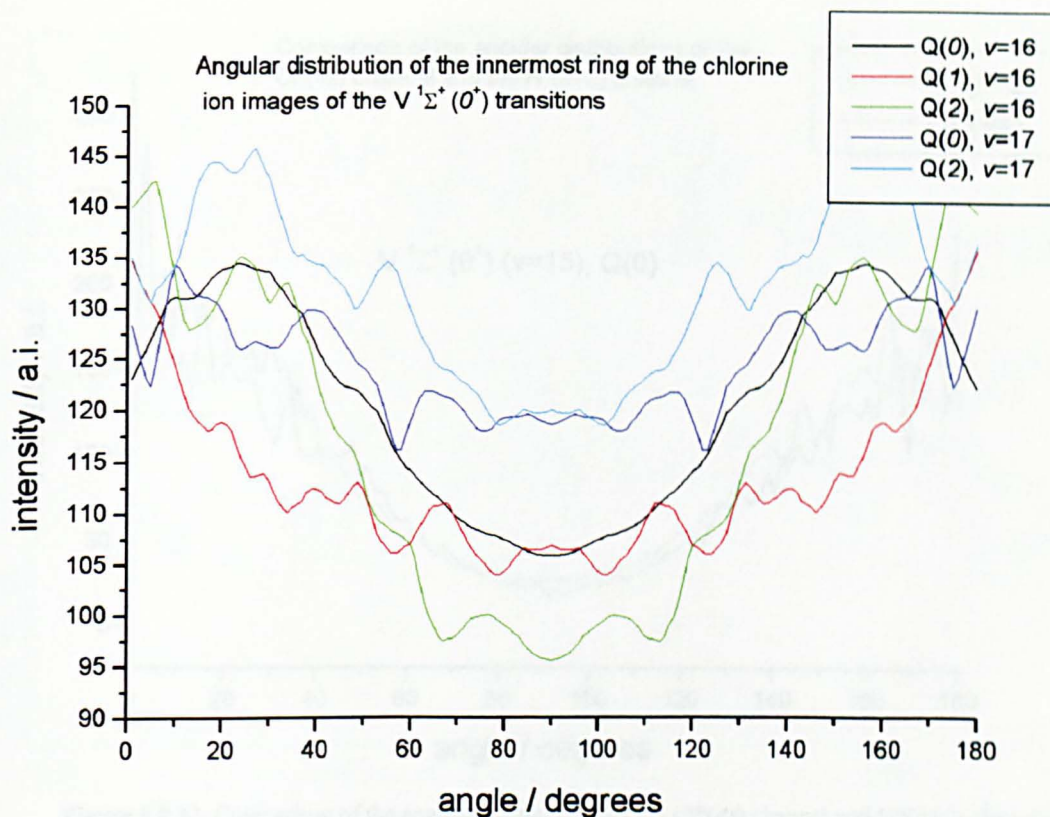
Figure 6.8.11. Angular distributions of the innermost ring of the chlorine ion images of the V $^1\Sigma^+$ (0^+) ($v = 16$ & 17) REMPI transitions.

The angular distribution of the H*($n=2$) channel contained in the hydrogen ion images displayed the same angular distribution behaviour as the chlorine 4s channel and the innermost chlorine channel of the Q (J) V $^1\Sigma^+$ (0^+) ($v = 16$ & 17) transitions. Furthermore, the angular distributions of the $4s$ channel and the H*($n = 2$) were very similar, see figure 6.8.12.
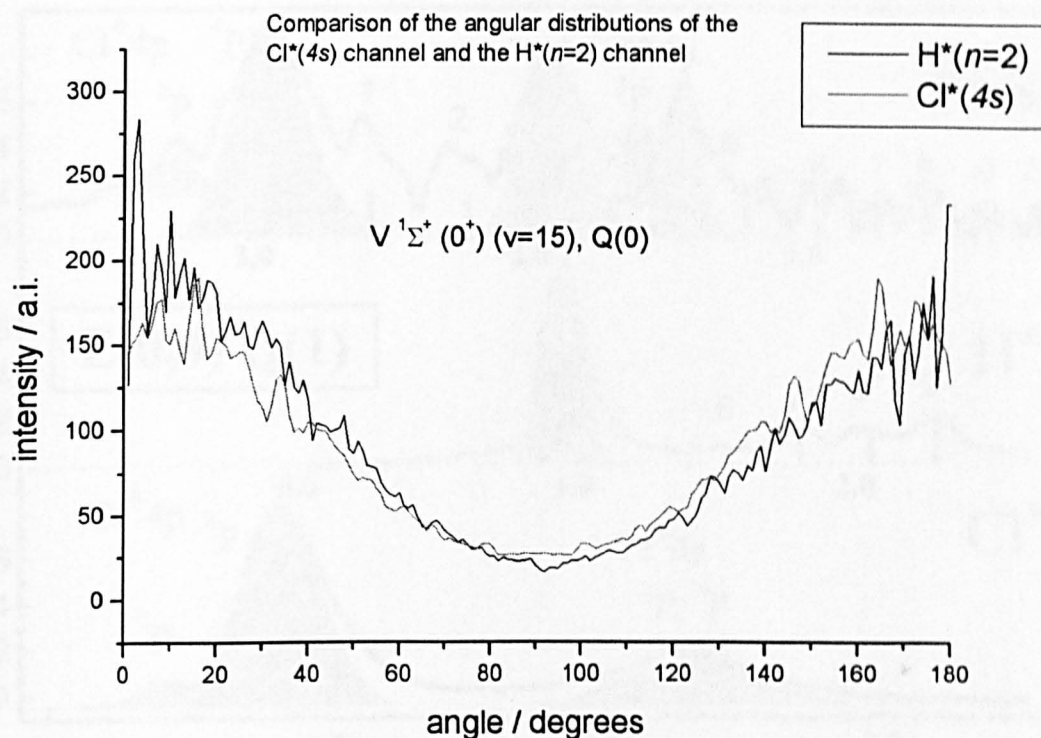
Figure 6.8.12. Comparison of the angular distributions of the Cl*(*4s*) channel and H*(*n=2*) channel of the Q(*0*) V $^1\Sigma^+$ (0^+) ($v = 15$) transition.

The H*($n = 2$) channel dominated the hydrogen images. However, as can be seen in figure 6.8.1. there were other rings present in the hydrogen ion images, despite H*($n \geq 3$) being energetically inaccessible. The speed distribution of the hydrogen ion image for the Q (1) E $^1\Sigma^+$ (0^+) ($v = 0$) transition is shown in figure 6.8.13, which clearly shows that the other hydrogen ions were formed by the photodissociation of HCl$^+$.

In addition, despite the photoelectron image demonstrating that HCl$^+$ was formed in a wide range of vibrational levels hydrogen ions were only observed from the vibrational states $v = 6 - 9$.
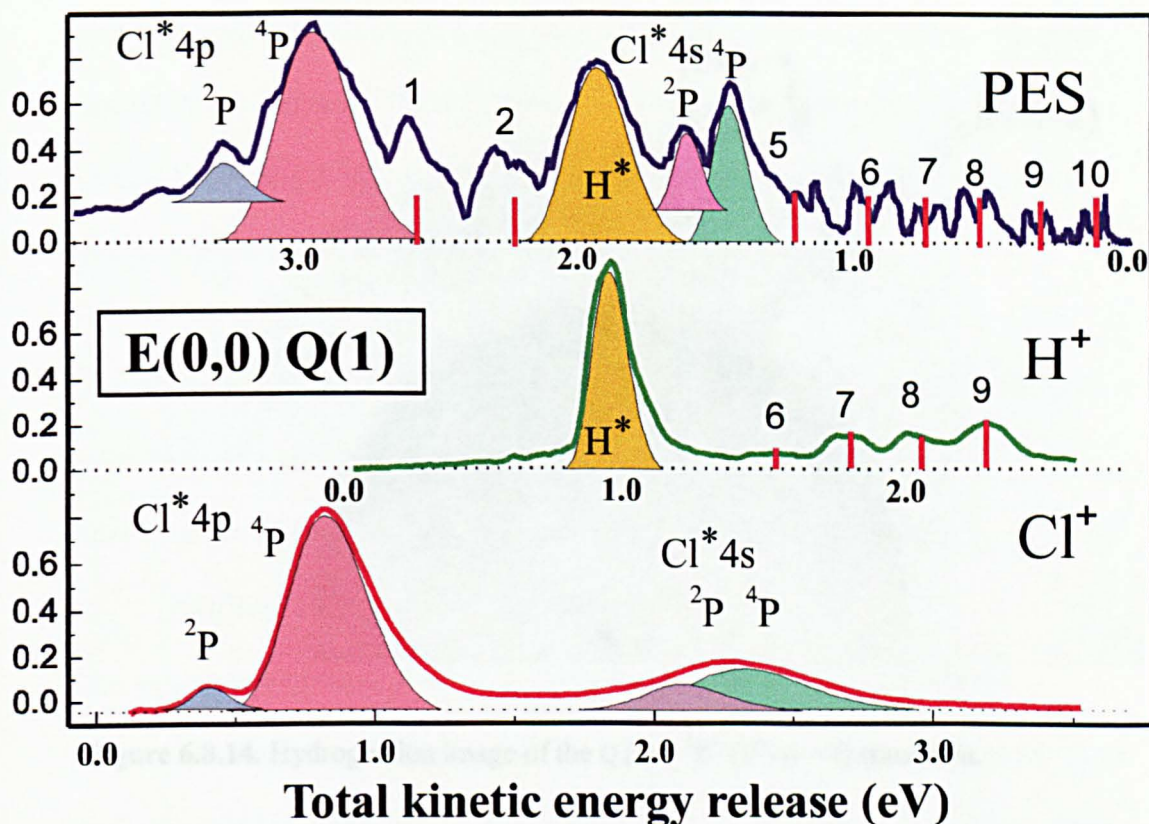
Figure 6.8.13. Photoelectron, hydrogen ion and chlorine ion images of (2+1) REMPI *via* the E $^1\Sigma^+$ (0^+) state.

Although these HCl^+ photodissociation fragments were much weaker than the H*(*n* = 2) signals they were readily visible in the images if the colour scheme was chosen judiciously, see figure 6.8.14. The spot in the centre of the ion image shown below was due to the slight leakage of HCl^+ ions.
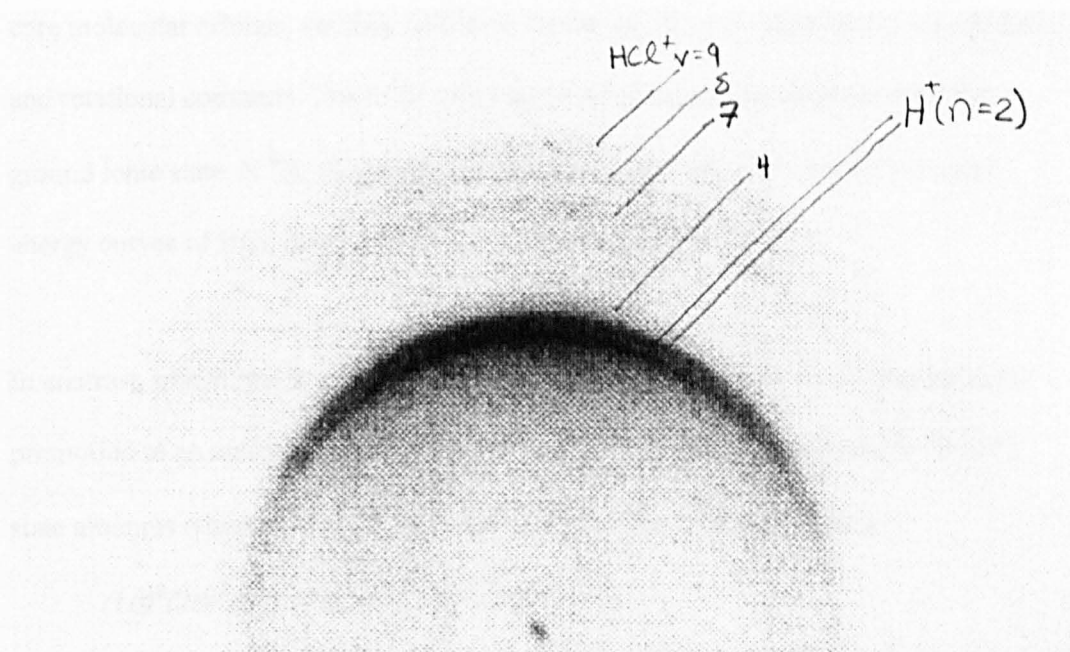
Figure 6.8.14. Hydrogen ion image of the Q (*1*) E $^1\Sigma^+$ (0^+) (*v = 0*) transition.

6.9 Discussion

In molecular orbital notation, at the equilibrium conformation the electron configuration

of ground state HCl, X $^1\Sigma^+$ (0^+), can be expressed as[23]

$$(1s\sigma)^2(2s\sigma)^2(2p\sigma)^2(2p\pi)^4(3s\sigma)^2(3p\sigma)^2(3p\pi)^4$$

This may also be written as

$$(1\sigma)^2(2\sigma)^2(3\sigma)^2(1\pi)^4(4\sigma)^2(5\sigma)^2(2\pi)^4$$

or more generally ... $\sigma^2\pi^4$. The Rydberg configuration resulting from promotion of the

$3p\pi$ electron is

$$[...\sigma^2\pi^3] \, n \, l \, \lambda$$

Where $l = 0$, 1, or 2 for an s, p, or d Rydberg electron, respectively, and $\lambda = l, l\text{-}1...0$

such that $\lambda = 0$, 1, or 2 corresponds to σ, π, or δ orbitals, respectively. A Rydberg

electron does not overlap strongly with the core molecular orbitals and does not

contribute to bonding. A Rydberg state will thus mimic the ionic state that has identical

204

core molecular orbitals, *i.e.* they will have similar equilibrium separations, vibrational and rotational constants. The E $^1\Sigma^+$ (0^+) state is a Rydberg state which mimics the ground ionic state, X $^2\Pi$, as can be seen in figure 6.9.1, which shows the potential energy curves of HCl, they have similar internuclear separations.

In contrast, transitions from the ground state bonding orbital, which involve electron promotion to an antibonding valence orbital, *i.e.* $\sigma^* \leftarrow \sigma$, give rise to the V $^1\Sigma^+$ (0^+) state amongst others. The V $^1\Sigma^+$ (0^+) states' equilibrium configuration is

$$(1\sigma)^2(2\sigma)^2(3\sigma)^2(1\pi)^4(4\sigma)^2(5\sigma)^1(6\sigma)^1(2\pi)^4$$

The equilibrium distance of the V $^1\Sigma^+$ (0^+) state is significantly larger and the vibrational constant much smaller than the Rydberg levels associated with the X $^2\Pi$ ion core, *e.g.* E $^1\Sigma^+$ (0^+). The near-adiabatic nature of the E $^1\Sigma^+$ (0^+) [$...\sigma^2\pi^3$] $3p\pi$ Rydberg state and V $^1\Sigma^+$ (0^+) state gives rise to a double-minimum potential of internuclear separation dependent character[23, 50, 52, 53]. Absorption through the double minimum potential can be separated into contributions from the inner Rydberg well (E $^1\Sigma^+$ (0^+) state) and from the outer valence well (V $^1\Sigma^+$ (0^+) state). Interactions between the vibrational levels of the two state's are seen as perturbations from the expected vibrational progression and vibrational & rotational constants[53].
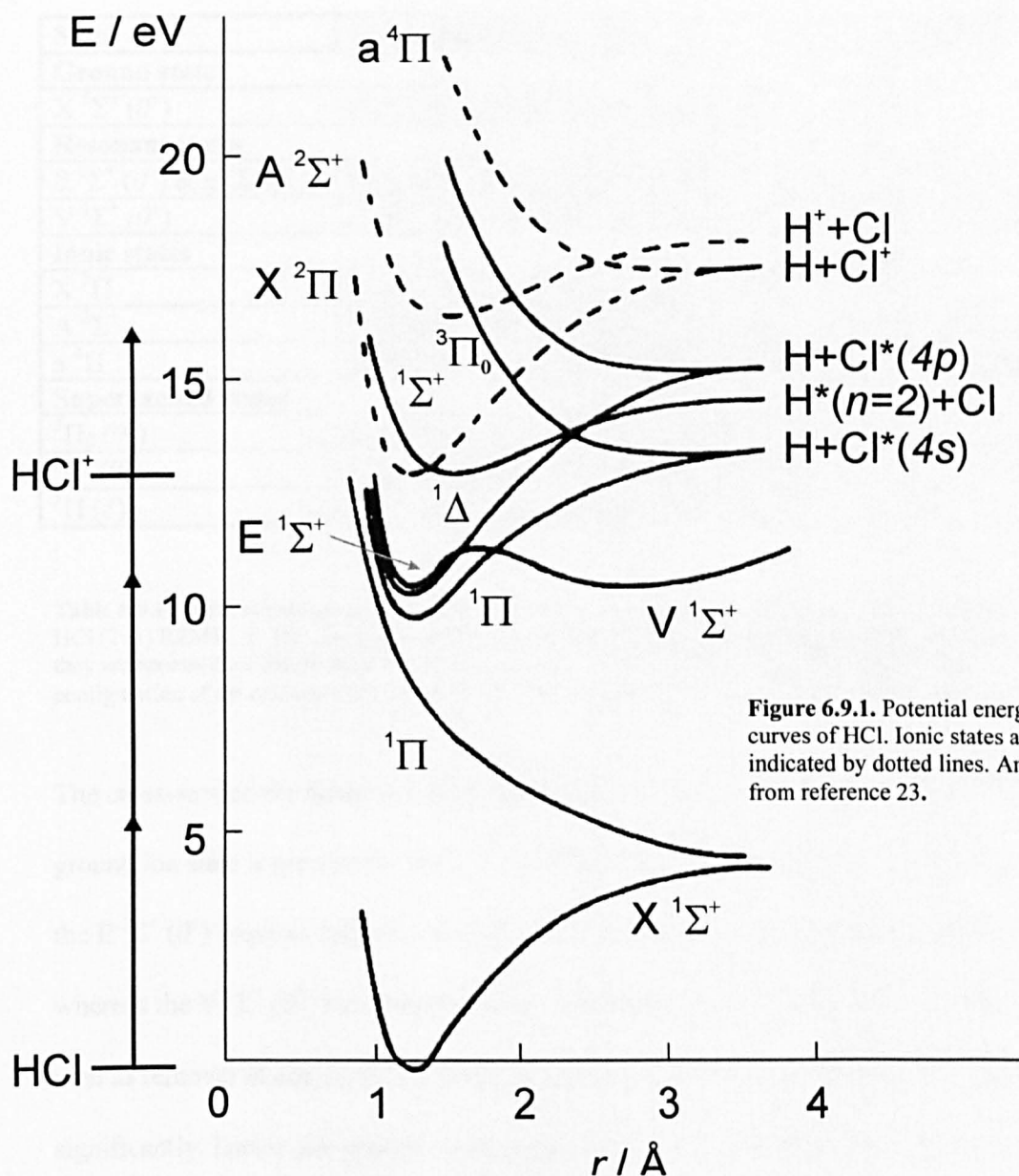
Figure 6.9.1. Potential energy curves of HCl. Ionic states are indicated by dotted lines. Amended from reference 23.

The competition between ionization and fragmentation with regard to the electronic configurations of the species involved is shown in table 6.9.1., which summarizes the electronic configurations of ground state HCl, the E $^1\Sigma^+$ (0^+), g $^3\Sigma^-$ (0^+) and V $^1\Sigma^+$ (0^+) resonant states, the ground state and the first excited states of HCl$^+$, and the superexcited states $^3\Pi_0$ (0^+), $^1\Pi$ (1) and $^1\Sigma^+$ (0^+).

State	Electronic configuration	Difference
Ground state		
X $^1\Sigma^+$ (0^+)	$(1\sigma)^2(2\sigma)^2(3\sigma)^2(1\pi)^4(4\sigma)^2(5\sigma)^2(2\pi)^4$	0
Resonant states		
E $^1\Sigma^+$ (0^+) & g $^3\Sigma^-$ (0^+)	$(1\sigma)^2(2\sigma)^2(3\sigma)^2(1\pi)^4(4\sigma)^2(5\sigma)^2(2\pi)^3 4p\pi$	$(2\pi) \to 4p\pi$
V $^1\Sigma^+$ (0^+)	$(1\sigma)^2(2\sigma)^2(3\sigma)^2(1\pi)^4(4\sigma)^2(5\sigma)^1(6\sigma)^1(2\pi)^4$	$(5\sigma) \to (6\sigma)$
Ionic states		
X $^2\Pi$	$(1\sigma)^2(2\sigma)^2(3\sigma)^2(1\pi)^4(4\sigma)^2(5\sigma)^2(2\pi)^3$	0
A $^2\Sigma^+$	$(1\sigma)^2(2\sigma)^2(3\sigma)^2(1\pi)^4(4\sigma)^2(5\sigma)^1(2\pi)^4$	$(5\sigma) \to (2\pi)$
a $^4\Pi$	$(1\sigma)^2(2\sigma)^2(3\sigma)^2(1\pi)^4(4\sigma)^2(5\sigma)^1(6\sigma)^1(2\pi)^3$	$(5\sigma) \to (6\sigma)$
Superexcited states		
$^3\Pi_0$ (0^+)	$(1\sigma)^2(2\sigma)^2(3\sigma)^2(1\pi)^4(4\sigma)^2(5\sigma)^1(6\sigma)^1(2\pi)^3 4s\sigma$	†
$^1\Sigma^+$ (0^+)	$(1\sigma)^2(2\sigma)^2(3\sigma)^2(1\pi)^4(4\sigma)^2(5\sigma)^1(2\pi)^4 4s\sigma$	†
$^1\Pi$ (1)	$(1\sigma)^2(2\sigma)^2(3\sigma)^2(1\pi)^4(4\sigma)^2(5\sigma)^1(2\pi)^4 4p\pi$	†

Table 6.9.1. Table summarizing the electron configurations of the species involved in the dynamics of HCl (2+1) REMPI. †: The changes in electron configuration on forming the superexcited states, since they are accessed *via* the resonant states, will be concerned about the changes from the electron configuration of the resonant states, each of the V $^1\Sigma^+$ (0^+) and E $^1\Sigma^+$ (0^+) state will be taken in turn.

The cross-section for direct one-photon ionization of the resonant states to the X $^2\Pi_i$ ground ion state is greatest for the E $^1\Sigma^+$ (0^+) Rydberg state. Formation of X $^2\Pi_i$ from the E $^1\Sigma^+$ (0^+) requires only the removal of the 3π electron, a one-electron process, whereas the V $^1\Sigma^+$ (0^+) state requires a two-electron process, namely $(6\sigma) \to (5\sigma)$ as well as removal of one of the 2π electrons, consequently the cross sections are reduced significantly. Direct one-photon ionization to form the $^4\pi$ excited repulsive ionic state will be largest for the V $^1\Sigma^+$ (0^+) state since this only requires removal of one 2π electron, whereas it is a two-electron process for the E $^1\Sigma^+$ (0^+) state. However, in the energy range studied only the ground ionic state is energetically accessible and thus direct one photon ionization can only be significant for the E $^1\Sigma^+$ (0^+) Rydberg state.

The HCl$^+$ observed for the V $^1\Sigma^+$ (0^+) state has been shown to have another origin; de Beer *et al.* demonstrated that HCl$^+$ is also formed *via* the superexcited state responsible for the detection of Cl*(4s, ^{2}P) and H*($n=2$)[23], namely the bound $^1\Sigma^+$ state shown in the above table[23].

From a variety of REMPI-PES experiments its clear that those superexcited states that can be reached by a transition of one core-electron are important. A one-electron transition from the intermediate V $^1\Sigma^+$ (0^+) state can produce the well known superexcited states $^1\Sigma^+$ (0^+) with $(5\sigma)^1(2\pi)^4 4s\sigma$ and $^1\Pi(1)$ with $(5\sigma)^1(2\pi)^4 4p\pi$, which both converge to the first excited ionic A $^2\Sigma^+$ $(5\sigma)^1(2\pi)^4$ state. The $^1\Sigma^+$ (0^+) superexcited state is a bound state that evolves to form H* ($n = 2$) and Cl past it's dissociation limit. However, at a large internuclear distance this state crosses a dissociative $^3\Pi(0)$ state with configuration $(5\sigma)^1(6\sigma)^1(2\pi)^3 4s\sigma$ that leads to formation of Cl*(4s, ^{2}P) and H. The spin-orbit coupling between these two states has been shown to be appreciable[44], thus accessing the $^1\Sigma^+$ (0^+) superexcited state *via* the intermediate V $^1\Sigma^+$ (0^+) states will result in the formation of both Cl*(*4s*) and H*($n = 2$). The common source of these two fragments is reflected in their similar angular distributions, re figure 6.8.12.

Due to the fact that a Rydberg state resembles its core ionic state, for example the E $^1\Sigma^+$ (0^+) Rydberg state and its X $^2\Pi_I$ ionic core, the vibrational structure of the two states are alike. As a result the ionization of a Rydberg state to its ionic core frequently displays $\Delta v = 0$ propensity, which was seen for the calibrant F $^1\Delta_2$ (*2*) Rydberg state, an X $^2\Pi_i$ *4p*π Rydberg state (data not shown). Similarly, the E $^1\Sigma^+$ (0^+) Rydberg state appeared to give a more intense HCl$^+$ $\Delta v = 0$ peak than the V $^1\Sigma^+$ (0^+) states (re figures 6.8.13 and 6.8.6 respectively, note the HCl$^+$ $\Delta v = 0$ peak of the E $^1\Sigma^+$ (0^+) state was superimposed with the Cl**4p* ^{4}P peak). The atomic fragments and the other vibrational states of HCl$^+$ observed with the REMPI via the E $^1\Sigma^+$ (0^+) state have been attributed to the mixing of the V $^1\Sigma^+$ (0^+) valence state; This mixing has subsequently been demonstrated[55].

It was briefly alluded to above that the similar angular distributions of the H*($n = 2$) and the Cl*(*4s*) photofragments reflected their common origin, namely the $^1\Sigma^+$ (0^+)

superexcited state. Similarly, although angular distribution behaviour of the Cl*(4p) and

Cl*(3d) was dependent on the vibrational state, in every case both photofragents

displayed the same angular distribution behaviour. By the same arguments as above

these channels are expected to have a common source, or at least the states from which

they are produced to be of the same symmetry.

One of the reported origins of the Cl* (4p), and by extension the Cl*(3d),

photofragments are illustrated in figure 6.9.2.

Figure 6.9.2. Predissociation of the superexcited states
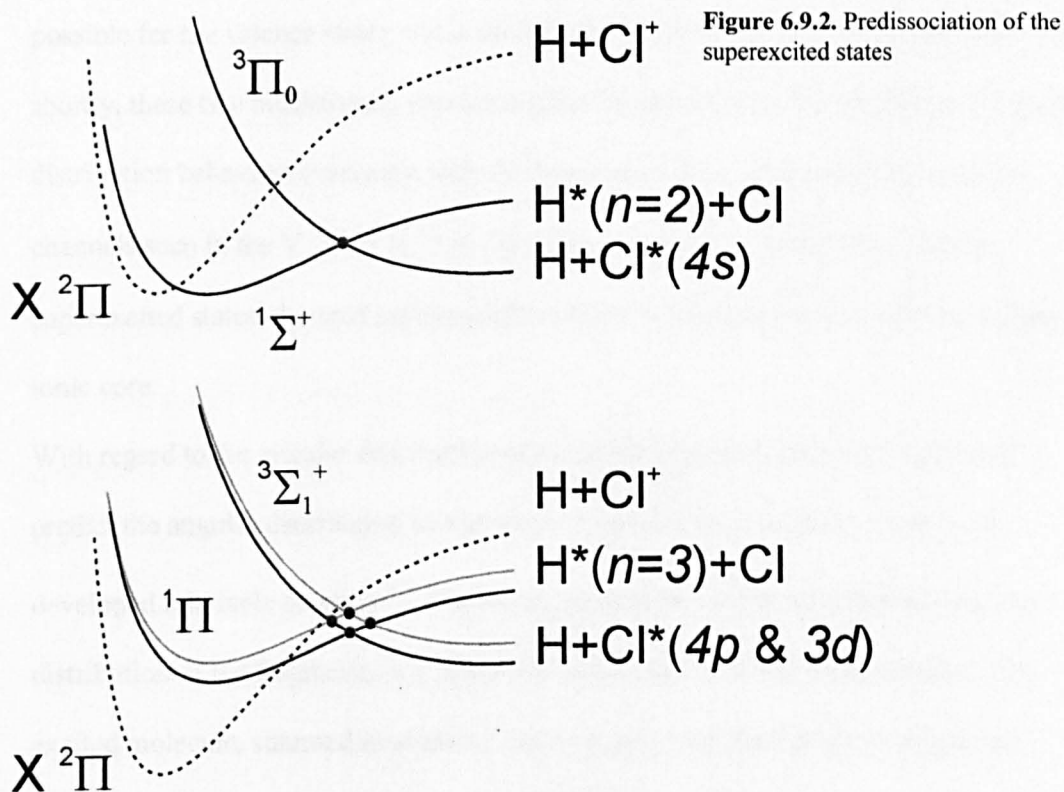
The top diagram in the above figure illustrates schematically the spin-orbit coupling

between the bound $^1\Sigma^+$ state and the repulsive $^3\Pi_0$ that is responsible for the formation

of Cl*(4s) as well as H*(n = 2). The highest occupied molecular orbital in both of these

states is a $4s\sigma$ Rydberg orbital. The analogous $4p\pi$ states, namely the intense bound $^1\Pi_1$

state and the dissociative $^3\Sigma_0$ state, interact by the same spin orbit mechanism[44] and can

give rise to the Cl*(4p) fragments (see bottom diagram in figure 6.9.2). Whereas the

$4s\sigma\ ^1\Sigma^+$ superexcited state was accessible only from the V $^1\Sigma^+$ valence state, the $4p\pi\ ^1\Pi$

(1) state can be accessed by the valence state and the E $^1\Sigma^+$ Rydberg state. Furthermore,

through l-mixing the $3d\pi$ and the $4p\pi$ states mix[44]. Consequently, when energetically

accessible both fragments are formed and display the same angular distributions, as

shown in the results.

The Cl*($4p$) have also been attributed to a direct one-photon transition from the valence

state (large internuclear distance) to the repulsive states[23]. Such a mechanism is

possible for the valence states, but is unlikely for the Rydberg states. As will be shown

shortly, these two mechanisms provide a plausible explanation for the different angular

distribution behaviors (variation with J). Presumably the additional predissociation

channels seen in the V $^1\Sigma^+$ (v = 16 & 17) chlorine images originate from similar

superexcited states, the next superexcited states in the Rydberg series with an excited

ionic core.

With regard to the angular distribution of the photofragments, formulae that could

predict the angular distribution of fragments formed at the two-photon level were

developed relatively recently[24]. The central idea of this model was that the angular

distribution of the fragments is a 'snapshot' of the square of the wavefunction of the

excited molecule, summed over initial and averaged over final projection quantum

numbers. More formally the angular distribution is described by

$$f(\theta)=\frac{2J''+1}{8\pi}\sum_{MM'}P(J'',\Omega'',M'':J,\Omega,M)\times\left|D_{M\Omega'}^{J'}(\theta,\phi,\chi)\right|^2 \qquad (6.9.i)$$

where P (J'', Ω'', M''; J, Ω, M) is the transition probability and $[(2J''+1)/8\pi]^{1/2}D^{J'}{}_{M'\Omega'}$ is

the rotational wavefunction of the upper level and $(\theta,\ \phi,\ \chi)$ are the Euler angles defining

the transition from molecular fixed frame to space fixed frame. The transition

probability is proportional to the matrix element involving transition dipoles[56]

$$M_{f0} = \left| \sum_i \frac{\langle f|\hat{\varepsilon}_1.r|i\rangle\langle i|\hat{\varepsilon}_2.r|0\rangle}{E_{i0} - \omega_1} + \frac{\langle f|\hat{\varepsilon}_2.r|i\rangle\langle i|\hat{\varepsilon}_1.r|0\rangle}{E_{i0} - \omega_2} \right|^2 \tag{6.9.ii}$$

where $|0\rangle$ denotes the ground state, $|f\rangle$ the final state, $|i\rangle$ the intermediate states; ε_j and ω_j are the unit polarization vector and angular frequency of photon j, respectively; r is the dipole operator in space fixed frame (SFF), $E_{ig} = E_i - E_0$ is the energy difference between the initial state $|0\rangle$ and the intermediate state $|i\rangle$.

A similar J dependent angular distribution, of the neutral predissociation fragments of HCl at the two-photon level, was explained using this model. If the two photon-state was the only resonant state then the angular distribution reported here would be expected to be explainable using the above equation. However, if this were true then the angular distribution of each fragment channel accessed through a single transition would be identical. Clearly this was not the case. For Q (J) transitions through the $^1\Sigma^+$ (0^+) states the Cl*(4s), Cl*(5p) and the H*($n = 2$) channels displayed a net parallel-like distribution that was independent of the rotational state whilst the angular distribution of the Cl*(4p) and Cl*(3d) channels were more complicated. For transitions via the V (v =12 & 15) states the Cl*(4p) and Cl*(3d) channels changed from parallel-like distributions for the Q (0) transitions to perpendicular-like distributions for the Q (J > 0) transitions. For transitions via the V ($v = 13$) state the ions displayed an almost isotropic distribution, whilst transitions via the E ($v = 0$) and g ($v = 0$) states displayed parallel-like distributions for all reaction channels.

Resonance at the three photon level as well as at the two-photon level provides a sensible explanation for the different angular distribution behavior of the different reaction channels. The symmetry of the excited state from which the different fragments are obtained would then also influence their angular distributions. A quantitative explanation of the angular distributions is difficult owing to the number of possible

states at the two- and three-photon levels and the interaction between these states[52, 54], and the lack of formulae for the angular distribution of the photofragments (formed at the three photon level from a process resonant at both the two- and three-photon levels). Nevertheless, some inferences can be made. With regard to the second point Liyanage *et al.* demonstrated that the character of the V $^1\Sigma^+$ (0^+) ($v = v$), E $^1\Sigma^+$ (0^+) ($v = v$) and g $^3\Sigma^-$ (0^+) ($v = v$) resonant states are dependent upon their vibrational and rotational states.[54] The character of the V ($v = 12$ & 11), E ($v = 0$) and the g $^3\Sigma^-$ (0^+) ($v = 0$) states as a function of the rotational state is shown in figure 6.9.3. Note the diagram below includes all of the states that were studied here and published by Liyanage *et al.*[57].
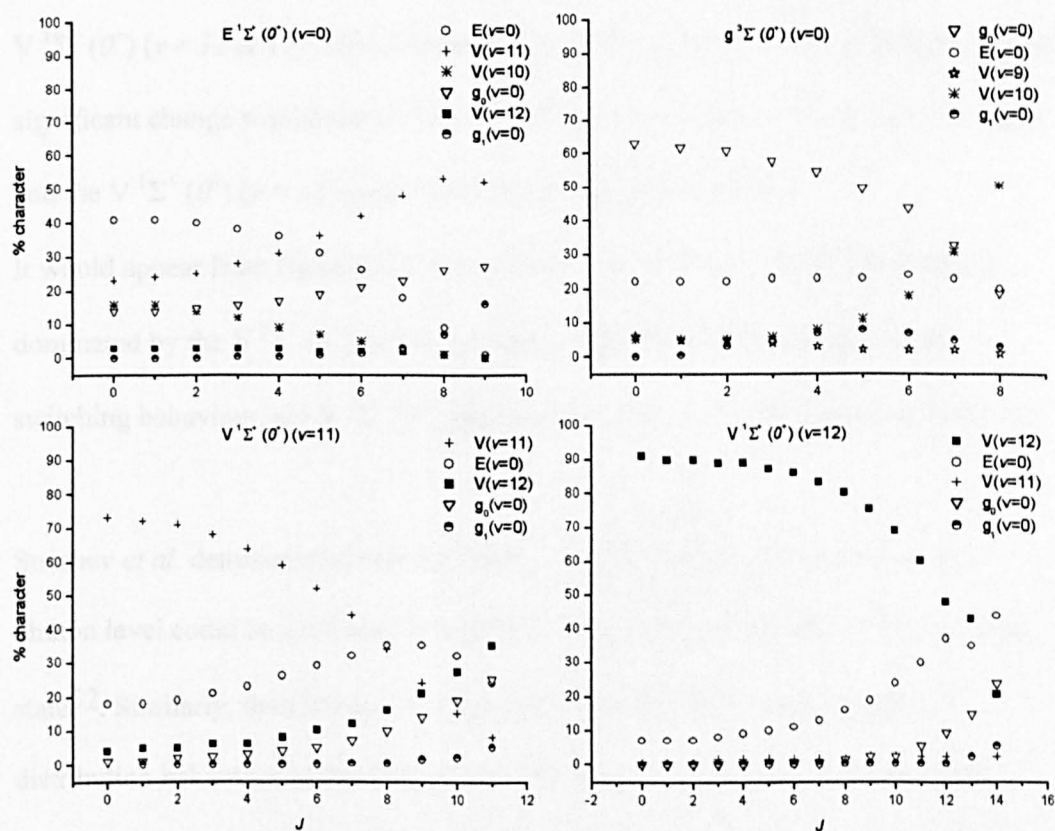
Figure 6.9.3. Diabatic state characters of the E $^1\Sigma^+$ (0^+) ($v = 0$), g $^3\Sigma^-$ (0^+) ($v = 0$), V $^1\Sigma^+$ (0^+) ($v = 11$ & 12) states of HCl. Data obtained from reference 57 (Note: any values referred to in this article as $\ll 1$, < 1, > 1, > 2, > 5 and > 9 have been plotted as 0.05, 0.5, 1.5, 2.5, 5.5 and 9.5 respectively).

As can be seen above each of the adiabatic states (strong coupling) include contributions from several diabatic states (weak coupling), the proportion of which is dependent on the rotational and vibrational state. It is evident that the V ($v = 12$) adiabatic state is dominated by the V ($v = 12$) diabatic state, whereas the E ($v = 0$) adiabatic state includes contributions from many diabatic states (E ($v = 0$) $\approx$ 40 %)) and the g ($v = 0$) contains significant E ($v = 0$) character as well g ($v = 0$).

As stated briefly earlier it has been suggested that the fragments obtained via the E state are due to an admixture of the V states[55]. Although the angular distributions of the Cl*($4s$) and H*($n=2$) were similar for all of the states studied, and as a result the admixture of V states theory holds, the same cannot be said for the Cl*($4p$) and Cl*($3d$). The velocity mapping images demonstrated that whereas the angular distributions of the V $^1\Sigma^+$ (0^+) ($v = 12$ & 15) states displayed the Q (0) $\rightarrow$ Q ($J \geq 0$) switching behaviour, no significant change was observed for the E $^1\Sigma^+$ (0^+) ($v = 0$) and g $^3\Sigma^-$ (0^+) ($v = 0$) states and the V $^1\Sigma^+$ (0^+) ($v = 13$) state was between these two extremes.

It would appear from figure 6.9.3. that, as the V $^1\Sigma^+$ (0^+) ($v = 12$) adiabatic state is dominated by the V $^1\Sigma^+$ (0^+) ($v = 12$) diabatic state and this state displayed the switching behaviour, the V $^1\Sigma^+$ (0^+) states are responsible for the switching behaviour.

Strizhev *et al.* demonstrated that the dynamics of the HCl predissociation at the 2-photon level could be explained by examining the diabatic character of the resonant state[52]. Similarly, the vibrational / electronic state dependency of the angular distribution behaviour of the Cl*($4p$) and Cl*($3d$) photofragments will reflect the composition of the resonant state (as well as the state character at the 3-photon level). For example, whereas REMPI via the V states can access the repulsive states directly as well as the $4p\pi$ and $3d\pi$ $^1\Pi$ bound states, the E and g states can only access the $4p\pi$ $^1\Pi$

bound superexcited state. The differing angular distributions reflect the different compositions of the resonant state, and hence the states accessible at the three photon level, as well as the composition of those three photon levels.

Clearly, for a quantitative analysis the diabatic analysis referred to above would need to be expanded to include the higher vibrational levels of the resonant states and the superexcited states, as well as the formulae that predict the angular distributions developed.

The potential energy curves of HCl^+ that are relevant to the photodissociation products detected are shown in figure 6.9.4.[58] The higher states evolve to fragments that were not detected in this work, namely Cl^+ ions, or were not energetically accessible.
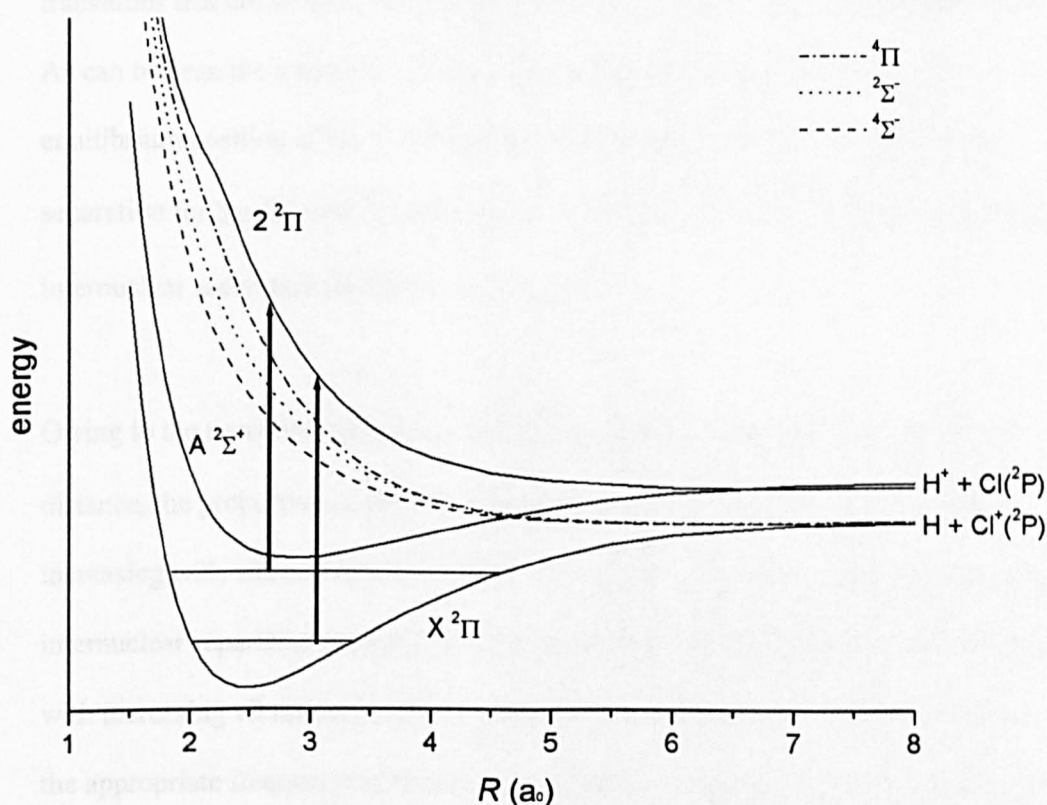
Figure 6.9.4. HCl^+ photodissociation. Potential energy curves plotted from the data in reference 58.

As can be seen above there is one bound state and four repulsive states. The bound state

and the 2 $^2\Pi$ state evolve to give protons whilst the other three repulsive states evolve to

chlorine ions. Owing to predissociation, above a certain energy level a transition to the

bound A $^2\Sigma^+$ state produces chlorine atoms[59-61]. No such photofragments were

detected, re figure 6.8.5.

The only remaining possibility involves a transition to the repulsive 2 $^2\Pi$ state, as

illustrated above. Such a transition would give a parallel distribution of photofragments,

in agreement with the ion images obtained, re figure 6.8.14.

The absence of chlorine photofragments and the vibrational state dependence of the

photodissociation to form H^+ ions can be rationalized using the potential energy curves

in figure 6.9.4. and the relevant transition moments. The transition moments for those

transitions that are allowed and are energetically accessible are shown in figure 6.9.5.[58]

As can be seen the transition moment for each transition is quite small at the

equilibrium position of HCl^+, with the moments increasing at lower internuclear

separation for the $^2\Sigma^+$ and $^2\Sigma^-$ states but increasing to a much greater degree at larger

internuclear separation for the $^2\Pi$ excited state.

Owing to the transition moment of the $^2\Pi$ state increasing rapidly with internuclear

distance, the proportion of the vibrational wavefunction near the turning points

increasing with vibrational state and the fact that the outer turning point occurs at larger

internuclear separation for a higher vibrational state, the transition moment will increase

with increasing vibrational state. Consequently, provided the photolysis radiation is of

the appropriate frequency for the transition, which is dependent on the vibrational state,

the H^+ fragment ions are expected to be more abundant for the higher vibrational states.

The arrows in figure 6.9.4. are scaled to represent the energy of the E $^1\Sigma^+$ (0^+) ($v = 0$)

(2+1) Q (0) photon, as can be seen the photon is of sufficient energy to access the (2) $^2\Pi$

215

state near the turning points of the intermediate vibrational levels (where the transition moment is greater) but nearer the center for the higher vibrational levels, where the transition moment is less and the wavefunction is small. It is the compromise between these two factors that is the cause of the observed vibrational state dependency.
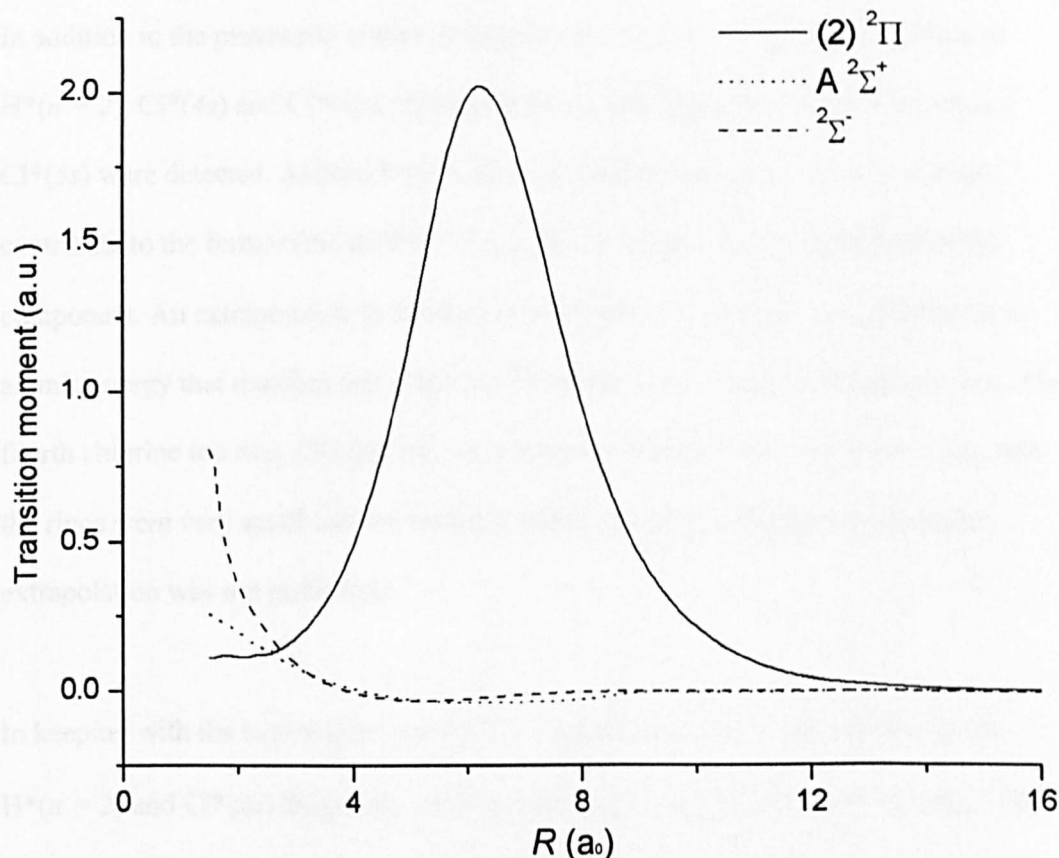
Figure 6.9.5. Transition moments for transitions to the (2) $^2\Pi$, A $^2\Sigma^+$ and $^2\Sigma^-$ states, data obtained from reference 56.

With regard to the absence of chlorine fragments, presumably this reflects the lower transition moment at the accessible internuclear distances (low vibrational states) and the asymmetric shape of the ground electronic state of HCl^+. As the inner wall of the potential well is much steeper than the outer wall, the internuclear separation of the inner turning points decreases much more slowly than that of the outer turning points increases. As a result the transition moment to the A $^2\Sigma^+$ and $^2\Sigma^-$ states increases more slowly with increasing vibrational state than that for the $^2\Pi$ state. A rigorous explanation would require the calculation of the energy dependent cross-section for

each vibrational state, similar to that performed by Pradhan *et al.* for the ground

vibrational state[58].

6.10 Conclusion

In addition to the previously observed fragmentation channels, namely formation of

H*($n = 2$), Cl*($4s$) and Cl*($4p$), chlorine ions and photofragments from Cl*($3d$) and

Cl*($5s$) were detected. Although there are many individual atomic states that could

contribute to the former (the third Cl$^+$ ring), the $3d$ ^{2}D state is thought to be a major

component. An extrapolation to threshold for the third chlorine ion ring resulted in an

atomic energy that matches that of the $3d$ ^{2}D atomic state within experimental error. The

fourth chlorine ion ring, Cl ($5p$), was only observed for the V ($v = 16$ & 17) states and

the rings were very small and the resolution obtained poor, consequently a similar

extrapolation was not performed.

In keeping with the explanation that the $^1\Sigma^+$ superexcited state is responsible for the

H*($n = 2$) and Cl*($4s$) fragments, their angular distributions were near - identical. The

angular distributions of the Cl*($4p$) and Cl*($3d$) channels, whilst identical were

dependent on the identity of the resonant state and the vibrational state of the V $^1\Sigma^+$

state. This is thought to reflect the diabatic character of the resonant state and

consequently, which superexcited states are accessible.

Finally, HCl$^+$ photodissociation to produce protons and ground state chlorine atoms was

observed from a fraction of the vibrational levels known to be present (from the

photoelectron images). This reflects the dependence of the transition moment on the

internuclear separation.

217

References

(1)   Sannes-Lowery, K.; Griffey, R. H.; Kruppa, G. H.; P, S. J.; Hofstadler, S. A.
        Rapid Comm. Mass Spectrom. **1998,** *12,* 1957-1961.

(2)   Gauthier, J. W.; Trautman, T. R.; Jacobsen, D. B. *Anal. Chim. Acta* **1991,** *246,*
        211-225.

(3)   McLuckey, S. A.; Goeringer, D. E. *J. Mass Spectrom.* **1997,** *32,* 461-474.

(4)   Chandler, D. W.; Houston, P. L. *J. Chem. Phys.* **1987,** *87,* 1445.

(5)   Heck, A. J. R.; Chandler, D. W. *Annu. Rev. Phys. Chem.* **1995,** *46,* 335.

(6)   Heck, A. J. R. *Eur. Mass Spectrom.* **1997,** *3,* 171.

(7)   Houston, P. L. *J. Phys. Chem.* **1996,** *100,* 12757.

(8)   Houston, P. L. *Acc. Chem. Res.* **1995,** *28,* 453.

(9)   McDonnell, L.; Heck, A. J. R. *J. Mass Spectrom.* **1998,** *33,* 415-428.

(10)   Whitaker, B. J. *Research in Chemical Kinetics*; Elsevier: Amsterdam, 1993.

(11)   Parker, D. H.; Eppink, A. T. J. B. *J. Chem. Phys.* **1997,** *1997,* 2357.

(12)   Eppink, A. T. J. B.; Parker, D. H. *Rev. Sci. Instrum.* **1997,** *68,* 3477.

(13)   Eppink, A. T. J. B.; Parker, D. H.; Janssen, M. H. M.; Buijsse, B.; Zande, J. v. d.
        J. Chem. Phys. **1998,** *108,* 1350.

(14)   Buntine, M. A.; Baldwin, D. P.; Chandler, D. W. *J. Chem. Phys.* **1992,** *96,* 5843.

(15)   Janssen, M. H. M.; Mastenbroek, J. W. G.; Stolte, S. *J. Phys. Chem. A* **1997,**
        101, 7605-7613.

(16)   Rodgers, L. J.; Ashfold, M. N. R.; Matsumi, Y.; Kawasaki, M.; Whitaker, B. J.
        J. Chem. Soc., Faraday Trans. **1996,** *92,* 5181-5183.

(17)   Rodgers, L. J.; Ashfold, M. N. R.; Matsumi, Y.; Kawasaki, M.; Whitaker, B. J.
        Chem. Phys. Lett. **1996,** *258,* 159-163.

(18)   Sanov, A.; Droz-Georget, T.; Zyrianov, M.; Reisler, H. *J. Chem. Phys.* **1997,**
        106, 7013.

(19)   Neyer, D. W.; Heck, A. J. R.; Chandler, D. W. *J. Chem. Phys.* **1999,** *103,*

10388-10397.

(20)   Neyer, D. W.; Heck, A. J. R.; Chandler, D. W. *J. Chem. Phys.* **1999,** *110,* 3411-

3417.

(21)   Hilosaka, Y.; Eland, J. H. D. *Rapid Comm. Mass Spectrom.* **2000,** *14,* 2305-

2311.

(22)   Ashfold, M. N. R.; Howe, J. D. *Annu. Rev. Phys. Chem.* **1994,** *45,* 57.

(23)   de Beer, E.; Koenders, B. G.; Koopmans, M. P.; Lange, C. A. *J. Chem. Soc.*

Faraday Trans. **1990,** *86,* 2035.

(24)   Liyanage, R.; Gordon, R. J. *J. Chem. Phys.* **1997,** *107,* 7209.

(25)   Bracewell, R. N. *The Fourier transform and its Applications*; McGraw-Hill:

New York, 1986.

(26)   Simpson, W. R.; Rakitzis, T. P.; Kandel, S. A.; Orrewing, A. J.; Zare, R. N. *J.*

Chem. Phys. **1995,** *103,* 7313-7335.

(27)   Simpson, W. R.; Rakitzis, T. P.; A.Kandel, S.; Levon, T.; Zare, R. N. *J. Phys.*

Chem. **1996,** *100,* 7938-7947.

(28)   Varley, D. F.; Dagdigian, P. J. *J. Phys. Chem.* **1995,** *99,* 9843-9853.

(29)   Varley, D. F.; Dagdigian, P. J. *J. Phys. Chem.* **1996,** *100,* 4365-4374.

(30)   Xie, Y.; Reilly, P. T. A.; Chilukuri, S.; Gordon, R. J. *J. Chem. Phys.* **1991,** *95,*

854.

(31)   Rinnen, K. D.; Kliner, D. A. V.; Zare, R. N.; Huo, W. M. *Isr. J. Chem.* **1989,** *29,*

269.

(32)   Spliganin, T. A.; Chandler, D. W.; Parker, D. H. *Chem. Phys. Lett.* **1987,** *137,*

414.

(33)   Liyanage, R.; Reilly, P. T. A.; Yang, Y.; Gordon, R. J.; Field, R. W. *Chem.*

Phys. Lett. **1993,** *216,* 544.

(34) Jacobs, D. C.; Madix, R. J.; Zare, R. N. *J. Chem. Phys.* **1986,** *85,* 5469.

(35) Hines, M. A.; Michelson, H. A.; Zare, R. N. *J. Chem. Phys.* **1990,** *93,* 8557.

(36) Rinnen, K. D.; Buntine, M. A.; Kliner, D. A. V.; Zare, R. N.; Huo, W. M. *J. Chem. Phys.* **1991,** *95,* 214.

(37) Nakamura, H. *Int. Rev. Phys. Chem.* **1991,** *10,* 123.

(38) Nakamura, H. *Chem. Phys. Lett.* **1975,** *33,* 151.

(39) Nakamura, H. *Chem. Phys.* **1975,** *10,* 271.

(40) Platzman, R. L. *Radiat. Res.* **1962,** *17,* 419.

(41) Platzman, R. L. *Vortex* **1962,** *23,* 372.

(42) Higo, M.; Ogawa, T. *Chem. Phys.* **1979,** *44,* 279.

(43) White, M. G.; Leroi, G. E.; Ho, M. H.; Poliakoff, E. D. *J. Chem. Phys.* **1987,** *87,* 6553.

(44) Lefebvre-Brion, H.; Keller, F. *J. Chem. Phys.* **1989,** *90,* 7176.

(45) Frolich, H.; Glass-Maujean, M. *Phys. Rev. A* **1990,** *42,* 40.

(46) Wang, K.; McKoy, V. *J. Chem. Phys.* **1991,** *95,* 8718.

(47) Green, D. S.; Bickel, G. A.; Wallace, S. C. *J. Mol. Spectrosc.* **1991,** *150,* 303-353.

(48) Green, D. S.; Bickel, G. A.; Wallace, S. C. *J. Mol. Spectrosc.* **1991,** *150,* 388-469.

(49) Green, D. S.; Bickel, G. A.; Wallace, S. C. *J. Mol. Spectrosc.* **1991,** *150,* 354-387.

(50) Green, D. S.; Wallace, S. C. *J. Chem. Phys.* **1992,** *96,* 5857.

(51) de Beer, E. , University of Amsterdam, Amsterdam, 1993.

(52) Strizhev, A.; Li, X.; Liyanage, R.; Gordon, R. J.; Field, R. W. *J. Chem. Phys.* **1998,** *108,* 984.

(53) Kvaran, A.; Logadottir, A.; Wang, H. *J. Chem. Phys.* **1998,** *109,* 5856.

(54)   Liyanage, R.; Gordon, R. J.; Field, R. W. *J. Chem. Phys.* **1998**, *109*, 8374.

(55)   Dagdigian, P. J.; Varley, D. F.; Liyanage, R.; Gordon, R. J.; Field, R. W. *J. Chem. Phys.* **1996**, *105*, 10251.

(56)   Chen, K.-m.; Yeung, E. S. *J. Chem. Phys.* **1978**, *69*, 43-52.

(57)   *See AIP document No. PAPS JCPSA6-109-009839. Obtainable by PAPS number and Journal reference (reference 54 above) from American Institute of Physics, Physics Auxiliary Publication service, 500 Sunnyside Boulevard, Woodbury, New York 11797-2999. Fax. 516-576-2223, email: paps@aip.org. .*

(58)   Pradhan, A. D.; Kirby, K. P.; Dalgarno, A. *J. Chem. Phys.* **1991**, *95*, 9009.

(59)   Korolkov, M.; Weitzel, K.-M.; Peyerimhoff, S. D. *Int. J. Mass Spectrom.* **2000**, *201*, 109-120.

(60)   Penno, M.; Holzwarth, A.; Weitzel, K.-M. *Mol. Phys.* **1999**, *97*, 43-52.

(61)   Michel, M.; Korolkov, M. V.; Malow, M.; Brembs, K.; Weitzel, K.-M. *Phys. Chem. Chem. Phys.* **2001**, *3*, 2253-2257.

7 Summary

A potential array investigation into multipole storage-assisted dissociation demonstrated that the average kinetic energy of an ion in the simulated hexapole was of the order $0.025 \times |z|$ eV, where z is the elementary charge of the ion. This value is similar to the energy of a single IR photon and the average kinetic energy an ion can possess during sustained off-resonance irradiation collision-induced dissociation (SORI-CID), and explains the similar fragments that have been obtained using these techniques[1, 2].

In agreement with the predictions of the adiabatic approximation, the simulations demonstrated that the average kinetic energy of the ion increased linearly with space charge and the ion's charge state, but was independent of the its mass and the applied RF potential. Under the conditions studied the average kinetic energy of the ion also appeared to increase linearly with the ion's mean free path ($R^2 = 0.98$). By fitting linear equations to the results of the simulations, the following expression for the average kinetic energy of the ion was obtained

$$KE_{average} / eV = |z| \times [(6.7 \pm 0.3) \times 10^{10} \times \gamma + (1.4 \pm 0.1) \times 10^{-3} \times \lambda - 10^{-4}]$$

where z is the ion's charge (in units of elementary charge), γ is the total space charge in the hexapole in coulombs in C and λ is the ion's mean free path in mm.

The number of collisions the ion experienced was found to increase with increasing space charge and decreasing mean free path. Furthermore, the increase in the number of collisions with a decreasing mean free path was much greater when space charge was high and this change could be greater than the decrease in the ion's average kinetic energy (through damping). Consequently, collisional activation is proposed to be greater at smaller mean free paths when space charge is high, in agreement with experiment.[2]

Whereas the average kinetic energy of the ion was independent of the ion's mass, the ion's average radial position was dependent on its mass. The resulting radial

stratification could lead to ions of larger *m/z* experiencing larger space charge fields. This *m/z* dependence is the likely explanation of the experimental finding that MSAD preferentially fragmented the lower charge states of reduced mononitrated lysozyme, despite intramolecular space-charge presumably favouring the opposite. Such a dependence is especially important for the observation of weakly bound oligomers (*e.g.* protein dimers) as the average *m/z* of the oligomers gradually increases with its size. MSAD represents one of the more recent and simpler fragmentation techniques available to the FTICR mass spectrometrist. However, in most experimental systems it does not permit the isolation of a parent ion. Collision-induced dissociation (CID) within a Fourier transform ion cyclotron resonance (FTICR) cell is one technique in which a parent ion can be isolated and fragmented. Furthermore, the inherent advantages of high resolution and high mass accuracy are available for the tandem mass spectrometry experiment as well as the standard mass spectrometry experiment. Although correctly estimating the ion population in the cell and performing an external calibration experiment (under near identical conditions) can be problematic, it was demonstrated that errors due to an incorrect estimate of space charge are readily identifiable as the relative mass error increases linearly with *m/z*.

Using this technique it was demonstrated that, without prior separation, FTICR mass spectrometry could identify all of the components of a previously unknown sample and structurally characterise the more intense components. This structural characterisation highlighted new information regarding the low-energy multiple collision CID of substituted polyesters. Included in these findings was the charge-induced nature of the 1,4-H rearrangement (McLafferty rearrangement), the participation of the amino groups in the diaminoanthraquinone-substituted polyester and the collisional ring-opening of the cyclic polymer.

In total, nine distinct polymers were identified in reactint blue of which only two were also present in the synthetic sample, namely polydiethyleneglycoladipate (added in excess) and the planned poly-AQ-poly. Whereas the other seven polymers found in the synthetic sample were the products of base-initiated side reactions, the seven remaining polymers found in reactint blue indicated that aminated polymers were produced prior to the formation of the diaminoanthraquinone polymeric dye. Additionally, polymers were also found in reactint blue that were indicative of an ethyleneglycol contaminant in the diethyleneglycol used to produce the polydiethyleneglycoladipate.

The polymers found in reactint blue were broad and the average molecular weight was dependent on the instrumental conditions used. Nevertheless, as was demonstrated in chapter 5 it was possible to obtain reliable average molecular weights for narrow polymers and copolymers, even though the ethylene oxide/propylene oxide (EO/PO) copolymer included many overlapping peaks. Furthermore, despite the average charge state of the polymer increasing with the polarity of the solvent, apart from the experiment that used a 90:10 H_2O:THF solvent system and yielded weak ion signals, in each case the average molecular weight calculated agreed to within 1 %. In line with the trend of increasing average charge state with increasing solvent polarity, for a specific charge state the average size of the polymer decreased with increasing solvent polarity.
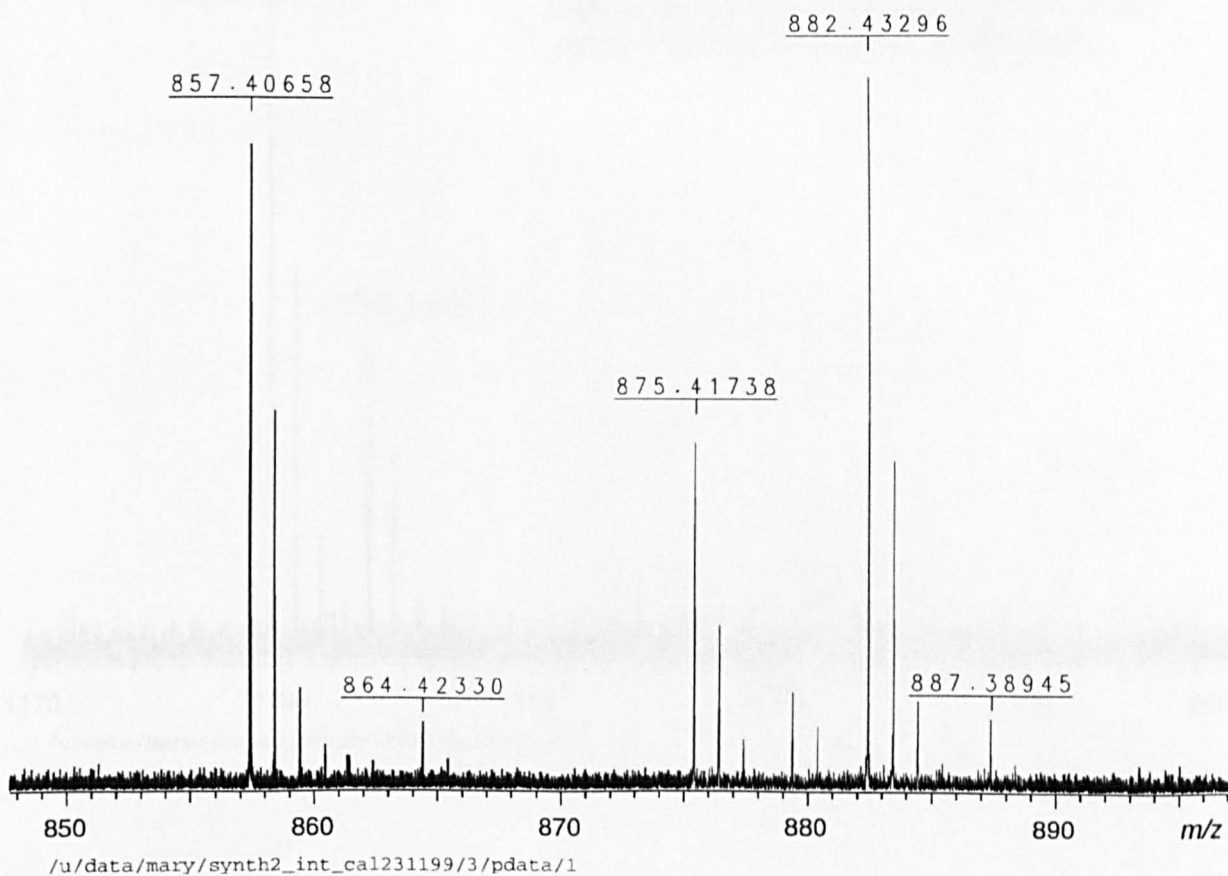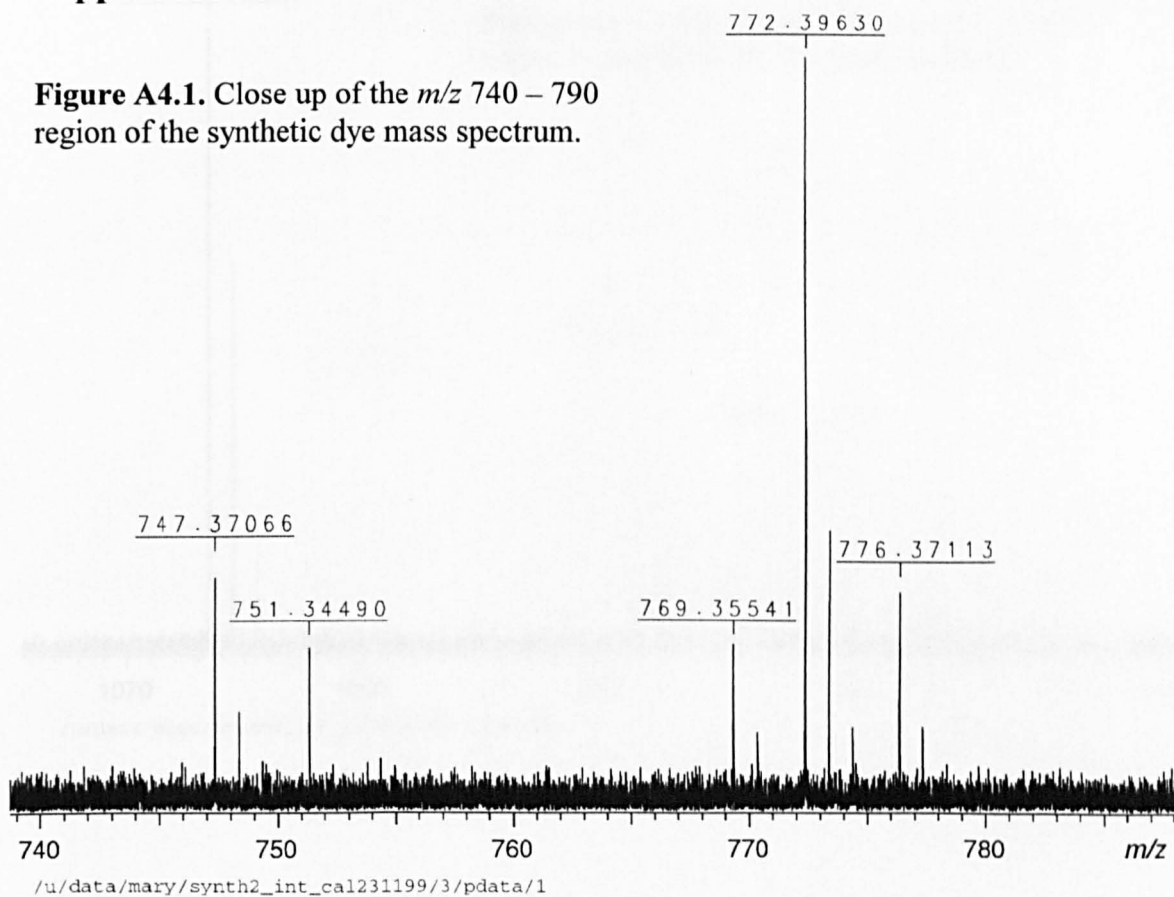
The final chapter concerned an ion imaging study of HCl (2+1) REMPI. In addition to the previously published fragmentation channels, namely production of H*($n = 2$), Cl*(*4s*) and Cl*(*4p*) excited atoms[3], at least two previously unreported channels were detected; one that produced Cl*(*3d*), of which an extrapolation to threshold indicated that the *3d* ^{2}D atomic state was a major contributor, and another that produced Cl*(*4s*).

In agreement with the notion that the $^1\Sigma^+$ superexcited state is responsible for the H*(n = 2) and Cl*($4s$) fragments, their angular distributions were almost superimposable. The angular distribution of the Cl*($4p$) and Cl*($3d$) channels were identical and dependent on the electronic and vibrational state of the resonant state. This was thought to reflect the diabatic character of the resonant state, which in turn determined which superexcited states were accessible.

Finally, vibrational state-dependent HCl$^+$ photodissociation that produced protons and ground state chlorine atoms was also observed. The vibrational state dependency reflected the variation of the transition moment to the $^2\Pi$ repulsive state and the overlap between the wavefunctions of each state.[4]
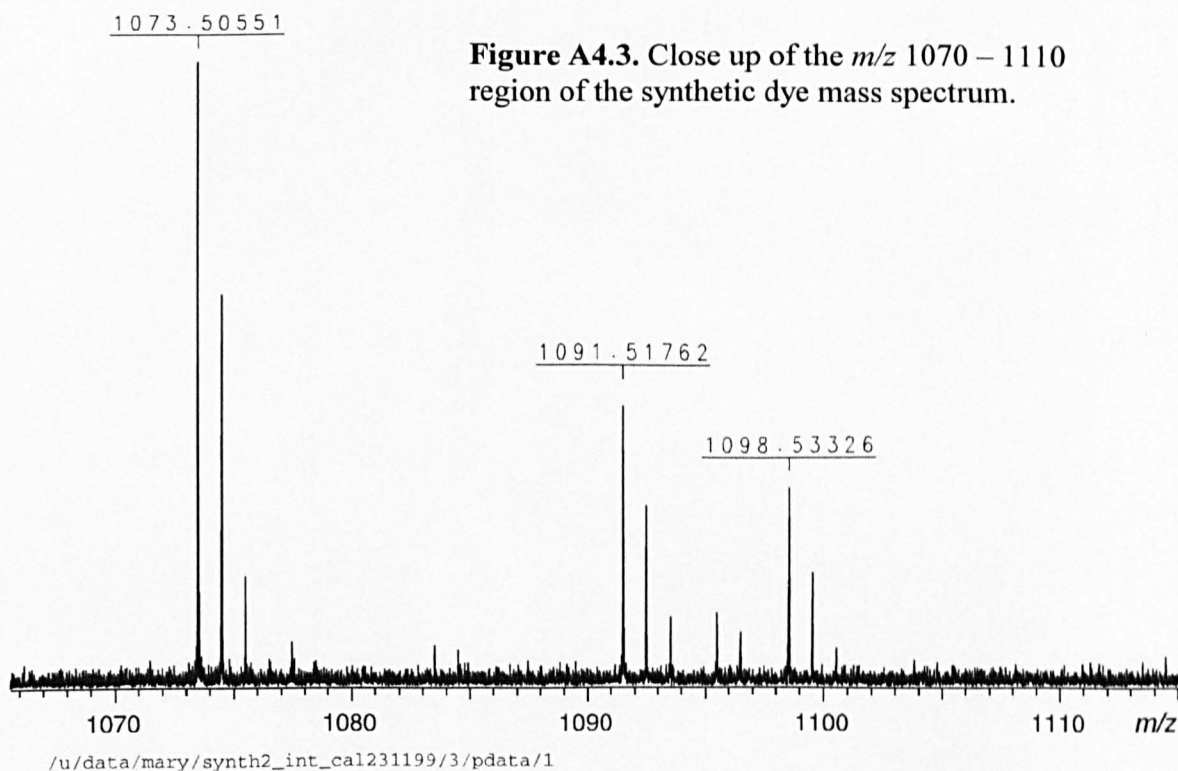
(1)   Gauthier, J. W.; Trautman, T. R.; Jacobsen, D. B. *Anal. Chim. Acta* **1991**, *246*, 211-225.

(2)   Häkansson, K.; Axelsson, J.; Palmblad, M.; Häkansson, P. *J. Am. Soc. Mass Spectrom.* **2000**, *11*, 210-217.

(3)   de Beer, E.; Koenders, B. G.; Koopmans, M. P.; Lange, C. A. *J. Chem. Soc. Faraday Trans.* **1990**, *86*, 2035.

(4)   Pradhan, A. D.; Kirby, K. P.; Dalgarno, A. *J. Chem. Phys.* **1991**, *95*, 9009.

Figure A4.1. Close up of the *m/z* 740 – 790
region of the synthetic dye mass spectrum.

/u/data/mary/synth2_int_cal231199/3/pdata/1

/u/data/mary/synth2_int_cal231199/3/pdata/1

Figure A4.2. Close up of the *m/z* 850 – 900 region of the synthetic dye mass spectrum.

Figure A4.3. Close up of the *m/z* 1070 – 1110 region of the synthetic dye mass spectrum.

/u/data/mary/synth2_int_cal231199/3/pdata/1
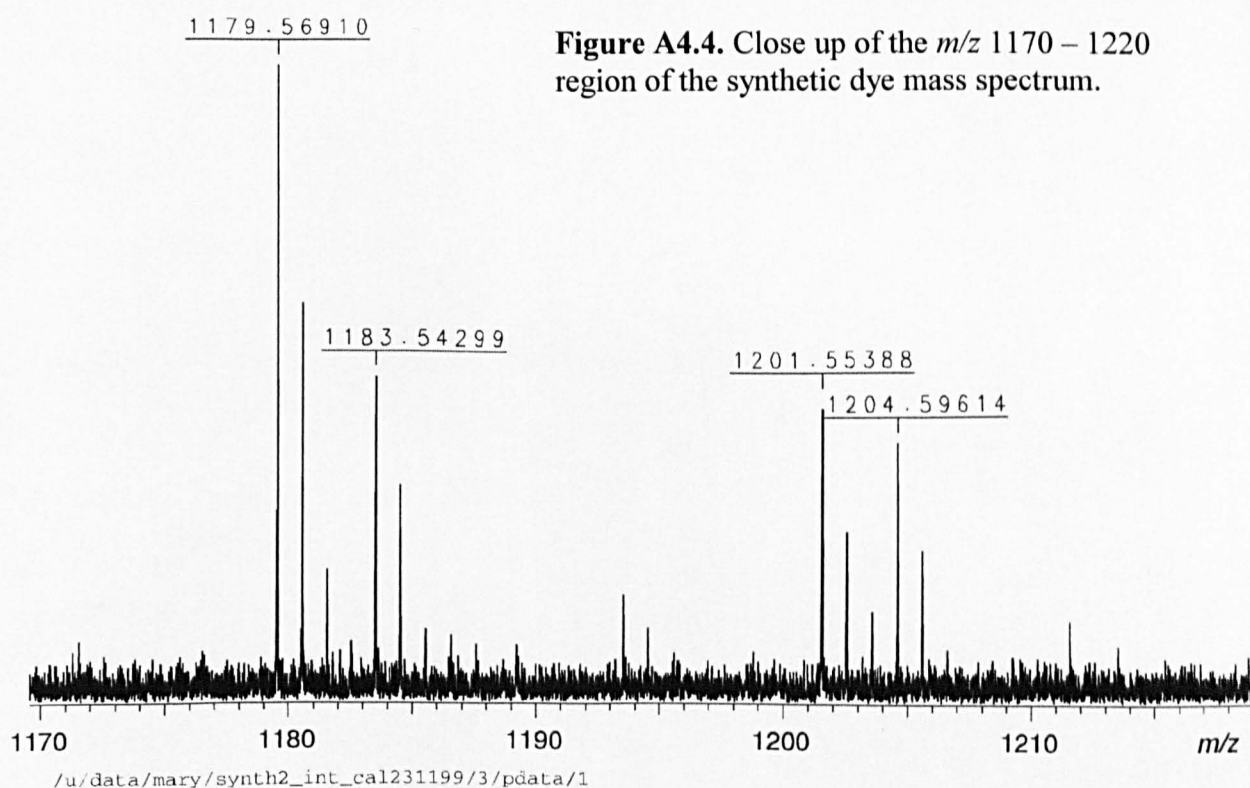
Figure A4.4. Close up of the *m/z* 1170 – 1220 region of the synthetic dye mass spectrum.

/u/data/mary/synth2_int_cal231199/3/pdata/1